



Durham E-Theses

Synthesis and analysis of pseudo-octahedral metal complexes as anticancer agents

CROSS, JASMINE,MARY

How to cite:

CROSS, JASMINE,MARY (2018) *Synthesis and analysis of pseudo-octahedral metal complexes as anticancer agents*, Durham theses, Durham University. Available at Durham E-Theses Online: <http://etheses.dur.ac.uk/12772/>

Use policy

The full-text may be used and/or reproduced, and given to third parties in any format or medium, without prior permission or charge, for personal research or study, educational, or not-for-profit purposes provided that:

- a full bibliographic reference is made to the original source
- a [link](#) is made to the metadata record in Durham E-Theses
- the full-text is not changed in any way

The full-text must not be sold in any format or medium without the formal permission of the copyright holders.

Please consult the [full Durham E-Theses policy](#) for further details.

Academic Support Office, Durham University, University Office, Old Elvet, Durham DH1 3HP
e-mail: e-theses.admin@dur.ac.uk Tel: +44 0191 334 6107
<http://etheses.dur.ac.uk>



**Synthesis and analysis of
pseudo-octahedral metal complexes
as anticancer agents**

Jasmine Mary Cross

A thesis submitted for the degree of Doctor of Philosophy

Department of Chemistry

June 2018

Abstract

Chemotherapy is one of the most predominantly used treatments for cancer. Identifying desirable features required of anticancer agents has rapidly developed alongside our growing understanding of the disease. Metal complexes are of interest as drug candidates as they provide advantages over purely organic systems via modular synthesis, variable geometries and oxidation states. Currently, platinum drugs such as cisplatin remain the most common metal-based treatments, despite their known toxicity towards healthy cells. Viable complexes are therefore sought as alternatives that overcome the limitations of platinum drugs.

The synthesis and analysis of three piano-stool metal complex series are described, each investigating a distinct mechanism of action. Firstly, pyridylphosphinate complexes were employed as potential DNA-binding agents. The complexes possess a labile monodentate halide ligand, which exchanges intracellularly, forming the aqua species, enabling the binding of DNA. The metal, arene and ligand substituents were varied to tune the properties of the complexes. Of the resulting systems, few displayed notable cytotoxicity, and these complexes were pursued no further.

The bulk of this thesis focusses on HDAC enzymes as a discrete target for anticancer therapy. New complexes were developed incorporating arene-metal motifs along with ligands designed to trigger HDAC inhibition. The biological properties of this series were explored and revealed moderate to good cytotoxicity, as well as HDAC inhibition to be the likely mechanism of action. Structural modifications of the parent complexes were devised to optimise selectivity between HDAC enzyme isoforms. Relative to the ligand alone, an increase in specificity of the metal-ligand complexes was observed, successfully demonstrating the benefits of incorporating a metal-arene motif. Biological assays including cellular uptake, catalytic domain selectivity and uptake mechanism are reported to examine the varied behaviour of these complexes.

Hypoxic activation was the final mechanism of action studied. Two complexes were synthesised possessing a reducible protecting group, to produce the active species selectively under conditions of hypoxia. Such activity was utilised to minimise off-target binding and enhance tumour region selectivity.

Declaration

The work described in this thesis was undertaken at the Department of Chemistry, Durham University between October 2014 and June 2018. All of the work reported is my own, except where specifically stated otherwise. No part has previously been submitted for a degree at this any other university.

Statement of Copyright

The copyright of this thesis rests with the author. No quotations should be published without prior consent and information derived from it must be acknowledged.

Acknowledgements

Mum, Dad and family.

Thank you for all the love and support, always.

Although, I'm not entirely convinced you believe this is what I've spent the last four years doing.

Dr. Tim Blower, Dr. Jason Gill, Dr. Robert Pal, Dr. Aileen Congreave, Dr. Matt Kitching,
Dr. Alan Kenwright, Dr. Chris Ottley, Prof. Paul Dyson and Alex Kingdon.

For your outstanding expertise, collaboration and aid.

Department of Chemistry, Durham and the EPSRC.

For the funding and research opportunity.

Jack, Luke, Chris, Archie, Kate, Brette, Aisha, Andrew, Phil, Akkharadet, Jiri, Anica and CG235.

For your time, knowledge, evening beers and the infinite banter throughout the PhD.

Beth, Mel, Kirstyn, Ruth, Libby, Eddy, Carl and Miranda.

For your friendship, understanding, patience and for truly enriched my time in Durham.

Everyone from the Spin Doctors, Ustinov College Pool Soc. and Durham University Cue Sports.

For the awesome (and highly competitive) downtime away from the PhD.

Ustinov College.

For allowing me to be part of an intercultural, interdisciplinary and enlightening community.

Bob, Crystal, Wean, Zoe, Triggy and Wee Rob.

For the good times and giving me long-lived friendship for so many years. Your friendship is
decidedly linked to my good mental health.

Dr James Walton.

Without you this thesis wouldn't have been possible. Your knowledge, enthusiasm, generosity and
encouragement have been invaluable. I couldn't have hoped for a better supervisor.

Finally, this thesis is dedicated to Yan.

Because whatever happens in the future, I wouldn't have made it to the end without you.

Expect to feel pleasure. Knowledge is sexy.

Expect to feel pain. Knowledge is torture.

– Jeff Noon

Abbreviations

Ala	alanine
Asp	aspartic acid
ASAP	atmospheric solids analysis probe
BHT	butylated hydroxytoluene
bpy	2,2'-bipyridine
BSA	bovine serum albumin
CDCl ₃	deuterated chloroform
CD ₃ OD	deuterated methanol
CHCl ₃	chloroform
d	doublet
DCF	2',7'-dichloro fluorescein
DCM	dichloromethane
dd	doublet of doublets
ddq	double of doublet of quartets
DMAP	dimethylaminopyridine
DMF	dimethylformamide
DMSO	dimethylsulfoxide
DFT	density functional theory
DIP	4,7-diphenyl-1,10-phenanthroline
DNA	deoxyribonucleic acid
en	diaminoethane

Abbreviations

ESI	electrospray ionisation
EtG	ethylguanine
EtOH	ethanol
FDA	Food and Drug Administration
Glu	glutamic acid
Gly	glycine
GSH	glutathione
GST	glutathione S-transferase
h	hour
HAT	histone acetyltransferase
HDAC	histone deacetylase
HeLa	immortal human cell line
His	histidine
HRMS	high resolution mass spectrometry
Hz	hertz
ICP	inductively coupled plasma
IC ₅₀	half maximal inhibitory concentration
<i>In situ</i>	in the original place
<i>In vivo</i>	in the living organism
<i>In vitro</i>	in the glass
K	Kelvin
K _a	acid dissociation constant
Leu	leucine

Abbreviations

M	molar concentration
MeOH	methanol
MFI	mean fluorescence intensity
MHz	megahertz
min	minutes
mM	millimolar
MTT	3-(4,5-dimethylthiazol-2-yl)-2,5-diphenyltetrazolium bromide
NAD	nicotinamide adenine dinucleotide
NaOMe	sodium methoxide
nm	nanometer
NMR	nuclear magnetic resonance
NSCLC	non-small cell lung cancer
$^1\text{O}_2$	singlet oxygen
PDT	photodynamic therapy
Phe	phenylalanine
P-pg	plasma membrane glycoprotein
Pro	proline
pta	1,3,5-triaza-7-phosphaadamantane
quin	quintet
RNA	ribonucleic acid
ROS	reactive oxygen species
s	singlet
SCLC	small cell lung cancer

Abbreviations

Ser	serine
SNP	sodium nitroprusside
TEM	transmission electron microscopy
Tf	transferrin
TFA	trifluoroacetic acid
THF	tetrahydrofuran
TopoII	topoisomerase II
TSA	trichostatin A
Tyr	tyrosine
UV	ultraviolet
wt.	weight
Å	angstrom
σ	sigma
π	pi
λ	wavelength
μL	microliter
μM	micromolar

Table of Contents

1. Introduction	8
1.1 Background to Cancer.....	8
1.1.1 Development of Medicine and Treatment.....	8
1.1.2 Chemotherapeutics.....	9
1.2 Metal Complexes as Anticancer Agents	10
1.2.1 Platinum Complexes.....	11
1.2.2 Ruthenium Complexes – A Platinum Group Alternative	15
1.2.3 Ruthenium(II) – Piano-Stool Complexes.....	18
1.2.4 Summary.....	26
1.3 Enzymes as Anticancer Targets	27
1.3.1 Post-Translational Modification.....	30
1.3.2 Histone Deacetylase Enzymes	30
1.3.3 Histone Deacetylase Inhibitors	31
1.3.4 Isoform-Selective HDAC Inhibitors	46
1.3.5 Summary	57
1.4 Hypoxic Activation.....	58
1.4.1 Summary.....	63
1.5 Aims and Specification	64
2. Pyridylphosphinate Metal Complexes	66
2.1 Introduction	66
2.2 Synthetic Aspects	67
2.2.1 Pyridylphosphinate Ligand Synthesis.....	67
2.2.2 Pseudo-Octahedral Pyridylphosphinate Complexes	70
2.3 X-Ray Crystallography.....	72
2.4 Aqueous Behaviour of Pyridylphosphinate Complexes.....	74
2.4.1 Hydrolysis and Ligand Exchange	74
2.4.2 Variable pH Conditions	75
2.5 Cytotoxicity	78
2.6 Binding Studies	80
2.7 Conclusions	83
3. Piano-Stool Complexes as HDAC Inhibitors.....	85
3.1 Introduction	85
3.2 Synthetic Aspects.....	86
3.2.1 Monodentate Ligand Approach.....	86

3.2.2 Bipyridyl Ligand Containing Complex	88
3.2.3 Synthesis of N^{20} -Hydroxy- N^{11} -(1,10-phenanthroline-5-yl)octane diamide (L^2) and Resulting Complexes	90
3.2.4 Metal-Based Belinostat Analogue.....	92
3.3 Hydrolysis Studies.....	94
3.4 Cytotoxicity	96
3.5 HDAC Inhibition Assay	97
3.6 DNA Binding	98
3.7 Protein Binding	100
3.8 Conclusions	102
4. Isoform-Selective Piano-Stool HDAC Inhibitors	104
4.1 Introduction	104
4.2 Synthetic Aspects.....	105
4.2.1 Arene Capping Group Modification	105
4.2.2 Chain Linker Modification.....	110
4.3 Cytotoxicity.....	112
4.3.1 Analysis of L^2 Complexes.....	113
4.3.2 Analysis of L^3 Complexes.....	114
4.4 Active Transport	115
4.5 Cellular Ruthenium Accumulation.....	116
4.6 Isoform Selective HDAC Assays.....	118
4.6.1 HDAC1 & HDAC6 – IC ₅₀ Results	122
4.6.2 HDAC6 Catalytic Domain Assay	124
4.7 Enzyme Modelling.....	126
4.8 Conclusions.....	130
5. Hypoxia-Activated HDAC Inhibitors	133
5.1 Introduction.....	133
5.2 Synthetic Aspects.....	134
5.3 NMR Studies.....	135
5.4 Cytotoxicity.....	138
5.5 Conclusions.....	139
6. Conclusions and Future Work.....	140
6.1 General Conclusions.....	140
6.2 Future Work	145
6.3 Final Remarks	147
7. Experimental.....	148

7.1 Experimental Procedures.....	148
7.1.1 General Procedures	148
7.1.2 X-Ray Studies	149
7.1.3 HPLC Analysis	149
7.1.4 Optical Techniques	150
7.1.5 DNA Binding Experiments.....	150
7.1.6 Cytotoxicity	151
7.1.7 Cellular Uptake	152
7.1.8 Enzyme Inhibition Assays	152
7.1.9 HDAC Catalytic Domain vis Ligation Dependent Cloning.....	153
7.1.10 Molecular Modelling.....	154
7.2 Synthetic Procedures.....	155
Appendix 1.....	199
Crystal Structure Data	199
Complex Ru1PP3	199
Complex Ir1PP6.....	202
Appendix 2.....	205
Equations and Derivations.....	205
Acid Dissociation Constant (K_a) – Chapter 2.....	205
Dose Response Curves – Chapters 2, 3 and 4.....	206
UV-Vis Titrations	207
Appendix 3.....	208
Key Ligands and Complexes.....	208
Appendix 4.....	211
Publications	211
Oral & Poster Presentations	211
References.....	212

1. Introduction

1.1 Background to Cancer

1.1.1 Development of Medicine and Treatment

Our understanding of cancer has progressed significantly in the last few decades. The relationship between prevention, cure and treatment has been widely discussed and studied. In modern medicine, initial screening of patients for cancer can prevent the spread of primary tumours by metastasis to other sites or organs. Early prognosis can improve patients' overall chances of survival and general recovery rate.¹

The advancement in technology and medicine has spawned a variety of treatments including: radiotherapy,² hormone therapy,³ chemotherapy,⁴ immunotherapy⁵ and other alternatives. The predominant combination method to treat cancer remains the surgical removal of malignant tumours, allied with chemotherapeutics or radiation therapy.⁶ Although this is the most common method of treatment, it is far from infallible. It is exceptionally difficult to remove every remnant of a tumour through surgery. This can inevitably lead to a resurgence of the cancer by metastasis or malignant cell proliferation.⁶ The use of both drug agents and ionizing radiation can also be damaging to normal, healthy cells.

A prominent issue facing cancer treatment development is the constant mutability of various types of cancer, including (but not limited to) oncogenic mutations of the p53 tumour suppressor protein which regulates cell cycle.⁷ Certain drug-based treatments may be successful initially, but the abnormally high mutation rate can cause rapid resistance. In such cases, the resistance can arise through prolonged use of a particular drug or with similar, analogous drug candidates. Current anticancer therapies often rely on the direct drug binding to DNA, leading to apoptosis. When normal cells undergo DNA damage they will arrest their cell cycle until they are repaired.⁶

The exposure to multiple chemotherapeutic agents (combination therapy) is becoming more and more common to target heterogenous tumour cell populations.⁶ It is also becoming more prevalent in anticancer drug research to target specific biomolecules that aim to prevent high levels of toxicity to normal cells and pin-point precise cancer mutations on a subcellular level. The progress of chemotherapy in this direction will be discussed further during the course of this work.

1.1.2 Chemotherapeutics

Humans have relied upon natural products with medicinal properties for centuries; the treatment of cancer is no different. Both doxorubicin and taxol (*Figure 1.1*) are early examples of natural products used as anticancer agents.

Doxorubicin is an organic molecule classified as an anthracycline, isolated from the bacterium *Streptomyces*. It has multiple sites of stereoisomerism and a large conjugated ring system providing its characteristic red pigmentation.⁸ Doxorubicin shows significant activity towards solid tumours e.g. small lung cell, breast cancer and ovarian carcinomas. It also has high efficacy for lymphomas.⁹

Anthracyclines including doxorubicin enter cells by passive diffusion.¹⁰ Once inside the cell, multiple pathways are thought to be the cause of the cytotoxicity. Kiyomira *et al.* suggest the mechanism proceeds by doxorubicin forming a drug-proteasome complex which is translocated to the nucleus of neoplastic cells.¹⁰ In the nucleus it preferentially binds via intercalation to the DNA of chromatin, mediating apoptosis. The basicity of the free amino-group allows hydrogen bonding to cytosine-19, increasing the affinity of the doxorubicin-DNA adduct.⁹

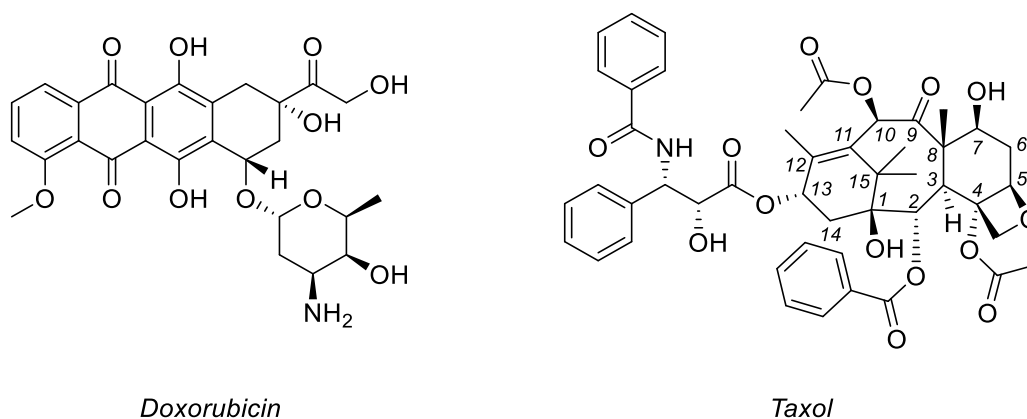


Figure 1.1 Examples of natural product anticancer agents.

Taxol is isolated from the *Taxus brevifolia* (yew tree) and is another example of a complex natural product used in cancer treatment. It was approved through clinical trials in 1992 and is primarily used in the treatment of breast and ovarian cancer.¹¹

The structure-activity relationship of taxol has been widely discussed because of the many functional groups and stereochemical topographies within the structure. Although considered a relation to the diterpene group of molecules, taxol includes an unusual oxetane ring addition (seen

at C4-C5). It has been observed that ring-opening of the oxetane moiety, yields products that are less active in cytotoxic assays.¹¹

Taxol works as an antimetabolic drug, targeting the polymerisation of the cellular protein tubulin. By binding to tubulin, it promotes the intracellular assembly of microtubules causing defects in cell division ultimately triggering apoptosis.¹¹ At concentrations of 0.25 μM the division of exponentially replicating HeLa cells can be inhibited, suggesting the proficiency of taxol as an antiproliferative agent as well.¹²

While the merits of natural products are observed keenly in these examples, both taxol and doxorubicin harbour significant disadvantages as cancer drugs. The isolation of taxol is exceptionally low yielding with even improved methods only reaching 0.014% of the desired product from the source.¹¹ Considering high doses of taxol are required for treatment, the issue of a limited supply lends to an equally unfavourable synthetic approach to produce this drug. In contrast the isolation of doxorubicin is much simpler due to its metal co-ordinating ability.¹³

Side effects such as vomiting, hair loss and myalgia are common with most forms of chemotherapy. However, specific side effects for taxol and doxorubicin vary in severity. The administration of taxol requires an emulsion with a polyethoxylated castor oil due to its poor solubility in water. Frequently, patients incur varying degrees of allergic reactions to this emulsion due to the quantity dosed intravenously¹¹. By comparison, treatment using doxorubicin has shown drug induced congestive heart failure, increasing the mortality risk to patients; especially those of advanced age.^{9,14}

1.2 Metal Complexes as Anticancer Agents

Not all metal ions are found naturally in biological systems. Labile metal ions that allow fast ligand exchange in their coordination sphere are preferred. These include Na^+ , K^+ , Mg^{2+} and Ca^{2+} , as well as first row transition metal ions - particularly Mn, Fe, Co, Ni, Cu and Zn. The first-row transition metals are often stabilised by binding to biomolecules and often form catalytic sites in metalloenzymes. The concentration of such metals is regulated by cellular processes to limit the potential toxicity in the body.

Heavy metal ions of the second and third-row transition metals are not commonly found in biology. Although originally displaying high levels of toxicity in biological systems, they have emerged as potent chemotherapeutics and valuable to diagnostic medicine.¹⁵ The use of transition metal-centred complexes as alternatives to organic extracts in chemotherapy provides some key advantages. Functional properties for drug design of inorganic compounds include: exchangeable

ligands, modular synthesis, as well as variable oxidation states and geometries. These factors allow metal centred complexes to be tuned for targeted treatment.

1.2.1 Platinum Complexes

The interest in platinum complexes was initiated by the serendipitous discovery of their ability to inhibit cell division in *Escherichia coli*. The discovery was made by Barnett Rosenberg and co-workers in 1965 during a biophysics experiment.¹⁶ It was proposed that the production of long-lived complexes occurred during electrolysis, from a reaction between the medium used and oxidised species formed from the platinum electrode. No specific species was identified at this time, but the low concentration of complexes (1 to 10 ppm) required to inhibit cell division in *E. coli* while not interfering with cell growth prompted further investigation.

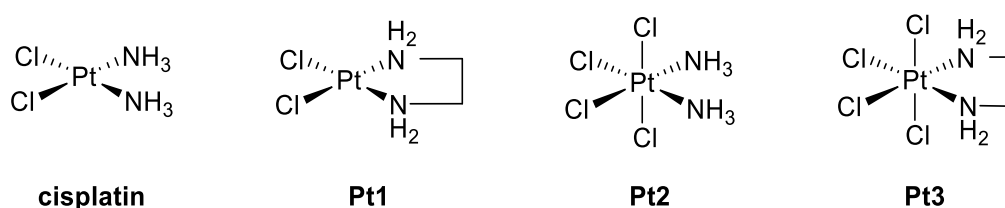


Figure 1.2 Platinum compounds tested for antitumour activity.^{17,18} **cisplatin** *cis*-[Pt(NH₃)₂Cl₂]; **Pt1** [Pt(1,2-diaminoethane)Cl₂]; **Pt2** *cis*-[Pt(NH₃)₂Cl₄]; and **Pt3** [Pt(1,2-diaminoethane)Cl₄].

By 1969 a range of platinum complexes were identified as potent antitumour agents (*Figure 1.2*). Both Pt(II) (cisplatin and **Pt1**) and Pt(IV) (**Pt2** and **Pt3**) complexes were tested *in vivo* against sarcoma 180 and leukaemia L1210. Cisplatin displayed the highest efficacy as an antileukemic agent with some mice appearing tumour free months after the treatment.¹⁷ By the late 1970s, cisplatin had completed phase III clinical trials and showed promising results in combination therapy for the treatment of numerous human cancers including bladder, testicular, ovarian and prostate.¹⁸ It was approved for medical use in 1978.

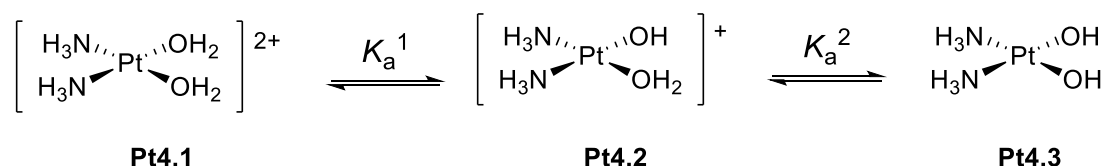


Figure 1.3 Aquated cisplatin at increasingly basic conditions. ($\text{p}K_a^1 : 5.51$, $\text{p}K_a^2 : 7.31$).¹⁸

The properties of cisplatin were later determined, to help elucidate correlations between its biological mechanism and chemical structure. As cisplatin is injected intravenously, high chloride ion concentration of extracellular fluid (0.1 M) prevents the exchange of chloride ligands, maintaining the chemical composition of the drug. Once inside the cell, the lower chloride ion

concentration (0.004 M) shifts the thermodynamic equilibrium, promoting dissociation of chloride ligands in favour of water or hydroxyl ligands.¹⁹ Using conductimetry, it was shown *in vitro* that the structure of the aqua species was pH dependent (*Figure 1.3*).¹⁸ In neutral conditions the molecule is predominantly the dihydroxy species **Pt4.3**, while a charged state at more acidic pH as aqua ligands are favoured (**Pt4.1** and **Pt4.2**).

After cisplatin crosses the cell membrane, the subsequent hydrolysis products can bind to their desired targets. Lippard discussed the significance of cisplatin forming the most stable linkages to definite nucleobases, detailing a binding preference for the N7 atom of guanine with a stabilised intramolecular hydrogen bonding by co-ordinated water and the exocyclic oxygen atom.²⁰ Gowda and co-workers would later conclude that the affinity of cisplatin for guanine bases can produce interstrand, intrastrand (*Figure 1.4*) and monofunctional adducts cross-linking DNA. This suggests the binding of cisplatin is not always exclusive to adjacent guanosine nucleosides.²¹

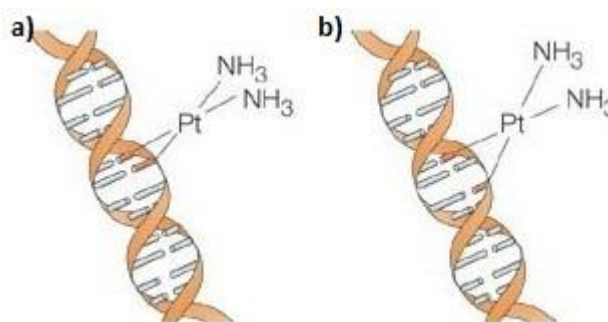


Figure 1.4 Cisplatin guanine-guanine base pair binding in DNA showing a) 1,2 crosslinks and b) 1,3 crosslinks.²¹

As early as 1970, Rosenberg was an advocate of the ability of cisplatin to selectively inhibit DNA synthesis.²² Nucleic acid interactions *in vitro* were further studied by Roberts and Pera displaying DNA as the most susceptible target at pharmacologically relevant doses, compared to previously speculated RNA and protein binding.²³ Inactivation of the DNA template for replication occurs when cisplatin is bound and the change is not recognised by repair enzymes. This causes drug-induced cell death as a function of chromosome damage, observed in the first or second mitotic cycle after treatment.²³ The *cis*-square planar geometry is integral to the highly mutagenic effects of cisplatin by allowing a bidentate chelate to the metal centre from the DNA double helix. The *trans* derivative is unable to form the same intrastrand cross-links in d(GpG),²⁴ showing the significance of isomerism and structure, for both the mechanism of action and potency of cisplatin.^{20,22,23,25}

Unfortunately, therapeutic complications are becoming more ubiquitous across a broad range of cell lines as tumour resistance to cisplatin continues to develop. Primary investigation of resistance in both ovarian and lung cancers found a correlation between levels of glutathione S-transferase

(GST) and platinum drug toxicity.^{26,27} A comparison of small cell lung cancer (SCLC) and non-small cell lung cancer (NSCLC) by Nakagawa *et al.* showed a higher sensitivity to cisplatin in SCLCs than NSCLCs, which possess much lower mRNA expression of the GST gene.²⁷ It is hypothesised that GSTs form cisplatin-thiol conjugates with highly reactive aquated cisplatin, prohibiting binding to DNA.²⁸

Resistance is now considered to be multifactorial. Various signalling pathways from cisplatin-induced cellular effects culminate in apoptosis, however resistance interferes with the activation of these pathways. For instance, drug accumulation within the cell has been reduced between 20-70% in many cases.²⁸ This mode of resistance arises from limiting passive diffusion by inhibition of drug uptake or increased drug efflux from the cell. Topoisomerase II - an enzyme linked to the repair of cisplatin-DNA adducts - is overexpressed in clinical cancer cases. The improved recognition of DNA damage is another factor associated with cisplatin resistance.²⁸

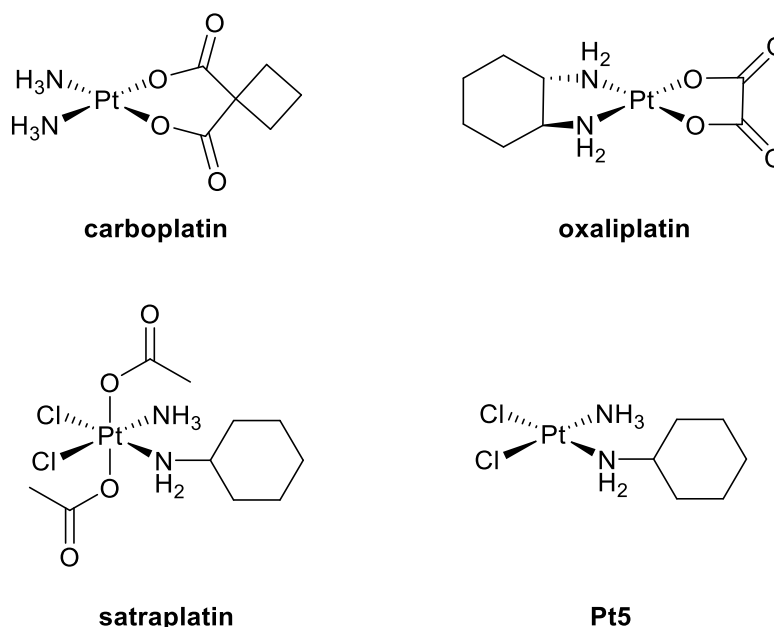


Figure 1.5 Alternative platinum drug candidates.

Cisplatin could evidently not be relied upon as the only inorganic anticancer drug candidate. Low solubility, systemic toxicity to normal tissues and more frequently reported cases of cisplatin resistance prompted the synthesis of second generation platinum compounds (*Figure 1.5*). The role of the ligands within cisplatin analogues was analysed by Zunino *et al.* in 1987.²⁵ Ligands bound too strongly were found to produce kinetically inert complexes while highly labile ligands produced candidates which were too toxic. Bidentate dicarboxylate ligands – seen in both carboplatin and oxaliplatin – are often favoured due to the requirement of intercellular metabolism to activate their cytotoxic effects. The non-leaving groups tend to be amines (aliphatic, branched or

bidentate) and generally accompany platinum to the target macromolecule. They appear to play a significant role in hydrogen bond interactions with polar groups of DNA, modulating toxicity and tumour effects depending on their structure.²⁵

Both carboplatin and oxaliplatin produced a comparable effect profile to cisplatin with less severe side effects and were approved for worldwide use in 1978 and 2002, respectively.²⁹ Unfortunately, carboplatin developed rapid cross-resistance to cisplatin, showing similar lack of drug accumulation. Complex oxaliplatin contains a 1,2-diaminocyclohexane ligand, that is thought to be responsible for the different spectrum of activity and the lack of cross-resistance it presents.²⁵ Subsequent trials explored combination therapies and found dosing cisplatin and oxaliplatin in an additive manner yielded promising synergistic results.³⁰

Satraplatin is a prospective candidate in the analogous cisplatin series, possessing more favourable physicochemical properties. Unlike existing platinum drugs that are limited to intravenous administration, the axial acetate ligands in satraplatin increase lipophilicity of the complex improving oral bioavailability.³¹ The reduction of satraplatin from its substitutionally inert, parent Pt(IV) form to the Pt(II) active complex, produces an analogous complex to cisplatin (**Pt5**), considered essential for activity. Initially, reduction of satraplatin was thought to proceed by reductive elimination and dissociation of the two axial acetate ligands in the blood, largely dependent on the presence of biological nucleophiles (GSH) or antioxidants (ascorbate).³² However, it was deemed naturally occurring concentrations of such biological molecules were not sufficient to reduce satraplatin to its active species (**Pt5**). An alternative mechanism was proposed by McLeage *et al.* suggesting red blood cells were necessary for the production of **Pt5**. Through *in vitro* experiments, they determined the involvement of iron atoms found within haem complexes (abundant in red blood cells) produced the reduced form of satraplatin (**Pt5**), concurrent with the oxidation of haemoglobin.³³ Binding of carbon monoxide to haemoglobin, inhibited this particular biotransformation, implying metal-containing redox proteins are required for the activation of satraplatin.^{32,33}

The asymmetric structure of **Pt5** adhered to the same mode of binding as cisplatin through inter- and intrastrand cross-links of DNA. However it is reported, DNA mismatch repair proteins fail to recognise the larger cyclohexylamine adduct, signalling a successful apoptotic response.³⁴ In some cisplatin-resistant cell lines, the DNA mismatch repair protein is defective. This mode of resistance is therefore avoided when using satraplatin as a chemotherapeutic agent.^{31,34} Although the attributes of satraplatin as a drug candidate are promising, it is yet to gain FDA approval.

For all its pitfalls, cisplatin remains one of the most extensively used anticancer agents in modern day chemotherapy. While platinum responsiveness is high in many patients, a relapse due to

resistance is commonplace. Combinatorial strategies employ existing natural product drugs (Section 1.1.2) which when used in tandem, can overcome toxicity towards normal tissue and increase sensitivity by targeting multiple mechanisms.³⁵ Alternative inorganic drug candidates are being currently investigated to find less hindered chemotherapeutic options.

1.2.2 Ruthenium Complexes – A Platinum Group Alternative

In response to platinum resistance, other platinum group metal complexes are being studied and, in some cases, have exhibited promising efficacy against solid tumours. Ruthenium is of particular interest as it displays notably lower toxicity towards healthy cells. Not only this, ruthenium boasts a variety of suitable biological properties encouraging its candidacy for medicinal applications.

As discussed previously, the benefits of tuneable ligand exchange are often linked to activity in anticancer agents. This promoted the use of Ru(II) and Ru(III) complexes as they host similar ligand exchange kinetics to Pt(II) centred complexes³⁶. Under physiological conditions, ruthenium is unique within the platinum group as Ru(II), Ru(III) and Ru(IV) oxidation states are all accessible. More biologically inert Ru(III) complexes are easily reduced by glutathione, single-electron transfer proteins or by cellular conditions like pH and oxygen concentration (Figure 1.6). It has been suggested that ruthenium drugs are also believed to mimic iron by binding to biomolecules such as transferrin (Tf).³⁷ Cancerous cells require heightened levels of iron due to rapid cell division. To accommodate this, transferrin receptors are overexpressed on the surface of these cells. This is thought to account for low levels of toxicity shown by ruthenium complexes towards healthy cells due to their potential affinity for transferrin.³⁷

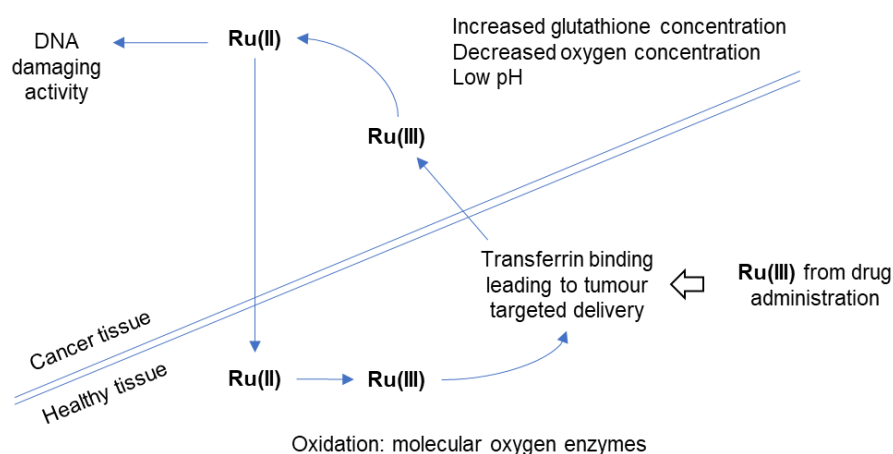
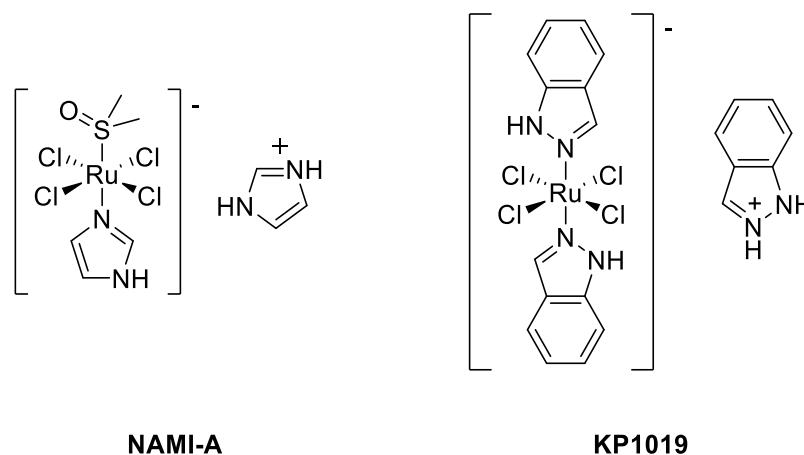


Figure 1.6 Observed oxidation state changes of ruthenium in cancer and healthy cells.³⁷

NAMI-A and KP-1019 are two examples of ruthenium based anticancer agents that entered clinical trials. They share an octahedral geometry, Ru(III) oxidation state and four in-plane chloride

ligands. Both complexes contain nitrogen-bound aromatic heterocycles as ligands; NAMI-A possessing asymmetry with the presence of a dimethylsulfoxido ligand *trans* to an imidazole.



A study in 1999 by Sava *et al.* probed the potential activity of NAMI-A compared to cisplatin. Predictions based upon similarities with cisplatin – sharing a heavy metal centre from the same group – were revoked when NAMI-A showed virtually no cytotoxicity *in vitro* at concentrations up to 100 μM .³⁸ Surprisingly, NAMI-A displayed unprecedented behaviour *in vivo* causing a marked reduction on lung metastasis in mice, implanted with Lewis lung carcinoma, TS/A adenocarcinoma or MCa mammary carcinoma. Post-surgical treatment with NAMI-A caused an increase in life expectancy comparable to cisplatin, in particular of mice bearing a MCa mammary carcinoma.³⁸

Following up on previous findings, Sava examined tissue samples from the organs of transplanted mice. Using TEM analysis, electron-dense ruthenium is highly visible. An abundance of NAMI-A was located along collagen fibres of the lung, particularly around collagen-rich metastatic foci regions.³⁹ The binding to extracellular matrix collagen is attributed to the slower release of NAMI-A from the lungs compared to other organs.³⁹ A dual-activity was proposed by Sava *et al.* suggesting not only is antimetastatic activity retained by the presence of NAMI-A in the lungs, but also through selective targeting of metastasising tumour cells.³⁹

The classical DNA-binding mechanism was also investigated as a mode of action by Pluim and co-workers in 2004.⁴⁰ Calf thymus DNA incubated with both cisplatin and NAMI-A showed both drugs bound in a linear fashion with NAMI-A mirroring the interstrand adducts formed by cisplatin. This experiment was not a concerted approach to assigning activity as it was already well publicised that NAMI-A enters cells by a facilitated mechanism like cisplatin but with much greater difficulty.⁴⁰ The poor cytotoxicity detailed by Pluim also fails to support DNA binding as the cause of activity. DNA interactions overall required concentrations which are not physiologically relevant when considering a drug candidate and despite numerous studies, the mechanism of NAMI-A is still debateable.⁴¹ Regrettably, during phase II clinical trials, no patients

exhibited partial remission as a best response from combination treatment of NAMI-A with gemcitabine. These results prompted the termination of clinical trials.⁴²

KP1019 is another ruthenium-based example of a tumour-inhibiting drug.⁴³ Primary issues with solubility were overcome by formulating the indazolium salt *in situ* from the more soluble sodium salt. Models using colorectal carcinomas in rats, which closely resemble the same tumours in humans, showed superiority of KP1019 over the standard drug administered.⁴³ Decrease in tumour volume to 40% was observed for 5-fluorouracil, an established and effective treatment for colorectal cancer, while KP1019 caused a more pronounced reduction in volume to only 8%.⁴⁴ Studies run in parallel, found KP1019 to maintain the general low toxicity improved upon from platinum drugs, similar to NAMI-A.

The glycoprotein transferrin (Tf) - already briefly mentioned - is credited for the low toxicity of KP1019 towards healthy cells, according to Keppler *et al*, along with serving as the pathway of uptake⁴⁵. Tf has two specific Fe(III) binding sites and a concentration of 35 μM in the blood, enabling it to act as an abundant, natural drug carrier for KP1019.⁴⁶ Keppler used a variety of tests to determine the likelihood of transferrin mediated transport. Adducts of KP1019 onto apolactotransferrin (a protein with high sequence homology to human transferrin) observed from crystal structure data, showed KP1019 bound specifically to histidine-253 amino acid and preserved co-ordination of the indazole ligands.⁴⁴ Saturation of transferrin is preferable as it binds more strongly to receptors on the surface of the cell when both iron-binding sites are occupied. Although competitive binding of Fe(III) ions and KP1019 was confirmed, *in vitro* experiments using SW480 cells loaded with equimolar concentrations of KP1019 and physiological Fe(III) (30%) showed a 2-fold higher uptake of ruthenium species into the cells versus incubation with only KP1019.⁴⁴ The bulky ligands of KP1019 are thought to cause conformational distortion of transferrin when bound to both sites which is less recognisable by the transferrin receptor, therefore binding of stoichiometric amounts of Fe(III) and KP1019 is desirable.

Apotransferrin binds KP1019 strongly and requires mild acidic conditions for its removal. Hypoxic conditions of tumours promote the release of KP1019 compared to that of normal tissue.⁴⁷ Activation by reduction is hypothesised to be the mechanism of action of some prodrugs. Ascorbic acid (a mild reducing agent) is predominantly found in the blood environment where minimal reduction of KP1019 is detected. Instead, it is proposed that once released from transferrin, KP1019 is reduced by thiol containing glutathione found between 0.5 to 10 mM concentration within the cell⁴⁸. This suggestion correlates an increase of Ru(III) reduction potential with increased antiproliferative activity in SW480 colon carcinoma cell line supporting the activation by reduction mode of action. Keppler and co-workers also noted apoptosis of SW480 cells occurs through the intrinsic mitochondrial pathway when dosed with KP1019 through a loss in

mitochondrial membrane potential. This implies the significance of ruthenium redox chemistry of this promising drug candidate.⁴⁷

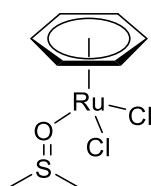
A combined effort of NAMI-A and KP1019 display the potential for ruthenium drug candidates. Even though both NAMI-A and KP1019 are structurally similar, it is apparent they do not share a mechanism of action or a specific target for activity.^{44,47} Indeed, the unconventional antimetastatic activity towards lung cancer of NAMI-A could not be more disparate to the colorectal, carcinoma neoplastic agent KP1019. Despite the shared oxidation state and geometry, these contrasting differences advocate the continued examination of ruthenium based anticancer drugs.

1.2.3 Ruthenium(II) – Piano-Stool Complexes

A more contemporary approach to metal-centred anticancer complex design has exploited the *pseudo*-octahedral, or “piano-stool” complexes. Unlike the coordination compounds discussed previously, the complexes here on in conform to the class of organometallic complexes, containing a lipophilic arene motif, stabilising the Ru(II) oxidation state. Reviews published by Dyson⁴⁹, Suss-Fink⁵⁰ and Sadler⁵¹ (among others) have detailed and compared a myriad of examples of half-sandwich piano-stool compounds that show varying success as potential anticancer agents. The following section will highlight the functionalities and properties of piano-stool complexes that are of key relevance to this project.

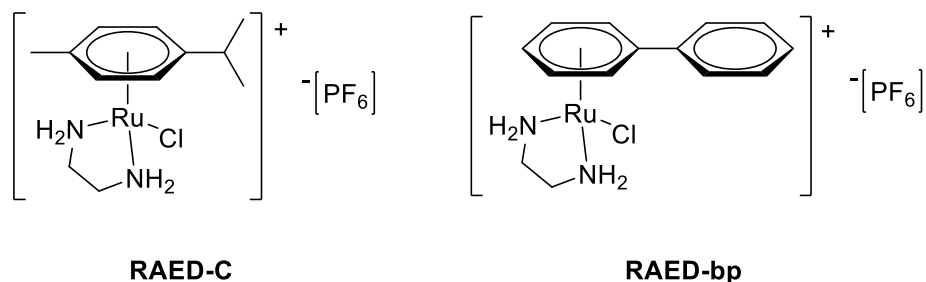
1.2.3.1 The First Examples

One of the earliest demonstrations of anticancer activity from a half-sandwich complex was by Kondapi *et al.* in 1999. A simple molecule RuDMSO, comprising a benzene arene, two chloride ligands and a dimethylsulfoxide ligand around a Ru(II) metal centre, was linked to poisoning of topoisomerase II (topoII) – an important enzyme in DNA religation – and yielded antiproliferative effects.⁵² At drug concentrations of 300 μM , Crit-2 (nonhodkins human lymphoma) displayed 87% inhibition of cell growth. Whilst the potency of this drug is considerably lower than other examples of antineoplastic agents, it was an intriguing result from a piano-stool complex at this time. Inhibition of enzyme targets as a mode of action for anticancer activity will be further analysed in *Section 1.3*.



RuDMSO

In 2001, Sadler *et al.* synthesised a range of positively charged piano-stool compounds containing a bidentate diaminoethane (en) ligand. Complex RAED-C showed good solubility in water, with substitution of the chloride ligand for water in dilute solution (0.2 mM) to provide 60% as the aqua adduct. Approximate physiological conditions of NaCl (0.1 M) suppressed hydrolysis leaving 81% of complex RAED-C intact. Known intercellular conditions indicate the potential activation of these complexes to the aqua species, permitting reactions with DNA by a similar mechanism to cisplatin.⁵³



Cellular assays on the human ovarian cancer cell line A2780 gave IC_{50} values of 9 and 6 μM for RAED-C and RAED-bp respectively, comparable to the control carboplatin (6 μM).⁵³ Increased hydrophobicity marked an overall trend in cytotoxicity. Follow up studies investigated *in vitro* and *in vivo* effects of the $[(\eta^6\text{-arene})\text{Ru}(\text{en})\text{Cl}]^+$ complexes on the A2780 cisplatin resistant (A2780cis) cell line and parent xenografts. A 10 mg kg^{-1} dose was the maximum tolerated administering cisplatin whereas, RAED-C allowed 25 mg kg^{-1} dose without weight loss of mice with an A2780 xenograft.⁵⁴ However, both complexes RAED-C and RAED-bp displayed significant cross-resistance with the A2780cis cell line, a reduced potency which was mirrored in the xenograft results.⁵⁴ The resistance mechanism was rationalised exclusively as an overexpression of the plasma membrane glycoprotein P-gp in A2780cis cells. Lipophilicity and a cationic centre are favourable in P-gp substrate recognition, increasing the efflux of $[(\eta^6\text{-arene})\text{Ru}(\text{en})\text{Cl}]^+$ complexes from the cell, reducing drug accumulation.⁵⁴

The positive results against A2780 cells prompted scrutiny into mode of action of these complexes. Crystallisation of RAED-bp with 9-ethylguanine and guanoside base (*Figure 1.7*) in place of the chloride ligand allowed spatial interpretations of potential DNA binding. Simultaneous N7 binding of guanine to the ruthenium centre, along with π -stacking interactions between the pendant phenyl of RAED-bp and the 5-membered purine ring encourage intercalation as a mechanism.⁵⁵ Strong hydrogen bonding of the carboxyl oxygen of guanine and the closest NH of the en ligand was specific to this base. These features support DNA recognition at guanine, correlating with oligonucleotide experiments which observed a favourable monoruthenated species at G₇ on DNA 14-mer d(ATACATG₇GTACATA).^{53,55,56} Continued optimisation of the $[(\eta^6\text{-arene})\text{Ru}(\text{en})\text{Cl}]^+$

complexes by Sadler *et al.* was justified by the specific DNA binding and promising antitumour activity of these complexes.

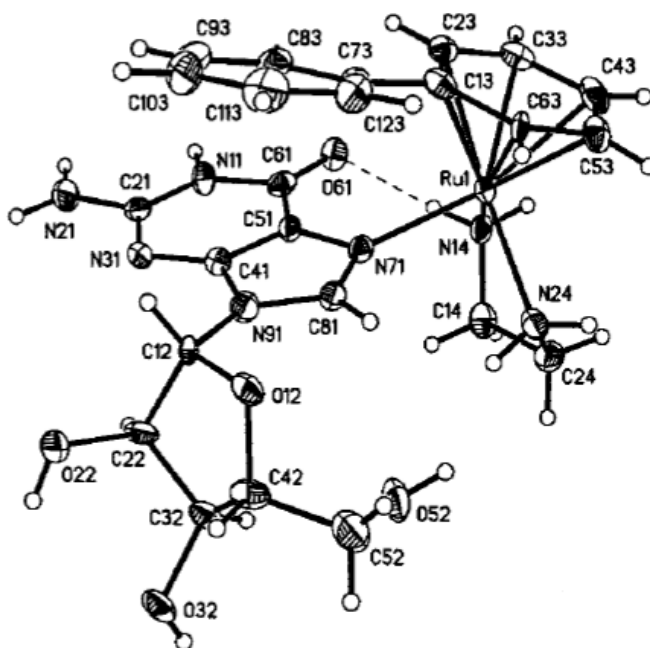


Figure 1.7 X-ray crystal structure of RAED-bp with chloride exchanged for a guanoside base showing 30% probability ellipsoids. H-bonding interactions of enamine NH and G O6 are indicated with a dotted line.⁵⁵

1.2.3.2 RAPTA Complexes

Another group of ruthenium half-sandwich complexes to consider are the RAPTA complexes (*Figure 1.8*) studied by Dyson *et al.* extensively. These compounds encompass a monodentate 1,3,5-triaza-7-phosphaadamantane (pta) ligand, bound through the phosphorus atom and are highly water soluble. Like many of the compounds mentioned previously, the prototype RAPTA complex (RAPTA-C) was tested for DNA binding in early experiments. Running gel electrophoresis on supercoiled (SC) DNA incubated with RAPTA-C over a 6.0-8.0 pH range showed a progressive increase in retardation of the DNA at reduced pH.⁵⁷ The pK_a of pta (6.5) would inherently promote the protonated species at such lower pH, facilitating interactions between negatively charged DNA slowing migration. These initial observations suggested the possibility of a higher affinity of RAPTA-DNA binding in a hypoxic environment.⁵⁷

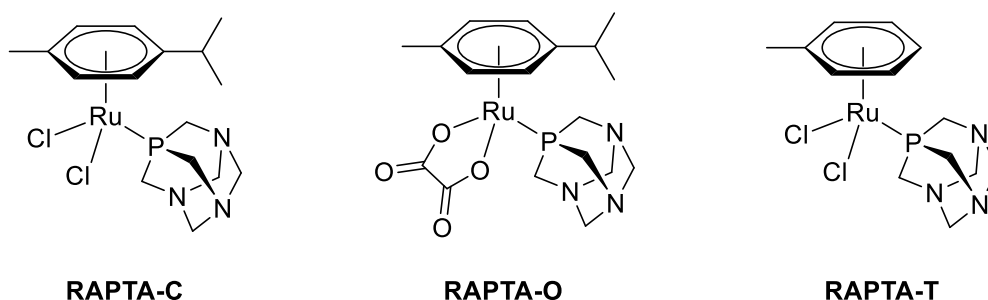


Figure 1.8 A selection of RAPTA complexes.

Behaviour of RAPTA-C in solution is partially akin to that of cisplatin. While cisplatin sees rapid hydrolysis of one chloride once inside the cell, the second chloride-water exchange is much slower, unlike RAPTA-C which undergoes rapid hydrolysis of both chloride ligands almost concurrently.⁵⁸ Adverse production of hydrolysis products have been known to stunt drug development, as the exact intercellular hydrolysed species is often unknown and interactions difficult to predict. For this reason, Dyson *et al.* modified RAPTA-C, by substituting a bidentate carboxylate for the chloride ligands to provide RAPTA-O. This adaptation enabled RAPTA-O to resist hydrolysis, improved solubility and lowered the pK_a of the coordinated pta ligand. Compared to its precursor, RAPTA-O showed little change in biological properties, exhibiting similar inhibition of cell proliferation and equally poor cytotoxicity ($>200 \mu\text{M}$) in the cell lines tested. This included negligible toxicity towards the HBL-100, non-tumourgenic cell line.⁵⁹

Further testing primarily utilised RAPTA-T which showed the best selectivity towards cancer cells over normal cells.⁵⁸ Along with standard *in vivo* tests, to simulate the main steps of metastasis progression, Dyson *et al.* used *in vitro* experiments on three cell lines: invasive MDA-MB-231 breast cancer, non-invasive MCF7 breast cancer and HBL-100 normal cells. In the detachment assay, when seeded onto extracellular matrix proteins (collagen and fibronectin), MDA-MB-231 cells remained up to 9-fold more attached to the substrate than control cells, upon treatment with RAPTA-T. Complex RAPTA-T also prevented re-adhesion in the comparative assay. Plasticity required for detachment and adhesion of cells is thought to be modified by RAPTA-T by hardening the cell body, hindering these processes. Effects on the MCF7 and HBL-100 cell lines were negligible for these assays. The migration tests were measured using both chemical and contact stimulus to encourage cell movement. Cell specificity was observed in these tests with only MDA-MB-231 cells inhibited from migration and invasion up to 50% compared to controls.⁶⁰ Structure of the cytoskeleton is also thought to be crucial for motility, additionally supporting RAPTA-T effect on plasticity. *In vivo* lung metastasis weight was reduced to 35% of the control weight dosing RAPTA-T into MCA mammary carcinoma. Tumour growth was not maintained after treatment, consistent with previous reports of fast elimination of RAPTA-T from organs.⁵⁸ Together these results showed that RAPTA complexes are effective antimetastatic agents.

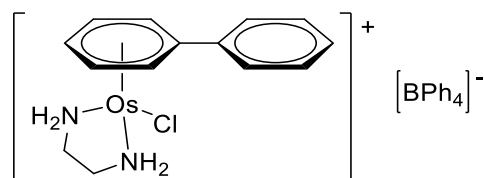
The most recent work on these compounds in 2017 utilised nanoscale secondary ion mass spectrometry and transmission electron microscopy to visualise the localisation of RAPTA-T at a subcellular level.⁶¹ Accumulation in the nucleolus of MDA-MB-231 cells was observed, corroborating with earlier studies of histone protein adduct formation of RAPTA-T in the nucleosome core.⁶² Distribution of RAPTA-T in MDA-MB-231 cells correlated accumulation with sulfur-rich regions. In contrast, treatment of MCF7 resulted in neither accumulation in the nucleus nor the cell membrane.⁶¹ The lower degree of malignancy in MCF7 cells appears to mitigate the effects of RAPTA-T claiming specificity instead over the invasive MDA-MB-231 cell line that possess the stronger inclination to invade and metastasise.^{60,61} The data discussed suggest a control of metastasis is through targeting proteins either prominently in the cell membrane or intracellularly.

In summary, a general comparison can be drawn between NAMI-A and RAPTA-T based on distinct similarities of results *in vitro* and *in vivo* despite starkly different chemical conformations of the complexes. Anti-metastatic activity prevails as a clinical benefit of these compounds, although NAMI-A is overall more potent, it nevertheless validates continued experiments within the RAPTA series.

1.2.3.3 Modifications of Half-Sandwich Complexes to Tune Activity

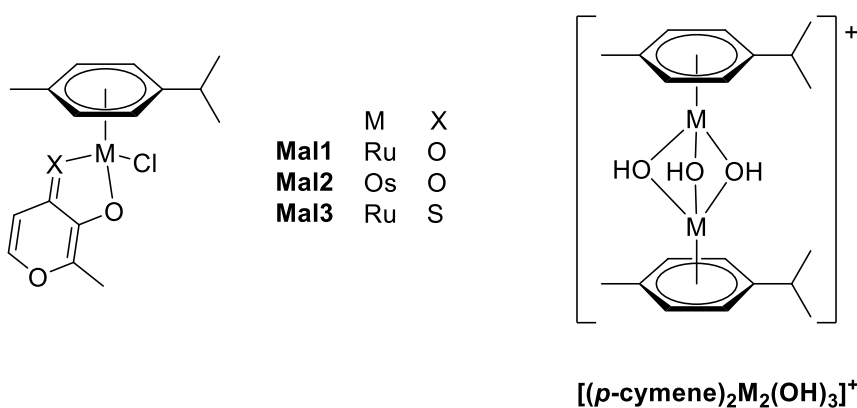
Already, it should be clear that half-sandwich complexes can provide different degrees and types of activity ostensibly linked to their combined structural components. There remains ample room to manipulate the various coordination sites to distinctly design a complex with a desired specific target and tuned activity. While some factors have already been discussed briefly (e.g. arene expansion to increase lipophilicity and potency), alternative ligand systems, the monodentate halide ligand and the metal centre are all readily interchangeable and worth discussion.

An ambidentate picolinate ligand system (*Figure 1.9*) was considered by McGowan *et al.* to evaluate the coordination of its complexes and their biological properties.⁶³ The simplest complex *Rupic1* was synthesised using readily available starting materials; picolinamide and dichloro(*p*-cymene)ruthenium dimer to form the *N,O*-chelated product. Poor cytotoxicity of complex *Rupic1* was attributed to the lability of the *N,O*-chelated picolinate system.⁶³ Incorporating a strongly electron withdrawing group adjacent to the amide was found to force the formation of the *N,N*-chelated system seen in complex *Rupic2*. The *para*-nitrophenyl substituent of *Rupic2* increases the acidity of the amide proton facilitating anion formation in solution, enabling *N,N*-coordination.⁶⁴



RAED-Os

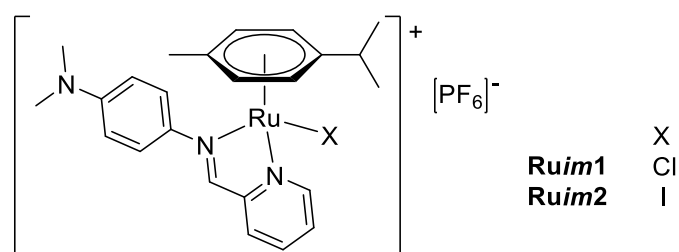
Within this series, an overarching relationship between rate of hydrolysis and potency is observed. This can be rationalised by considering the neutral complexes undergo rapid hydrolysis in solution compared to those that are positively charged. It is unfavourable for the Group VIII metal complexes in this case to gain an overall 2+ positive charge by loss of coordinated halide and therefore show significantly slower hydrolysis. Even though a π -acceptor ligand usually slows hydrolysis, when paired with the anionic character of the deprotonated amide (seen in *Rupic2*, *Rupic3* and *Ospic1*), the negative coordinated ligand forms a neutral complex which hydrolyses too fast to measure by $^1\text{H-NMR}$.⁶⁴ This is the case for both ruthenium and osmium analogues. By comparison, the Sadler diaminoethane *N,N*-chelating neutral ligand forms positive complexes, displaying the expected slower rate of hydrolysis in the osmium complex (RAED-Os) compared to the ruthenium analogue (RAED-bp). The slower ligand exchange rate and the lower $\text{p}K_{\text{a}}$ (6.3) of the aquated RAED-Os could be the cause of the negligible toxicity of the complex ($\text{IC}_{50} = >100 \mu\text{M}$) compared to the ruthenium RAED-bp congener ($\text{IC}_{50} = 5 \mu\text{M}$) in this case.⁶⁵



Keppler *et al.* investigated complexes incorporating the natural product maltol and its derivatives. Similar to McGowan's anionic *N,N* coordinated complexes, the negative *O,O* maltol ligand also provided complexes Mal1 and Mal2 which observed rapid hydrolysis to the monocationic species under aqueous conditions; irrespective of their metal centres.⁶⁶ However, limitations arose at both physiological temperature (310 K) and in dilute solution. The maltol ligand was completely dissociated at 310 K in concentrations of $2 \mu\text{M}$ after ten minutes in both Mal1 and Mal2. In solution, to mimic extracellular conditions of 0.1 M NaCl, the ligand was also fully dissociated in favour of the inert hydroxo-bridged dimer $[(p\text{-cymene})_2\text{M}_2(\text{OH})_3]^+$.⁶⁶ Proton-donor solvents such as

water were predicted by DFT to form hydrogen bonds with the coordinated oxygen promoting the hydrolysis.

Unsurprisingly, these complexes gave insignificant IC_{50} values ($>50 \mu M$) when dosed to both A549 lung cancer and A2780 ovarian cancer cells, assumed to be due to the formation of $[(p\text{-cymene})_2M_2(OH)_3]^+$ under physiological conditions. The weakly coordinated carbonyl oxygen was replaced by a thiocarbonyl derivative in complex Mal3. Complex Mal3 was significantly more stable in aqueous conditions observing only a small amount of dimer formation over 24 h. The stronger binding of the *O,S*-chelated complex is thought to be responsible for the improved potency of Mal3 compared to its *O,O* analogues with 13 and $5.1 \mu M$ IC_{50} values against CH1 and SW480 cancer cell lines, respectively.⁶⁷



The monodentate halide is the remaining coordination site available for variation. Sadler *et al.* presented a study of the contrasting cellular uptake pathways of chloride versus iodide iminopyridine ruthenium complexes.⁶⁸ An immediate distinction in cytotoxicity between the complexes was apparent when testing the antiproliferative activity in A2780 ovarian cancer cells. The iodide complex Ruim2 showed similar potency to cisplatin (3.0 and $1.2 \mu M$, respectively) and was 5-fold more active than the chloride analogue Ruim1 ($15 \mu M$).⁶⁸ The cellular accumulation of drug Ruim2 after 24 h incubated at 310 K was also greater than Ruim1, showing the correlation between higher drug accumulation and increased potency.

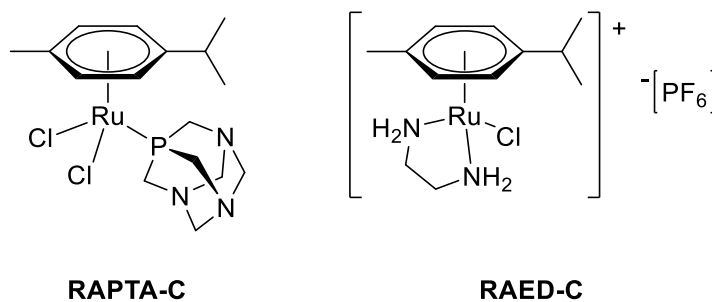
At low temperatures (277 K) no cellular accumulation of cisplatin was observed in contrast to Ruim2, which showed significant uptake at 277 K; increasing uptake with increasing temperature. This result indicates a partially passive uptake pathway which is energy-independent, compared to cisplatin which requires facilitated diffusion into the cell. Both complexes exhibit hydrolysis up to 64% at $2 \mu M$ concentrations and yet iodide in Ruim2 is not exchanged for chloride in physiologically relevant concentrations of NaCl. As the structure of these complexes is retained extracellularly, their biological behaviour can likely be attributed to cell recognition and specific transport of the iodo and chloride species. This could intrinsically be linking to membrane potential as displayed by *in vitro* tests of the endocytosis pathway. Ruthenium accumulation of both complexes was reduced by co-administration with ouabain, which modifies the function of the Na^+/K^+ pump and alters the membrane potential. DFT calculations suggested the chloride face of

Ruim1 is less positively-charged than the iodide face of complex Ruim2. These combined factors enhance the proposition that the difference in polarisation between complexes Ruim1 and Ruim2 plays a substantial role in overall cellular uptake.

1.2.4 Summary

Metal complexes offer many qualities that are advantageous to drug design including: modular synthesis, exchangeable ligands, variable geometries and oxidation states. It is apparent from the examples of half sandwich complexes discussed, that a combination of ligands in the available coordination sites, along with the metal centre must possess complementary characteristics to provide desirable anticancer activity. While only a few have been analysed in detail here, there are evidently thousands of possible complexes with the pseudo-octahedral geometry that could be synthesised and explored for medicinal applications.

It has been shown that the tuning of ligands can strongly influence the properties of the complex and can evoke changes in the mechanism of action seen explicitly when comparing the ruthenium complexes RAPTA-C and RAED-C. Dyson's complex RAPTA-C has a proclivity for forming adducts on chromatin-associated proteins and displays activity as an antimetastatic agent.^{57,69,70} The subtle ligand substitution with ethylene diamine provides the RAED-C complex, which by contrast displays preferential binding to DNA.^{53,55} Although these complexes are structurally similar, they illustrate the influence coordinating ligands can have on the target of a complex.⁷¹



Current drug limitations including chemotherapeutic resistance and toxicity to healthy tissue can be circumvented by the use of less toxic platinum group metals such as ruthenium. This valuable property is a contributing factor to the promising use of half-sandwich complexes as alternative anticancer agents. Still, it is clear that more understanding and investigation is necessary to determine the fate of such half-sandwich complexes within the cellular environment and to establish how such structural changes can directly affect their activity.

1.3 Enzymes as Anticancer Targets

There are a copious amount of processes occurring simultaneously inside and outside of cells. Factors within the cell cycle vary between healthy and cancerous cells; providing more discrete therapeutic targets at a subcellular level. The manipulation of these vital biological processes by drug targets can have a variety of consequences. Complexes already discussed have exhibited inhibition of antimetastatic activity through protein binding, while other compounds trigger apoptotic pathways in malignant cells by DNA adduct formation, DNA intercalation or even enzyme poisoning.

Enzymes are naturally occurring biomolecules that catalyse numerous regulatory processes and metabolic pathways. The catalytic activity of enzymes is often selective to a single substrate different to each enzyme family. Dysregulation of enzyme function is associated with mutations in cancerous cells propagating the disease.⁷² For this reason, enzymes are considered an appropriate target for metal-based drug design, with frequently targeted examples displayed in *Table 1.1*.

Candidates will most commonly interact with the enzyme through weak intermolecular forces, hydrogen bonding or binding to the catalytic site, inhibiting activity. The role of the metal centre within the drug influences the classification of potential enzyme inhibitors.⁷²

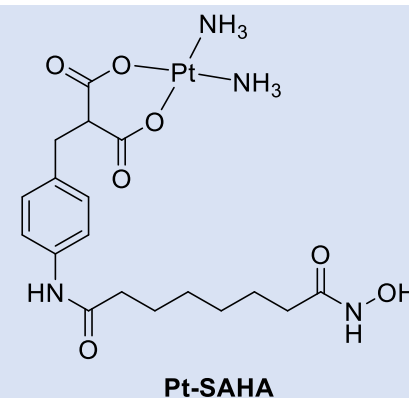
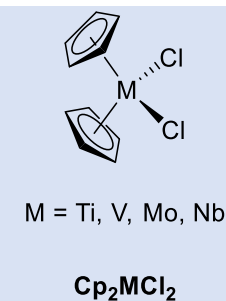
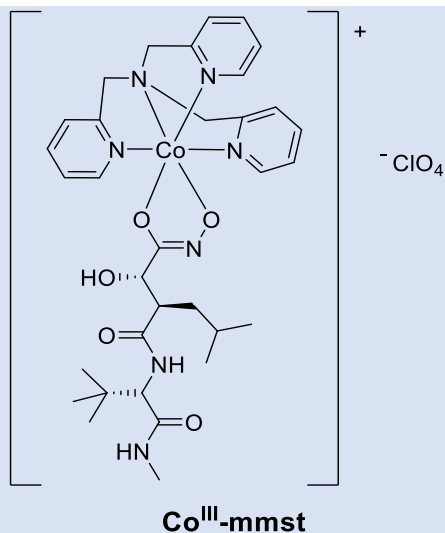
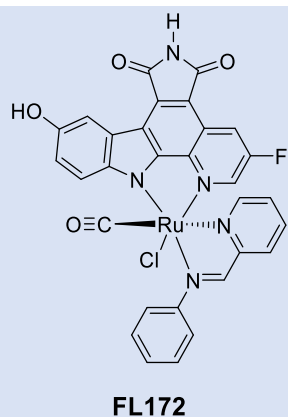
- 1) The metal centre of the complexes does not directly bind to the enzyme. The ligands are the biologically active motif, while the metal's redox potential may enhance the overall effects of the compounds.
- 2) The metal ion is the active part of the molecule; directly interacting with the enzyme target. In this case the ligands are used to stabilise the reactive metal centre.
- 3) Complexes where the metal and ligand components are biologically active and both are responsible for activity.
- 4) The metal atom can add electron density and facilitate x-ray phasing for cocrystal structure determinations.

The protein kinase inhibitor **FL172** uses ruthenium as an inert metal scaffold, acting as a hypervalent carbon. The complex carries the active organic ligand, analogous to the natural product kinase inhibitor staurosporine.⁷³ The rigid three-dimensional structure of **FL172** enabled a highly competitive binding affinity with ATP substrates for protein kinase and acts as a potent inhibitor in the nanomolar range (130 nM).⁷⁴ Complex **Co^{III}-mmst** also falls into the first category as the Co(III) metal centre is a reduction activated chaperone for the existing marimastat antimetastatic agent. The hypoxic environment of tumour sites causes Co(III) to Co(II) reduction and subsequently allows displacement of the stereospecific ligand and increases the magnitude of

activity two-fold compared to the organic molecule alone. This activation inhibits matrix metalloproteinase activity, linked to metastasis.⁷⁵ Meanwhile, Marmion *et al.* demonstrated the ability of a metal containing prodrug **Pt-SAHA** to possess dual action upon hydrolysis. While the cisplatin fragment binds DNA, the organic ligand inhibits histone deacetylase enzymes demonstrating dual activity within a single complex.⁷⁶ Metallocene dihalides (**Cp₂MCl₂**) have been noted to possess qualities of the second example, inhibiting the activity of topoisomerase II by metal coordination to the enzyme surface.⁷⁷ Rapid hydrolysis of the chloride ligands forms the active species (**Cp₂Mⁿ⁺**), enabling the formation of enzyme-complex adducts, with overall cellular accumulation aided by the presence of the hydrophobic Cp ligands.

Table 1.1 Possible enzyme targets for inhibition and examples of metal-based inhibitors.⁷⁴⁻⁷⁷

Enzyme family	Protein and lipid kinases	Matrix metalloproteinases	Topoisomerase II	Histone Deacetylases
Function	Facilitate phosphorylation of protein substrates, altering their cellular location and function.	Tissue remodelling and degradation of protein mass which provides structural and biochemical support extracellularly.	Regulation of DNA supercoiling and separation of replicated chromosomes prior to cell division.	Deacetylation of various proteins, transcriptional repression.
Contribution to malignancy	Dysregulation in coordination of cellular processes.	Cause excessive degradation of extracellular matrices.	Rapid proliferation.	Dysregulation of DNA damage repair, cell cycle control, autophagy, metabolism, senescence and chaperone function.

Metal-based inhibitor

1.3.1 Post-Translational Modification

Chromatin is the highly ordered storage structure of DNA in the nucleus. Nucleosomes, the structural subunits of chromatin comprise DNA wrapped around basic histone proteins (*Figure 1.10*). The complex structure of chromatin helps control the regulation of DNA repair, replication and gene expression. Mechanisms such as methylation, acetylation and phosphorylation of proteins are dynamic processes that coordinate transcription, culminating in cell proliferation. These post-translational modifications occur on histone proteins, creating or stabilising binding sites for regulatory proteins, DNA damage-repair proteins and transcription factors; modulating biological signals and response.⁷⁸ Deviation from the balance shaped by these post-translational modifications can alter gene expression, generating cellular transformation and malignancies.⁷⁸

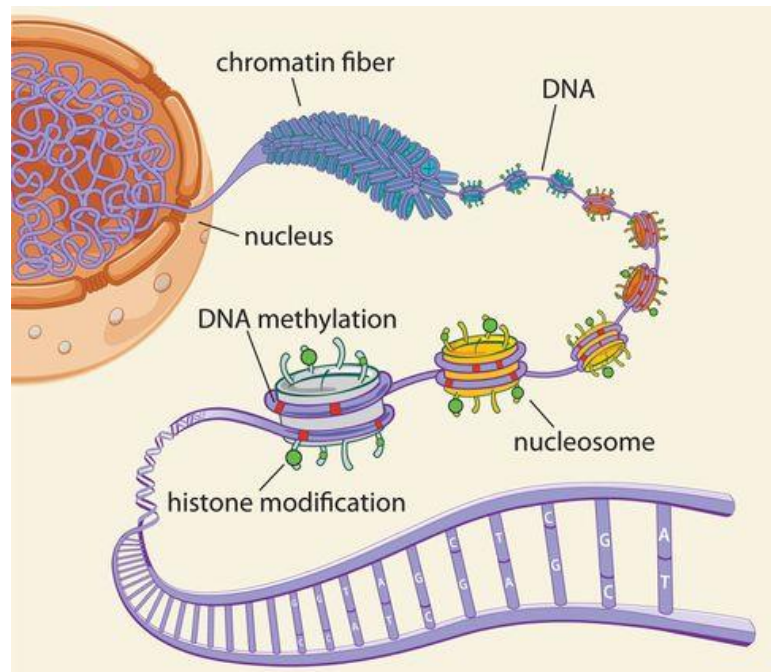


Figure 1.10 Structure and composition of chromatin.⁷⁹

1.3.2 Histone Deacetylase Enzymes

The acetylation of histone lysine residues is a post-translational covalent modification. Lysine acetylation is reversible and primarily occurs at the flexible *N*-terminal tails that extend from the nucleosome core. The dynamic equilibrium of this modification is controlled by cooperative deacetylase and acetylase enzymes (*Figure 1.11*). The acetylation process is catalysed by histone acetyltransferase (HAT) enzymes, generally associated with transcriptional activation via chromatin relaxation.⁸⁰ The new surface topology promotes transcriptional factor recognition. Histone deacetylase (HDAC) enzymes work with opposing effect to catalyse removal of acetyl groups. Positively charged lysine residues formed from deacetylation increase ionic interactions

with the negatively charged DNA-phosphate backbone, making the chromatin structure more compact. This conformational change reduces accessibility of transcription proteins causing transcriptional repression.

Traditionally, histone acetylation is known to play an important role in chromatin remodelling, however HDACs have also been documented to deacetylate non-histone proteins regulating other cellular functions including cell-cycle progression, differentiation and apoptosis.^{80,81} Aberrant HDAC activity has been characterised in tumours, through abnormal recruitment, translocation or overexpression. Due to the prolific activity of the HDAC enzyme family in various processes, along with showing a marked change in cancerous cells compared to healthy cells, HDAC enzymes are considered a viable target for anticancer therapy.⁸²

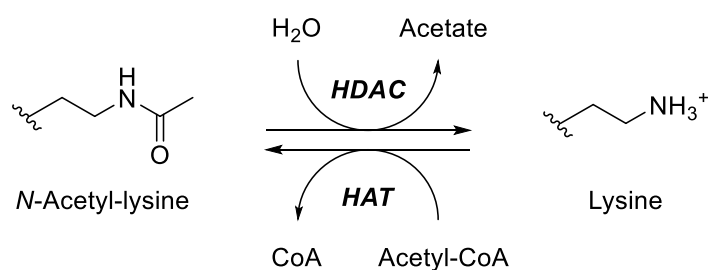


Figure 1.11 Reversible acetylation of lysine residues by histone deacetylase (HDAC) and histone acetyltransferase (HAT) enzymes.⁸³

The function of individual HDACs is largely dependent on their intracellular location and domain organisation. There are eighteen known mammalian HDAC enzymes that are divided into four classes (namely I, II, III and IV) based upon their comparative structural homology to yeast HDACs.⁸² Classes I and II are considered “classical HDACs” and share a Zn²⁺ catalytic domain character with class IV. Class III are divergent as NAD⁺-dependent proteins and will not be covered in this work.

Class I HDACs (including 1, 2, 3, and 8) are found almost exclusively in the nucleus. HDAC3 is an exceptional case, with the ability for recruitment outside of the nucleus by nuclear localisation signals or co-localisation with other proteins.⁸⁴ Class II HDACs shuttle in and out of the nucleus via similar cellular signals and can be further subdivided into Class IIa and IIb. Class IIa (4, 5, 7 and 9) HDACs are carefully regulated by a calmodulin(Ca²⁺)-dependent kinase channel while class IIb (6 and 10) are predominantly confined to the cytoplasm.^{82,84}

1.3.3 Histone Deacetylase Inhibitors

HDAC inhibitors block the catalytic site of histone deacetylase enzymes, directly altering the acetylation levels of chromatin and other non-histone proteins. This dysregulation modifies gene

expression initiating cell death, apoptosis, cell cycle arrest and causes inhibition of angiogenesis and metastasis.⁸⁵ Treatment with HDAC inhibitors can promote tumour cell apoptosis by both intrinsic and extrinsic pathways through inactivation of anti-apoptotic proteins and/or the upregulation of pro-apoptotic proteins. An advantage of utilising HDAC inhibitors is their enhanced sensitivity towards transformed cells compared with normal cells, alleviating any undesirable toxicity in healthy tissue.⁸⁵

1.3.3.1 Clinically-Trialled Small Molecules

Currently, there are many structurally disparate organic based HDAC inhibitors at different stages of clinical trials. Structural similarities of these compounds assist in HDAC inhibitor classification. Groups under investigation include, but are not limited to: cyclic tetrapeptides, benzamides, aliphatic acids and hydroxamic acids.⁸² The strong zinc-binding character of the bidentate hydroxamic acid moiety encouraged a particular interest in this group as potent classical HDAC inhibitors.⁸⁶

The natural product (*R*)-Trichostatin A (*Figure 1.12*, TSA) was formerly isolated from *Streptomyces hygroscopicus* and utilised as an antifungal antibiotic in the 1970s.⁸⁷ Yoshida *et al.* later described nanomolar concentrations (10 ng/mL) of TSA caused apparent hyperacetylation to histones *in vivo* and strongly inhibited the activity of partially purified histone deacetylase *in vitro*.⁸⁸ Neither the synthesised (*S*)-TSA nor the trichostatic acid analogue displayed any signs of biological activity.⁸⁹ The difference in activity between the TSA enantiomers indicates the target molecule is stereospecific to (*R*)-TSA as a substrate.

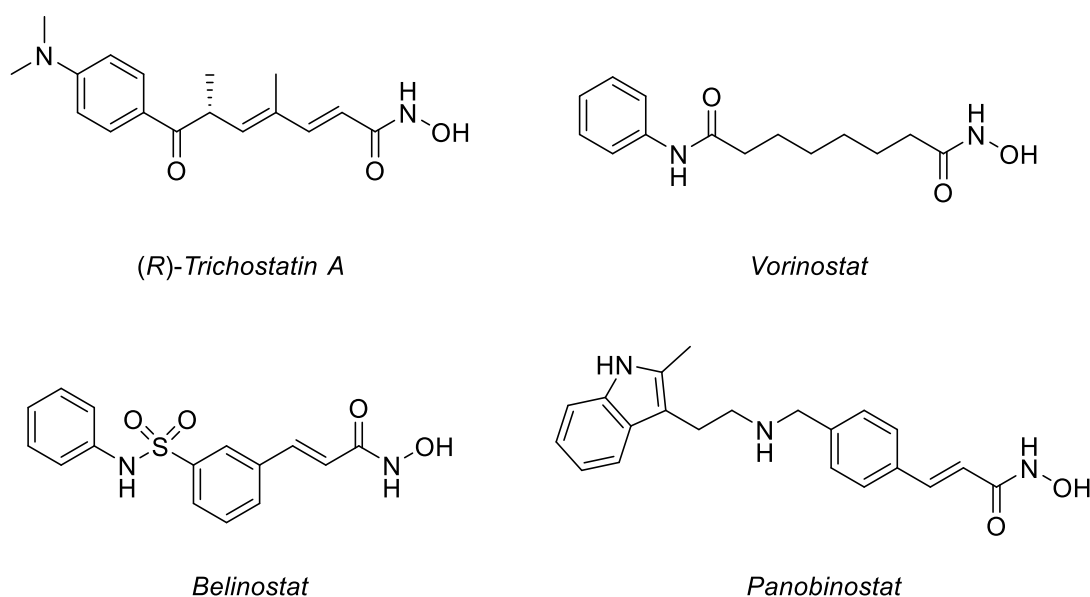


Figure 1.12 Hydroxamic derived HDAC enzyme inhibitors. (*R*)-Trichostatin A (TSA); Vorinostat (Suberoylanilide, SAHA); Belinostat (PXD101); Panobinostat (LBH589).

Experiments to extend the suggestion of TSA involvement in histone deacetylase inhibition were undertaken using a pulse-chase method. The protocol exposed mice FM3A cells to labelled [^3H]acetate for 30 minutes (pulse) followed by dosing with TSA (100 ng/mL, chase) in parallel with an absence of TSA as a control.⁸⁸ Distribution of radioactive species was analysed using fluorography of the cellular histone, H4. All bands on the electrophoresis gel disappeared in the chase without TSA present, while radioactivity of tri- and tetra-acetylated species of H4 increased in the presence of TSA. This result implied histone deacetylase enzyme inhibition as the mode of action for TSA, enhancing its potency.

Although TSA was one of the first hydroxamic acids to be noted for its inhibitory effects of HDAC enzymes, it was pulled from clinical trials in 2013 owing to its adverse pharmacokinetic profile including metabolic instability.^{90,91} A study by Singh and co-workers compared the structurally similar TSA and SAHA (Figure 1.12) and proposed a rationale for the preferred thermodynamic and kinetic binding ability of SAHA to HDAC 8.⁹¹ At a molecular level, SAHA possesses a much more flexible aliphatic chain and can rotate more freely within the enzyme pocket than the rotationally constrained, bulkier TSA. Enthalpic favourability is thought to directly link to such structural features of the TSA-HDAC8 and SAHA complexes. Binding to HDAC8 of SAHA requires more structural adjustments but the interactions are more specific. For example, the carbonyl of the amide group in SAHA forms a hydrogen-bond with Asp101 of HDAC8 which could stabilize the SAHA complex by 3-4 kcal/mol.⁹¹

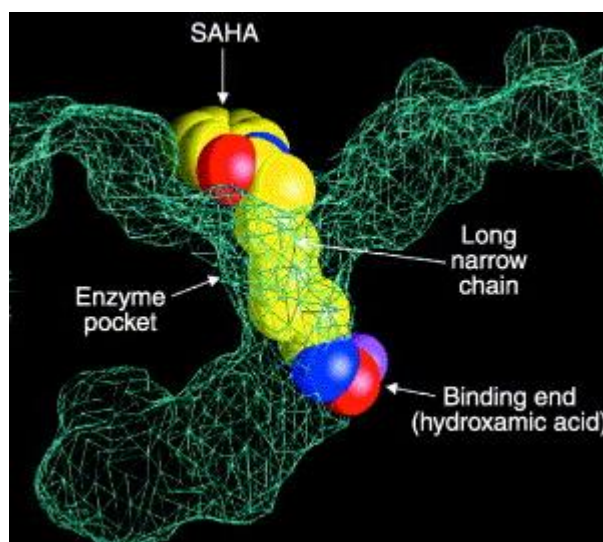


Figure 1.13 SAHA (suberoylanilide hydroxamic acid) bound to an HDAC1-like protein.⁹²

Association and dissociation of the inhibitors was also measured. A two-step binding mechanism was determined for both TSA and SAHA with HDAC8: fast bimolecular association step driven by enthalpic changes followed by a slower isomerisation step, to enhance binding affinity of the

phenyl head group of SAHA acts as a surface recognition domain, promoting additional interactions with the rim of the enzyme pocket.⁹³

SAHA displayed promising results along with favourable pharmacokinetics and has been investigated as an anticancer agent extensively. The anticancer activity of SAHA was initially studied by Marks *et al.* measuring the induced differentiation of murine erythroleukemia (MEL) cells.⁹⁵ The optimal concentration of SAHA for MEL cell differentiation was 2 μM along with inhibition of cell proliferation in the micromolar range.⁹⁵ This early, auspicious result encouraged testing in a broader range of transformed cells.

The follow up study examined the effects of SAHA on the growth suppression of prostate cancer cells *in vitro* and *in vivo*. SAHA displayed a dose-dependent inhibition of proliferation in three prostate cancer cell lines (LNCaP, PC-3 and TSU-Pr1) at micromolar concentrations (2.5-7.5 μM).⁹⁶ LNCaP was the most sensitive cell line and at higher doses (5-7.5 μM), cell death was induced within 48 h of culture. *In vivo* daily dosage of SAHA (50 mg/kg/day) for 21 days showed a mean 97% reduction of CWR22 tumour xenograft in nude mice compared to the vehicle control (DMSO), with minimal evidence of side effects.⁹⁶ An increased accumulation of core acetylated histones was also observed in both LNCaP prostate cancer cells and in the CWR22 tumours after treatment with SAHA. Results from other experiments^{96,97} show an increase of acetylation in both normal and malignant cells implying HDAC inhibition remains a likely mechanism of action. Nevertheless, these reports maintain the apoptotic and growth-suppression induced by SAHA to be confined to only transformed cells.⁹⁶

As an HDAC inhibitor, SAHA alters the expression of a number of genes (2% - 17%).⁹⁸ One of the most common upregulated genes in transformed cells induced by the treatment of SAHA is the cyclic dependent kinase inhibitor p21^{WAF1}.⁹⁹ Zhang *et al.* examined the effects of SAHA on cutaneous T-cell lymphoma (CTCL) cells in 2005, finding low concentrations of SAHA (1-5 μM) selectively induced apoptosis via the p21^{WAF1} pathway.⁹⁹ The therapeutic action of SAHA was also investigated using peripheral blood lymphocytes from patients with high levels of malignant T-cells to provide mirrored results to the *in vitro* testing. The suitability of SAHA as a specific HDAC inhibitor with anticancer activity was evidenced by Marks, Zhang and others alongside successful progression through clinical trials. In 2006, shortly after the study by Zhang, SAHA was approved by the FDA for the treatment of cutaneous T-cell lymphoma.¹⁰⁰ More recently, alternative hydroxamic acid containing HDAC inhibitors belinostat and panobinostat (*Figure 1.12*) were approved for the same treatment, most recently panobinostat in 2015.¹⁰¹

Moreover, it is imperative to note that while hydroxamic acids demonstrate potent examples of HDAC inhibitors, their less favourable attributes should not be neglected. Aside from off target

binding, hydroxamic acids including TSA have shown mutagenic effects, often through formation of isocyanates via a Lossen rearrangement.¹⁰² Isocyanates are unstable and can react readily with imidazole groups within enzymes, with the subsequent ureatype products more susceptible to hydrolysis and breakdown. While deprotonation of the N atom within the hydroxamic acid (required for the Lossen rearrangement to take place) is unlikely under physiological conditions ($pK_a \sim 8.5$), metal catalytic sites have been shown to aid this unwanted transformation.¹⁰² Alternative zinc-binding groups have been designed to curtail such effects (discussed in *Section 1.3.4*), however the use of hydroxamic acids has prevailed due to their efficacy *in vivo*.

1.3.3.2 Metal-Based HDAC Inhibitors

The concept of exploiting metals in medicine with specific target molecules has been briefly explored (*Section 1.3*). Incorporating a metal centre can provide a scaffold for biologically active ligands, enable transport of an active metal ion by the stabilisation of coordinated ligands or combine activity of both the metal and organic component of a complex.⁷² Although metal-based HDAC inhibitors are limited across the literature, examples exist utilising each kind of metal centre classification.

Short-chain fatty acids primarily target class I and IIa HDAC enzymes and are considered the weakest group of organic HDAC inhibitors, with activity in the millimolar range.^{98,103} However, valproic acid (*Figure 1.15*) has displayed not only antitumour effects but an ability to potentiate the chemotherapeutic action of cisplatin in ovarian cancer cells.¹⁰⁴ Marmion *et al.* synthesised **Pt(II)-(va)₂** as a modified derivative of the biologically inactive transplatin. While substitution of an amino ligand with a *N*-donor heterocycle (such as pyridine) was already documented to enhance the cytotoxicity profile of trans-platinum compounds,¹⁰⁵ the additional use of valproate ligands was intended to also utilise HDAC inhibitory activity. Testing of **Pt(II)-(va)₂** against A2780 and A2780cis ovarian cancer cell lines gave high IC₅₀ values of 86.5 and 76.3 μM , respectively.¹⁰⁶ In this instance, the attempt to create a viable platinum based drug with dual action and improved potency was unsuccessful and would require significant development.

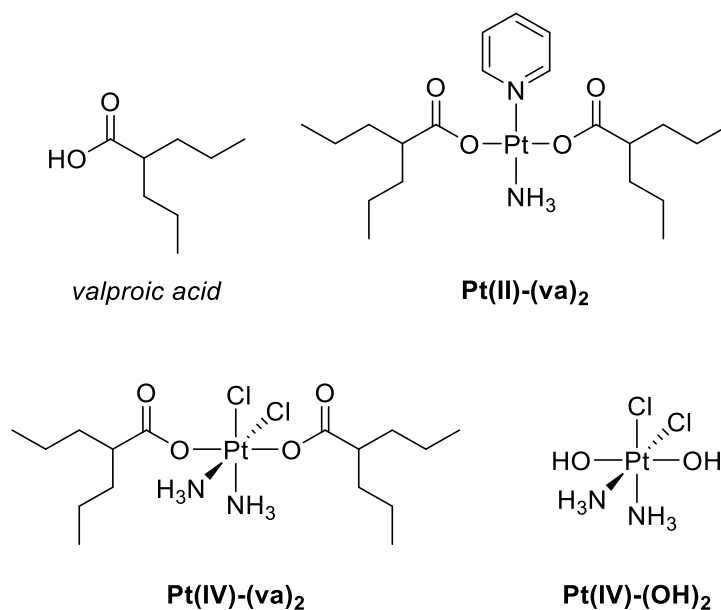


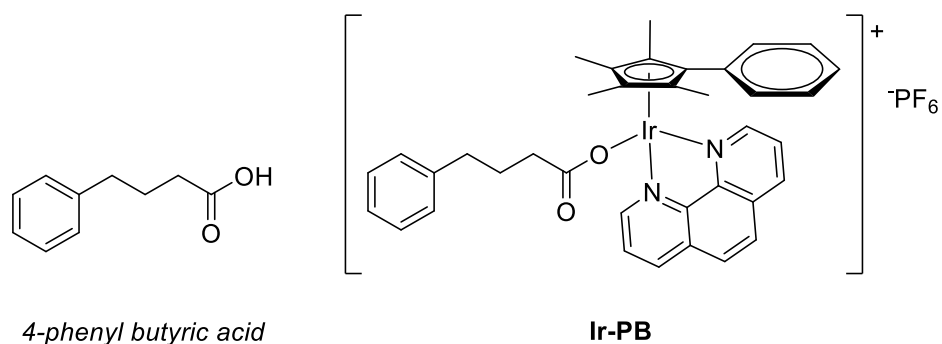
Figure 1.15 HDAC inhibitor valproic acid and some metal complex derivatives.

An alternative approach to employ valproic acid as a bioactive ligand within a complex was achieved by Yang *et al.* Analogous to the previously synthesised Pt(IV) prodrug satraplatin (Figure 1.5), complex **Pt(IV)-(va)₂** is designed with the same octahedral geometry, chloride ligands and axial aliphatic carboxylic acid ligands adding valuable lipophilic character. Satraplatin also possessed desirable low toxicity in the more kinetically inert Pt(IV) oxidation state prior to intracellular reduction to the active Pt(II) species.³¹

Biological studies analysed the HDAC inhibitory activity of valproic acid and **Pt(IV)-(va)₂** using nuclear extract from HeLa cells. At 5 mM dose concentrations valproic acid inhibited HDAC activity 66% while **Pt(IV)-(va)₂** showed less than half the inhibitory activity at 24%.¹⁰⁷ When incubating **Pt(IV)-(va)₂** with a reducing agent ascorbic acid for 10 h, the HDAC inhibitory activity of **Pt(IV)-(va)₂** dramatically increased to 70%. This improvement in activity advocated the reduction of **Pt(IV)-(va)₂** to Pt(II) and subsequent dissociation of valproic acid to elicit HDAC inhibitory activity. Complex **Pt(IV)-(va)₂** continued to display high potency in both *in vitro* and *in vivo* assessment. Across a range of cell lines (SKOV-3 ovarian, HepG2 liver and A549 lung cancer), **Pt(IV)-(va)₂** exhibited significantly increased activity compared to the cisplatin control with the lowest IC₅₀ concentration of 0.15 μM against A549 lung epithelial carcinoma cells, 12-fold more than that of cisplatin.¹⁰⁷ Mice bearing A549 xenograft tumours when dosed with **Pt(IV)-va₂** (10 mg/kg twice a day for 12 days) showed an 87% inhibition of tumour growth with gradual increase in mice weight, indicating minimal side effects.

The pronounced potency of **Pt(IV)-(va)₂** was attributed to its cellular accumulation and dual activity. Over 4 h the platinum accumulation of **Pt(IV)-(va)₂** increased from 80.6 ng (2 x 10⁷ cells)

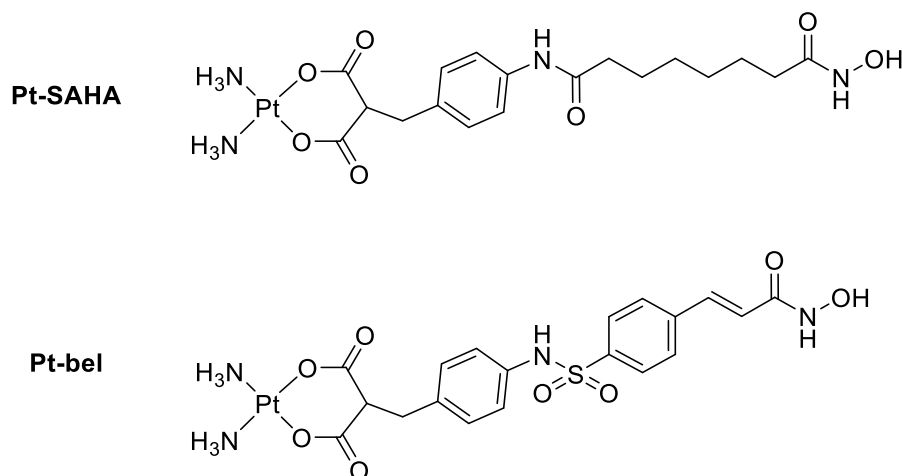
located mostly in the cell membrane, up to 252.2 ng (2×10^7 cells) distributed between the cytosol and cell membrane after 24 h incubation. By comparison, the hydroxy counterpart **Pt(IV)-(OH)₂** showed a decrease in cytosol Pt accumulation from 28.6 ng (2×10^7 cells) to 9.4 ng (2×10^7 cells) over 24 h suggesting rapid cellular efflux. The lipophilic character of the valproic ligands of **Pt(IV)-(va)₂** is thought to aid the cell membrane accumulation, followed by efficient diffusion into the cytosol.¹⁰⁷ Considering the design of this prodrug, the mechanism of action was proposed to involve the loss of valproic ligands intracellularly to promote acetylation of nuclear histones through HDAC inhibition, relaxing chromatin and allowing the synergistic DNA binding action of the Pt(II) complex to yield such potent cytotoxicity. Further investigation into the drug efficacy of **Pt(IV)-(va)₂** as a conjugate Pt(IV) prodrug is notable due to the combination of these positive primary biological results.



Herchel *et al.* provide another complex designed to merge the HDAC inhibitory activity of a short-chain fatty acid (in this case 4-phenyl butyric acid¹⁰⁸) with the DNA binding capability of an iridium(III) half sandwich complex.¹⁰⁹ Release of the *O*-monodentate phenyl butyrate ligand from **Ir-PB** was measured using ¹H-NMR experiments in the presence of the biologically prevalent glutathione (GSH). At ambient temperatures in aqueous conditions, equilibrium of free phenyl butyrate (60%) was reached within 4 h. By contrast, complete dissociation of the carboxylate ligand was observed within 30 mins using 2 molar equivalents of GSH where new signals were observed in the spectrum, implying formation of a GSH adduct - $[\text{Ir}(\eta^5\text{-Cp}^{\text{ph}})(\text{phen})(\text{SG})]^+$ as the major species.¹⁰⁹

Cisplatin resistant ovarian A2780cis cells contain higher levels of GSH than the cisplatin-sensitive A2780 cells. Differences in intracellular levels of GSH was thought to provoke the similar trend in potency of **Ir-PB** towards A2780 and A2780cis cell lines with IC₅₀ concentrations of 15.8 and 13.0 μM, respectively. Compared to its monodentate chloride analogue, **Ir-PB** shows 2-fold higher potency towards A2780cis cells, implying the concept of GSH-activation increases cytotoxicity of **Ir-PB** through release of the bioactive phenyl butyrate.¹⁰⁹ HDAC inhibitory activity was reduced to 66.6% by **Ir-PB** in a cell free assay in contrast to 74.5% by the sodium phenyl butyrate salt.¹⁰⁹ HDAC inhibition by **Ir-PB** suggests the half sandwich iridium(III) fragment could play a role in

this activity. Complex **Ir-PB** is an interesting enzyme inhibitor example as it also uses the previously discussed piano-stool complex structure.

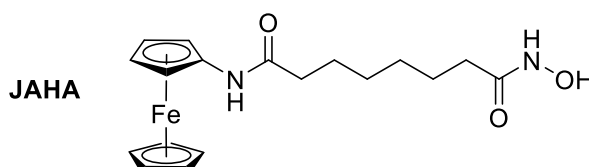


Marmion *et al.* synthesised two other conjugate platinum compounds **Pt-SAHA** and **Pt-bel** which incorporate *O,O*-malonate analogues of the FDA approved HDAC inhibitor drugs, SAHA and belinostat (*Figure 1.11*). The bidentate binding motif in these platinum complexes is also similar to the cyclobutane-1,1-dicarboxylate ligand of carboplatin (*Figure 1.5*). Compared to the aforementioned aliphatic acids, the hydroxamic acids are significantly more potent and utilising such an organic fragment was intended to reduce the indiscriminate toxicity to healthy cells, often associated with platinum containing drugs.

A gel electrophoresis technique was used to monitor DNA-metal interactions between negative supercoiled DNA (closed circular pUC19 plasmid) and complex **Pt-SAHA**. DNA incubated with **Pt-SAHA** at 10 μ M concentration observed a decrease in the rate of migration, suggesting uncoiling of DNA through formation of DNA adducts.⁷⁶ There was an apparent correlation between Pt accumulation in the cancer cell lines tested with **Pt-SAHA** and its corresponding IC₅₀ values; the higher the Pt uptake the lower the IC₅₀. However, despite general cellular uptake of Pt for cisplatin being almost 10-fold less in all cell lines compared to **Pt-SAHA**, cisplatin was more toxic in each case.¹¹⁰ This observation could be attested to by multiple factors. Firstly, the aliphatic chain of the SAHA-derived ligand is likely to provide increased lipophilicity to the overall complex, facilitating transport into cells more efficiently than cisplatin. Secondly, a chelating effect of the malonate ligand was shown to reduce hydrolysis of the complex⁷⁶, while testing *in situ* with sulfur containing biomolecules such as GSH showed DNA binding of Pt from **Pt-SAHA** was enhanced by a factor of 5.¹¹⁰ It was proposed that the mechanism of action when binding DNA is aided by the coordination of a bionucleophile causing ring opening, followed by ligand displacement. This activates the compound in a prodrug manner which could be either rate

dependent or biomolecular concentration dependent, hence the lower toxicity of **Pt-SAHA** compared to the cisplatin control.

In a cell-free assay, inhibition of HDAC1 by **Pt-SAHA** was studied. The complex **Pt-SAHA** gave an IC_{50} of 1.1 μ M, lower in potency than the control HDAC inhibitor SAHA with an IC_{50} value of 0.08 μ M.⁷⁶ The malonate ligand alone gave an IC_{50} value of 0.14 μ M suggesting the HDAC activity is hindered by the complex retaining its structure, assuming hydrolysis or facilitated dissociation of the ligand are unlikely in cell-free conditions. Complex **Pt-bel** containing the belinostat-malonate ligand displayed heightened potency for cisplatin resistant cell line A2780cis (11.7 μ M) compared to **Pt-SAHA** (70.0 μ M).¹¹¹ Most importantly, both **Pt-bel** and **Pt-SAHA** showed significantly reduced toxicity towards the non-tumorigenic cell line NHDF. While there is no specific HDAC inhibition data for **Pt-bel** currently, the HDAC IC_{50} for belinostat is 0.03 μ M demonstrating the potential in future analysis of **Pt-bel**.



A novel organometallic SAHA analogue (**JAHA**), containing a ferrocenyl capping group as a phenyl bioisostere was developed by Spencer *et al.* Docking studies were performed using an existing HDAC8-SAHA complex to illustrate any similar binding modes between SAHA and **JAHA**. The archetypal chelating effect of hydroxamic acid with the zinc catalytic site was observed in both molecules, along with a hydrogen-bond interaction with the amide carbonyl and Asp101 (*Figure 1.16*).¹¹² The malleable, shallow pocket of the enzyme was also able to accommodate the ferrocene motif, forming key interactions with Tyr100, Phe152 and Tyr306 at the enzyme surface.¹¹² *In vitro*, complex **JAHA** gave selective HDAC inhibition towards class I over class IIa HDACs which showed no notable inhibition. HDAC8 inhibition by **JAHA** (IC_{50} value 1.36 μ M) was akin to that of SAHA (1.41 μ M), a similarity alluded to from the docking study.¹¹²

Initially, the cytotoxicity of **JAHA** was tested against MCF7 breast adenocarcinoma cells, which showed potency similar to SAHA; 2.44 and 0.73 μ M, respectively.¹¹² Continued testing of **JAHA** explored its toxicity towards the more aggressive, triple-negative MDA-MB231 breast cancer cells, known for their poor response to hormone therapy. MDA-MB231 cells exposed to **JAHA** for 72 h yielded an IC_{50} value of 8.45 μ M¹¹³, compared to the SAHA control (0.73 μ M)¹¹². Such low micromolar potency against highly tumorigenic cells as well as distinct non-apoptotic cell death compared to other HDAC inhibitors⁹⁹ prompted further insight into the biological profile of **JAHA** and its mechanism of action. It was later determined that multiple processes were involved in the

cytotoxicity of **JAHA**. Cell cycle transitions were perturbed through incubation with **JAHA**, similar to activity of other HDAC inhibitor examples, while additional factors such as up-regulation of reactive oxygen species (ROS) and inhibition of autophagy were also attributed to overall cytotoxicity.¹¹³

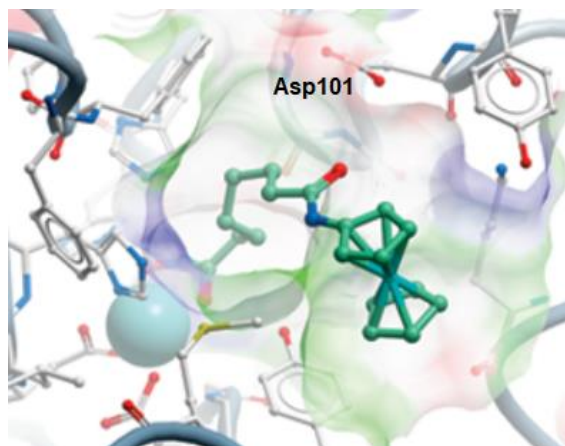


Figure 1.16 Docking of JAHA into HDAC8. The zinc ion is shown in cyan.¹¹²

Intracellular ROS are usually maintained by the mitochondria to balance requirements of ROS in the cellular environment. However, an increase in ROS generation by an external factor can overwhelm the mitochondria, propagating ROS production, leading to mitochondrial membrane potential collapse.^{113,114} Total intracellular ROS in MDA-MB231 cells increased 3-fold after 24 h incubation with **JAHA** (using IC_{50} concentration, 8.45 μ M). To demonstrate up-regulation of ROS triggered by **JAHA** was contributing to cytotoxicity, the same experiment was run in the presence of the antioxidant butylated hydroxytoluene (BHT). Cotreatment of MDA-MB231 cells with **JAHA** and BHT (50 μ M) induced reversing of the cytotoxic effect with a marked increase in viable cells after 24 h compared to **JAHA** alone, implying ROS production and subsequent oxidative damage is vital for the activity of **JAHA**.¹¹³

Depolarisation of the mitochondrial membrane is also reported to inhibit autophagy in the malignant MDA-MB231 cells. Due to heightened levels of metabolic stress in cancerous tissue, autophagy is conceptually utilised as a prosurvival mechanism to deliver necessary nutrients to tumour cells.¹¹⁵ Therefore, inhibition of autophagy is thought to indirectly sensitise MDA-MB231 cells. This was tested by comparing dosing of MDA-MB231 cells with **JAHA** versus coinubation of **JAHA** with autophagy promoter, rapamycin. Similar to cotreatment with BHT to reduce cellular ROS, incubation with rapamycin also reversed the **JAHA**-triggered decrease in cell number.¹¹³

Impaired gene expression caused by **JAHA** showed selective 4-fold increase in expression of oxidative-stress related genes NTRK-2 and RAD-50. The latter is of particular interest due to its function within the DNA damage repair complex MRN, with MRE11 and NBS1 proteins.¹¹⁶ The

HDAC inhibitory activity acting simultaneously with an up-regulation of DNA repair proteins of **JAHA** is not demonstrated by its parent analogue SAHA. Complex **JAHA** displays a more unique impact at a cellular level than its organic SAHA derivative and the cytotoxic pathways discussed provide substantial evidence towards continued investigation of this organometallic anticancer agent.

Multifaceted system design was approached in a different way by Mao and co-workers. Their octahedral complexes primarily contained ligands analogous to SAHA to coerce desirable HDAC inhibitory effects, while the remaining coordination sites were tuned with stringent luminescent properties in mind. The development of such complexes (*Figure 1.17*) that combined therapeutic HDAC inhibition effects and exploitable luminescence was aimed to target photodynamic therapy (PDT) which presents high efficacy and reduced side effects compared to radiotherapy and chemotherapy.

The prototype in the luminescent series synthesised by Mao *et al.* was the Ru(II) polypyridyl complex (**RuDIP**) which incorporated two 4,7-diphenyl-1,10-phenanthroline (DIP) ligands and a phenanthroline derivative of SAHA (*N*¹-hydroxy-*N*⁸-(1,10-phenanthrolin-5-yl)octanediamide).¹¹⁷ Cellular accumulation of **RuDIP** was measured using mean fluorescence intensity (MFI) of the incubated cell population. After 6 h, the control cells exhibited MFI : 2.41 background fluorescence which increased drastically with 50 μ M dose of **RuDIP** to give MFI : 503. High cellular uptake was attributed to the bulky hydrophobic DIP ligands, thought to correlate with low IC₅₀ values in a range of cell lines, compared to cisplatin. Notably, complex **RuDIP** was 16-fold less cytotoxic than cisplatin towards healthy liver LO2 cells (IC₅₀ = 33.2 μ M) as well as being particularly potent towards the cisplatin resistant A549cis cell line (IC₅₀ = 1.41 μ M) indicating the ability of **RuDIP** to overcome resistance.¹¹⁷

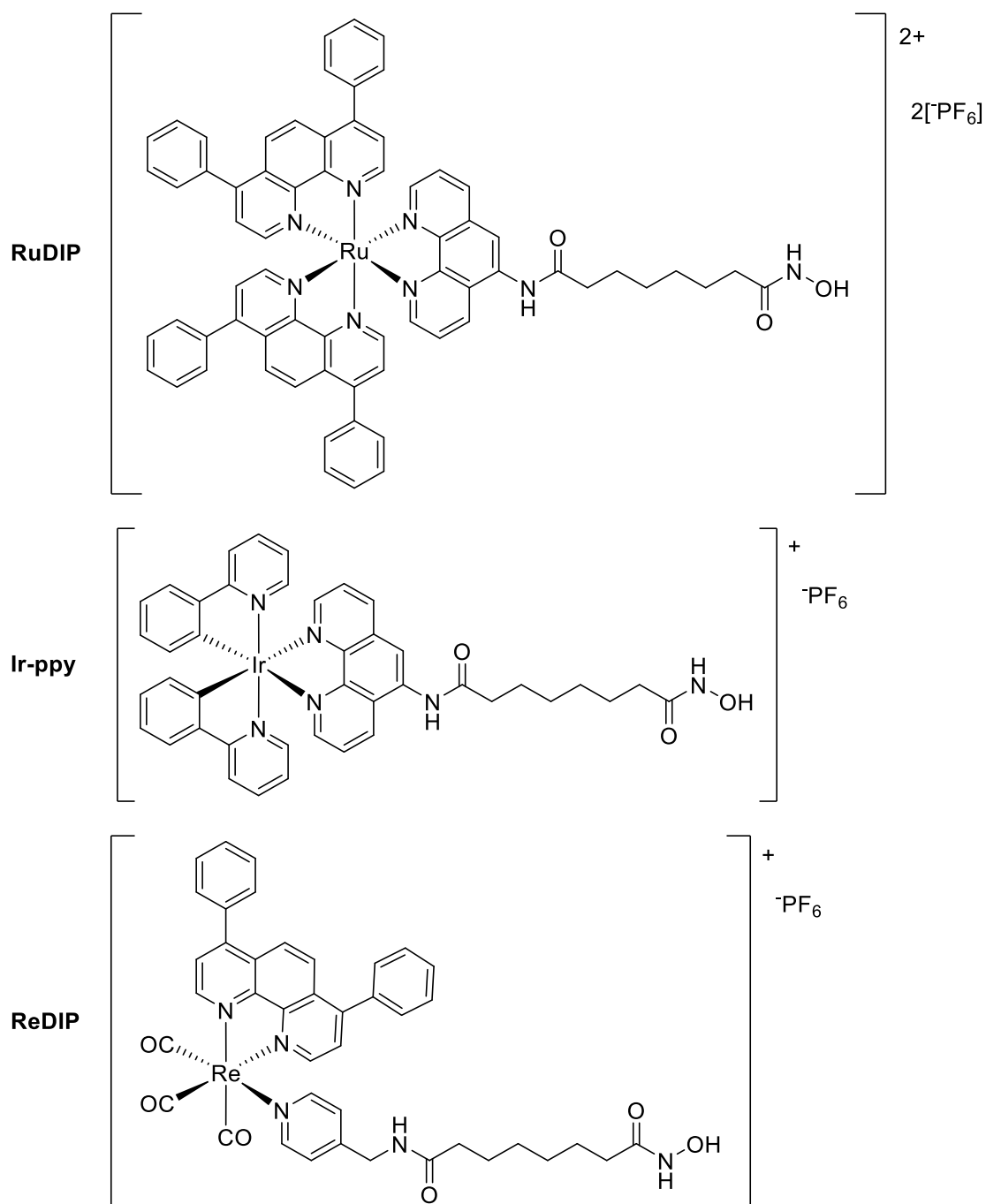


Figure 1.17 A range of multifunctional systems from the Mao group with HDAC inhibitory activity.^{117–119}

In some cases, modification to the capping group of existing HDAC inhibitors although intended to be beneficial for activity i.e. increasing interactions between inhibitor and enzyme can be flawed. Surprisingly, the large DIP ligands of complex **RuDIP** did not appear to hinder the HDAC inhibitory activity when measured against nuclear extract from HeLa cells, providing an IC_{50} value in the micromolar range ($6.66 \mu\text{M}$).¹¹⁷ Docking studies using the aforementioned HDAC8-SAHA complex suggested HDAC8 was capable of accommodating the Ru(II)-polypyridyl groups of

RuDIP into the shallow pocket with even remote interactions between a phenyl group of the DIP ligand and residue Leu308 at the enzyme surface a probable occurrence (*Figure 1.18*).

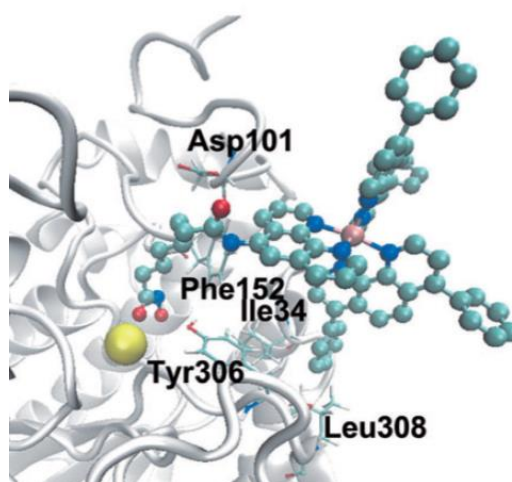


Figure 1.18 Docking conformation of complex **RuDIP** as a ball and stick representation in the active site of HDAC8. The zinc ion is shown in yellow.¹¹⁷

As previously reported for other HDAC inhibitors, elevation of ROS species can be intrinsically linked to death of cancer cells. Oxidation of 2',7'-dichlorofluorescein diacetate to its fluorescent product 2',7'-dichlorofluorescein (DCF) was used to measure the increase in ROS production by flow cytometric analysis. The SAHA control showed no significant DCF fluorescence in cells incubated for 6 h at 25 μM , whereas treatment with **RuDIP** resulted in a 4.4-fold increase in DCF fluorescence (MFI : 419) compared to the vehicle control (MFI : 96).¹¹⁷ Irregular production of ROS was considered the likely cause of activity for complex **RuDIP**, along with HDAC inhibition.

Existing cyclometalated Ir(III) complexes exhibit high quantum yields, good cell permeability and long-lived luminescence; behaviour that was also exploited for selective photodynamic cancer therapy by Mao *et al.* Complex **Ir-ppy** was synthesised with the active HDAC inhibitor *N*¹-hydroxy-*N*⁸-(1,10-phenanthroline-5-yl)octanediamide ligand along with two 2-phenylpyridine cyclometalated ligands. *In vitro* cytotoxicity of **Ir-ppy** was tested against A549, A549cis and HeLa malignant cells, in the absence and presence of UV light (365 nm). Poor toxicity (>100 μM) was displayed across all cell lines incubated in the dark with complex **Ir-ppy**. However, exposure to UV light (365 nm) showed an increase in cytotoxicity of **Ir-ppy** across all cell lines, including HeLa cells which gave an IC_{50} value of 6.8 μM under visible light (425 nm).¹¹⁸ Irradiation at this wavelength was also able to produce singlet oxygen ($^1\text{O}_2$) in the presence of **Ir-ppy** in aerated DMSO, known to be the most cytotoxic species generated from PDT. Clinically-approved PDT agents typically make use of excitation wavelengths in the therapeutic window (600 – 800 nm).¹²⁰ Despite the low wavelength of excitation required to generate activity of **Ir-ppy**, it still represents an interesting approach in combining PDT and HDAC inhibition.

Similar to the ruthenium complex (**RuDIP**) tested by Mao *et al.*, complex **Ir-ppy** was also examined for up-regulation of ROS using the DCF fluorescence assay. In the dark, a moderate concentration-dependent increase in ROS generation was observed in HeLa cells over 6 h, compared to the considerable 5-fold increase in fluorescence upon irradiation at 365 nm.¹¹⁸ Additionally, the HDAC inhibitory activity was measured using nuclear HeLa extract which showed similar potency of **Ir-ppy** to SAHA with IC₅₀ concentrations of 0.11 and 0.072 μM, respectively.¹¹⁸ Dosing HeLa cells with **Ir-ppy** led to an increase in histone H3 acetylation level, irrespective of the presence of irradiation. The anticancer mechanism of complex **Ir-ppy** was surmised to employ both photo-induced toxicity originating from the reaction of Ir(III) and oxygen alongside HDAC inhibition to induce cell death.

Rhenium(I) tricarbonyl complexes are another example that possess valuable luminescent properties and have been widely studied for the purpose of cell imaging and biological probes.¹²¹ Complex **ReDIP** contains the rhenium(I) tricarbonyl motif, a pyridine derivative of SAHA as an *N*-donor ligand and a single DIP ligand previously utilised in complex **RuDIP**. The DIP ligand serves a dual purpose, increasing the hydrophobic surface within the molecule and allowing high-energy intrastand (π - π^*) transitions improving overall emission. Countless examples already advocate that enhancing lipophilic character can play a major role in cellular location and uptake.

As anticipated, complex **ReDIP** was effectively taken up by HeLa cells after 2 h incubation at 37 °C, compared to a significant reduction of cellular uptake observed at 4 °C. Treatment with a metabolic inhibitor (carbonyl cyanide 3-chloro-phenylhydrazone) also showed a decrease in accumulation efficiency, implying an energy-dependent pathway was responsible for cellular uptake.¹¹⁹ Cytotoxicity of **ReDIP** was evaluated against the same range of cell lines (A549, A549cis, HepG2 and LO2) as the previously discussed Mao complexes. Unlike complex **Ir-ppy**, irradiation was not required to illicit cytotoxic effects of complex **ReDIP** which showed low IC₅₀ values between 7.5 and 12.2 μM without any illumination. Selectivity was exhibited by **ReDIP** with a 7-fold higher toxicity for cancerous HepG2 cells over healthy LO2 cells.¹¹⁹ Continuing the general trend for these luminescent complexes, production of ROS species was measured to determine if it was attributed to the activity of **ReDIP**. Using DCF as a measure of oxidation induced fluorescence, HeLa cells dosed with 50 μM showed a marked increase of luminescence (MFI : 551) compared to the vehicle control (MFI : 90). Cytotoxicity was reduced in cells pre-treated with *N*-acetylcysteine - a known ROS scavenger - suggesting activity of **ReDIP** relies somewhat on upregulation of ROS.¹¹⁹

Intracellular localisation of **ReDIP** was preferential towards the mitochondria, thought to be influenced by a unique combination of lipophilicity and positive charge. Localisation of class IIa HDAC7 to the inner mitochondrial membrane prompted testing inhibition of recombinant HDAC7

enzyme specifically, with incubation of both complex **ReDIP** and SAHA displaying moderate IC_{50} values; 0.68 and 0.53 μM , respectively. Investigation into the morphological changes of organelles such as mitochondria in HeLa cells treated with **ReDIP** suggested cell death was not caused by the classical apoptotic pathway. Cells incubated with 20 μM of **ReDIP** for 12 h were analysed using TEM which revealed an increase in mitochondria-derived vacuoles and widening of the nuclear membrane space although the nucleus remained intact.¹¹⁹ Caspase involvement was also tested showing no increase in activity when treated with **ReDIP** (50 μM , 6 h) in contrast with the cisplatin control which caused a 6-fold increase in caspase-3/7 activity, a common observation in cell apoptosis.¹¹⁹ Morphological dysfunction of organelles and a caspase-independent mechanism are distinguishing features of paraptosis.

The complexes described in *Section 1.3.3.2* reveal the wealth and variety of properties that can be combined with HDAC enzyme inhibition to create potential theranostic (therapeutic and diagnostic), multifunctional systems. Specific development of compounds with tuneable PDT application offers the advantage of spatial control of treatment, circumventing undesirable toxicity in healthy tissue that can arise from other less selective drugs such as cisplatin. While Mao present a novel direction of HDAC inhibitors, there are no *in vivo* results reported thus far regarding complexes **RuDIP**, **Ir-ppy** and **ReDIP**.¹¹⁷⁻¹¹⁹ Future experiments could probe their potential as genuine anticancer drug candidates with multifaceted character.

1.3.4 Isoform-Selective HDAC Inhibitors

As our understanding of specific biomolecular targets for drugs has advanced, first generation HDAC inhibitors such as SAHA are now recognised as pan-inhibitors due to their lack of selectivity within the classical HDAC family. The discrete intracellular localisation and substrate diversity¹²² of the HDAC classes means pan-HDAC inhibition can result in unwanted side effects including gastrointestinal disturbances and arrhythmia.¹²³ Hence the current design of HDAC inhibitors is focussed heavily on specificity. To target the distinct biological topographies of individual isoforms the pharmacophore model of HDAC inhibitors (*Figure 1.19*) can be modified in a variety of ways. The most popular zinc binding group (ZBG) is the hydroxamic acid due to its strong chelating ability to the Zn^{2+} catalytic site, however other moieties have shown increased potency for selective classes, improving efficacy of those drug candidates. The capping group and chain linker have also been extensively varied to enhance surface and pocket recognition by increasing inhibitor-residue interactions.¹²⁴

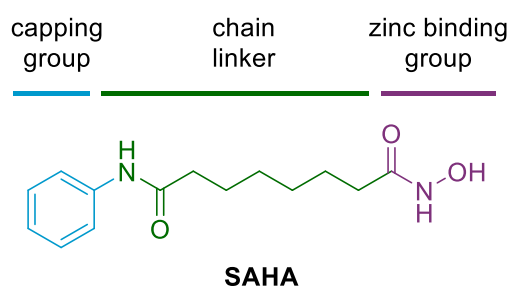


Figure 1.19 Typical structural features of an HDAC inhibitor.

1.3.4.1 Class I – HDAC1, 2 and 3

With the exception of HDAC8, the class I HDAC enzymes form co-complexes with other proteins to form large macromolecules that define their function. Interaction between HDAC1 and HDAC2 is essential for their catalytic activity, forming the core of transcription repressor Sin3A and chromatin remodelling NuRD multiprotein complexes.¹²³ This is demonstrated in the role of HDAC1 and HDAC2 in cell cycle regulation and DNA damage control of both malignant and healthy cells. HDAC3 on the other hand assists activity of nuclear receptor corepressors and can also form complexes with class IIa HDACs.¹²³ A general feature shared by the multiprotein complexes of HDAC 1-3 is their feature of sequence-specific DNA interactions causing transcriptional repression. It is important to note that the occurrence and regulation of these multiprotein complexes is cell-type specific.¹²³

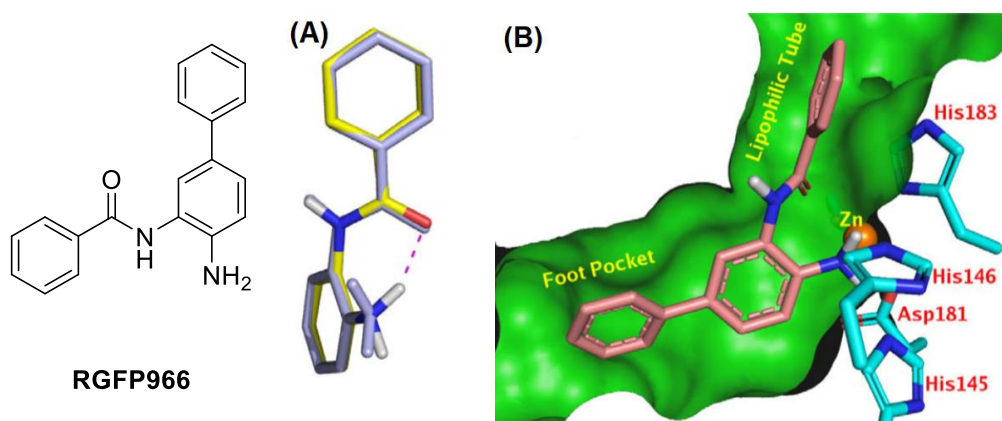
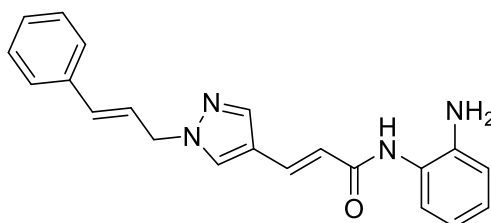


Figure 1.20 (A) Comparison of bound ligand (light blue) and unbound (yellow). Internal hydrogen bond indicated by pink dashed line. (B) X-ray crystal co-complex of bound RGFP966, zinc atom is displayed in orange and the enzyme surface in green.¹²⁵

Specificity towards HDACs 1-3 has been proposed by several groups in the form of 2-aminoanilides. Crystal structures of these enzymes showed a pocket region adjacent to the Zn^{2+} catalytic site that could be accessed by the 2-aminoanilide group with room for functionality at the

5-position.¹²⁵ Bressi *et al.* investigated the structure activity relationship of a range of 2-aminoanilides with HDAC2 and determined that time-dependent inhibition was crucial for some candidates. Compound RGFP966 saw a marked increase in inhibition of HDAC2 activity from an IC_{50} value of 0.90 μM in the 1 h assay to 0.027 μM when pre-incubated for 24 h with the enzyme.¹²⁵ Simulation software showed unbound RGFP966 formed an internal hydrogen bond between the *ortho*- NH_2 and the carbonyl of the amide (Figure 1.20A). The bound form does not contain this hydrogen bond, instead forming complementary interactions with the enzyme active site. Hydrogen atoms of the *ortho*- NH_2 group form H-bonds with histidine 145 and 146 residues, while the nitrogen of this moiety forms part of the chelate to zinc. The time-dependence inhibition is thought to be due to the conformation change needed to reach an equilibrium where the phenyl moiety can fit the foot pocket of the enzyme (Figure 1.20B) and form these favourable interactions that the hydroxamate of SAHA cannot.¹²⁵ Essentially, while the kinetics are slow for the inhibitor to access the foot pocket, the enzyme-inhibitor complex with RGFP966 is much more thermodynamically favourable.



PDAA-01

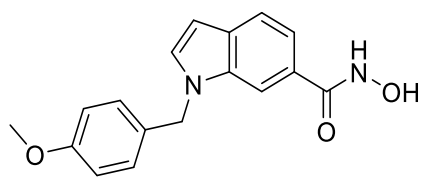
An example of cell-type HDAC abundancy is HDAC3 which is the most highly expressed class I HDAC in the brain and has been linked to learning and memory formation.¹²⁶ Compound **PDAA-01** displayed substantial selectivity towards HDAC3 with an IC_{50} value of 0.08 μM and no inhibition towards any other HDACs up to 15 μM .¹²³ The potent inhibition of HDAC3 was adapted by Malvaez *et al.* into potential behavioural therapy for drug-seeking disorders due to its specificity. In mice, they showed treatment with **PDAA-01** (10 mg/kg) was able to block relapse of cocaine-seeking behaviour suggesting HDAC3 inhibition induced a positive response against maladaptive behaviours.¹²⁷ Although not a potential anticancer treatment, this clearly illustrates the outcome through unique targeting of selective isozymes.

1.3.4.2 Class I - HDAC8

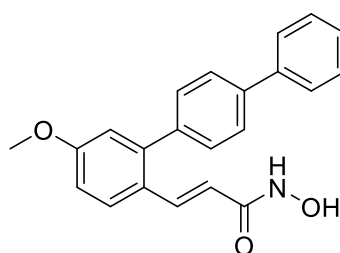
Of the class I HDACs, HDAC8 is anomalous in structure. Substitution of tryptophan 141 in place of a leucine residue prevents the accommodation of bulky groups such as 2-aminoanilides into the active site pocket.¹²⁸ However, a region of high plasticity adjacent to the active site channel of

HDAC8 allows dynamic changes that can form a hydrophobic binding cavity if required by an inhibitors conformation. HDAC8 does not contain the C-terminal domain for recruiting other proteins, acting as an individual protein regulating the differentiation of smooth muscle cells and inducing antiproliferation, particularly in neuroblastoma cells.^{128,129}

Table 1.2 Inhibition constants (IC₅₀ values) for **PCI-34051** against a selection of HDAC enzyme isoforms.¹³⁰

	Enzyme isoform	IC ₅₀ / μM
 <p>PCI-34051</p>	<i>HDAC1</i>	4
	<i>HDAC2</i>	>50
	<i>HDAC3</i>	>50
	<i>HDAC6</i>	2.9
	<i>HDAC8</i>	0.01
	<i>HDAC10</i>	13

Balasubramanian and co-workers synthesised compound **PCI-34051** to encourage interactions of the tryptophan moiety with the aforementioned subpocket. Compound **PCI-34051** exhibited >200-fold selectivity of HDAC8 (IC₅₀ = 0.01 μM) compared to HDACs 1-3, 6 and 10 (*Table 1.2*), while showing higher potency than its hydroxamic counterpart SAHA (IC₅₀ = 0.41 μM); thought to have a lower affinity for HDAC8 due to negligible available interactions around the malleable active site.¹³⁰ *In vitro* testing of **PCI-34051** revealed antiproliferative activity of T-cell derived lines with IC₅₀ values ranging from 2.4 – 4 μM with **PCI-34051** showing no such effect on solid tumours.¹³⁰



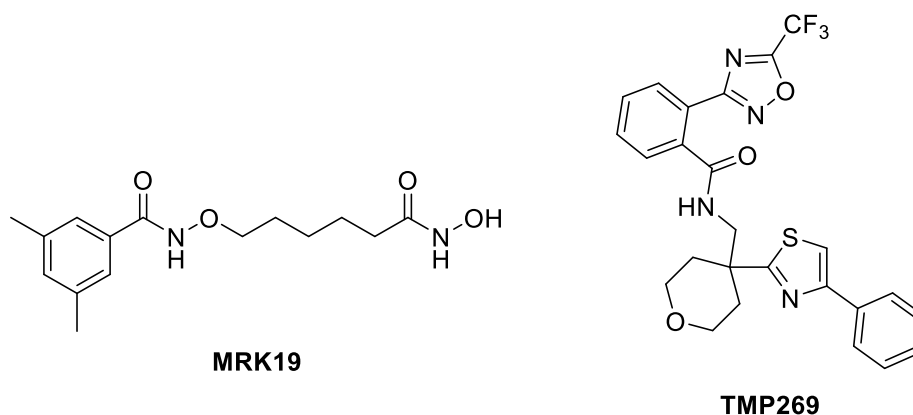
HUA1

Compound **HUA1** is another HDAC8-selective inhibitor, utilising *ortho*-coplanar phenyl groups as the hydrophobic substituents to increase selectivity. Huang *et al.* found **HUA1** gave moderate IC₅₀ values for HDAC 1 and 3 (3 μM) but obvious specificity for HDAC8 with an IC₅₀ value of 0.027 μM.¹²⁹ The superiority of **HUA1** over compound **PCI-34051** was attested to by the additional cytotoxicity of **HUA1** towards lung cancer cell lines A549 and H1299 (IC₅₀ values of 7.9 and 7.2

μM , respectively).¹²⁹ The limited flexibility shown by **PCI-34051** and **HUA1** is evidently not detrimental to HDAC8-selective inhibitor design.

1.3.4.3 Class IIa HDACs

HDACs 4, 5, 7 and 9 are of the class IIa HDAC family and contain a C-terminal domain and an N-terminal adaptor domain. The N-terminal domain distinguishes class IIa from class I by providing binding sites for chaperone proteins (14-3-3) which regulate the localisation of class IIa HDACs between the nucleus and the cytoplasm, along with sites that allow nuclear localisation signalling.¹³¹ Generally, the class IIa HDAC isoforms show restricted expression levels and activity relative to class I isoforms. HDAC4 is moderately expressed in the brain and is integral to skeleton formation, HDAC5 and 9 are fundamental to muscle and heart growth and function while HDAC7 is relevant in vascular cohesion.¹²³ Their involvement in cancer ranges from cell proliferation and survival to differentiation. Most importantly, although class IIa largely retain the conserved structure of class I HDACs, a tyrosine residue in the active site is replaced with a histidine residue. The tyrosine is professed to stabilise the transition-state of acetyl-lysine hydrolysis⁹⁴ and in its absence, the *in vitro* activity of class IIa HDACs is weakened for the canonical acetyl-lysine substrate.¹³²



A class IIa inhibitor (**MRK19**) was synthesised by Marek *et al.* containing a novel alkoxyamide connecting unit in the linker region of the molecule. **MRK19** was tested against A2780 and chemoresistant A2780cis ovarian cell lines in an MTT assay. The subsequent IC_{50} values yielded were 0.49 and 0.32 μM respectively; equipotent to the control drug SAHA.¹³³ Upon screening for HDAC isoform selectivity, **MRK19** showed particularly low IC_{50} values for HDAC4 and 5 (0.012 and 0.004 μM), at least 5-fold more potent than against class I or IIb HDACs, while the analogous SAHA displayed >2000-fold less inhibition for class IIa compared to **MRK19**.¹³³ Docking studies were used to investigate the possible binding mode of **MRK19** to HDAC4 and HDAC8. The phenyl capping group was shown to orientate itself into the groove of the HDAC4 surface, enabling

a more favourable interaction with the catalytic site than for HDAC8. The nitrogen of the alkoxyamide formed a hydrogen bond with the carboxylate group of Asp115 in HDAC4, whereas the equivalent Met274 residue in HDAC8 formed a much weaker interaction.¹³³ While **MRK19** retains the common hydroxamic acid zinc binding group, the novel functionality of the linker is the likely promoter of its selectivity.

Due to the poor deacetylation activity of acetyl-lysine, alternative substrates were explored. The synthetic substrate trifluoroacetyl-lysine was identified by Lahm *et al.* as a more readily deacetylated substrate by class IIa HDACs. This increased activity is thought to be due to the more electrophilic trifluoroacetamide group containing a weaker amide bond, removing the need for a tyrosine mediated transition-state.¹³² Knowledge of this moiety was exploited by GlaxoSmithKline through screening to offer the trifluoromethyloxadiazole as a binding group for potential inhibitors (seen in **TMP269**), possessing bulky character that can also be accommodated by the class IIa subpocket.¹³⁴ This unusual group formed interactions with the zinc catalytic site through the oxadiazole oxygen and a fluorine atom (*Figure 1.21B*). While the large volume of the site is not fully occupied by SAHA, the lipophilic tail of **TMP269** was able to displace the His843 residue to allow an additional edge to face interaction of the phenyl group adjacent to the oxadiazole ring with Phe679 (*Figure 1.21A*).

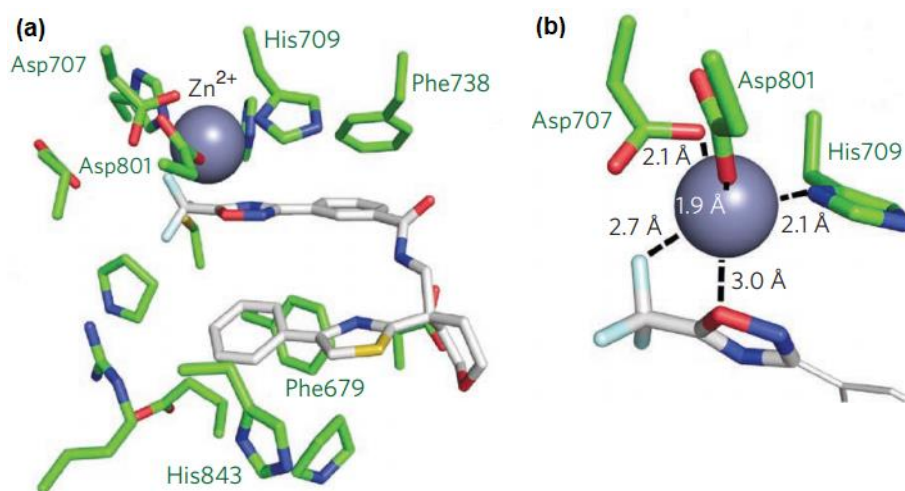


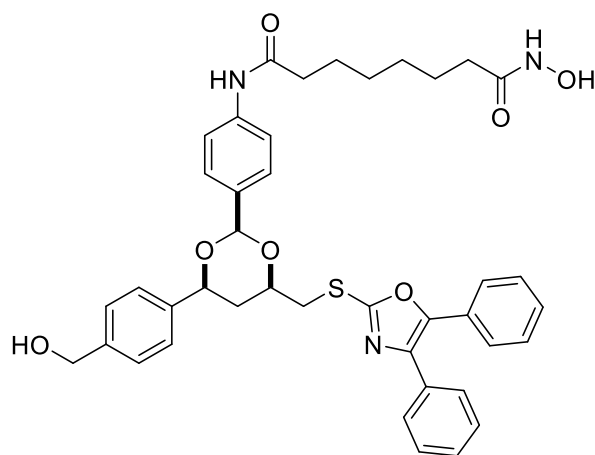
Figure 1.21 (a) Collapsed U-shape of **TMP269** to fill active site. (b) Active site zinc interactions. Bond lengths of zinc-trifluoro fluorine and oxygen of the oxadiazole ring displayed.¹³⁴

TMP269 gave IC₅₀ values ranging from 0.13 to 0.019 μ M against the class IIa HDACs, with 10-fold less inhibition of the other isoforms.¹³⁴ The existing clinical success of SAHA against cutaneous T-cell lymphoma prompted Lobera *et al.* to test the activity of class IIa inhibition on the genome expression of white blood cells (T-cells, B-cells and monocytes). Although **TMP269** showed an overall minimal influence on aberrant gene expression in lymphocytes, CD14⁺

monocytes were transcriptionally sensitive to class IIa HDAC inhibition, suggesting the overall suitability of immunological diseases as a target for class IIa inhibition.^{123,134} The most significant advantage of the trifluoromethyloxadiazole functionality was its generally weak affinity for metal binding, predicted to limit off-target biomolecule interactions. The zinc anion containing matrix metalloproteases 9 and 12 were incubated with **TMP269** up to 50 μM and failed to yield an IC_{50} at this concentration. This result postulated the novel trifluoromethyloxadiazole metal-chelating approach could enhance the efficacy of class IIa HDAC inhibitors like **TMP269** by reducing competitive interactions with other enzymes, often brought about by strongly chelating moieties such as hydroxamic acids.¹³⁴

1.3.4.4 Class IIb – HDAC6

Of all the HDAC enzymes, HDAC6 exclusively features two independent catalytic domains as well as cysteine and histidine-rich regions responsible for ubiquitin protein binding.^{123,135} HDAC6 is located primarily in the cytoplasm by a nuclear export signal (NES) motif and incorporation of a Ser-Glu tetrapeptide (SE14).^{123,135} Within the class II HDACs, a predominant substrate unique to HDAC6 is α -tubulin. Deacetylation of α -tubulin by HDAC6 both *in vitro* and *in vivo* has been shown to mediate cytoskeleton regulation, cell migration and cell-cell interactions.¹³⁶ Due to its localisation, non-histone proteins are the favoured substrates of HDAC6 with minor substrates including the chaperone protein Hsp90; possessing the ability to stabilise particular proteins required for tumour growth.¹³⁵



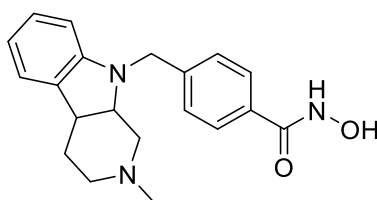
tubacin

Aberrant HDAC6 activity has been reported to produce effects ranging from tumorigenesis, cell proliferation, increased cell motility leading to metastasis, along with an irregular translational or transcriptional response in transformed cells.¹³⁵ For example, overexpression of HDAC6 has demonstrated an increase in chemotactic fibroblast cell motility, intrinsically linked to tumour

metastasis. Inhibition of HDAC6, promoting acetylation of α -tubulin has displayed stabilisation of microtubule growth; reducing cell movement with antimetastatic effect.¹³⁷ HDAC6 is also involved in neurological diseases such as central nervous system (CNS) injury, although the exact mechanism remains undecided it was proposed that HDAC6 regulates the formation of aggresomes (groupings of misfolded proteins) which can be poisonous to neurons causing cell death.¹³⁸ HDAC6 inhibition appeared to encourage regeneration of neurons, promoting its specific inhibition for CNS injury.¹³⁸

Using combinatorial chemistry, tubacin was identified as an HDAC6-selective inhibitor in 2003.¹³⁹ Screening against all 11 HDAC isozymes revealed an IC_{50} value of 0.004 μ M for tubacin against HDAC6; displaying over 300-fold selectivity for HDAC6 compared to the other HDAC enzymes. Cultured A549 cells were dosed with 10 μ M tubacin which induced a 3-fold increase in α -tubulin acetylation, consistent with HDAC6 enzyme inhibition. The carboxylate analogue (nil-tubacin) of tubacin showed no notable change in α -tubulin acetylation levels, suggesting the hydroxamic acid zinc-binding group is essential for tubacin activity.¹³⁹

Marks *et al.* explored the possible synergistic effects of HDAC6 inhibition by tubacin with existing anticancer agents. Transformed LNCaP human prostate cancer cells displayed an enhanced loss of cell viability (80%) when dosed with both SAHA and tubacin (2.5 and 8.0 μ M, respectively) after 72 h incubation, while SAHA alone (2.5 μ M) showed no change in cell viability.¹³⁷ To determine if the cytotoxicity was increased as a result of selective HDAC6 inhibition, nil-tubacin was co-incubated with SAHA and did not increase LNCaP cell death. LNCaP cells were also used to determine a potential pathway for cell death and whether influenced - in part - by tubacin. Poly(ADP ribose) polymerase (PARP) is specifically cleaved by caspase-3 from 116-kDa to the smaller 85-kDa protein fragment and can be used as a marker for apoptosis. Incubation of LNCaP cells with SAHA at 2.5 μ M (a concentration demonstrated to not cause cell death), showed no PARP cleavage. An increase in cleaved PARP resulted from co-incubation with tubacin and SAHA (2.5 μ M), illustrating the contribution of caspase activation to the pathway for cell death when treated with tubacin.¹³⁷ Although tubacin was shown to be highly specific in its biomolecular target, its high lipophilicity and challenging synthesis inspired scope for more appropriate drug candidates as HDAC6 inhibitors.

**tubastatin A**

Prompted by the superior selectivity of tubacin, Kozikowski *et al.* proposed the rational design of the drug-like molecule tubastatin-A as a simpler alternative. Due to the high lipophilicity of carbazole, the large capping group was adapted to reduce planarity by introducing a tertiary amine that could also aid the formation of pharmaceutical salts improving solubility.¹⁴⁰ Homology models of HDAC1 and HDAC6 were generated to predict interactions of tubastatin-A with the different classes of protein. While the catalytic site is highly conserved in both isozymes, the channel and pocket rim dimensions greatly differ. The channel rim of HDAC6 is much wider and shorter than HDAC1, providing a region to target specifically for HDAC6.¹⁴⁰ The tolyl linker of tubastatin A was predicted to form interactions with the apolar channel lining (Phe620, Pro608 and Cys621 residues) of HDAC6, forcing a bent conformation which also enhanced interactions of the tricyclic group with the channel rim. The bulky capping group allowed π - π stacking of the aromatic ring with phenylalanine residues along with polar interactions of the tertiary amine with surface Asp567 and Ser568.¹⁴⁰ The multiple interactions of tubastatin A with HDAC6 was reflected in its preferential activity towards this isozyme. The IC_{50} value against HDAC6 was 0.015 μ M for tubastatin A, similar to that of tubacin (0.004 μ M) and 50-fold more potent than against any other HDAC enzyme. The large capping group motif in both tubacin and tubastatin A is thought to enable this selectivity.

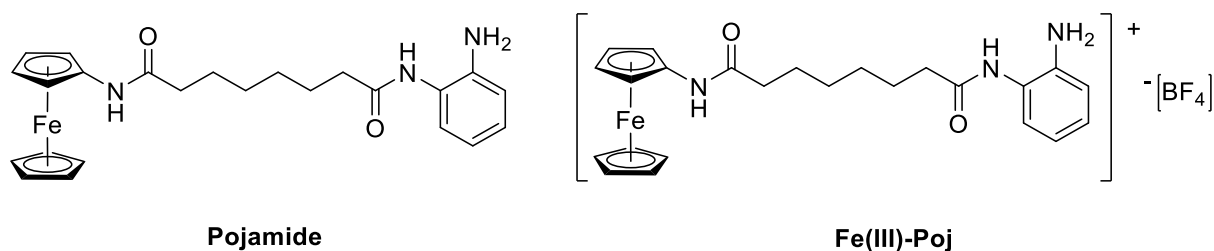
Table 1.3 Selected HDAC isoform inhibition IC_{50} values for nexturastat A.¹⁴¹

	Enzyme isoform	IC_{50} / μM
<p>nexturastat A</p>	<i>HDAC1</i>	3.0
	<i>HDAC2</i>	6.9
	<i>HDAC5</i>	11
	<i>HDAC6</i>	0.0050
	<i>HDAC8</i>	0.95
	<i>HDAC10</i>	7.6

Kozikowski *et al.* proceeded to exploit an additional lipophilic side cavity of the HDAC6 shallow channel rim using branched urea linkers. Nexturastat A was designed with an *n*-butyl group from the nitrogen distal to the phenyl capping group to occupy the cavity with the desire to enhance potency and specificity.¹⁴¹ Increased selectivity was achieved by nexturastat A, providing IC₅₀ values of 3.02 and 0.005 μM for HDAC1 and HDAC6 (Table 1.3), respectively; 3-fold more potent towards HDAC6 than tubastatin A.^{123,140,141} Hyperacetylation of the major HDAC6 substrate α-tubulin was measured in B16 murine melanoma cells treated with nexturastat A. At nanomolar concentrations a dose-dependent increase in α-tubulin acetylation was observed with no elevation in H3 histone acetylation until micromolar concentrations were used.¹⁴¹ This result correlates the inhibition profile of nexturastat A with the preference of HDAC6 inhibition over HDAC1 (whose major substrate is histone proteins), within a cellular environment. Nexturastat A displayed moderate growth inhibition of B16 melanoma cells (IC₅₀ = 14.3 μM) compared to more polar analogues and tubastatin A. While the full mechanism leading to cell death is not yet explored, the ideal parameters of drug-likeness suggest the lipophilic *n*-butyl group contributes to efficient cell permeability and activity of nexturastat A.¹⁴¹

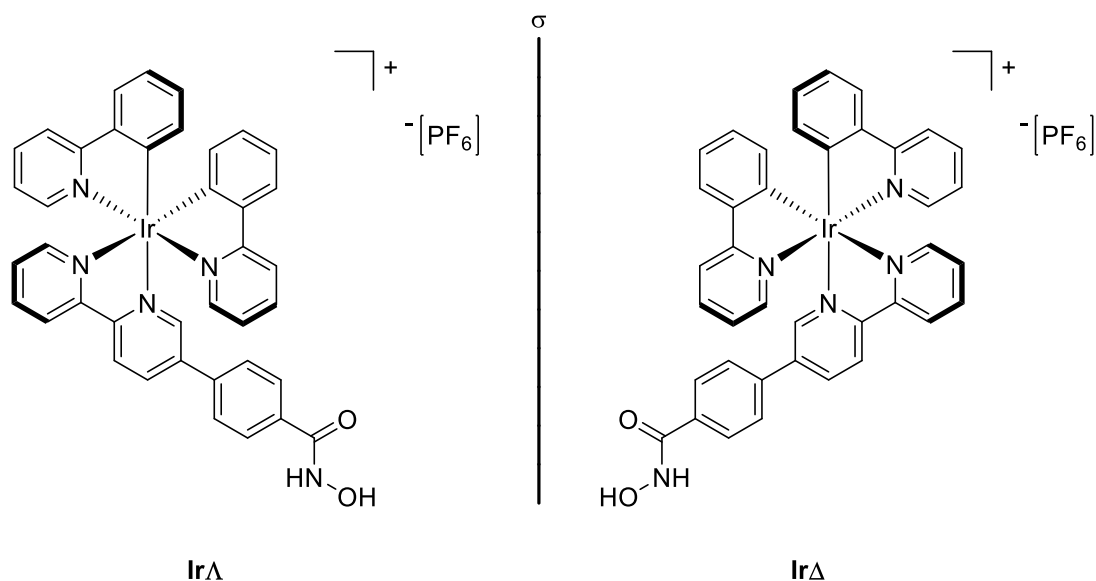
1.3.4.5 Metal-Based Isoform-Selective HDAC Inhibitors

While metal-based HDAC inhibitors are becoming more frequently utilised due to their exploitable oxidation states, geometries and modular synthesis, isoform selective metal-based HDAC inhibitors remain scarce in the literature. JAHA for example (Section 1.3.3.2), although displaying good potency for HDAC inhibition, showed no distinguishable selectivity for an individual isoform with IC₅₀ values for class I HDACs 1, 2 and 3 in the small range between 0.011 and 0.018 μM. With this in mind, in 2017 Spencer *et al.* synthesised Pojamide: an HDAC3-selective inhibitor analogous to the ferrocene containing complex JAHA, incorporating the aforementioned 2-aminoanilide class I selective zinc-binding group (Section 1.3.4.1). Docking studies were performed to determine selective interactions of Pojamide with the HDAC3 isozyme. Hydrogen bonds formed between the amide N-H and the carbonyl of the Asp90 residue, benzamide amide N-H and the carbonyl of Gly143, along with the an interaction between the aniline NH₂ and the nitrogen of the His134 in the catalytic site.¹⁴² Shortening of the carbon chain linker forced rotation of the benzamide group which reduced these key interactions.



Pojamide activity towards HDAC isozymes was comparable to other 2-aminoanilide inhibitors, displaying an IC_{50} of 0.09 μM against HDAC3, 11- and 22-fold more active than against HDAC1 and 2 along with no notable inhibition of the other HDAC enzymes ($>30 \mu M$)¹⁴². HDAC3-specificity of Pojamide was measured using *Xenopus laevis* embryos as a model for deacetylase activity. H4K12 is a histone lysine residue shown to be deacetylated specifically by HDAC3¹⁴³, accumulation of acetylated H4K12 in the *Xenopus laevis* was observed in a concentration-dependent manner when dosed with Pojamide, while no apparent effect on α -tubulin was shown. Along with HDAC3-isoform selectivity, Pojamide displayed moderate inhibition of cell proliferation in HCT116 human colon carcinoma cells providing a GC_{50} value (the amount of compound required to cause 50% reduction in cell proliferation) of 8.9 μM .¹⁴²

The ability of the ferrocenium cation to induce DNA damage by generation of reactive oxygen species (hydroxyl radicals specifically) is documented in MCF-7 and MCF10A cells.¹⁴⁴ Through oxidation of the ferrocene capping group with nitrosium (NO^+) tetrafluoroborate, Spencer *et al.* were able to exploit the additional cytotoxicity of ferrocenium in the form of Fe(III)-Poj. Intracellular sodium nitroprusside (SNP) produces NO^+ which can be balanced by the antioxidant GSH. Due to the high toxicity of SNP alone ($>30 \mu M$ can cause apoptosis), optimal concentrations of SNP and GSH were dosed alongside the Pojamide inhibitor. In combination with SNP/GSH, at 4 μM concentration of Pojamide for 6 days, similar levels of DNA damage were observed in HCT116 cells as the cisplatin control.¹⁴² Reactive oxygen species generation in HCT116 cells was shown to increase 3.3-fold when dosed with Pojamide/SNP despite the presence of GSH. The results from combination treatment suggest the oxidation of Pojamide to the Fe(III)-Poj species by SNP increases ROS production enhancing cytotoxicity. This metal-based isoform selective inhibitor is of particular interest due to its two distinct modes of action. While Pojamide possesses HDAC3 selective inhibitory character, the addition of the ferrocene provides a novel redox quality not found in organic HDAC inhibitor examples; providing DNA damage alongside enzyme inhibition, enhancing the efficacy of Pojamide as a potential drug candidate.



Chiral *bis*-cyclometalated octahedral organoiridium(III) complexes are another recent example displaying moderate HDAC-isoform selectivity. Meggers *et al.* wanted to determine any specific molecular recognition of iridium complex enantiomers by designing propeller type complexes that could bind the enzyme active site and allow the coordination sphere to accommodate the enzyme pocket.¹⁴⁵ A pair of enantiomeric iridium propeller complexes (**IrA** and **IrΔ**) were tested for HDAC inhibition against HDACs 1, 6 and 8. Both enantiomers exhibited 10-fold more potency towards HDAC6 than HDAC1 in the nanomolar range (HDAC6 IC₅₀ values for **IrA** and **IrΔ**: 110 and 202 nM, respectively).¹⁴⁵ Interestingly, complex **IrA** observed 2-fold increase in potency for all HDAC enzymes tested compared to **IrΔ**. It was proposed that in this instance, the low stereodiscrimination between enantiomers is driven by the hydrophobic nature of these complexes. Stronger stereodiscrimination is thought to occur more readily between functional groups and specific aminoacid residues, enhancing molecular recognition for a single enantiomer.

1.3.5 Summary

Remarkable progress has been made into identifying specific molecular targets in the treatment for cancer. Upregulation of HDAC enzyme activity is one of many mutations observed in malignant cells and therefore exploited as a suitable target for anticancer drug candidates. The first generation of HDAC inhibitors (including SAHA) provided a new platform for drug design, displaying high selectivity towards cancerous cells over healthy cells establishing early improvements to therapeutic efficacy. Gradually, as our understanding of subcellular processes has advanced, the undesirable qualities of pan-inhibitors such as SAHA became more apparent and the need for HDAC-isoform specificity was recognised.

Like many enzyme families, HDAC isoforms are divided into classes dependent on their topological similarities. Their classes also denote more specific substrates and cellular localisation. These findings prompted the design of second generation HDAC inhibitors with much higher degrees of selectivity. It is clear that while the literature is awash with small organic molecule examples, metal-based HDAC-isoform selective inhibitors offer alternative properties in enzyme inhibition design and could be further exploited.

1.4 Hypoxic Activation

Although briefly touched upon in some previous examples, a key point of consideration when formulating anticancer agents is their behaviour in the targeted environment. For instance, solid tumours contain low levels of oxygen (hypoxia) due to an imbalance between oxygen supply and consumption.¹⁴⁶ Rapid tumour growth, whilst increasing the demand for oxygen gives rise to cells located too distant from blood vessels that deliver essential metabolites including oxygen, generating regions of hypoxia and internal tumour necrosis.¹⁴⁷ Tumour hypoxia is known to promote the development of a more aggressive phenotype that has demonstrated an upregulation in genes associated with angiogenesis and enhanced metastasis.^{148,149} Not only do these factors compromise the efficacy of tumour removal by surgery, such a malignant phenotype also boasts resistance to ionising radiation and chemotherapeutic treatment.^{146,148,150}

Radiotherapy creates radicals on DNA which are either oxidised (largely by oxygen), propagating the damage to DNA or competitively reduced by thiol containing biomolecules, evading any permanent DNA damage. In the absence of oxygen, less DNA damage occurs rendering radiotherapy less effective under hypoxic conditions.¹⁴⁸ By contrast, resistance to chemotherapy is multifaceted. Some classes of drugs act during specific phases of the cell cycle, which is slower in hypoxic cells reducing overall drug performance. Hypoxic conditions increase the activity of DNA-repair enzymes, compromising the efficacy of DNA-binding drugs. The location of viable hypoxic cells is between 50 – 250 μm from blood vessels,¹⁵¹ restricting drug delivery and distribution. And finally, while normal intracellular pH is maintained during tumorigenesis, the extracellular hypoxic conditions possess a much lower pH, creating a pH gradient which can reduce intracellular accumulation of weakly basic drug candidates.¹⁴⁶ These collective drawbacks in treating solid tumours can be overcome by designing drugs that exploit such unique hypoxic conditions. Designing hypoxia-activated prodrugs is one strategy that utilises initially non-toxic compounds that generate an active species upon bioreduction. This objective has been pursued extensively using organic frameworks including: quinones, nitroaromatics, tertiary amine *N*-oxides and aromatic di-*N*-oxides.¹⁵⁰

One of the first hypoxia-activated drugs to show distinctive specificity towards hypoxic cells was developed by Brown *et al.* as tirapazamine (TPZ, *Figure 1.22*), a benzotriazine di-*N*-oxide.¹⁵² Testing was undertaken on human malignant cell lines HCT-8 and A549 as well as normal AG 1522 cells under aerobic and hypoxic conditions with cells dosed in a concentration range between 1.5 mM and 5 μ M. A hypoxic cytotoxicity ratio was calculated (concentration of drug in aerobic conditions divided by concentration of drug in hypoxic conditions to produce the same level of cell death) and was found to be between 15 – 50 for the cell lines tested.¹⁵² *In vivo* experiments were performed using SCC VII murine tumours in a clonogenic assay to measure the surviving fraction of the tumour after injection of TPZ (0.3 mmol/kg). After 24 h incubation, tumours treated alone with TPZ showed the surviving fraction reduced by a factor of 3.1 compared to those treated with additional radiation that reduced by a factor of 43.1.¹⁵² A decrease in the hypoxic cell survival implied TPZ not only possess its own intrinsic cytotoxicity but significantly sensitises hypoxic cells to radiation therapy.

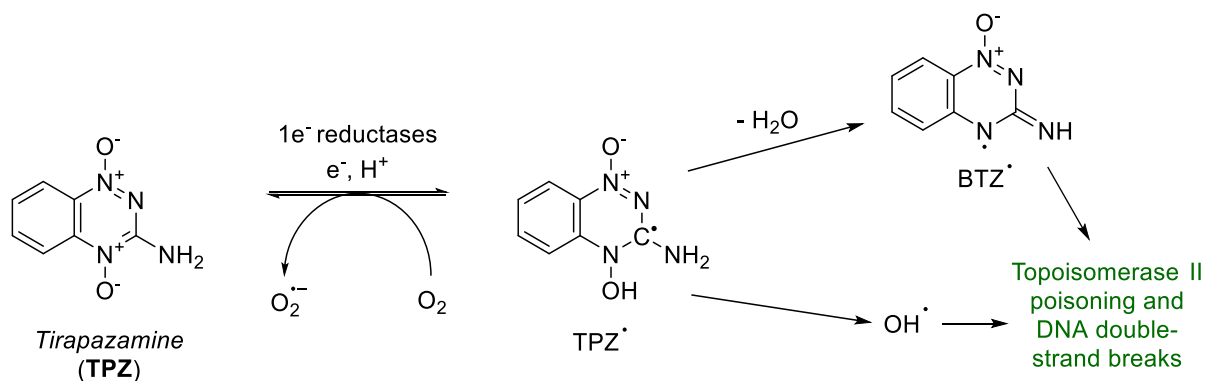


Figure 1.22 Clinical trialled, hypoxic active benzotriazine drug *Tirapazamine* and predicted mechanism of action.^{153,154}

Further investigation by Brown and Peters into the properties of tirapazamine revealed the formation of highly reactive free radical species as the mechanism of action (*Figure 1.22*). TPZ is converted to a TPZ• radical by one electron reductase enzymes, found to be highly expressed in hypoxic tumours.¹⁵⁵ If oxygen is present, TPZ• is back-oxidised to the nontoxic parent compound.¹⁵⁴ Spontaneous decay of TPZ• provides the oxidising OH• radical or an BTZ• radical. While these oxidizing radicals were considered directly responsible for DNA double-strand breaks (DBSs), later evidence suggested the involvement of topoisomerase II (topoII) poisoning.¹⁴⁸ To test the participation of topoII in TPZ toxicity, H69 small cell lung carcinoma were co-incubated with TPZ and aclarubicin – a topoII inhibitor – under hypoxic conditions. DNA DSBs caused by TPZ were reduced by over 60% when co-incubated with aclarubicin.¹⁵⁶ Hydroxyl radicals are documented to damage topoII enzymes, stimulating topoII-mediated cleavage creating DNA DSBs. It is therefore proposed that cytotoxicity of TPZ is in part, through poisoning of topoII by hydroxyl

radicals formed by TPZ' decay under hypoxic conditions.¹⁵⁶ Despite the promising results shown by TPZ in phase I and II clinical trials over the past decade, phase III trials failed to demonstrate any survival benefit to patients when using TPZ alongside conventional chemotherapy or radiotherapy.¹⁵⁷ However, phase III trials are still ongoing.

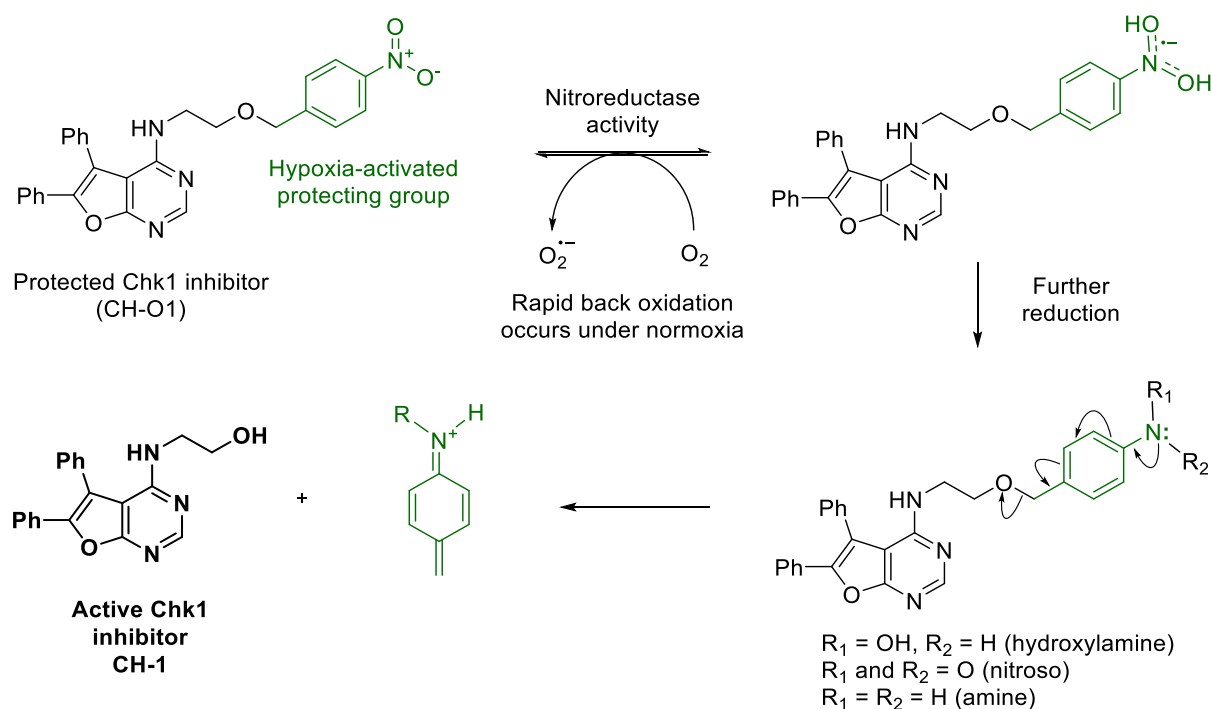


Figure 1.23 Attachment of the 4-nitrobenzyl group to the terminal hydroxyl group of CH-1 kinase inhibitor. Under hypoxic conditions the nitro group is reduced to give the active drug CH-1.¹⁵⁸

Enzyme inhibitors are an alternative class of compounds where applying the principle of bioactivation under hypoxic conditions has also produced encouraging results. One noteworthy example is the protected Chk1 kinase inhibitor (CH-O1) synthesised by Conway *et al.* which utilises a bioreductive 4-nitrobenzyl group, that upon reduction releases the active inhibitor CH-1 (Figure 1.23).^{158,159} The simple synthetic modification by addition of the 4-nitrobenzyl group and its subsequent reduction and removal under hypoxic conditions was effectively monitored using multiple reduction assays. Initially the prodrug CH-O1 was treated with zinc in a solution of DMF and NH_4Cl ($1 : 1 \times 10^{-5}$) to mimic enzyme reduction and the reaction was monitored by HPLC over 24 h. The 4-nitro group was fully reduced to provide the amine product which was combined with a potassium phosphate buffer (pH 7.4), promoting fragmentation (Figure 1.23) to afford the active kinase inhibitor CH-1.¹⁵⁸ In an alternative assay, bacterial human NADPH-cytochrome (CYP) reductase was incubated in potassium phosphate buffer with the CH-O1 prodrug. Under normoxic conditions CH-O1 remained intact with no fragmentation observed compared to complete release of the active CH-1 species under hypoxic conditions.¹⁵⁸ These results suggest CH-O1 is reduced via

chemical conditions and through incubation under hypoxic conditions in the presence of reductase enzyme; consistent with the proposed mechanism.

Chk1 is involved in the cell cycle and its inhibition can directly induce DNA damage. *In vitro* testing of CH-01 was undertaken to determine such potential toxicity and measure the extent of inhibitor activity under varying conditions. The DNA damage response protein 53BP1 accumulates after DNA double-strand breaks occur. Using Western blotting analysis, Conway *et al.* determined an accumulation of 53BP1 foci in over 50% of RKO colon carcinoma cells exposed to CH-01 under hypoxia.¹⁵⁹ A colony survival assay followed to discern the effects of CH-01 on RKO cell viability at oxygen tensions between 20% to $\leq 0.02\%$ O₂. At 3% O₂ (normal tissue concentration), little to no effect was observed on cell viability, whereas lower levels of O₂ incubation suggested reduced cell viability was oxygen-dependent.¹⁵⁹ Control tests with an ethanol substituted 4-nitrobenzyl compound which released ethanol upon reduction had no effect on cell viability when dosed to RKO cells alone under hypoxic conditions, implying the reduced side-product is nontoxic and was not an additive towards toxicity. Under normoxic conditions neither CH-01 or the control compound exhibited significant effect on cell viability, correlating with early findings that suggested alkylation of the primary hydroxyl markedly reduced overall activity of CH-1.¹⁵⁹ These results display the extent of improved sensitivity of the protected Chk1 kinase inhibitor CH-01 towards hypoxic cells via an oxygen-dependent activation pathway, with the enzyme inhibitor properties retained as the parent compound, CH-1.^{158,159}

Hypoxic-activation is not just limited to organic systems, it can also be effectively utilised through the redox properties of metals. As previously discussed in *Section 1.3*, metal-based enzyme inhibitors can contain a metal acting as a chaperone for a biologically active ligand and upon reduction the organic drug is released. In forming coordination complexes, metals can associatively change the pharmacological properties of organic based drugs through tumour targeting, cellular localisation and can even enhance cellular uptake with additional lipophilic carrier ligands.¹⁶⁰

The matrix metalloproteinase inhibitor **Co^{III}-mmst** seen in *Table 1.1 (Section 1.3)* is reiterated as one of two particular examples discussed here of exploitable redox activity of a metal complex. Clinical trials of the organic drug marimastat (active species of **Co^{III}-mmst**, *Figure 1.24*) were terminated as the drug failed to display progressive results when compared to existing therapies.¹⁶¹ It was proposed that the chelating ability of the hydroxamate to other metal ions contributed to the reduced efficacy of marimastat *in vivo*. Hambley and co-workers used a scaffold comprising a tris(methylpyridyl)amine (tpa) around an inert Co(III) metal centre, leaving two free coordination sites for the active marimastat molecule to bind. The use of the Co(III)tpa chaperone had been previously documented to possess a suitable reduction potential, consistent with reduction induced under hypoxic conditions.⁷⁵ Therefore, the design of **Co^{III}-mmst** encompassed the binding of the

the redox potential of the platinum metal centre. Although, unlike the Co(III) complexes, upon reduction and subsequent ligand substitution, it is the Pt(II) metal centre binding directly to DNA that is the cause of platinum drug cytotoxicity.^{160,164} While the Pt(IV) prodrug satraplatin (*Section 1.2.1*) has progressed through clinical trials, there is still great contention over the reduction mechanism of Pt(IV) prodrugs and the resulting efficacy of the active species. It is widely accepted that naturally occurring biomolecules such as ascorbate and glutathione can reduce Pt(IV) prodrugs by distinct mechanisms often dependent on the axial ligands.¹⁶⁴ The examples illustrated above give a keen insight into the exploitable redox properties of metals, a characteristic often favoured when utilising metals in attempting to progress the efficacy of a drug candidate beyond *in vitro* testing.

Rational drug design in organic chemistry is often inspired by nature and focuses on a compounds shape. This factor can be enhanced by the presence of a metal adding a 3D geometry, difficult to achieve with a purely organic system. One solution that could combine the two areas that is relatively untouched in the literature is the use of the metal complex to provide a specific shape - whether this allows enhanced DNA-binding or selective enzyme targeting - while incorporating an organic ligand that is activated in a reducing environment. This amalgamation of characteristics, if considered judiciously, could enhance overall activity by a new and interesting pathway. Naturally, the construction of such a complex would require a strongly chelating motif to the metal centre, along with a metal centre that would be largely unaffected under hypoxic conditions, meanwhile retaining the intended anticancer properties. Such an alternative could expose a novel use for metal complexes as hypoxic-active prodrugs.

1.4.1 Summary

The presence of hypoxia in solid tumours is an impediment on the effects of preferred treatments such as radiotherapy and chemotherapy. However, the existence of hypoxia presents an opportunity for tumour-selective therapy. One of the predominant methods to target these regions is via hypoxia-activated prodrugs. The initial form of a prodrug is designed to be inert prior to activation, which largely avoids damage to healthy tissue and aids specific tumour targeting in the more reducing environment. In some cases, part of the drug is intended to act as a carrier aiding the delivery to the appropriate area where the active species can be released. It has been shown in this section that there are multiple chemical pathways to exploit hypoxia, depending on the structure of the inactive species. Furthermore, the examples discussed have highlighted the requirement for tuning complimentary properties to ensure that hypoxia-activated prodrugs are fit for purpose.

1.5 Aims and Specification

The aim of this project is to design, synthesise and characterise novel piano-stool complexes to act as anticancer agents while investigating their potential mechanisms of action, as described above. Currently, there are countless examples of complexes which employ the pseudo-octahedral geometry to formulate potential drug candidates with varying degrees of success. It is clear from such examples discussed that the combined properties of the metal ion along with its coordinating ligands must complement each other to conserve the most desirable properties for biological applications. Factors which must be taken into account include: aqueous stability, behaviour in variable physiological conditions and specific biomolecular targets. The specification for the piano-stool complexes is as follows:

- a) Design and synthesise DNA binding piano-stool complexes with good cytotoxicity against transformed cells.
 - i. Incorporation of a ^{31}P spectroscopic handle into a bidentate ligand system – Allowing a secondary mode of monitoring complex properties under various conditions using ^{31}P -NMR Spectroscopy.
 - ii. Aqueous availability – The design should ensure the monodentate halide ligand is able to undergo exchange in intracellular conditions for the labile aqua species and favour this formation to allow subsequent DNA-binding.
 - iii. Retention of phosphinate ligands – Complex structure should be kinetically and thermodynamically stable towards dissociation induced by competing ligands. Substituents within the phosphinate ligand should promote the strength of ligand coordination.
- b) Target histone deacetylase enzyme inhibition with piano-stool complexes.
 - i. The specific biomolecule should have clear influence and contribution to malignancies – dysregulation of epigenetic modifiers such as HDAC enzymes directly affect gene expression leading to cellular transformation. From the discussion in *Section 1.3.4*, this biomolecular target was considered appropriate.
 - ii. Determine inhibition of the target molecule is the likely mechanism of action providing cytotoxicity – This could be achieved using DNA-binding, protein-binding and enzyme inhibition assays.
- c) Optimise selectivity towards specific HDAC isoforms.
 - i. Choose suitable complex modifications – Maximise enzyme-surface interactions by constructing a more complex arene. Improve selectivity through adjusting the chain-linker. From the discussion in *Section 1.3.4.4* introducing a tolyl linker should promote HDAC6 selectivity.

- ii. Minimise off-target binding – optimised complexes should observe minimal additive effects from off-target binding, minimising unwanted side-effects.
- d) Incorporate a hypoxic-active motif – modify the organic ligand through protection of the catalytic-site binding group.
 - i. Assess the efficiency of the protecting group – Ease of reducibility under hypoxic conditions and monitor formation of the desired active species. The discussion in *Section 1.4*, suggests the use of a *p*-nitrobenzyl group would be the simplest synthetic route to a protected hydroxamic acid.
 - ii. Ensure reduction to the active species *in vitro* – Provide appropriate changes in cytotoxicity under conditions of hypoxia and normoxia.

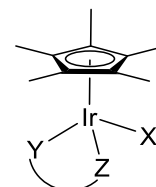
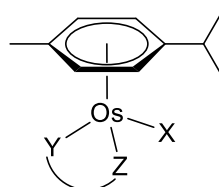
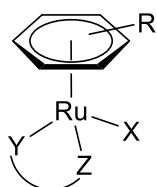
The following chapters detail the synthesis and characterisation of a range of piano-stool complexes which aim to meet one or more of the specifications above. The focus of *Chapter 2* is to show a selection of pyridylphosphinate containing complexes and their properties. *Chapter 3* introduces the concept of alternative biomolecular targets, followed by optimisation of enzyme class specificity in *Chapter 4*. Finally, *Chapter 5* details the early stages of developing a hypoxic active piano-stool complex, not yet seen in the literature.

2. Pyridylphosphinate Metal Complexes

2.1 Introduction

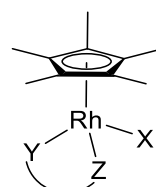
The pyridylphosphinate ligand was established by Parker *et al.* and has been used in a variety of systems with applications in numerous areas of bioinorganic chemistry.^{165–167} This study reports the synthesis, structural characterisation, aqueous behaviour and toxicity of a series of 25 novel half-sandwich piano-stool complexes (*Table 2.1*) incorporating the pyridylphosphinate ligand (*Table 2.2*) to investigate the potential anticancer properties of this ligand system.

Table 2.1 Pyridylphosphinate complexes (*pCy* = *p*-cymene; *Bnz* = benzene). ^aSynthesised by other members of the Walton group.



Complex	R	YZ	X
Ru1PP1^a	<i>pCy</i>	<i>PP1</i>	Cl
Ru1PP2^a	<i>pCy</i>	<i>PP2</i>	Cl
Ru1PP3	<i>pCy</i>	<i>PP3</i>	Cl
Ru1PP4	<i>pCy</i>	<i>PP4</i>	Cl
Ru1PP5	<i>pCy</i>	<i>PP5</i>	Cl
Ru1PP6	<i>pCy</i>	<i>PP6</i>	Cl
Ru1PP7	<i>pCy</i>	<i>PP7</i>	Cl
Ru1PP8^a	<i>pCy</i>	<i>PP8</i>	Cl
Ru1PP9^a	<i>pCy</i>	<i>PP9</i>	Cl
Ru2PP1^a	<i>pCy</i>	<i>PP1</i>	I
Ru2PP2^a	<i>pCy</i>	<i>PP2</i>	I
Ru2PP6^a	<i>pCy</i>	<i>PP6</i>	I
Ru2PP3^a	<i>pCy</i>	<i>PP3</i>	I
Ru3PP1^a	<i>Bnz</i>	<i>PP1</i>	Cl
Ru3PP2^a	<i>Bnz</i>	<i>PP2</i>	Cl

Complex	YZ	X
OsPP1^a	<i>PP1</i>	Cl
OsPP2^a	<i>PP2</i>	Cl



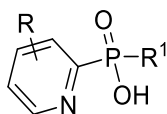
Complex	YZ	X
RhPP1^a	<i>PP1</i>	Cl
RhPP2^a	<i>PP2</i>	Cl
RhPP5	<i>PP5</i>	Cl
RhPP6	<i>PP6</i>	Cl

Complex	YZ	X
Ir1PP1^a	<i>PP1</i>	Cl
Ir1PP2^a	<i>PP2</i>	Cl
Ir1PP6	<i>PP6</i>	Cl
Ir2PP1^a	<i>PP1</i>	I
Ir2PP2^a	<i>PP2</i>	I

Advantages of the pyridylphosphinate ligand include: the inclusion of a ³¹P-NMR spectroscopic handle; biocompatibility; lipophilic control of the R¹ group on the phosphorus; modular synthesis and the presence of stereogenic phosphorus, presenting the opportunity to develop enantiomerically pure metal-based drugs.¹⁶⁸

Table 2.2 Pyridylphosphinate ligands (^asynthesised by other members of the Walton group).

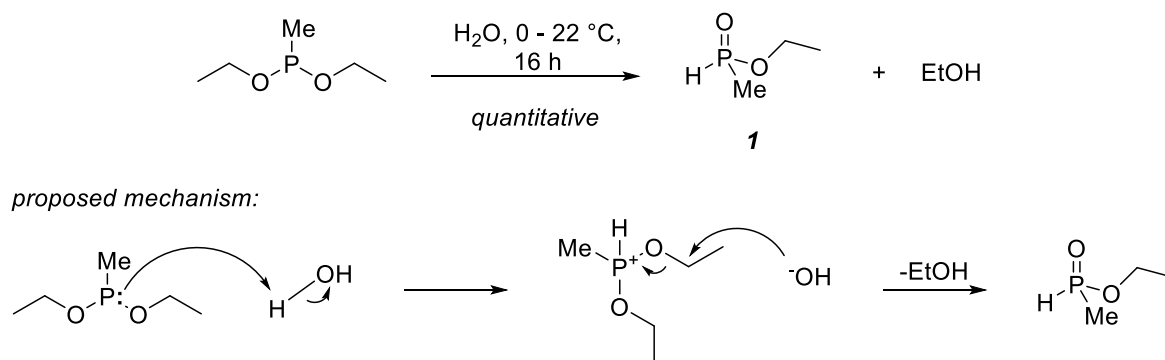
Ligand	R	R ¹
<i>PP1^a</i>	H	Ph
<i>PP2^a</i>	H	Me
<i>PP3</i>	3-Me	Ph
<i>PP4</i>	3-Me	Me
<i>PP5</i>	4-Me	Ph
<i>PP6</i>	4-Me	Me
<i>PP7</i>	4-OCD ₃	Ph
<i>PP8^a</i>	4-Cl	Ph
<i>PP9^a</i>	4-NH ₂	Ph



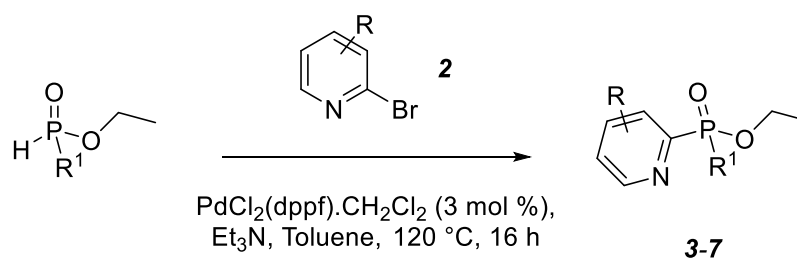
2.2 Synthetic Aspects

2.2.1 Pyridylphosphinate Ligand Synthesis

The initial step to synthesise pyridylphosphinate involves the formation of ethyl methylphosphinate (*I*) from commercially available diethyl methylphosphonite. The synthesis of *I* has been previously published¹⁶⁹ and proceeds by cooling the starting material diethyl methylphosphonite to 0 °C under an argon atmosphere, followed by the addition of water (1 equivalent) and the solution allowed to heat to room temperature overnight (*Scheme 2.1*). The product, *I*, was formed in quantitative yield and confirmed by ¹H NMR along with an equimolar amount of ethanol. The phenyl analogue of *I* is commercially available. A mechanism is suggested in *Scheme 2.1* inspired by the known Michaelis-Arbusov reaction. While this mechanism would likely encourage scepticism, a proton-phosphorus bond is undoubtedly formed denoted from the large coupling constant (¹J_{HP} 537 Hz) observed in the ¹H-NMR spectrum.

**Scheme 2.1**

The following step involved the palladium catalysed coupling of a range of substituted and unsubstituted 2-bromopyridines (**2**) with **1** or the readily available ethyl phenylphosphinate precursors. The respective phosphinate, **2** and triethylamine were dissolved in toluene and the mixture degassed. After 1 h the Pd-catalyst was added and the reaction heated overnight at 120 °C (Scheme 2.2). The resulting reaction mixture was diluted into dichloromethane and washed with 1 M HCl and water. The organic layer was dried over MgSO₄ and purified by column chromatography on silica using a gradient mobile phase of varying DCM:MeOH ratios, depending on the compound (**3-7**). The yields for compounds **3-7** are displayed in Table 2.3.

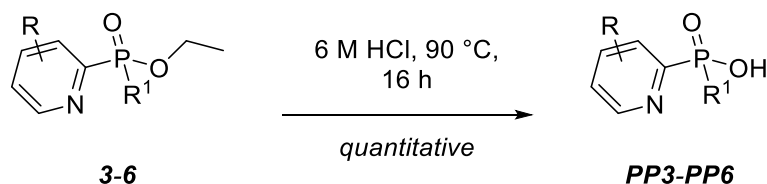


Scheme 2.2

Table 2.3 Yields (%) of compounds **3-7**.

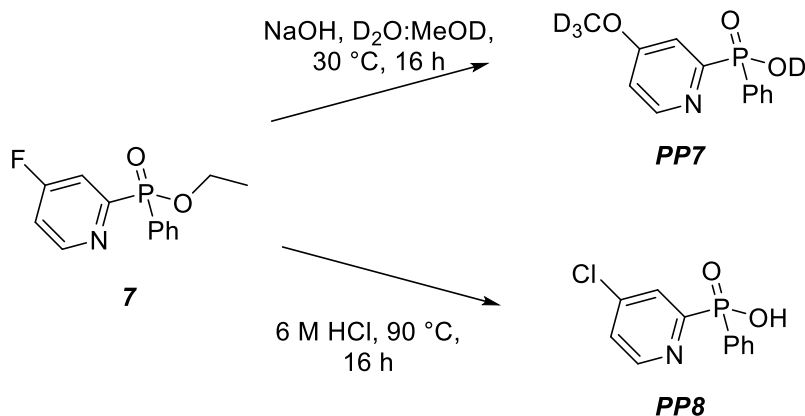
	R	R ¹	Yield (%)
3	3-Me	Ph	80
4	3-Me	Me	32
5	4-Me	Ph	34
6	4-Me	Me	51
7	4-F	Ph	17

A solution of 6 M HCl was used to hydrolyse the ethyl group of compounds **3-6** by stirring at 90 °C overnight (Scheme 2.3). The majority of the acid was removed by repeated washing with MeOH to give quantitative yields for ligands **PP3-PP6**. The reaction is catalysed by the formation of a hydroxonium ion in acidic solution, proceeding via an addition-elimination mechanism. A change to lower frequency (between 22-16 ppm) of the phosphorus peak was observed in the ³¹P-NMR spectra for compounds **PP3-PP6**, confirming formation of the phosphinic acid group. In addition, no observed aliphatic ethyl protons were observed in the ¹H NMR spectra, confirming the successful cleavage of the ethoxy group. All ligands from Table 2.2 were synthesised using the same acid hydrolysis method unless otherwise stated.



Scheme 2.3

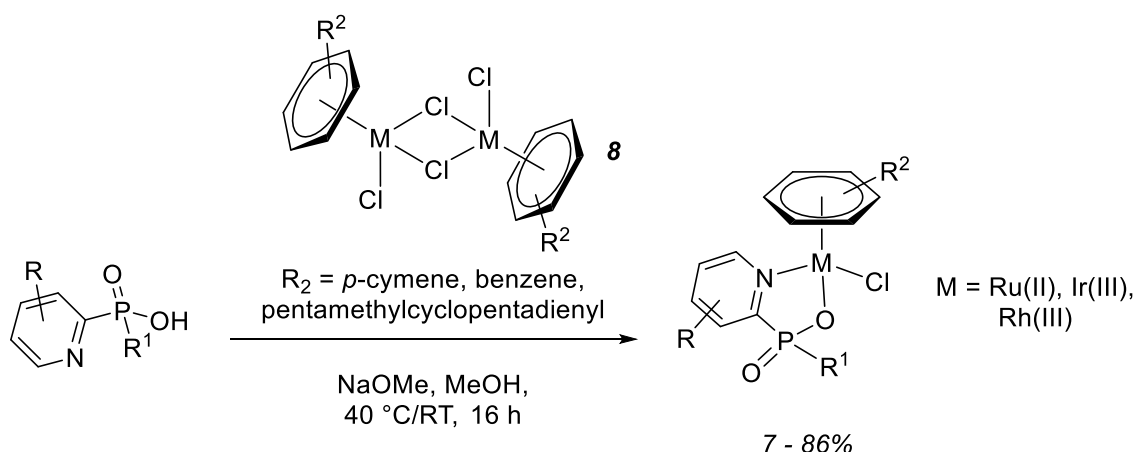
The synthesis of ligands **PP7** and **PP8** proceeded via the 4-fluoropyridylphosphinate (**7**) intermediate. The removal of the ethyl group was attempted using either an acid or base catalysed mechanism (Scheme 2.4). In both cases, nucleophilic aromatic substitution was observed of the fluorine atom from **7** to form an electron-rich 4- OCD_3 substituted ligand (**PP7**) or an electron-poor 4-Cl substituted pyridylphosphinate (**PP8**), depending on the hydrolysis conditions.



Scheme 2.4

The synthesis of ligand **PP7** was undertaken in deuterated solvent to monitor the ^{19}F -NMR signal. As the reaction progressed, alongside the removal of the ethyl group protons, the absence of the fluorine signal was also apparent. The formation of the 4- OCD_3 substituted ligand was confirmed by mass spectrometry, providing an m/z of 236.0483 in the positive ion spectrum implying the substitution of the fluorine by $^-\text{OCD}_3$ acting as the nucleophile. Although unplanned, these ligands were taken forward as electron-rich (**PP7**) and electron-poor (**PP8**) derivatives.

2.2.2 Pseudo-Octahedral Pyridylphosphinate Complexes

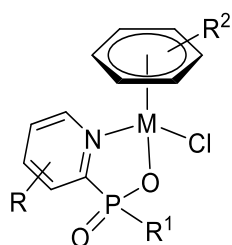


Scheme 2.5

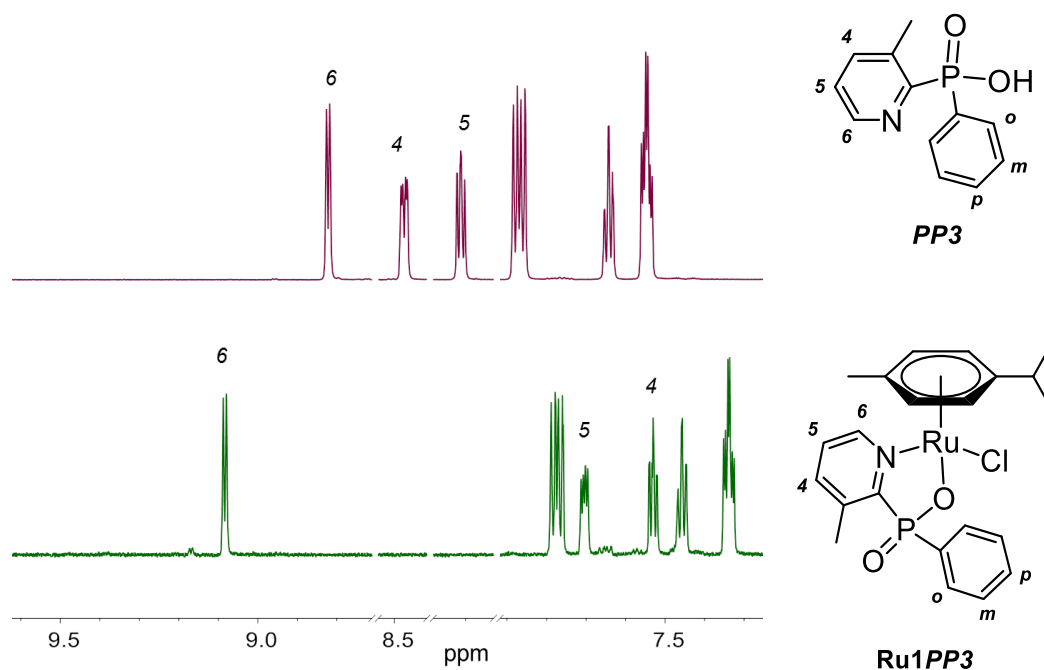
Nine half-sandwich complexes were synthesised using ligands **PP3-PP7**. The ligands **PP3-PP6** were neutralised to pH 7 using a freshly prepared solution of NaOMe in methanol before reacting with the commercially available metal chloride dimers (**8**). To neutralise **PP7** a drop of conc. HCl was added to the ligand dissolved in MeOH. The chosen ligand and half an equivalent of metal dimer were dissolved in MeOH and the reaction mixture was stirred at either room temperature or 40 °C overnight, depending on the desired complex (*Scheme 2.5*). The resulting solution was reduced in volume and dropped into a solution of cold diethyl ether to afford the complexes as a precipitate in various yields (*Table 2.4*). The synthesis of the complexes was confirmed using ^1H , ^{13}C , ^{31}P NMR and High-Resolution Mass Spectrometry. Reasoning for the poor yields of complexes **Ru1PP7** and **Ru3PP5** are indeterminate. The benzene arene (**Ru1PP7**) could be less stable than the other arenes, leading to a lower yield of the final complex. By contrast, the low yield of complex **Ru1PP7** could be due to the previous ligand solution neutralisation step if the solution remained slightly basic, subsequently affording some of an unwanted hydroxyl-bridged dimer during the reaction shown in *Scheme 2.5*.

Table 2.4 Half-sandwich complexes: structural aspects and yields.

Complex	R	R ¹	{M(R ²)}	Yield [%]
Ru1PP3	3-Me	Ph	{Ru(<i>p</i> -cymene)}	52
Ru1PP4	3-Me	Me	{Ru(<i>p</i> -cymene)}	54
Ru1PP5	4-Me	Ph	{Ru(<i>p</i> -cymene)}	86
Ru1PP6	4-Me	Me	{Ru(<i>p</i> -cymene)}	45
Ru1PP7	4-OCD ₃	Ph	{Ru(<i>p</i> -cymene)}	17
Ru3PP5	4-Me	Ph	{Ru(benzene)}	7
Ir1PP6	4-Me	Me	{Ir(Cp*)}	38
RhPP5	4-Me	Ph	{Rh(Cp*)}	33
RhPP6	4-Me	Me	{Rh(Cp*)}	63



The ¹H-NMR spectra are compared in *Figure 2.1* to show the clear proton shift from the free ligand (**PP3**) versus coordination to the metal (**Ru1PP3**). The pyridylphosphinate is coordinated in an *N,O*-bidentate fashion to the metal through the nitrogen atom of the pyridine and the negative oxygen of the phosphinate. The σ -donor character of the pyridine moiety causes a characteristic downfield shift of the adjacent proton (H⁶) when bound in **Ru1PP3**. This shift to a higher frequency by 0.27 ppm is observed in all the complex NMR spectra and aids confirmation of the ligand coordinated to the metal.

**Figure 2.1** ¹H-NMR analysis of ligand **PP3** and complex **Ru1PP3** (MeOD-d₄, 298 K, 400 MHz).

2.3 X-Ray Crystallography

A single crystal of **Ru1PP3** was grown using a slow diffusion method. **Ru1PP3** (2.1 mg, 0.0039 mmol) was dissolved in MeOH (0.2 mL) and the anti-solvent diethyl ether (2 mL) was added to an external vial and left for 6 days. The resulting crystal was analysed by x-ray diffraction to provide the structure shown in *Figure 2.2A* of complex **Ru1PP3** in the solid state. Complex **Ru1PP3** crystallised in a monoclinic crystal system with $P2_1/c$ space group symmetry and displayed the expected pseudo-octahedral geometry, with the η^6 bound *p*-cymene occupying one vertex. The bond lengths observed in **Ru1PP3**: Ru-Cl (2.4155(6) Å), Ru-O (2.0809(14) Å) and Ru-N (2.1109(17) Å) are comparable to those reported for the analogous picolinate complex $[(\eta^6\text{-}p\text{-cymene})\text{Ru}(\text{picolinate})\text{Cl}]$.⁶³ The picolinate complex N-Ru-O bite angle (77.95(7)°) is slightly smaller than the corresponding phosphinate N-Ru-O bite angle (80.50(6)°) a consequence of the larger size of the phosphinate group.

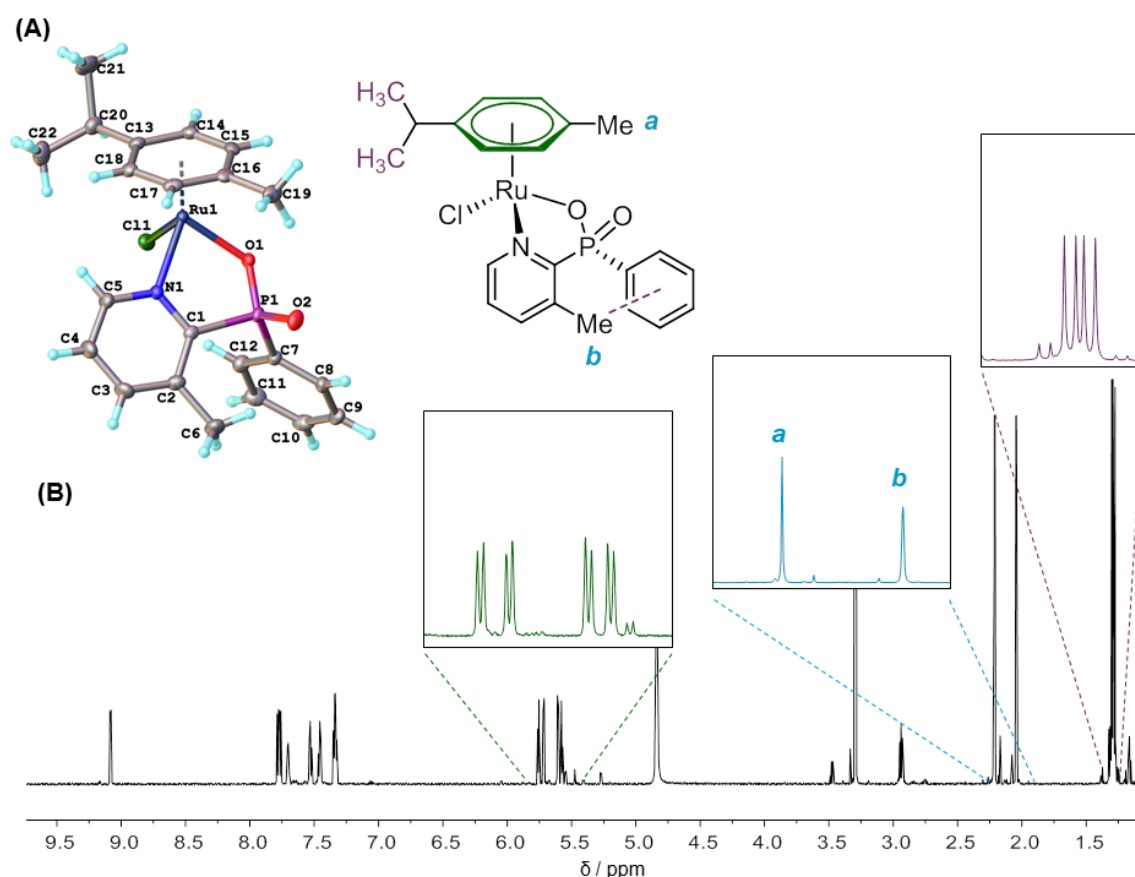


Figure 2.2 (A) X-ray crystal structure of complex **Ru1PP3** (Ru_SP_R) and (B) ^1H -NMR spectrum (MeOD- d_4 , 298 K, 400 MHz) with expansion of the *p*-cymene protons and the methyl substituents between 2.5 and 2.0 ppm.

Due to the incorporation of stereogenic centres at the ruthenium and the phosphorus atoms (*R* or *S* at Ru and P, denoted by $\text{Ru}_{R/S}$ and $\text{P}_{R/S}$, respectively), the pyridylphosphinate complexes can form

four possible stereoisomers. In the solid-state structure only one enantiomeric pair is observed - Ru_RP_S and Ru_SP_R (Figure 2.2A showing Ru_SP_R), this is also evidenced in solution with ^1H NMR displaying one set of diastereotopic *p*-cymene protons between 5 and 6 ppm (Figure 2.2B). The isopropyl CH_3 groups of the *p*-cymene also show diastereotopic environments as two doublets rather than a single doublet due to the presence of the ruthenium stereogenic centre leading to chemical inequivalence hence the slight difference in chemical shift. The stereoselectivity observed in complex **Ru1PP3** has been previously reported in lanthanide pyridylphosphinate complexes¹⁷⁰ and is rationalised in terms of steric interactions between the arene and phosphorus substituents. The conformation observed in the crystal structure (Figure 2.2A) of **Ru1PP3** is the most favourable diastereomer, providing minimal interactions between the P-phenyl group and the *p*-cymene ligand. Other interactions that may contribute to the preferred stereochemistry are weak hydrogen bonds between the P=O and *p*-cymene methyl-H (2.587 Å) and P-phenyl with pyridyl methyl-H (3.065 Å). Broadening of the pyridyl Me peak (Figure 2.2B) reflects its proximity to the aromatic P-phenyl group, while the *p*-cymene Me appears as a sharp singlet suggesting the free rotation of the arene ligand; expected in η^6 -arene-metal systems.¹⁷¹

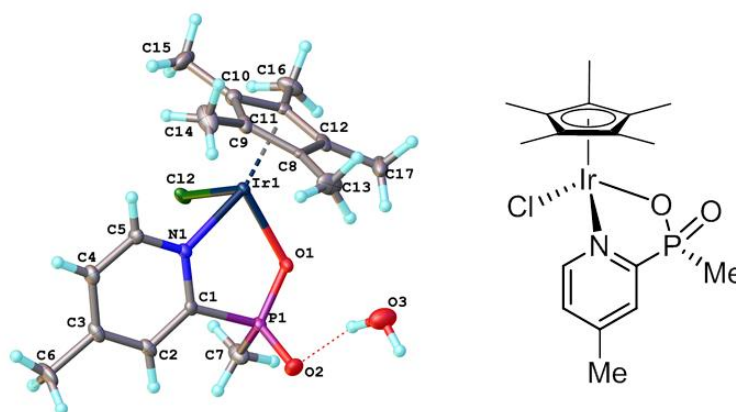


Figure 2.3 X-ray crystal structure of complex **Ir1PP6**.

Complex **Ir1PP6** (0.0014 g, 0.0025 mmol) was dissolved in DCM (0.2 mL) and crystallised by slow diffusion using hexane as an anti-solvent. **Ir1PP6** crystallised in a monoclinic crystal system with a Cc space group, displaying longer bond lengths between the metal and coordinated ligands ($\text{Ir-Cl} = 2.4328(11)$ Å, $\text{Ir-N} = 2.1112(3)$ Å and $\text{Ir-O} = 2.125(3)$ Å) than the ruthenium pyridylphosphinate complex **Ru1PP3**, as well as a wider N-Ir-O bite angle ($80.00(11)^\circ$). Complex **Ir1PP6** was crystallised in a 1:1 stoichiometric ratio with water (Figure 2.3), which formed a hydrogen bond to the P=O oxygen in the crystal lattice, however no intramolecular H-bonds were observed in the solid state as seen for complex **Ru1PP3**. Although the P-methyl substituted ligand **PP6** is less sterically demanding, only a single diastereomer was observed - Ir_RP_S and Ir_SP_R . The lack of intramolecular ligand interactions observed in complex **Ir1PP6** implies the

pyridylphosphinate ligand structure has little influence on stereoselectivity of the final complex and may originate instead from the initial attack of the phosphinate ligand on the metal dimer.

2.4 Aqueous Behaviour of Pyridylphosphinate Complexes

2.4.1 Hydrolysis and Ligand Exchange

As seen in other examples, the aqueous behaviour of half-sandwich complexes is often relevant to their activity.^{59,65,66,172} Complexes containing a monodentate halide often exhibit ligand exchange in aqueous conditions to form an aqua species. The subsequent complex offers more lability at the monodentate coordination site, allowing DNA binding within the cell as a potential mechanism for activity.

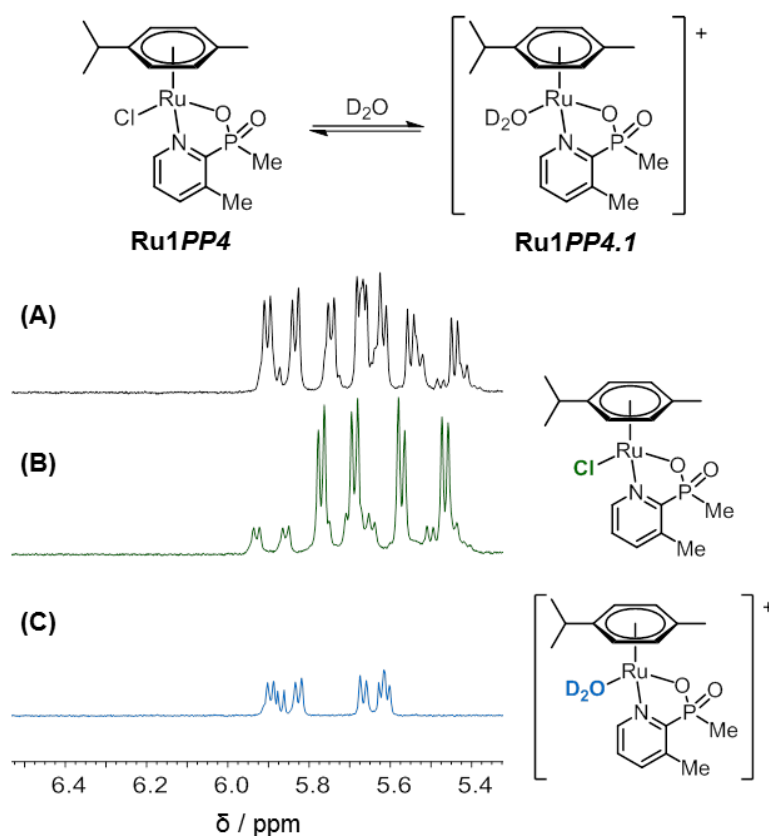


Figure 2.4 1H -NMR spectra (D_2O : $MeOD-d_4$ 9:1, 298 K, 400 MHz) of complex **Ru1PP4** (A) in D_2O , (B) 0.1 M NaCl solution and (C) addition of $AgNO_3$ and filtration of $AgCl$.

To test the properties of the pyridylphosphinate complexes under aqueous conditions, complex **Ru1PP4** was dissolved in a D_2O : CD_3OD (9 : 1) mix and 1H -NMR was used to determine the extent of ligand exchange by monitoring the p -cymene protons (5.4-6.0 ppm). Equilibrium was reached between the chloride (**Ru1PP4**) and aqua (**Ru1PP4.1**) species in solution (Figure 2.4A) within 5 min and remained stable at room temperature over 24 h. To mimic extracellular chloride

concentration, the complex was dissolved in 100 mM NaCl solution (*Figure 2.4B*) to provide chloride bound species (**Ru1PP4**) as the major adduct and confirmed the chemical shift of the *p*-cymene protons of the chloride species in D₂O. To remove the chloride ligand and force the formation of the aqua species (**Ru1PP4.1**), AgNO₃ was dissolved in solution, followed by filtration of the AgCl salt through a 0.2 μm pore filter to provide only the aqua species in solution (*Figure 2.4C*). Having identified the respective chloride (**Ru1PP4**) and aqua (**Ru1PP4.1**) diastereotopic proton peaks, the equilibrium reached in D₂O after 24 h (*Figure 2.4A*) displays approximately 62% of the aqua and 38% of the chloride species. These NMR experiments suggest the chloride complex would be the major species in the extracellular environment (chloride concentration of approximately 100 mM) while once inside the cell, the lower chloride concentration (approximately 20 mM) would encourage the formation of the aqua species. The analogous Ru-iodide complex also undergoes rapid hydrolysis in D₂O however 60% of the iodide species remains intact, implying an increased stability of the Ru-I bond compared to Ru-Cl.

2.4.2 Variable pH Conditions

Alongside hydrolysis, other physiological factors such as pH can play a significant role in the activity of potential metal complexes as anticancer agents.¹⁷³ While generally pH varies depending on cell location and function, rapid proliferation of malignant cells causes a reduction in oxygen supply to tumour areas which become more hypoxic (acidic).¹⁷³ This microenvironment can directly affect the structure and hence overall efficacy of a drug candidate. The stability of the aqua species is desirable within the cellular environment, with the pH influencing deprotonation of the bound water molecule, forming the hydroxyl ligand (*Figure 2.5*). The hydroxyl ligand is much less labile than water and could prevent binding of the metal centre to nucleobase.¹⁷³ Due to the fast rate of hydrolysis observed for the pyridylphosphinate complexes, the effect of pH on the aquated species was investigated. Calculation of p*K*_a values of the water bound molecule in the pyridylphosphinate complexes was therefore of interest to determine the likelihood of DNA binding and how the p*K*_a varies depending on the coordinated ligands and the metal centre.

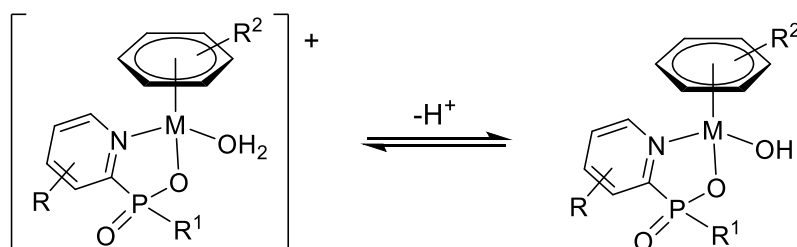


Figure 2.5 Deprotonation of the aqua bound molecule to form the neutral, hydroxyl species.

NMR spectroscopy is a common methodology used for calculating pK_a . The chemical shifts of NMR-active nuclei (e.g. ^1H and ^{13}C) depend on the chemical environment. Alteration of pH can cause deprotonation or protonation of acidic or basic sites which can be monitored by an adjacent atom's chemical shift.¹⁷⁴ In this case, the deprotonation of the water bound molecule was monitored by peaks H^δ -adjacent to the pyridine nitrogen, the phosphorus peak and the arene protons of the selected complexes. To reduce discrepancies, dioxane (^1H -NMR) and triphenylphosphine (^{31}P -NMR) were used as reference compounds. To a solution of pyridylphosphinate complex ($\text{D}_2\text{O} : \text{MeOH-d}_6$ 9:1), AgNO_3 (2.5 equivalents) was added to form the aqua adduct and the AgCl salt was removed by filtration. The selected peak shifts in the ^1H and ^{31}P -NMR spectra were measured at intervals in the pH range 2.0-14.0; adjusted using 0.1 M NaOD and DCl solutions. The initial calculation of the raw data was a correction of chemical shift observed ($\delta_{\text{peak}} - \delta_{\text{reference}}$) and was plotted as a function of pH. Using an established method (equations noted in Appendix 2) the pK_a was extracted from the inflection point of the resulting sigmoidal curve (Figure 2.6) for all complexes (Table 2.5) - calculated as an average of the three nuclei monitored.

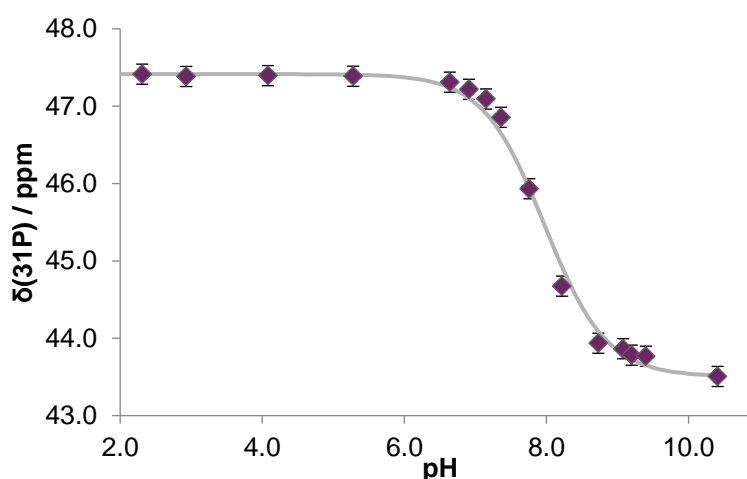


Figure 2.6 Measurement of the pK_a of aqua complex **Ru1PP5.1** by monitoring the ^{31}P -NMR spectrum ($\text{D}_2\text{O} : \text{MeOH-d}_6$ 9:1, 298 K, 162 MHz) as a function of pH.

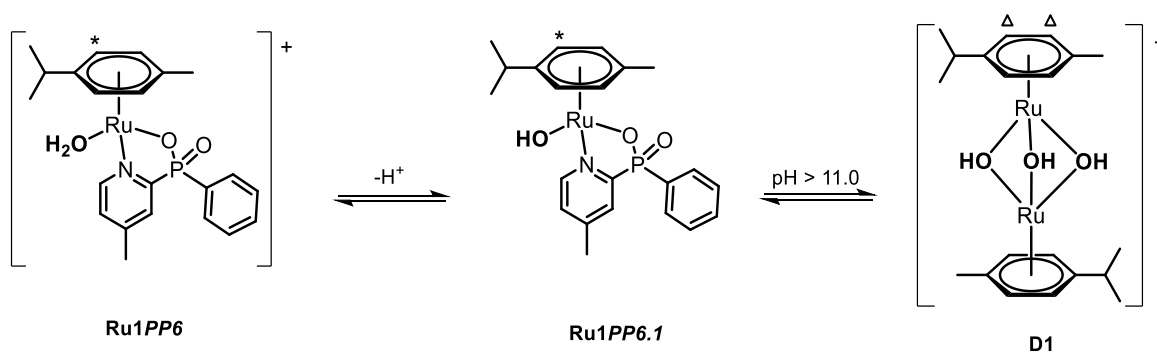
The pK_a values for all the aqua complexes tested were higher than physiological pH (7.4) indicating the complexes would be present in their aqua form and not the less reactive hydroxo species in this environment. By comparing the pK_a values of the different aqua complexes (Table 2.5), some trends become apparent. The electron-donating group on the pyridyl ligand appears to promote a higher pK_a of the water bound molecule. This is shown by the increase in values in the order **Ru1PP5.1** < **Ru1PP3.1** < **Ru1PP7.1** considering 4-Me, 3-Me and 4- OCD_3 pyridyl substituents (R), respectively. The highest pK_a of the Ru(II) centred complexes is that of **Ru1PP7.1** with the 4- OCD_3 pyridyl substituent. The significant increase in pK_a could be attributed to the more electron donating nature of the 4- OCD_3 group, which creates a more electron rich metal centre requiring a

higher pH to deprotonate the coordinated H₂O, compared to the poorer electron donating alkyl substituents of complexes **Ru1PP3.1** and **Ru1PP5.1**.

Table 2.5 p*K*_a values for selected aqua complexes (D₂O : MeOD-d₆ 9:1, 298 K). p*K*_a* values were measured by monitoring changes in ¹H-NMR and ³¹P-NMR spectra and converted to p*K*_a using the equation p*K*_a = 0.929p*K*_a* + 0.42.¹⁷⁵

Complex	R	R ¹	{M(R ²)}	p <i>K</i> _a
Ru1PP3.1	3-Me	Ph	{Ru(<i>p</i> -cymene)}	9.34 ± 0.04
Ru1PP4.1	3-Me	Me	{Ru(<i>p</i> -cymene)}	9.18 ± 0.19
Ru1PP5.1	4-Me	Ph	{Ru(<i>p</i> -cymene)}	7.76 ± 0.13
Ru1PP7.1	4-OCD ₃	Ph	{Ru(<i>p</i> -cymene)}	10.08 ± 0.05
Ir1PP6.1	4-Me	Me	{Ir(Cp*)}	9.31 ± 0.07
RhPP6.1	4-Me	Me	{Rh(Cp*)}	10.95 ± 0.04

The phosphorus R¹ substituent has little effect on the p*K*_a as shown in complexes **Ru1PP3.1** and **Ru1PP4.1** although the electron withdrawing inductive effect of the phenyl group could have influenced the p*K*_a, this effect is clearly negligible. The significance of the metal centre is illustrated when comparing the complexes **Ir1PP6.1** and **RhPP6.1**. The water bound molecule of the rhodium(III) aqua complex is less acidic than the iridium(III) analogue, reflecting the increased metal-oxygen bond length of the heavier congener¹⁷⁶; a trend also observed in analogous complexes of ruthenium(II) and osmium(II).¹⁷⁷



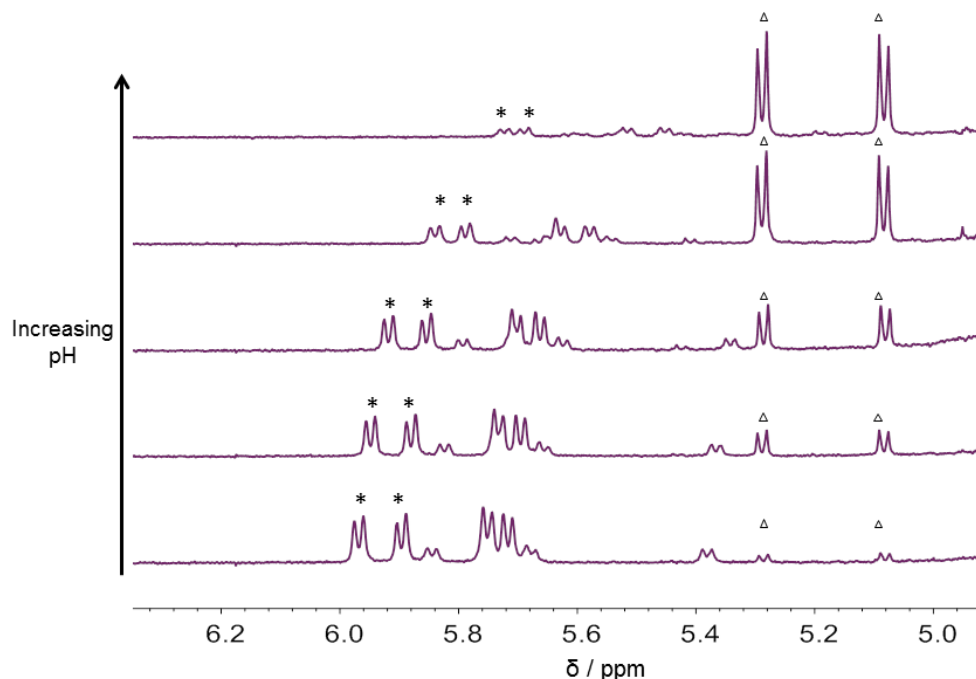


Figure 2.7 ^1H -NMR spectra showing the deprotonation of **Ru1PP6** to form the hydroxyl species **Ru1PP6.1** with irreversible formation of the $[(p\text{-cymene})_2\text{Ru}_2(\text{OH})_3]^+$ dimer above pH 11.0.

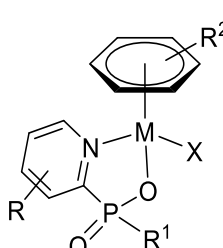
While the pK_a values suggest relative stability of the aqua complexes at physiological pH, at strongly basic conditions the formation of a new species was observed. The ^1H -NMR spectrum of the ruthenium complexes (*Figure 2.7*) showed an increased intensity of two doublets in the arene-bound proton region (5.0 – 6.0 ppm) indicating a loss of stereogenic centre within the new species. Subsequent reduction of the pyridylphosphinate complex peaks was accompanied by an increase in free ligand peaks showing dissociation of the pyridylphosphinate ligand. Upon lowering the pH of the sample, only partial regeneration of the original complexes was observed. The new species was consistently formed for each of the ruthenium complexes at elevated pH (>11.0) and was identified as the hydroxyl-bridged dimer (**D1**, *Figure 2.7*). The formation of the dimeric ruthenium species (**D1**) has been previously noted for other half-sandwich complexes under strongly basic conditions and is known to be non-cytotoxic.^{178,179}

2.5 Cytotoxicity

Following the studies into aqueous behaviour, the pyridylphosphinate complex series were tested for their viability as potential anticancer agents. Cytotoxicity of the complexes was quantified by calculating IC_{50} values - the concentration of a given compound required to inhibit cellular activity by 50%. To calculate the IC_{50} values, H460 non-small lung carcinoma cells were grown in 96-well plates and incubated for 24 hours. The cells were then dosed with each complex at concentrations ranging 0.002 to 200 μM and incubated for a further 72 hours. A solution of MTT

(3-(4,5-dimethylthiazol-2-yl)-2,5-diphenyltetrazolium bromide) was then added. MTT provides a measure of cell viability through metabolic reduction by mitochondrial dehydrogenase of viable cells to give formazan, a bright purple, insoluble compound. The quantity of formazan produced indicates the amount of viable cells present after incubation with a complex. After 4 hours of incubation with MTT, the solution was removed and the remaining formazan crystals were dissolved in DMSO (200 μL per well). Colorimetric analysis was used to quantify the amount of formazan produced. The IC_{50} value was determined as the concentration of complex required to reduce absorbance to 50% compared to that of the untreated, control wells.

Table 2.6 IC_{50} values for selected complexes measured using the MTT assay (96 h) against the non-small cell lung carcinoma H460 cell line. Entries are the mean value from three experiments. Complexes excluded were found to have $\text{IC}_{50} > 200 \mu\text{M}$.



Complex	R	R ¹	{M(R ²)}	X	$\text{IC}_{50}/\mu\text{M}$
Ru1PP1	H	Ph	{Ru(<i>p</i> -cymene)}	Cl	>200
Ru2PP1	H	Ph	{Ru(<i>p</i> -cymene)}	I	65 ± 12
Ru2PP2	H	Me	{Ru(<i>p</i> -cymene)}	I	>200
Ir1PP1	H	Ph	{Ir(Cp*)}	Cl	>200
Ir1PP2	H	Me	{Ir(Cp*)}	Cl	>200
Ir1PP6	4-Me	Me	{Ir(Cp*)}	Cl	140 ± 40
Ir2PP1	H	Ph	{Ir(Cp*)}	I	52 ± 2
Ir2PP2	H	Me	{Ir(Cp*)}	I	53 ± 4
RhPP6	4-Me	Me	{Rh(Cp*)}	Cl	135 ± 17
Cisplatin	-	-	-	-	0.80 ± 0.01

Although all the compounds synthesised were tested against the H460 non-small lung carcinoma cell line, many candidates showed poor toxicity (>200 μM) and will not be discussed. All complexes in the series displayed low toxicity with no comparable potency to the control complex cisplatin. However, some IC_{50} values of interest are displayed in *Table 2.6*. All ruthenium chloride complexes were considered inactive with IC_{50} values of >200 μM . A direct comparison between complexes **Ru1PP1** and **Ru2PP1** shows a 3-fold lower IC_{50} value for the iodide (**Ru2PP1**) complex compared to the chloride analogue (**Ru1PP1**). This trend is also shown in the most potent complexes within the series, **Ir2PP1** and **Ir2PP2** which gave IC_{50} values of 52 and 53 μM , respectively. The key feature of the aforementioned complexes is the iridium metal centre which when paired with an iodide ligand appears to provide consistent toxicity compared to ruthenium, in the case of **Ru2PP2**. Complexes **Ir1PP6** and **RhPP6** contain identical coordinating ligands,

including a monodentate chloride and possess similar IC_{50} values (140 and 135 μM , respectively). While there is no other rhodium complex for comparison, **Ir1PP2** has a higher IC_{50} value along with only hydrogen as the R substituent on the pyridyl suggesting the increased potency of **Ir1PP6** and **RhPP6** could be influenced by the additional 4-Me group. However, based on the pK_a values of complexes **Ir1PP6** and **RhPP6** and a slower hydrolysis for the iodide analogues, it is likely a combination of metal centre and halide ligand that gives rise to the increased potency across the series. Additionally, in the case for ruthenium complexes **Ru2PPI** and **Ru2PP2**, the phosphorus R¹ substituent has an apparent effect; potentially due to the phenyl group increasing overall lipophilicity of **Ru2PPI** which is known to aid cellular uptake.^{63,107}

Previously published reports have inferred the relationship between iodide half-sandwich complexes and more potent activity compared to chloride complexes evidenced by alternate, favourable mechanisms of cellular uptake.⁶⁸ While the mechanism of action for these pyridylphosphinate complexes is currently uncertain, similar existing piano-stool complexes have demonstrated variable toxicity linked to the rate of hydrolysis followed by DNA binding as a likely mode of action. This observation would be consistent within this series with the iodide complexes generally displaying higher cytotoxicity.^{180,181}

2.6 Binding Studies

In an attempt to rationalise the poor cytotoxicity displayed by the ruthenium complexes in the series (>200 μM), binding studies were carried out to determine the relative stability of these complexes in the presence of various biomolecules. The following experiments were intended to mimic alternative or competitive reactions that could occur in a cellular environment. Complex **Ru1PPI** was dissolved in D_2O and treated with AgNO_3 , the resulting AgCl precipitate was removed by filtration to give the aqua adduct, **Ru1PPI.1**. To measure the presence and extent of biomolecule binding, mass spectrometry and NMR spectroscopy were used (^1H and ^{31}P). Additions of one and two equivalents of the selected biomolecule were added to the D_2O solution of **Ru1PPI.1** and the spectra monitored at 1h and 16 h intervals. The biomolecules selected for investigation were L-alanine (L-Ala), L-threonine (L-Thr), L-histidine (L-His), imidazole and 9-ethylguanine (9-EtG).

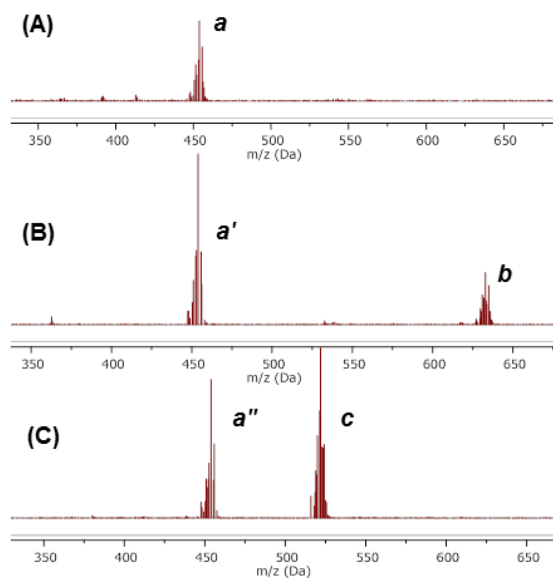


Figure 2.8 ESI⁺ mass spectra of **Ru1PPI.1** in the presence of (A) L-alanine, (B) 9-ethylguanine and (C) imidazole. Peaks labelled *a – c* correlate to *Table 2.7*.

No binding was observed between **Ru1PPI.1** and one equivalent of amino acids L-Ala and L-Thr after 1 h, illustrated by the m/z peak at 454.3 identified as **Ru1PPI.1** with loss of H₂O (*Figure 2.8A*). No significant binding was observed for these small amino acids up to two equivalents over 24 h. By contrast, the addition of one equivalent of 9-EtG (*Figure 2.8B*) led to a new peak in the mass spectrum (*Figure 2.8B, b*) corresponding to loss of H₂O and subsequent formation of the 9-EtG-adduct of **Ru1PPI.1** with an m/z of 632.9. This observation was consistent with the ¹H-NMR which indicated the formation of a bond between Ru and N7 on 9-EtG and showed around 50% of the bound 9-EtG-**Ru1PPI.1** adduct in solution. The Ru-N7 guanine binding is often observed as preferential in oligonucleotides^{55,171,182}, consistent with DNA binding as a proposed mechanism of action for existing ruthenium anticancer complexes which leads to apoptosis and cell death. The ability of **Ru1PPI.1** to bind 9-EtG is consistent with previous reports implying DNA binding as a likely mode of action for these complexes. ¹H-NMR spectroscopy of a solution of **Ru1PPI.1** with the addition of two equivalents of imidazole showed a 1:1 imidazole adduct formation with loss of H₂O after 16 h, also observed in the mass spectrum at m/z 522.4 (*Figure 2.8C, c*). The coordination of imidazole would be expected due to its stronger σ -donor character than H₂O, however formation of only the imidazole-adduct species may be disfavoured as H₂O is the coordinating solvent and is in excess.

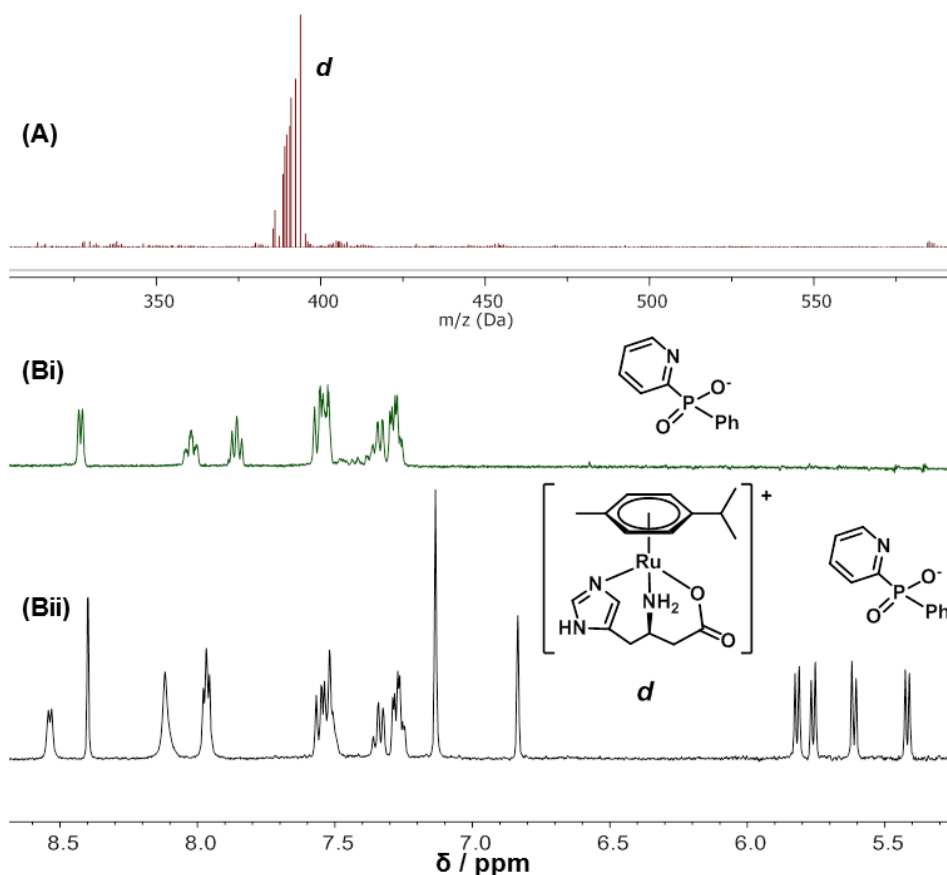
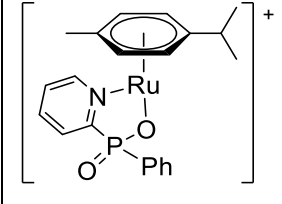
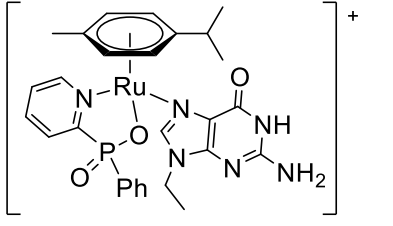
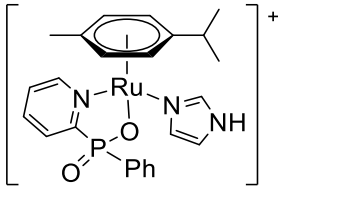
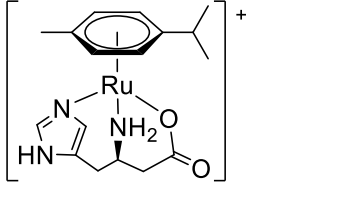


Figure 2.9 (A) ESI⁺ mass spectrum for complex **Ru1PPI.1** in the presence of two equivalents of L-histidine (L-His), **d** correlates to *Table 2.7*. ¹H NMR spectra (D₂O : CD₃OD 9:1, 298 K, 400 MHz) of (Bi) uncomplexed **PPI** ligand and (Bii) products of the addition of two equivalents of L-histidine to complex **Ru1PPI.1** showing the formation of the L-His complex.

The most notable biomolecule interaction with **Ru1PPI.1** was that of L-histidine. Upon addition of one equivalent of L-His, an adduct was observed corresponding to the substitution of H₂O with L-His. The ¹H-NMR spectrum implied the initial binding of L-His through an imidazole N. After a second equivalent of L-His was added, the sample was monitored over 16 h. A new species formed via displacement of the pyridylphosphinate ligand in favour of the L-His bound κ³. The mass spectrum gave an *m/z* of 390.6, corresponding to species **d** (*Figure 2.9*) and was confirmed by ¹H-NMR showing the free ligand (*Figure 2.9Bi*) and a mixture of the free ligand and new complex (*Figure 2.9Bii*) in the sample solution. The tridentate binding of the L-His amino acid forms a new ruthenium stereogenic centre. Using enantiomerically pure L-His could therefore result in two possible diastereomers. However, it has previously been reported that the tridentate binding motif of L-His can only generate a single diastereomer with the ruthenium in the *R* configuration.¹⁸³ This is observed in the ¹H-NMR spectrum (*Figure 2.9Bii*) by one set of *p*-cymene protons (6.0-5.0 ppm) shown in solution, corresponding to the Ru_R(L-His)_S diastereomer. The Ru-(L-His) complex is known to be non-toxic.¹⁸³ Displacement of the pyridylphosphinate ligand could also be partially attributed to the hard P-O⁻ coordinating the softer Ru(II) centre.

Table 2.7 Proposed species that give rise to mass peaks in *Figure 2.8*, upon addition of selective biomolecules. Tabulated m/z values correspond to *a – d* peaks in *Figure 2.8*.

Biomolecule	m/z	Species
L-Ala	<i>a</i> : 454.3	Ru1PPI.1 
L-Thr	454.6	Ru1PPI.1
9-EtG	<i>a'</i> : 453.8	Ru1PPI.1
	<i>b</i> : 632.9	
Imidazole	<i>a''</i> : 454.0	Ru1PPI.1
	<i>c</i> : 522.4	
L-His	<i>d</i> : 390.6	

The formation of such non-toxic species presents a potential explanation for the low cytotoxicity observed for the Ru chloride complexes (*Table 2.6*). By contrast, the iodide complexes **Ru2PPI**, **Ir2PPI** and **Ir2PP2** possess higher cytotoxicity due to the metal-iodide bond being less labile and less likely to hydrolyse to the aqua adduct. This structural integrity of the iodide complexes could prevent decomplexation by chelating biomolecules that can competitively bind to the ruthenium centre.

2.7 Conclusions

The initial aim of this study was to synthesise novel piano-stool complexes, containing a ^{31}P spectroscopic handle with desirable anticancer properties. A series of 25 novel half-sandwich complexes were synthesised by reacting pyridylphosphinate ligands possessing a range of substituents with selected metal-halide dimers. The complexes were tested against the H460 non-

small lung carcinoma cell line with the iridium-iodide complexes **Ir2PPI** and **Ir2PP2** displaying the greatest IC_{50} values around 50 μ M. All the ruthenium-chloride complexes tested gave poor toxicity (>200 μ M), which can be justified by a combination of their chemical properties, behaviour under intracellular conditions and interactions with biomolecules.

Compared to the iodide complexes, the chloride complexes showed rapid hydrolysis to the aqua species with equilibrium favouring the aqua complex (62%). This is thought to contribute to the poor cytotoxicity of the ruthenium-chloride complexes, allowing chelation of biomolecules in a cellular environment. NMR and mass spectrometry studies on complex **Ru1PPI** confirmed the ability of two equivalents of L-His to fully displace the pyridylphosphinate ligand to bind κ^3 to the ruthenium centre. This example of amino acid interaction implies the potential of other available biomolecules within the cell to preferentially coordinate to the ruthenium centre, altering the structure of the complex and reducing its potency. Model binding studies using 9-EtG showed the formation of a ruthenium-(9-EtG) adduct, suggesting the possibility of DNA-binding as a mode of action. The iodide complexes, retaining the metal-halide bond would not necessarily bind in the same manner and may act via a different mechanism.

The pK_a values of the aqua-adduct species tested were all higher than physiological pH (7.4), suggesting deprotonation of the water ligand forming the less reactive hydroxyl species is unlikely to contribute to the poor toxicity of the complexes. Partial variation in pK_a values was attributed to the more electron donating OCD_3 substituent creating a more electron rich metal centre in the case of **Ru1PP7** or influenced by a heavier congener forming a longer metal-oxygen bond increasing the acidity of the water ligand protons.

Having rationalised the pitfalls of these pyridylphosphinate complexes and proposed reasoning for their relatively poor toxicity, further investigation would be useful. It is quite apparent that the labile nature of the chloride bond must be improved upon to enhance activity. This could be achieved by tuning the substituents on the pyridyl ring, or even adding multiple groups to form a more electron deficient metal centre. Addition of a lipophilic substituent such as phenyl or trifluoromethyl group may also improve cellular uptake.

The biological profile of these complexes could also be examined more thoroughly. Measuring cellular uptake and accumulation could quantify the ability of the complexes to enter the cell, which is often reported to be proportional to activity. Testing against alternative cell lines could broaden the potential target for these complexes and is worthy of attention.

3. Piano-Stool Complexes as HDAC Inhibitors

3.1 Introduction

Due to the progression of modern drug design becoming increasingly focused towards targeting specific biomolecules, the attention of this study shifted to exploit the structural geometry of piano-stool complexes as potential enzyme inhibitors. Zinc-dependent histone deacetylase (HDAC) enzymes were considered an appropriate target due to their well-established biological function, including post-translational modification, which if dysregulated can contribute to malignancies.⁷⁸ Piano-stool metal complexes were designed to possess ligands analogous to existing HDAC inhibitors (*Figure 3.1*), with the desire to enhance interactions between inhibitor and enzyme as well as improve overall cytotoxicity.

It was deemed prudent to construct complexes that had increased stability in aqueous conditions and would not undergo ligand exchange or excessive hydrolysis that were detrimental factors to those complexes discussed in *Chapter 2*. Of the target molecules, only **Ru1L²** and **RhL²** were successfully purified and tested, with the phenanthroline bidentate motif proving beneficial to overall complex stability. In this instance, the complexes showed improved cytotoxicity against the H460 cell line with the desirable HDAC inhibition activity rationalised as the likely mode of action via multiple biological assays.

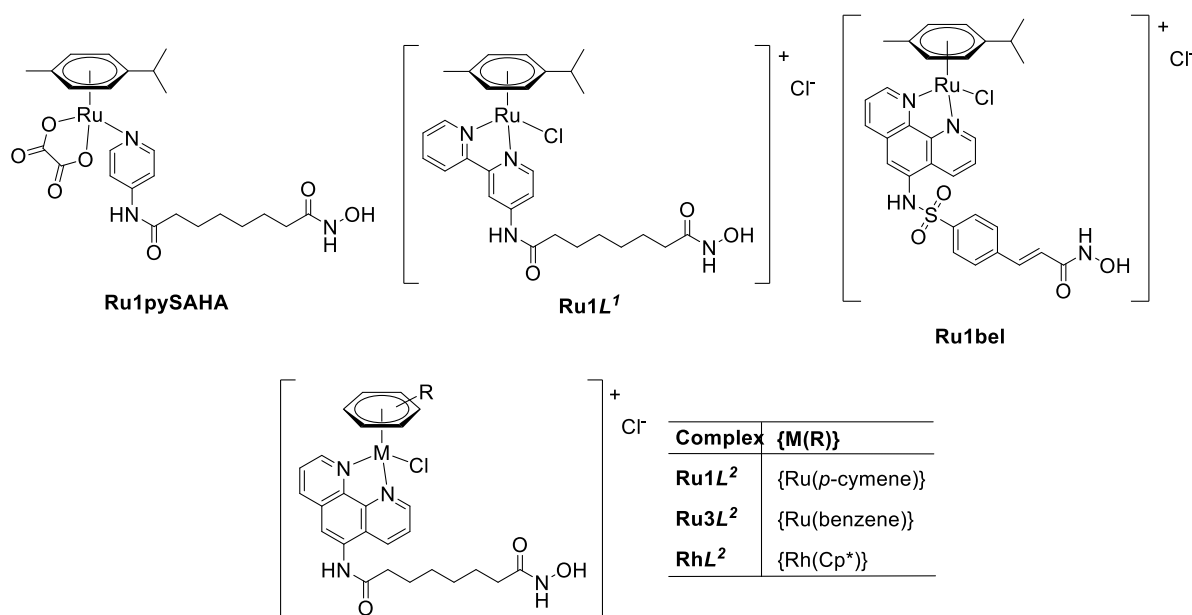
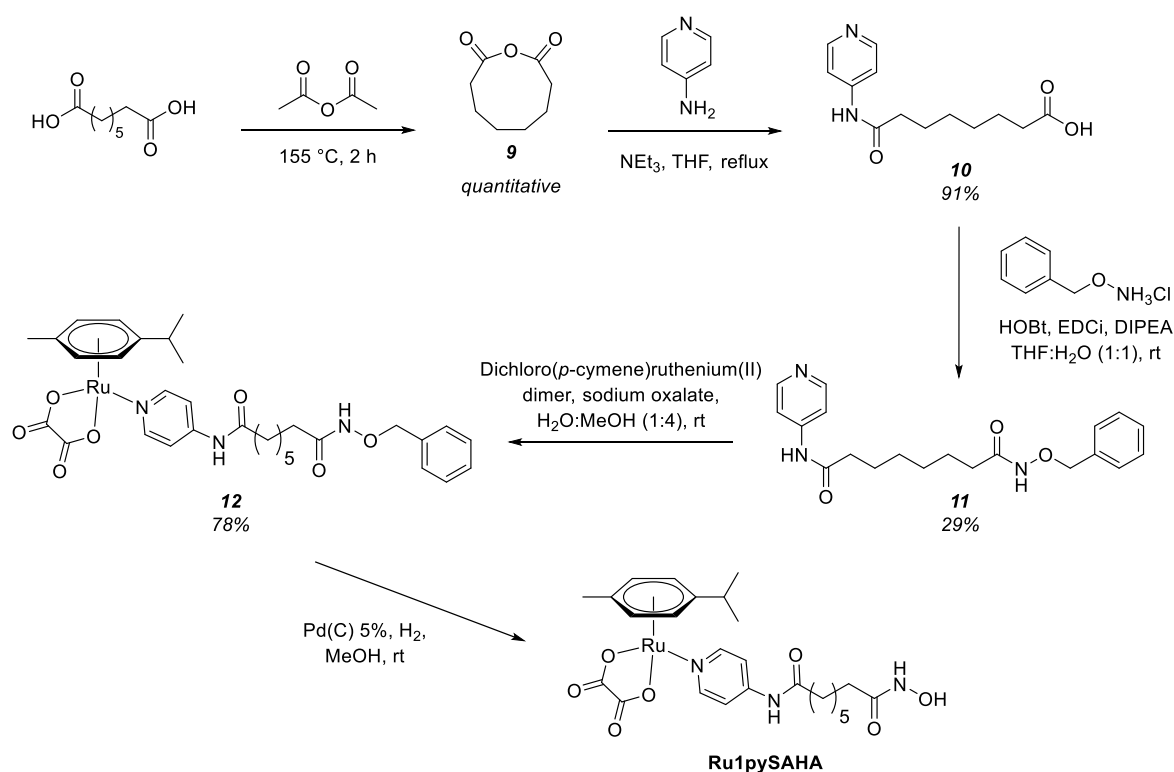


Figure 3.1 Metal-based HDAC inhibitor target molecules (Cp* = Pentamethylcyclopentadienyl).

3.2 Synthetic Aspects

3.2.1 Monodentate Ligand Approach

The attempted synthetic route to complex **Ru1pySAHA** is shown in *Scheme 3.1*. A ligand was required with the ability to bind to a ruthenium metal centre while retaining a structure analogous to SAHA. To synthesise a ligand with appropriate functionality, suberic acid containing a six-carbon aliphatic chain was initially dissolved in acetic anhydride and refluxed for 2 h. The solvent was removed *in vacuo* to provide suberic anhydride (**9**) in a quantitative yield. Compound **9** was dissolved in THF and subsequently reacted with 4-aminopyridine in the presence of base. Compound **10** was purified by column chromatography on SiO₂ using a DCM (5% MeOH) mobile phase and isolated in a high yield.



Scheme 3.1

The formation of the protected hydroxamic acid was necessary to avoid chelation of this functional group to the ruthenium metal centre and ensure binding through the pyridine moiety. While chelation would be thermodynamically favourable for the ligand, in this case the unbound hydroxamic acid is known to be crucial for HDAC inhibition activity. By coupling *O*-benzylhydroxylamine hydrochloride to the carboxylic acid of **10**, this ensured protection of the hydroxamic acid. The coupling agents selected were HOBt and EDCi, frequently used as a method

of peptide coupling.^{184,185} Compound **II** was purified by recrystallisation from ethyl acetate. It was established that a one pot synthesis of **12** was the optimal route and could be done at room temperature. Initially the ruthenium dimer was dissolved in MeOH and the sodium oxalate dissolved in water. These solutions were then combined and the ligand (**II**) added. After 16 h the solution was filtered and the solvent removed to provide **12** in good yield (78%).

The final step in the synthesis of complex **Ru1pySAHA** was a hydrogenation to remove the benzyl group to provide the hydroxamic acid product. Complex **12** was dissolved in MeOH with palladium 5% on carbon, under a hydrogen atmosphere using a Dräger balloon and stirred vigorously to allow H₂ to dissolve. Unfortunately, this hydrogenation method was not successful for the ruthenium complex **Ru1pySAHA**. The initial attempt at H₂ dosed for 1 h, minimal starting material was present in the reaction mixture (*Figure 3.2*). Purification of this mixture was achieved using HPLC but due to the small scale of reaction and column conditions, no product was recovered.

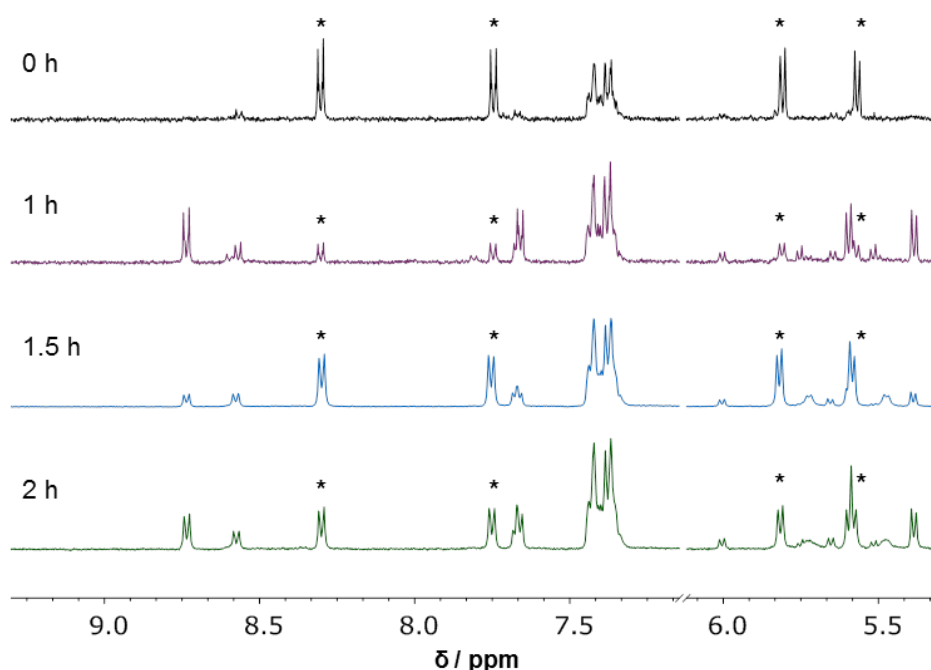


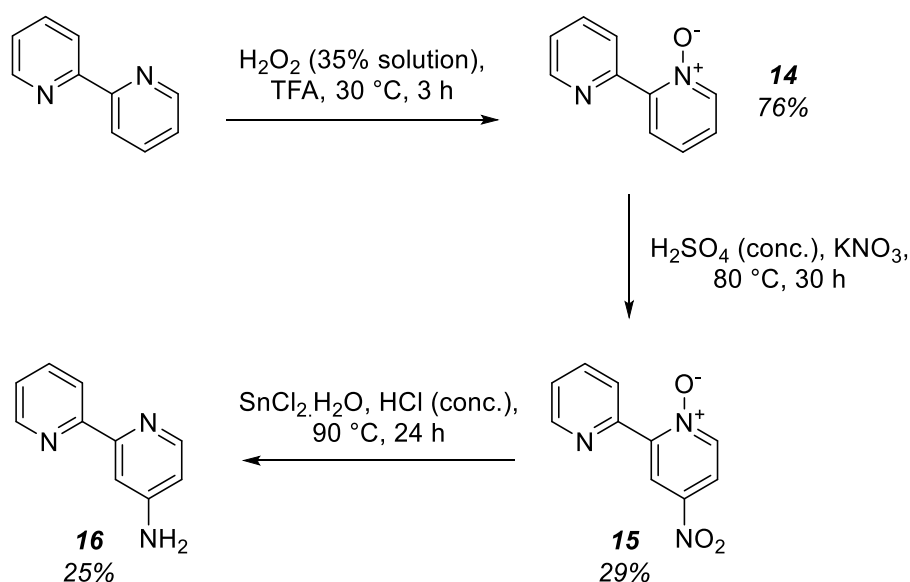
Figure 3.2 ¹H-NMR spectra (MeOD-d₆, 298 K, 400 MHz) of three attempted hydrogenation reactions to synthesise **Ru1pySAHA**. (*Proton peaks of starting material, **12**).

The method was adjusted to dose H₂ for longer periods of 1.5 and 2 h (*Figure 3.2*) with the desire to force the reaction to completion. It was observed that the reaction was not as effective on a longer timescale. An explanation for these irregular results could be the degradation of the palladium catalyst, the H₂ pressure was variable or stirring was not consistent upon repeat experiments. However, using mass spectrometry, upon closer inspection, a new product gave an *m/z* of 572.62 consistently across all repeat experiments. This mass suggested hydrogenation to the amide and not the desired hydroxamic product. The significant upfield shift for the *p*-cymene

protons (6.0 – 5.0 ppm, *Figure 3.2*) implies the formation of an additional product, with a change of ligand coordination at the Ru metal centre. A decrease in size of the pyridine peaks (8.2 and 7.7 ppm) would support the notion that the pyridine moiety is no longer bound to ruthenium, instead suggesting coordination through the amide or hydroxamic acid reduced product. Due to the ineffective replication of the literature procedure for complex **13**, an alternative complex was proposed.

3.2.2 Bipyridyl Ligand Containing Complex

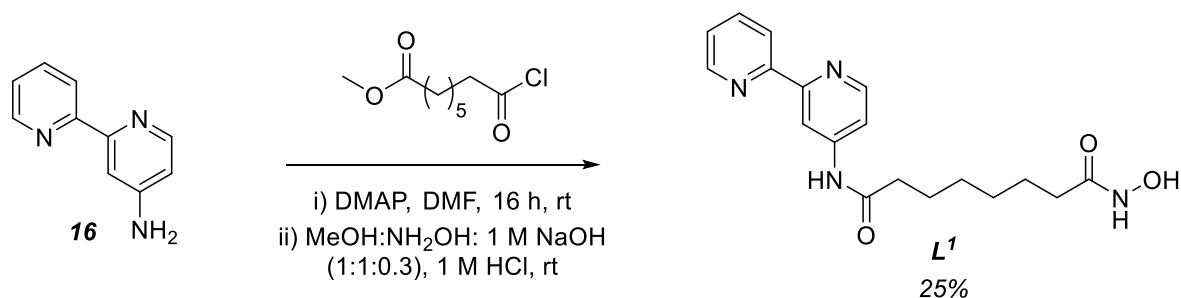
To formulate a more stable complex from the active ligand perspective, a ligand with a chelating group able to preferentially bind ruthenium over the hydroxamic acid seemed the next logical step. The commonly used bipyridine ligand was chosen as the starting point. The commercially available 2,2'-bipyridine was dissolved in trifluoroacetic acid in the presence of hydrogen peroxide solution (*Scheme 3.2*). The reaction mixture was added to chloroform and washed with 3 M NaOH solution and the combined organic layers dried over Na₂SO₄, filtered and solvent removed. The formation of the *N*-oxide was confirmed by ¹H-NMR: the starting material contains only 4 proton environments in the aromatic region as the structure is symmetrical, whereas the product contains 8 proton environments implying the formation of only a single *N*-oxide, resulting in one of the rings being more electron rich. The chemical shift of the from 8.71 to 8.86 ppm of the proton now adjacent to the *N*-oxide illustrates the electron withdrawing nature of the resulting *N*-oxide (**14**).



Scheme 3.2

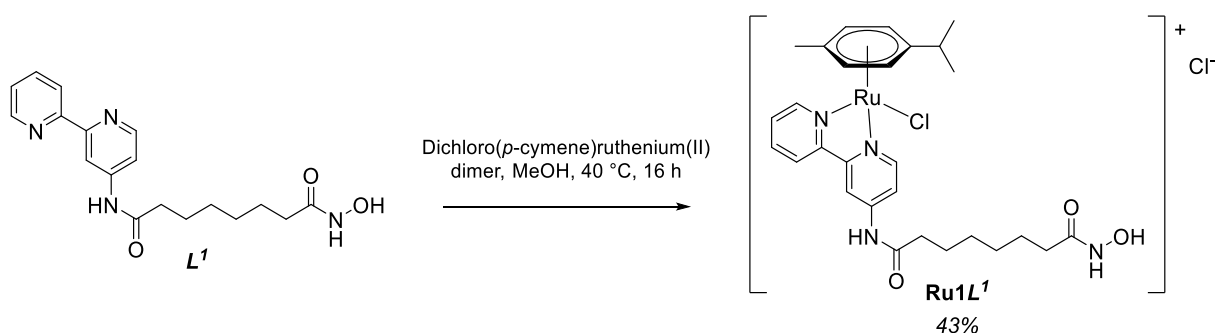
The second step involved the dissolution of **14** in concentrated sulfuric acid at 80 °C followed by the addition of potassium nitrate. After 30 h the reaction mixture was poured over ice and basified

using 3 M NaOH solution. This basifying step is likely to account for the low yield of **15** (29%) as if the solution became too basic the precipitate no longer formed; a process that could not be reversed. Presence of the *N*-oxide activated the pyridine to allow electrophilic aromatic substitution at the *para* position. The loss of a proton in the aromatic region, along with formation of a doublet for H³, adjacent to the nitro group with only a *meta* proton-proton coupling (⁴J_{HH} 3.0 Hz) confirmed the substitution at the *para* position. Reduction of **15** was attempted using palladium (10% on carbon) and NaBH₄, reagents taken from a known procedure with reported high yields.¹⁸⁶ This method did not yield good results, instead giving a mixture of multiple products and remaining starting material. The reaction was adjusted by using more NaBH₄ with no noticeable difference in conversion to product. An alternative synthesis using tin(II) chloride in concentrated HCl was used, providing significant improvement on conversion to the product (**16**). A sublimation technique was used to effectively purify **16**, and the structure and purity confirmed by ¹H-NMR (CDCl₃) displaying a broad amino peak at 4.29 ppm.



Scheme 3.3

With compound **16** in hand, the final synthesis of the ligand was carried out (Scheme 3.3). An alternative synthesis to suberoyl anhydride (**9**) ring opening was used due to the poor nucleophilicity of the amino group in **16**. Instead the commercially available methyl 8-chloro-8-oxooctanoate was used, containing a more favourable chloride leaving group. DMF was removed by vacuum distillation and the impure methyl ester was dissolved in MeOH and hydroxylamine solution (1:1) in the presence of 1 M NaOH. After 30 minutes the reaction mixture was neutralised and the resulting precipitate washed with water to afford **L¹**.

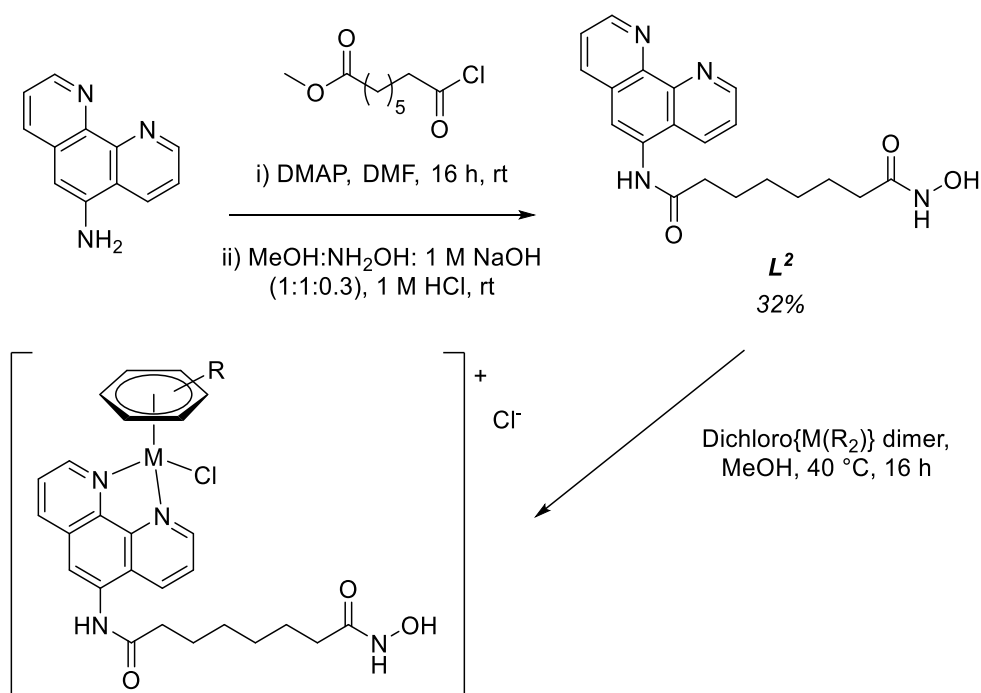


Scheme 3.4

The formation of complex **Ru1L¹** was achieved by reacting **L¹** with dichloro(*p*-cymene)ruthenium(II) dimer. Excess solvent was removed and the crude product was purified by recrystallisation by dropping diethyl ether into a concentrated solution of MeOH. The ¹H-NMR spectrum showed the *p*-cymene peaks in the anticipated region 5.0 – 6.5 ppm as four doublets. The complexation forms a stereogenic centre at the ruthenium metal, consequently giving rise to chemical inequivalence in the *p*-cymene protons.

3.2.3 Synthesis of *N*²⁰-Hydroxy-*N*¹¹-(1,10-phenanthrolin-5-yl)octane diamide (**L²**) and Resulting Complexes

The synthesis of *N*²⁰-hydroxy-*N*¹¹-(1,10-phenanthrolin-5-yl)octanediamide (**L²**) was undertaken using an existing procedure reacting 1,10-phenanthrolin-5-amine with methyl 8-chloro-8-oxooctanoate in DMF using DMAP as a nucleophilic catalyst.¹¹⁷ Conversion to the hydroxamic acid was done using the same method described above (Section 3.2.2). It was found that cooling the solution upon neutralisation partially improved the yield.



Formation of the complexes containing L^2 was achieved using the same method as described previously, reacting the ligand with half an equivalent of dichloro{metal(arene)} dimer, and purified using the precipitation technique from concentrated MeOH into diethyl ether. Yields and structure of the complexes are displayed in *Table 3.1*.

Table 3.1 Half-sandwich complexes containing L^2 : structures and yields.

	Complex	{M(R)}	Yield [%]
		Ru1 L^2	{Ru(<i>p</i> -cymene)}
	Ru3 L^2	{Ru(benzene)}	55
	Rh L^2	{Rh(Cp*)}	61

Synthesis was confirmed using $^1\text{H-NMR}$, mass spectrometry and elemental analysis with 2D NMR spectroscopy allowing full assignment of all protons. An example spectrum is shown in *Figure 3.3* of the complex **Ru1** L^2 in DMSO- d_6 with some important characteristics highlighted. $^1\text{H-NMR}$ in an aprotic solvent such as DMSO- d_6 allows identification of the intact hydroxamic acid, showing broad resonances at 10.30 and 8.63 ppm corresponding to the hydroxamic acid OH and NH protons, (*Figure 3.3, c* and *b*) respectively. The NOESY spectrum aided this assignment with a clear interaction between these protons. These resonances are near identical to those observed in the spectrum of L^2 confirming the ligand coordination to ruthenium occurs through the phenanthroline *N*-donors. Resonances for the protons adjacent to the phenanthroline *N* atoms (H^2

and H⁹) shift by almost 1 ppm upon complexation due to the σ -donor character of the phenanthroline ligand.

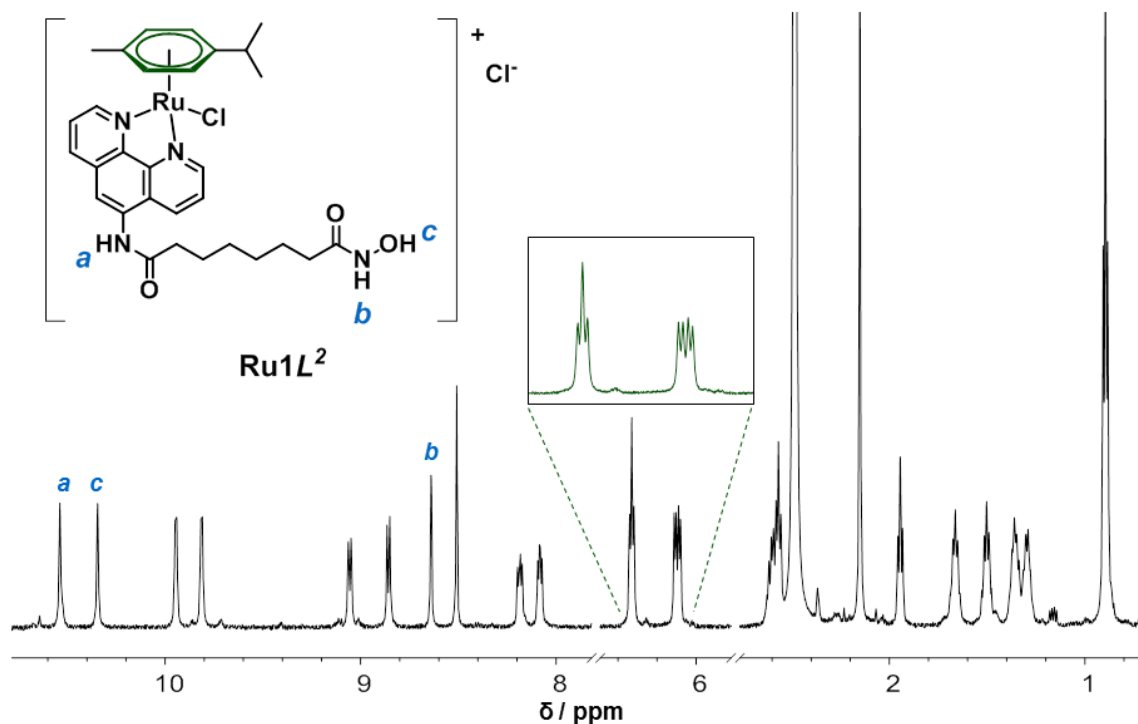
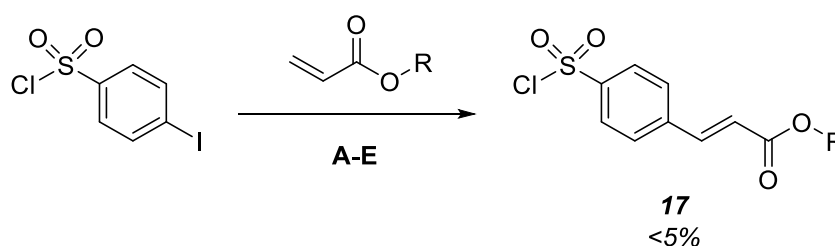


Figure 3.3 ¹H-NMR spectrum (DMSO-d₆, 298 K, 400 MHz) of complex **Ru1L²**. Proton expansion in the *p*-cymene region (6.0 -7.0 ppm) has been done for clarity and the labile NH and OH protons are labelled.

3.2.4 Metal-Based Belinostat Analogue

Following the successful synthesis of complexes **Ru1L²** and **RhL²**, multiple routes were attempted to synthesise a belinostat (*Chapter 1*) analogue. 4-Iodobenzene sulfonyl chloride was chosen as the commercially available starting material. Initial attempts to react 4-iodobenzene sulfonyl chloride with 1,10-phenanthroline-5-amine were unsuccessful. Although sulfonyl halides are documented to react readily with nucleophiles such as alcohols and amines in the presence of base, the iodobenzene moiety could have prevented the simple substitution reaction. Instead, this prompted attempts at the Heck Coupling reaction (*Scheme 3.6*).



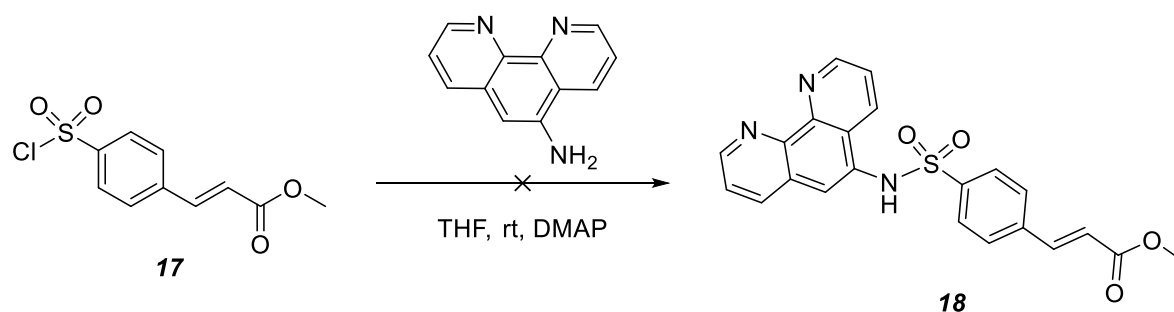
Scheme 3.6

Selected examples of reaction conditions attempted for the Heck Couplings are listed in *Table 3.2*. A previous synthetic procedure postulated by Lavoie *et al.* utilised the unusual route **A** in DMF using acrylic acid¹⁸⁷. This route was unsuccessful. Experiments were undertaken using both Pd(0) and Pd(II) catalytic sources in the presence of silver acetate, base and varying phosphines gave equally poor results with very low or negligible yields of **17**. The reaction was repeated due to the known reliable *trans* selectivity of the Heck coupling, easily identifying the product using ¹H-NMR with coupling constants of 16 Hz. The small quantity collected and purified from multiple reactions was taken forward as **17**.

Table 3.2 Selected examples of Heck Coupling reaction attempts.

	R	Pd cat. (mol %)	Phosphine (mol %)	Reagents and conditions	Yield [%]
A ¹⁸⁷	H	Pd ₂ (dpa) ₃ (5%)	P(<i>o</i> -tolyl) ₃ (5%)	Et ₃ N, DMF, 100 °C	7
B	Me	Pd ₂ (dpa) ₃ (5%)	P(<i>o</i> -tolyl) ₃ (5%)	Et ₃ N, AgOAc (2 eq.), MeCN, 50 °C	10
C	Me	Pd(PPh ₃) ₄ (5%)	P(<i>o</i> -tolyl) ₃ (10%)	Et ₃ N, AgOAc (2 eq.), MeCN, 50 °C	-
D	Me	Pd(OAc) ₂ (5%)	P(Ph) ₃ (10%)	Et ₃ N, AgOAc (2 eq.), MeCN, 50 °C	12
E	^t Bu	Pd(PPh ₃) ₄ (5%)	P(<i>o</i> -tolyl) ₃ (10%)	Et ₃ N, MeCN, 50 °C	-

With a total of 100 mg of compound **17** in hand, it was then reacted with 1,10-phenanthroline-5-amine at room temperature in THF using DMAP as a base. This reaction was based on the first step in *Scheme 3.5*, with the nucleophilic substitution of a chloride for an amine to produce compound **18**. Unfortunately this reaction was also unsuccessful. This could be due to the poor nucleophilicity of the phenanthroline amine or overall poor solubility of 1,10-phenanthroline-5-amine. While changes to all reactions could be made to optimise this synthetic route, due to time constraints only complexes **Ru1L**² and **RhL**² were carried forward.



Scheme 3.7

3.3 Hydrolysis Studies

The anticipated HDAC enzyme inhibition of these complexes relies on their ability to enter cells to access their intended target. The stability of a complex is often crucial in both the extracellular and intracellular environment to ensure the drug candidate reaches the target in its desired form. For this reason, the behaviour of the complexes was assessed under aqueous conditions to determine their stability. Complex **Ru1L²** was dissolved in D₂O and monitored by ¹H-NMR spectroscopy over the course of 96 h (Figure 3.4A). After 1 h there was little exchange, however over the course of 96 h an equilibrium was established between the chlorido complex **Ru1L²** and the aqua species **Ru1.1L²**. The **Ru1L²**:**Ru1.1L²** ratio is approximated 9:1, implying the chlorido species is likely to be the major species intracellularly where chloride concentration is 4 mM.¹⁹ This result is in stark contrast with the pyridylphosphinate complexes, showing the influence of the ligand system on the more labile monodentate halide ligands. Also, as observed by similar ruthenium arenes synthesised by McGowan *et al.*, it is unfavourable for group VIII metals to gain a 2+ overall positive charge by loss of the coordinating halide. In lieu of this, hydrolysis is slow and unfavourable as is the case for **Ru1L²** shown here.⁶⁴

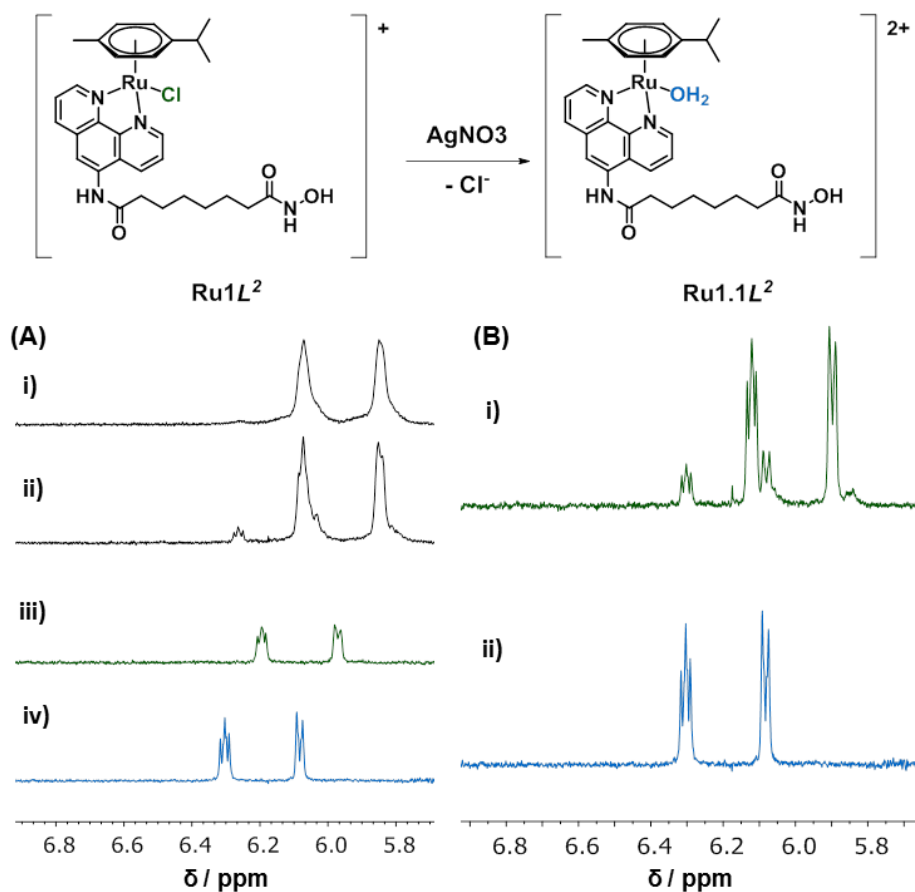


Figure 3.4 $^1\text{H-NMR}$ spectra (D_2O , 298 K, 400 MHz) p -cymene proton region of complex Ru1L^2 . (A) i) D_2O , 1 h; ii) D_2O , 96 h; iii) 100 mM NaCl; iv) AgNO_3 , 24 h. (B) i) AgNO_3 , 1 h; ii) AgNO_3 , 24 h.

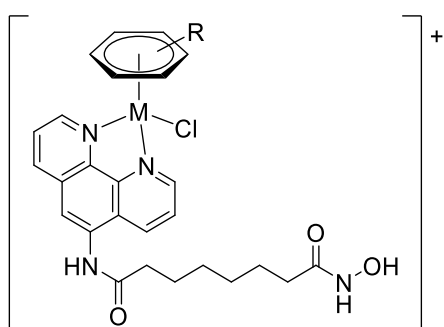
To mimic extracellular chloride concentration, the complex was dissolved in 100 mM NaCl solution (Figure 3.4Aiii) to provide only the chloride bound species (Ru1L^2) as the major adduct and confirmed the chemical shift of the p -cymene protons of the chloride species in D_2O . A solution of complex Ru1L^2 was then treated with AgNO_3 and monitored over 24 h (Figure 3.4B) at which time the AgCl salt was removed by filtration. After 1 h in solution, new p -cymene proton peaks were observed. Within 24 h only the new species was present, implying the full conversion to the aqua species (Ru1.1L^2). Similar to the chloride species existing as the major adduct in aqueous conditions, the removal of the chloride using AgNO_3 is also slow signifying the strength of the chloride-ruthenium bond, or that the loss of a negatively charged coordinating ligand is unfavourable. Throughout these experiments there was no evidence of the non-toxic dimer species ($[(p\text{-cymene})_2\text{Ru}_2(\text{OH})_3]^+$) formation, previously observed for the pyridylphosphinate complexes. This is likely to be due to the improved stability of the chelating phenanthroline ligand and is an encouraging result with regard to complex stability.

3.4 Cytotoxicity

With these new complexes in hand, their viability as anticancer agents was assessed against the H460 non-small-cell lung carcinoma cell line¹ by measuring inhibition of cell proliferation. Cells were exposed for 96 h to selected complexes **Ru1L²** and **RhL²**, ligand **L²** and the known HDAC inhibitor SAHA, at concentrations ranging from 0.01 to 200 μM . Cell survival was determined using an MTT assay (as described in Section 2.5), the IC₅₀ values were calculated using a dose-response curve (Appendix 2) and are displayed in Table 3.3.

Table 3.3 IC₅₀ values measured using the MTT assay (96 h) against the non-small-cell lung carcinoma H460 cell line and are reported as the mean value of three experiments.¹⁸⁸

Compound	{M(R)}	IC ₅₀ [μM]
Ru1L²	{Ru(<i>p</i> -cymene)}	21 \pm 6
Ru3L²	{Ru(benzene)}	45.1 \pm 19
RhL²	{Rh(Cp*)}	4.1 \pm 0.4
L²	-	1.5 \pm 0.2
SAHA	-	1.4 \pm 0.2



These new complexes show significant inhibition to cell proliferation compared to the primarily investigated pyridylphosphinate complexes. The IC₅₀ values of the complexes is clearly influenced by the metal-arene motif, with the benzene capped complex **Ru3L²** possessing moderate cytotoxicity (45.1 μM) while the rhodium-Cp* (**RhL²**) showed 10-fold more potency with an IC₅₀ value of 4.1 μM . Between the two ruthenium complexes, the *p*-cymene capped complex **Ru1L²** showed the lowest toxicity, although 15-fold higher than the SAHA control. The difference in IC₅₀ values between the ruthenium centred complexes could be due to the *p*-cymene complex (**Ru1L²**) possessing mildly electron donating alkyl substituents on the arene, increasing the stability of this motif. The alkyl substituents also provide an increase in overall lipophilicity of the complex that could improve cell accumulation and activity. By contrast, the rhodium complex **RhL²** showed much lower cytotoxic efficacy (IC₅₀ = 4.1 μM) and is comparable to the most active rhodium(III) piano-stool complexes in the literature to date.¹⁸⁹ The IC₅₀ value of the ligand **L²** alone is also notable, existing within experimental error of the SAHA control. These results advocate the potential of piano-stool complexes as potential HDAC inhibitors with the **RhL²** complex in particular illustrating that a metal complex can be tuned to possess *in vitro* cytotoxic potency akin to its clinically approved analogue.

¹ MTT cytotoxicity assays on the H460 cell line were attempted under the supervision of N. Gallagher, J. H. Gill, M. Jain and K. L. Rockley at the School of Medicine, Pharmacy and Health, Stockton Campus, Durham University.

3.5 HDAC Inhibition Assay

Once encouraging efficacy was determined for cytotoxic activity, it was then necessary to investigate the mechanism of action and whether these complexes act by HDAC inhibition as proposed. An HDAC inhibition assay was therefore carried out using a commercially available kit (Section 7.1.8, Enzo Life Sciences). Firstly, appropriate dilutions of assay components were made using assay buffer and stored on ice. The known HDAC inhibitor SAHA, L^2 and complexes $\mathbf{Ru1L}^2$ and \mathbf{RhL}^2 were dosed at 1 and 0.1 μM concentrations with a nuclear extract source of HDACs, prior to the addition of an acetylated substrate. As a positive control, the assay was also run in the absence of any inhibitor. The plate was incubated at 37 °C for 30 minutes. After this time, a developer was added and the plate incubated at room temperature for a further 15 minutes. Deacetylation of the substrate sensitizes it to the developer, which then generates a fluorophore. The fluorophore is excited and the subsequent fluorescence emission used to measure the extent of HDAC activity using a fluorescence plate-reader. In the presence of an inhibitor, no fluorescence indicates complete HDAC inhibition. Results were calculated as a percentage of HDAC activity, relative to the positive control and are displayed in Table 3.4. All reactions and repeats were done concurrently in one 96-well plate.

Table 3.4 HDAC activity in presence of potential inhibitors at 0.1 and 1 μM concentration, measured using a commercially available assay kit (Enzo Life Sciences). Values are reported as percentage activity relative to a positive control (no inhibitor).

Inhibitor Conc ⁿ [μM]	HDAC Activity [%]				
	Control	SAHA	$\mathbf{Ru1L}^2$	\mathbf{RhL}^2	L^2
1	100	0.5	1.6	1.1	4.9
0.1	100	6.3	17.3	15.4	10.7

Low HDAC activity was exhibited at 1 μM dose concentration for all compounds tested (<5% activity), suggesting that these species are effective HDAC inhibitors. Inhibitory potency of these compounds is supported by HDAC activity, while showing a slight increase, remains low at the 0.1 μM concentration tested. At 0.1 μM the difference in HDAC inhibition between the compounds is more distinct following the order SAHA> L^2 > \mathbf{RhL}^2 > $\mathbf{Ru1L}^2$. This order corresponds with the *in vitro* activity displayed by these compounds, which supports the hypothesis that HDAC inhibition is the likely mechanism of action.

While the compounds HDAC inhibition activity follows this general trend, there are some variances compared to the *in vitro* observations. For example, the cytotoxicity of \mathbf{RhL}^2 is 4-fold higher than for $\mathbf{Ru1L}^2$ where as their HDAC inhibition is the same order of magnitude at both concentrations. This observation could be rationalised by assuming cytotoxicity is dependent on factors such as cell uptake and localisation, which do not contribute in a more rudimentary enzyme

assay. Another point to consider is the activity of L^2 relative to the metal complexes. Despite being more active at 0.1 μM , L^2 is 4-fold less active than either metal complex, exhibiting less enzyme inhibition at the higher 1 μM concentration. The planar aromatic L^2 may form aggregates at the higher concentration resulting in less available compound to bind to the enzyme, or lower solubility of L^2 in the assay medium could contribute to the reduced activity. An additional control experiment was undertaken, to measure the extent of HDAC inhibitory activity of the known complex $[(p\text{-cymene})\text{Ru}(\text{phen})\text{Cl}]\text{Cl}$.¹⁹⁰ No inhibition (100% HDAC activity) was observed at 1 μM , confirming the zinc chelating hydroxamic acid group is vital for HDAC inhibition activity.

3.6 DNA Binding

The enzyme assays clearly suggest this set of compounds are effective at inhibiting HDAC activity as proposed. However, cytotoxicity of metal complexes is often documented to be induced through DNA binding; commonly observed in both existing drugs such as cisplatin, along with other anticancer ruthenium piano-stool examples.⁵¹ To discern that DNA binding is not a contributing factor to the cytotoxicity of these compounds, assays were performed to test for DNA intercalation and covalent modification.²

Firstly, to probe the ability of these complexes to covalently modify DNA, an Electrophoretic Mobility Shift assay was undertaken (*Section 7.1.5*). In this assay, supercoiled plasmid pSG483 DNA was used as a potential binding substrate. Supercoiled DNA is dense and can move quickly through the pores of agarose gel. Therefore, the tighter the DNA, the faster it will move down the plate. Covalent binding reduces the ability of the DNA to supercoil and in a relaxed, larger state, moves slower down the plate. Plasmid pSG483 DNA was exposed to increasing concentrations of $\text{Rh}L^2$ from 0.3 to 20 μM and incubated for 24 h at 37 °C. Cisplatin was also tested as a covalent DNA binding control under identical conditions. After the incubation period, the resulting products were separated by gel electrophoresis on a 1.4% TAE (Tris-base, acetic acid and EDTA) agarose gel. Ethidium bromide can intercalate DNA and is a UV active compound which was used as a stain to visualise the position of DNA on the gels under UV illumination (*Figure 3.5*).

In comparison to the solvent only control (*Figure 3.5A*, lane 1) the migration of the supercoiled DNA is largely unaffected by $\text{Rh}L^2$. By contrast, at 2.5 μM concentration of cisplatin (*Figure 3.5B*) the DNA displayed minimal migration, suggesting the formation of multiple cisplatin-DNA adducts, preventing supercoiling. Above this concentration, the DNA appears much more dispersed. Cisplatin forms very strong bonds with guanosine nucleotides in DNA,¹⁹¹ which could be a cause

² DNA binding assays were attempted under the supervision of T. R. Blower, Department of Biological Sciences, Durham University.

of DNA degradation at higher concentrations. It is clear from this comparison that **RhL**² does not interact with DNA in the same covalent binding manner as cisplatin.

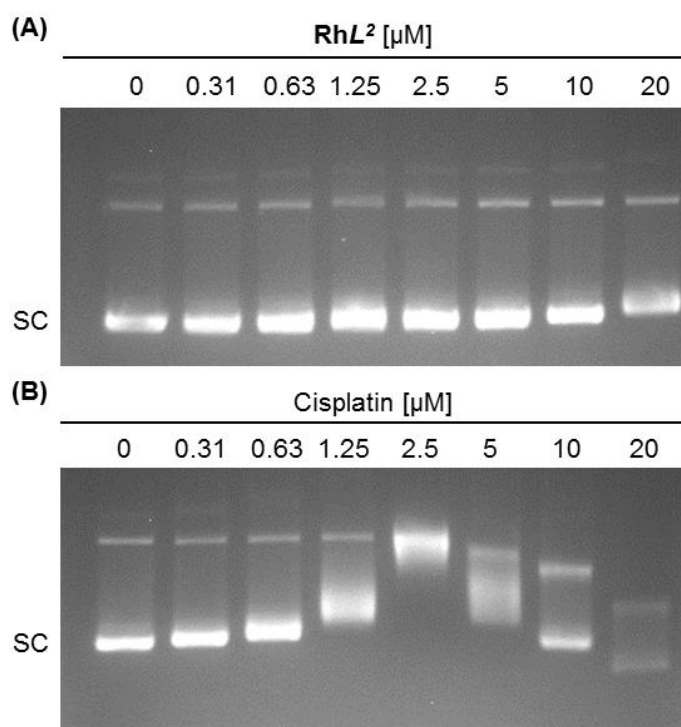


Figure 3.5 Covalent modification of DNA as determined by migration of substrate DNA during agarose gel electrophoresis. Supercoiled plasmid DNA was treated with increasing concentrations of (A) complex **RhL**² and (B) cisplatin. SC = supercoiled DNA.

Having confirmed that covalent modification is an unlikely mechanism of action for these complexes, intercalation was another mechanism explored. Intercalation occurs when ligands fit between base pairs of DNA and is frequently observed with polycyclic, aromatic and planar ligands. Phenanthroline has been previously documented to partake in DNA intercalation¹⁹², and due to the presence of a phenanthroline ligand in these complexes, there was potential for intercalation to occur and was investigated using a similar gel electrophoresis experiment.

For the intercalation assay, nicked pSG483 plasmid DNA was used as the substrate and was exposed to increasing concentrations of **RhL**² from 1.25 to 80 μM. Known DNA intercalator, acridine orange was utilised as a positive control and the reactions with the substrate were run simultaneously. The mixtures were incubated for 30 mins at 37 °C, followed by treatment of DNA ligase. The ligase acts to reseal the nicked DNA, trapping the current supercoiling state of the plasmid. In this case, intercalation induces an increase in supercoiling within plasmid DNA, whereas non-intercalated nicked DNA treated with ligase will be sealed in a distribution of relaxed DNA topoisomers (*Figure 3.6*, lane 3). Gel electrophoresis and visualisation were done using the same method as the covalent modification assay (*Section 7.1.5*) and is shown in *Figure 3.6*. Minimal intercalation was observed below 20 μM for complex **RhL**², while moderate intercalation

occurred at doses up to 80 μM . This result suggests that intercalation does not occur at concentrations capable of causing HDAC inhibition or cytotoxicity. In *Figure 3.6* the higher concentrations of acridine orange are omitted for clarity. At doses 1.25 μM and above, DNA migration was comparable to untreated supercoiled DNA as expected for a known intercalator. These results suggest that the moderate intercalating ability observed for complex **RhL²** is unlikely a contributing factor to overall cytotoxicity of the complex.

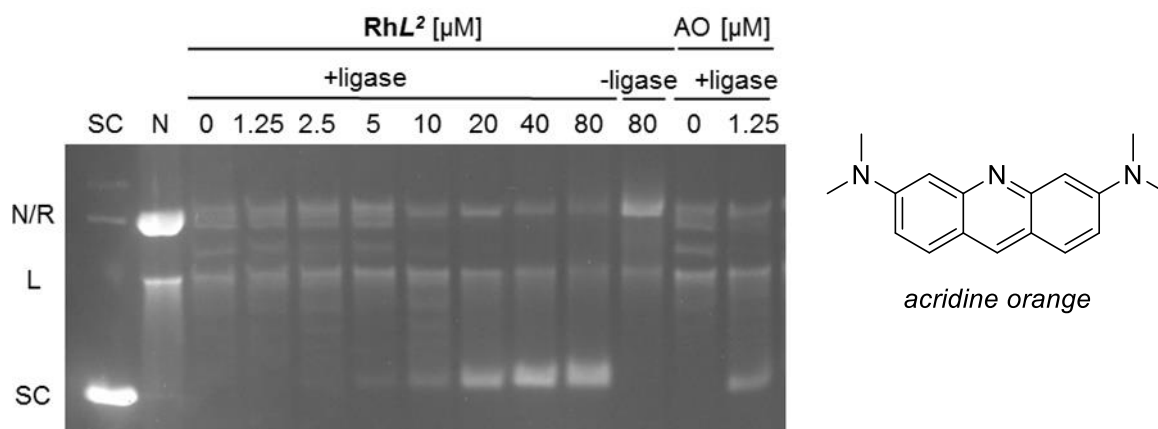


Figure 3.6 Intercalation of DNA demonstrated by the production of supercoiled DNA. Nicked plasmid DNA was treated with increasing concentrations of complex **RhL²** and a positive control, acridine orange (AO). The supercoiled state was trapped by the addition of DNA ligase, where indicated. N/R = nicked/relaxed DNA, SC = supercoiled DNA, L = linear DNA.

3.7 Protein Binding

Along with DNA binding, protein binding is also a potential competitive mechanism of activity. Off-target protein binding can also be detrimental to the desired activity of a drug candidate. Bulky proteins such as human serum albumin (HSA) provide a large hydrophobic surface to which lipophilic or hydrophobic drugs can bind; directly affecting their drug delivery. Binding to proteins such as HSA ensures the drug stays in the blood, rendering it unable to access its intended target and reducing overall bioavailability.¹⁹³

To test whether these complexes bind to large proteins, bovine serum albumin (BSA, a similar serum protein to HSA) was used as a protein substrate and a UV-Vis titration was used to calculate a binding constant. To determine the extent of protein binding, first an acceptable concentration of complex had to be established. This was achieved by calculating the extinction coefficient (ϵ) according to the Beer-Lambert law (*Appendix 2, UV-Vis titrations*) from a set of concentration values at 380 nm (*Figure 3.7A*). It is important to note that amino acid residues, phenylalanine, tyrosine and tryptophan present in the BSA protein absorb UV at lower wavelengths (tryptophan absorbing highly at ~ 280 nm) corresponding to $\pi \rightarrow \pi^*$ transitions in the aromatic systems. For this

reason, the wavelength 380 nm was chosen as it is less likely to be affected by the absorbance of such conjugated substituents present in BSA.

The solution at 93 μM concentration was chosen with the optimal absorbance at 380 nm and was consequently used to undertake the UV/Vis titration for the protein binding experiment. Increasing amounts of BSA were dissolved in the complex solution (TRIS buffer, 0.05 M; NaCl, 0.1 M) and the absorbance measured. In tandem, the same quantities of BSA were dissolved in the same buffer solution and the absorbance of BSA alone was measured. To observe any new bound species, the absorbance was adjusted by subtracting the unbound BSA from the complex-BSA solution (Figure 3.7B). The broadening and shifting of the absorbance peak between 360 – 380 nm suggesting this absorbance could correspond with protein-complex binding interactions.

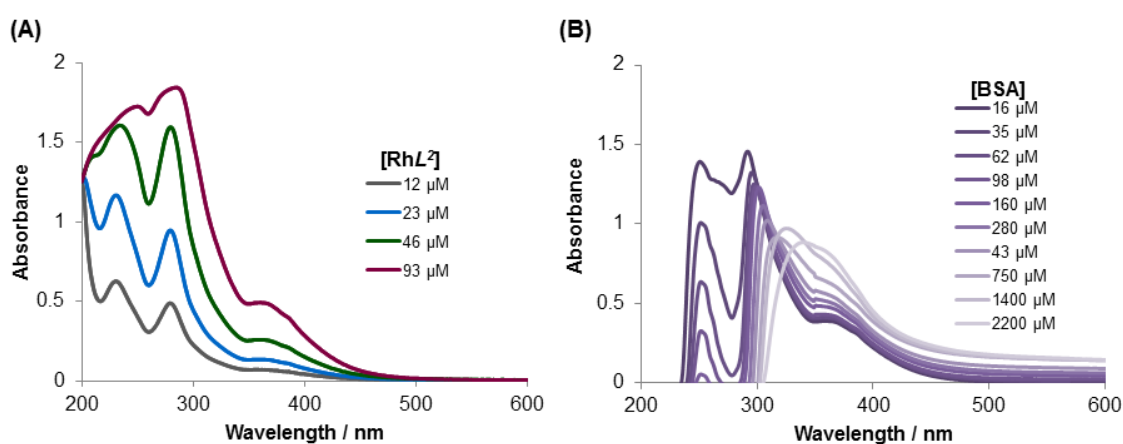
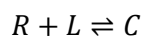


Figure 3.7 (A) Absorbance of increasing concentrations of complex RhL^2 in TRIS buffer. (B) RhL^2 -protein absorbance, corrected against absorbance of unbound BSA at increasing concentrations ($[\text{RhL}^2] = 93 \mu\text{M}$).

Binding constants for complexes Ru1L^2 and RhL^2 were calculated using the straight-line equation:

$$[C]^2 + \left(-\frac{1}{K} - [\text{Ru}]_0 - [\text{L}]_0\right)[C] + ([\text{Ru}]_0[\text{L}]_0) = 0$$

This was derived from the general equation where R = receptor (in this case the metal complex), L = BSA protein ligand and C = BSA-complex:



Concentration of BSA was plotted against absorbance data at 380 nm for Ru1L^2 and 370 nm for RhL^2 as a binding isotherm curve, assuming 1:1 binding. The binding constants $[K]$ were then calculated using the straight-line equation and are shown in Table 3.5.

Table 3.5 Binding constants [K] for the binding of complexes **Ru1L²** and **RhL²** with BSA. (TRIS buffer 0.05 M; NaCl 0.1 M; pH 7.4, 298 K).

Complex	Binding Constant [K]
Ru1L²	331 ± 13
RhL²	661 ± 49

Both complexes **Ru1L²** and **RhL²** provided relatively low binding constants evidence of a moderate binding affinity towards BSA. While the binding constants are low, the values calculated imply a notable interaction between the complexes and the BSA protein, anticipated due to the highly lipophilic surface of BSA and amphiphilic character of the complexes.

3.8 Conclusions

Three metal-based HDAC analogues were successfully synthesised and two lead complexes (**Ru1L²** and **RhL²**) were tested in biological assays. The complexes presented are the first examples of Ru and Rh half-sandwich complexes that inhibit HDAC enzymes, leading to growth inhibition of a lung carcinoma cell line. Under aqueous conditions, complex **Ru1L²** exhibited minimal hydrolysis, implying the chloride species is likely to be structurally stable in the cellular environment. Overall, the complexes display moderate to good cytotoxicity against the H460 non-small-cell lung carcinoma cell line. Complex **RhL²** showed comparable cytotoxicity to the clinically approved SAHA with IC₅₀ values of 4.1 and 1.4 µM, respectively. The IC₅₀ of the ruthenium complex is 5-fold higher than that of the rhodium. Due to the complexes being structurally similar, this could be justified by differences in cellular uptake or localisation, considering both complexes showed similar levels of HDAC inhibition.

HDAC inhibition was rationalised as the mechanism of action by eliminating other possible causes of cytotoxicity. Complex **RhL²** showed no covalent modification of plasmid DNA compared to the cisplatin control. The ability of the complex to retain the chloride ligand supports this, as in piano-stool examples the monodentate ligand undergoes substitution for water to allow DNA-adducts to form. The intercalation assay established the ability of **RhL²** to elicit supercoiling at concentrations of 20 µM or above. These concentrations are significantly higher than those required for HDAC inhibition or general cytotoxicity. Binding constants of the complexes to the protein BSA were also low. In comparison, HDAC activity remained <20% after incubation with complexes **Ru1L²** and **RhL²** at 0.1 µM concentration, displaying overall good potency only 2-fold higher than that of SAHA. These combined results support HDAC inhibition as the likely mode of action for complexes **Ru1L²** and **RhL²**.

An inherent quality of piano-stool complexes is their geometry, and ease with which the structure of the complex can be varied. In this case the metal does not directly bind and can act as a

hypervalent-carbon, allowing the ligands to form multiple interactions with the enzyme active site, enzyme pocket and surface. The halide, arene capping group and chain linker could all be modified to improve upon these results; an advantage over organic counterparts which often require more challenging synthetic pathways to form complex 3D scaffolds with the same desired outcome. The results of this study demonstrate the potential for metal piano-stool complexes as HDAC inhibitors, providing a platform for more efficient binding and improved toxicity. To develop a more succinct rationale for differences in cytotoxicity between the complexes, it is apparent that investigation into factors such as accumulation and localisation is the next step.

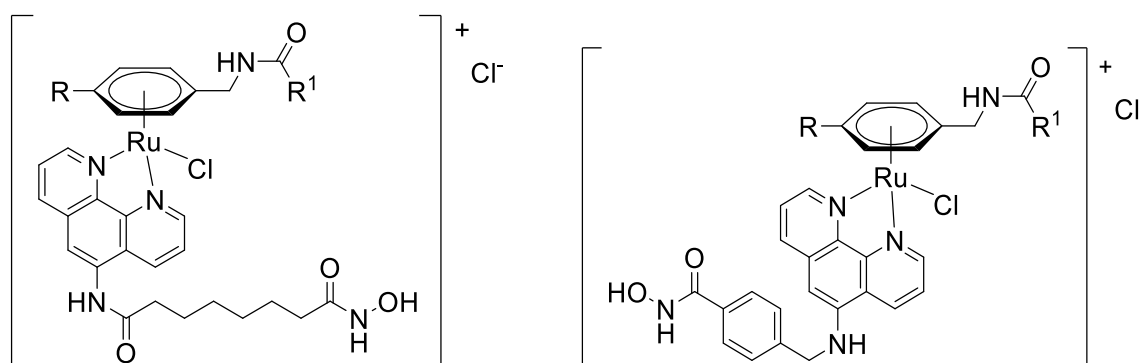
4. Isoform-Selective Piano-Stool HDAC Inhibitors

4.1 Introduction

As the previous chapter reported, the complexes **Ru1L²** and **RhL²** displayed promising results with regard to cytotoxicity and it was determined HDAC inhibition was the likely mode of action, as desired. Incorporation of **L²** allowed the complexes to be built with a structure analogous to SAHA with the additional exploitation of a pseudo-octahedral metal centre as the capping group. With positive results in hand, at this stage of the project, attention was focused towards establishing specificity of the complexes towards one enzyme of the HDAC family. Tuning the structure of the complexes was proposed to achieve selectivity between the 11 zinc-dependent HDAC isoforms. Selectivity is anticipated to evade off target binding, reducing adverse side effects while improving overall drug efficacy.

In an effort to achieve selectivity, this chapter explores the modification of two different structural components of the existing piano-stool HDAC inhibitor, **Ru1L²**. The first aim was to adapt the arene motif to improve enzyme surface interactions and garner specificity by the 3D geometry of the metal complex. The second was the development of an alternative phenanthroline-based ligand that would enhance selectivity through specific interactions in the enzyme channel.

This chapter details the synthesis of eight new arene motifs, along with the development of the new ligand **L³**. A total of thirteen novel complexes were synthesised (*Table 4.1*), characterised and investigated for their biological properties. Cytotoxicity, cellular accumulation, cellular uptake pathways and isoform selectivity assays were performed to provide evidence of activity and any selectivity achieved by the complexes diverse structural changes. The direction of selectivity towards HDAC6 prompted the task of enzyme modelling, employed to probe the likely binding mode to HDAC6-CD2 of the moderately HDAC6-selective **Ru1L³** and insight into the likely protein-ligand interactions that could arise.

Table 4.1 Novel complexes containing modified arene capping groups and commercially available arenes.

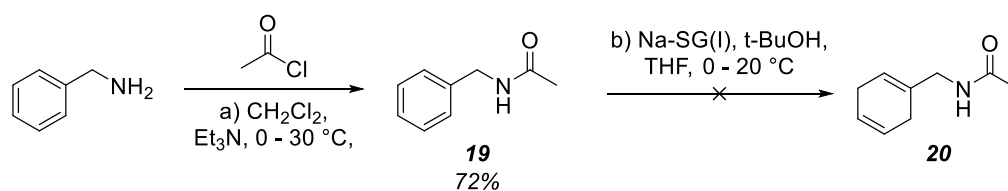
Complex	R	R ¹	Yield [%]
Ru1L²	<i>p</i> -cymene		58
Ru4AL²	H	Me	76
Ru4BL²	H	tBu	60
Ru4CL²	H	Ph	31
Ru4DL²	H	2-Thiophene	48
Ru5AL²	Me	Me	85
Ru5BL²	Me	tBu	75
Ru5CL²	Me	Ph	67
Ru5DL²	Me	2-Thiophene	50

Complex	R	R ¹	Yield [%]
Ru1L³	<i>p</i> -cymene		36
Ru5AL³	Me	Me	39
Ru5BL³	Me	tBu	63
Ru5CL³	Me	Ph	23
Ru5DL³	Me	2-Thiophene	46

4.2 Synthetic Aspects

4.2.1 Arene Capping Group Modification

Synthesis of 1,4-cyclohexadiene precursors was chosen as a feasible route to ultimately form the η^6 -arene bound to the metal. This was attempted using a range of synthetic methods. Firstly, modification was made to the commercially available aryl starting material benzylamine (*Scheme 4.1a*). Benzylamine was reacted with one equivalent of acetyl chloride using triethylamine as a base at 0 °C for 3 h before the reaction was allowed to heat to 30 °C. The reaction proceeded via a nucleophilic substitution to provide the amide product (**19**). After work up, purification by column chromatography provided **19** in good yield (72%).



Scheme 4.1

Reduction of the aryl group was attempted using a sodium-loaded silica gel (Na-SG(I)) as an alternative to the Birch reduction to form compound **20** (Scheme 4.1b). The Na-SG(I) reagent from the outset was documented to have advantages over the standard Birch reduction by boasting a safer, more convenient and air stable form of metallic sodium.¹⁹⁴ To reduce compound **19**, 3.5 equivalents of Na-SG(I) were used in anhydrous THF at 0 °C using t-BuOH as a proton source. No product was observed and an alternative route was sought.

Another synthetic option to form the 1,4-cyclohexadienes was to exploit a Diels-Alder [4+2]-cycloaddition between a diene and an alkyne. Propiolic acid and isoprene were reacted together to synthesise **21** using procedures A-E (Scheme 4.2). The multiple methods employed from literature sources included utilising copper as a catalyst (C), AlCl₃ as a Lewis acid catalyst (E) to coordinate the dienophile (propiolic acid) making it more electrophilic and more reactive to the diene, as well as a standard reflux in toluene in the presence of hydroquinone (B), as a few examples.

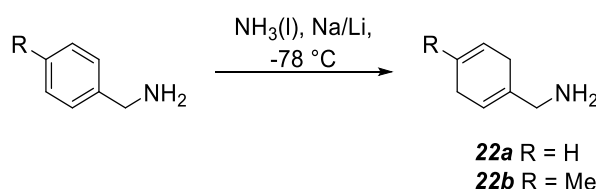


Scheme 4.2 Alternative reaction conditions to synthesise **19**. (A) CH₂Cl₂, rt, 16 h; (B) Hydroquinone, toluene, 120 °C;¹⁹⁵ (C) Sealed vessel, toluene, 120 °C; (D) CuI, Et₃N, CH₂Cl₂, rt;¹⁹⁶ (E) AlCl₃, CH₂Cl₂, 40 °C.¹⁹⁷

All the procedures listed in Scheme 4.2 gave exceptionally poor yields of **21** (<5%). A factor likely accountable for the low yields is the boiling point of isoprene (34 °C). As the majority of the procedures required prolonged heating, this highly volatile starting material could have been lost before the reaction could take place. Although this was a challenge in undertaking the reaction, it was repeated in a sealed vessel and submitted to microwave radiation (C) to, unfortunately, yield a similar result. Continued work was proposed using a more electron deficient disubstituted alkyne (acetylene dicarboxylic acid) as an alternative to propiolic acid, however this reaction was not attempted.

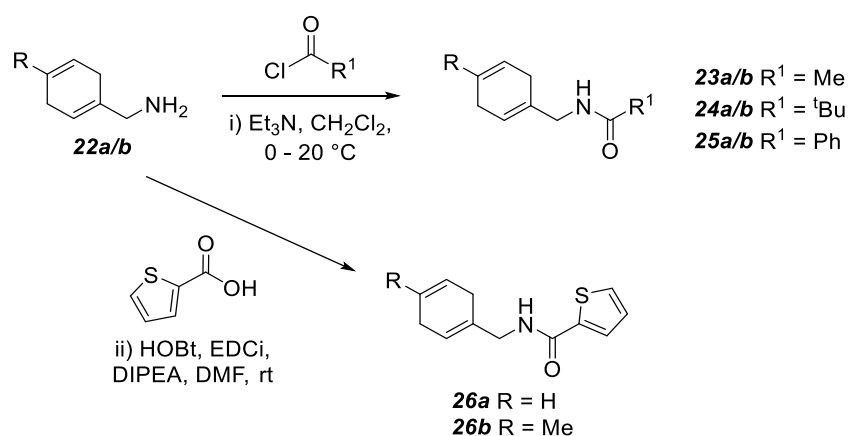
While persistence towards an alternative route to the 1,4-cyclohexadienes had merit, the Birch reduction was eventually employed to synthesise the desired precursors (Scheme 4.3). Ammonia

gas was condensed at $-78\text{ }^{\circ}\text{C}$ *in situ*, prior to the addition of benzylamine or a 4-methyl derivative. Sodium or lithium metal were added and the reaction stirred vigorously. The reaction was then quenched with methanol and the ammonia allowed to evaporate. The resulting mixture was extracted into diethyl ether, dried over MgSO_4 , filtered and solvent removed *in vacuo* to provide an oily product.



Scheme 4.3

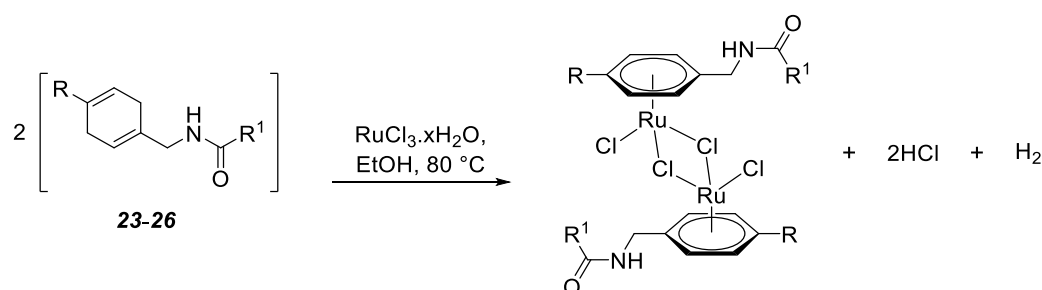
Variations of the reaction were undertaken altering the alkali metal, the mole equivalents of metal, and the time the reaction was allowed to proceed. Regrettably, none of the Birch reductions fully converted the aryl starting material to the diene product (**22a** and **b**) with conversion of reactants to products calculated using $^1\text{H-NMR}$. The most effective combination of these variables was observed in the reaction of benzylamine with two equivalents of sodium metal over 2 h providing 80% conversion to compound **22a**. The most effective use of lithium (4 equivalents) was observed in the conversion of 4-methylbenzylamine over 4 h with 62% conversion to **22b**. It is postulated that the specific metal used for the Birch reduction is more effective depending on the substrate, a factor supported by these results. Due to the viscous oil state of the product and the difficulty in purifying multiple amines, compounds **22a** and **b** were carried forward without further purification; crude mixtures contained some remaining starting materials.



Scheme 4.4

The successive step to the Birch reduction was forming an amide linker with a range of R¹ groups. This was achieved by reacting acetyl chlorides for the methyl (**23a/b**), t-butyl (**24a/b**) and phenyl (**25a/b**) products (Scheme 4.4i). Naturally, both the amines from **22** and Birch reduction starting

material (benzylamine/4-methylbenzylamine) react with the acyl chlorides, providing a mixture of aryl and diene products. Post work-up, separation was attempted by column chromatography, gradually increasing the polarity of the mobile phase using a methanol gradient in 200 mL increments (from 0.5% to 8%) in dichloromethane. Owing to the similar R_f values of the arene and diene, purification between the two compounds at this stage was not successful and again the arene/diene mixture was carried forward. The R^1 group 2-thiophene was additionally chosen due to the existing availability of starting material (2-thiophenecarboxylic acid) and its inclusion providing a hydrogen bond acceptor atom (S). Synthesis of **26a/b** was achieved by reacting 2-thiophene carboxylic acid with **22a/b** using coupling agents HOBt and EDCi in the presence of diisopropylethylamine (DIPEA) base (Scheme 4.4ii). The reaction mixture was poured over 1M HCl and extracted into ethyl acetate. The resulting crude product was columned in the same method as those mentioned previously, with similarly poor separation.



Scheme 4.5

The general method to oxidise C6-dienes was reported by Bennett *et al.* using hydrated RuCl_3 .¹⁹⁸ All 1,4-cyclohexadiene derivatives (**23-26**) were therefore subjected to dehydrogenation with $\text{RuCl}_3 \cdot x\text{H}_2\text{O}$ in EtOH at 80 °C where the reaction turned a dark green. After 16 h the reaction solution had transformed to a dark red colour and was subsequently cooled to room temperature and a precipitate formed. The filtrate was decanted and the solid washed with diethyl ether to remove any remaining aryl impurities, to provide the respective dichloro(arene) ruthenium dimers (Table 4.2).

Table 4.2 Yields of synthesised ruthenium chloride dimers.

Dimer	R	R ¹	Yield [%]
Ru4A	H	Me	17
Ru4B	H	tBu	25
Ru4C	H	Ph	38
Ru4D	H	2-Thiophene	36
Ru5A	Me	Me	29
Ru5B	Me	tBu	27
Ru5C	Me	Ph	45
Ru5D	Me	2-Thiophene	16

The dimeric species synthesised (Table 4.2) were sparingly soluble in most solvents and were therefore characterised in DMSO- d_6 , Figure 4.1 displays the ^1H -NMR spectrum of dimer **Ru4D** as an example. Using an aprotic solvent such as DMSO allowed structural assignment of the amide proton (**f**, 9.01 ppm). Another important structural feature identified from the spectrum is protons **a**, **b** and **c** appearing between 5.5-6.5 ppm, characteristic of η^6 -arene bound protons. Figure 4.1 displays the assumed dimer structure in solution. One set of proton shifts suggests the dimer remains symmetrical, but doesn't rule out competitive binding by the potentially coordinating DMSO solvent. Additional confirmation of the synthesis of the dimer species was observed using solid-state high-resolution mass spectrometry (ASAP⁺), where the mass spectrum showed an m/z at 744.8296. This mass accounts for the loss of a chloride ligand from the dimer species $[\text{M}-\text{Cl}]^+$ with the mass also implying the structure contained two different chloride isotopes (two ^{35}Cl and one ^{37}Cl) along with two ^{102}Ru metal atoms.

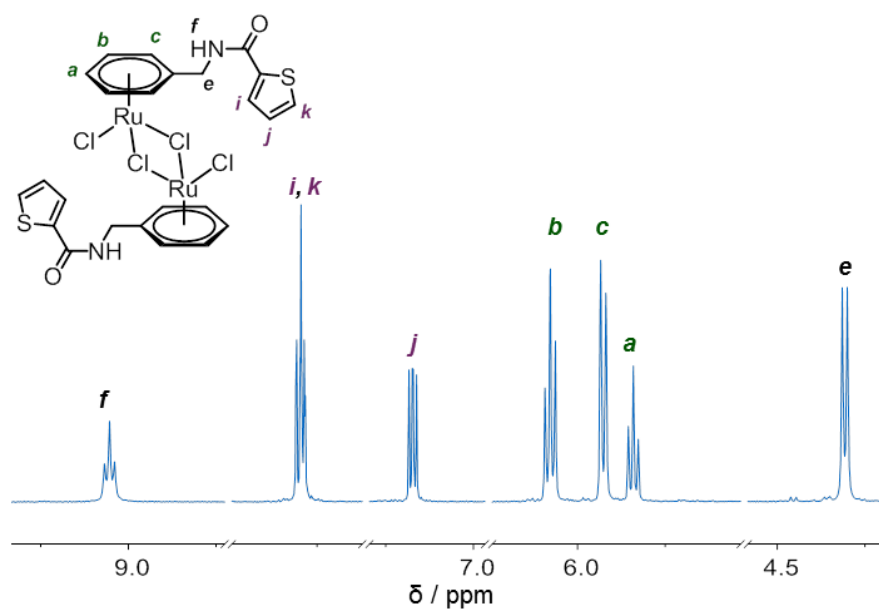
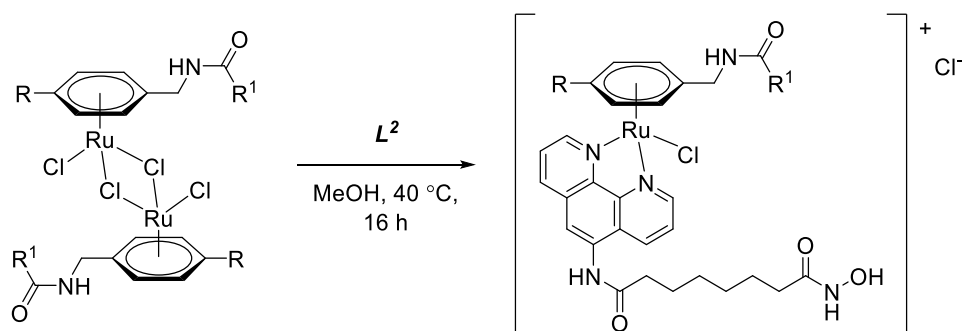


Figure 4.1 ^1H -NMR spectrum of dimer **Ru4D** with all protons labelled (DMSO- d_6 , 298 K, 400 MHz).

Finally, with the ruthenium chloride dimers in hand, each was reacted with 2 equivalents of L^2 (Scheme 4.6) - previously synthesised and discussed in Chapter 3. The ligand and dimer were suspended in MeOH and heated to 40 °C to see full dissolution of both starting components. After 16 h the reaction solution was reduced in volume and recrystallised from diethyl ether. The complexes were subsequently purified by reverse phase HPLC to provide the final complexes (Table 4.3).



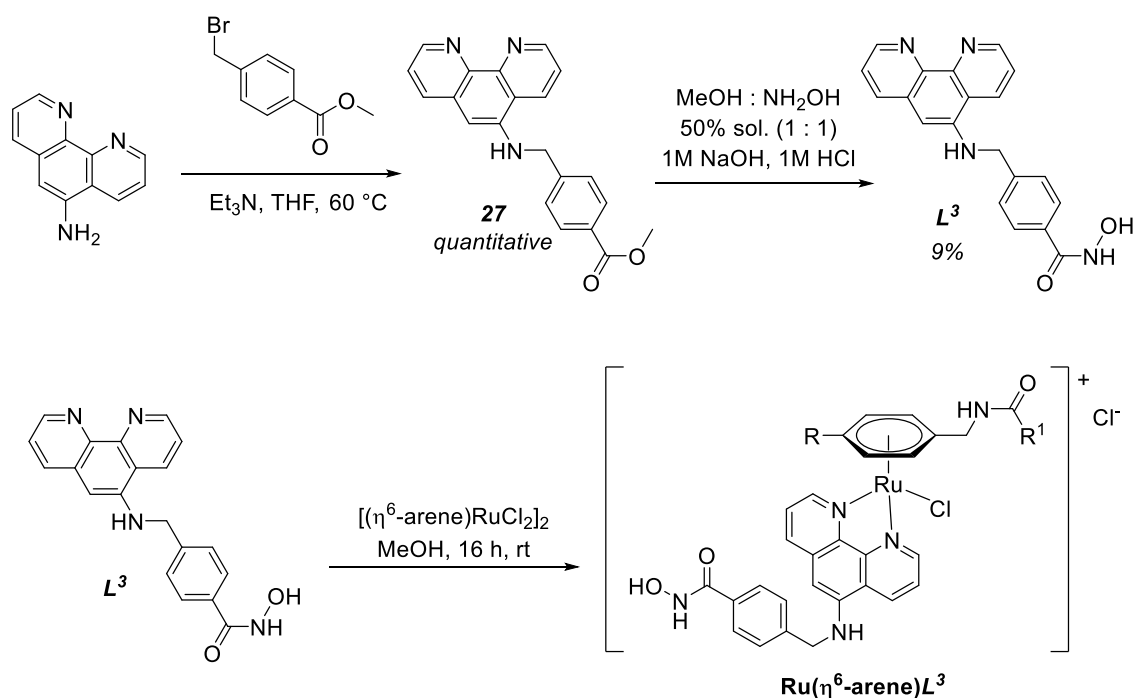
Scheme 4.6

Table 4.3 Modified arene capping group complexes and yields [%].

Complex	R	R ¹	Yield [%]
Ru4AL²	H	Me	76
Ru4BL²	H	tBu	60
Ru4CL²	H	Ph	31
Ru4DL²	H	2-Thiophene	48
Ru5AL²	Me	Me	85
Ru5BL²	Me	tBu	75
Ru5CL²	Me	Ph	67
Ru5DL²	Me	2-Thiophene	50

4.2.2 Chain Linker Modification

A new ligand, analogous to the HDAC6 selective compound tubastatin A, was synthesised in two consecutive steps. Firstly, 1,10-phenanthroline-5-amine was reacted with methyl 4-(bromomethyl)benzoate in THF at 60 °C in the presence of triethylamine base (Scheme 4.7). In this instance, the alkyl bromide is much more susceptible to nucleophilic substitution than the methyl ester and the reaction proceeded to compound **27** in 16 h. After work-up the product was reacted without further purification to the hydroxamic acid, **L³**.



Complexes containing L^3 were synthesised using the same reaction conditions used to synthesise L^2 complexes, with two equivalents of ligand for each mole of complex, suspended in MeOH and heated to 40 °C for 16 h. After this time, the volume of solvent was reduced *in vacuo* and the complex recrystallised out of diethyl ether. This series were also subjected to HPLC reverse phase purification (Table 4.4). The methylated dimer series (**Ru5A-D**) were favoured for reaction with L^3 due to their ease of purification compared to the unsubstituted dimers (**Ru4A-D**).

Table 4.4 Yields of complexes containing L^3 (crude yield = prior to HPLC purification)

Complex	R		Crude Yield [%]
	R	R	
Ru1L³	<i>p</i> -cymene		36
Ru5AL³	Me	Me	39
Ru5BL³	Me	tBu	63
Ru5CL³	Me	Ph	23
Ru5DL³	Me	thiophene	46

The spectrum of **Ru1L³** shown in Figure 4.3 is a crude sample taken in deuterated DMSO of the complex prior to HPLC purification, with protons of interest labelled. In contrast to the L^2 containing complexes whose proton with the highest chemical shift is the NH proton of the amide (10.5 ppm), the highest shifted labile proton in complex **Ru1L³** is the OH (11.1 ppm) observing a 0.8 ppm shift compared to complex **Ru1L²** (OH = 10.3 ppm). This is likely due to the adjacent *N*-acetylphenyl conjugated system causing the downfield shift. Due to the incorporation of the substituted phenanthroline ligand, this creates a stereogenic centre at the ruthenium. This is

evidenced (as observed previously) by protons *c* and *d* of the arene giving rise to a set of diastereotopic protons. This character is mirrored by the isopropyl CH₃ groups of the arene (proton *g*) affording two sets of doublets with similar chemical shift.

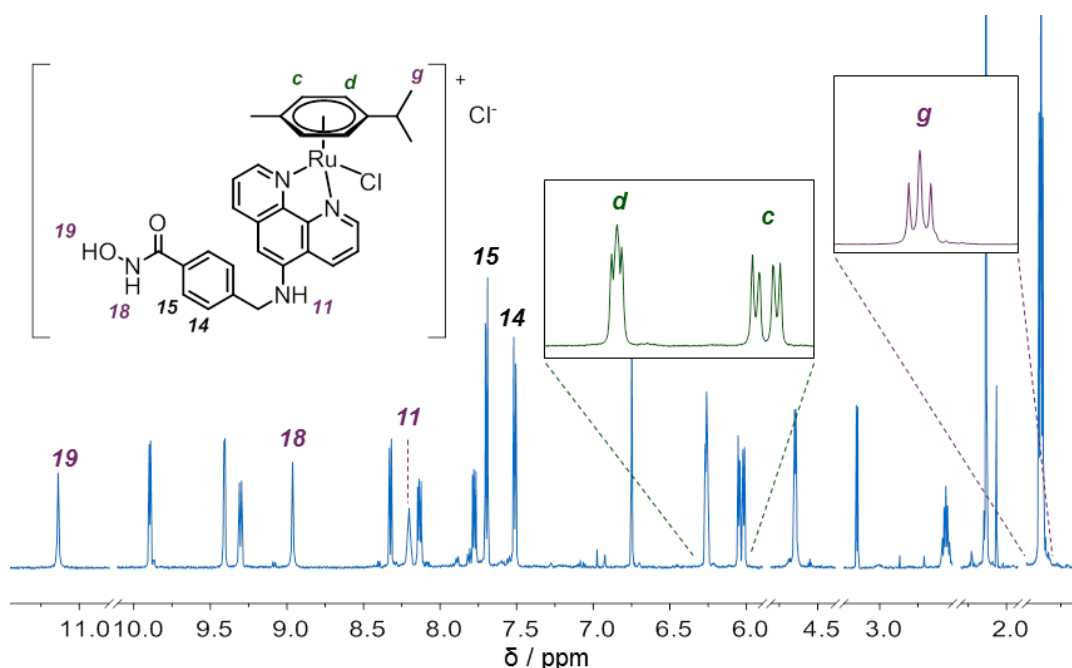


Figure 4.3 Crude ¹H-NMR spectrum of complex **Ru1L³** with selected protons labelled (DMSO-d₆, 298 K, 400 MHz).

4.3 Cytotoxicity

With these two series of complexes in hand, their viability as anticancer agents was assessed against MCF7 human breast adenocarcinoma cell line by measuring cell viability,³ accounting for cell proliferation and the cytotoxicity of the complexes was quantified by calculating IC₅₀ values. To calculate the IC₅₀ values, MCF7 cells were seeded in 12-well plates and allowed to grow to 40 – 60% confluence (an estimate of the number of cells adherent to the flask or vessel surface, referring to the portion of the surface covered). Cellular medium was replaced and cells were treated with complexes **Ru1L²**, **RhL²**, those listed in *Tables 4.5* and *4.6*, along with control compounds, at concentrations ranging from 0.8 to 100 μM. The cells were then incubated for 96 h at 37 °C. Cellular stain acridine orange was subsequently used for cell detection and the nucleic acid stain DAPI (4',6-Diamidino-2-phenylindole dihydrochloride) was used to detect non-viable cells. Fluorescence microscopy was used to calculate cell viability. Values were corrected using a proliferation correction factor (insert in experimental), the IC₅₀ values were subsequently calculated

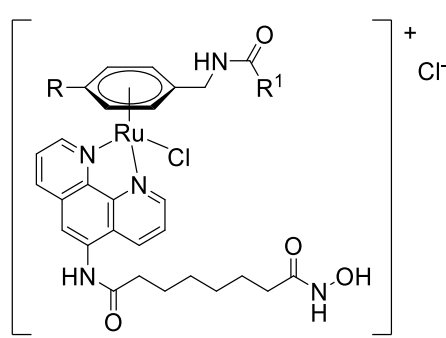
³ Cell viability assays against MCF7 cells were undertaken by R. Pal, Department of Chemistry, Durham University.

using a dose-response curve and are displayed in *Table 4.5* (L^2) and *Table 4.6* (L^3). Discussion of complexes containing L^2 and L^3 has been separated for added clarity.

4.3.1 Analysis of L^2 Complexes

The first crucial observation of the L^2 data is the parent complexes **Ru1L²** and **RhL²** show improved toxicity towards the MCF7 cells compared to the previously tested H460 non-small lung carcinoma cell line (IC₅₀ values of 21 and 4.1 μM, respectively). **Ru1L²** in particular showed 13-fold increase in cytotoxicity between the cell lines along with an IC₅₀ value comparable to that of the clinically approved control drug, SAHA. Of the 8 new L^2 complexes tested, there were some interesting trends.

Table 4.5 IC₅₀ values for L^2 containing complexes measured using the cell viability assay (96 h) against the human breast adenocarcinoma MCF7 cell lines. Entries are the mean value from three experiments. Control compounds include ligand L^2 along with known HDAC inhibitor SAHA. (***RhL²** tested as a non-ruthenium comparison).



Compound	R	R ¹	IC ₅₀ [μM]
Ru1L²	{Ru(<i>p</i> -cymene)}	-	1.53 ± 0.4
RhL²	{Rh(Cp)}	-	2.44 ± 0.1
Ru4AL²	H	Me	32.5 ± 2.2
Ru4BL²	H	tBu	1.36 ± 0.2
Ru4CL²	H	Ph	1.68 ± 0.3
Ru4DL²	H	2-thiophene	5.76 ± 1.5
Ru5AL²	Me	Me	1.24 ± 0.3
Ru5BL²	Me	tBu	5.19 ± 1.5
Ru5CL²	Me	Ph	2.1 ± 0.2
Ru5DL²	Me	2-thiophene	1.72 ± 0.3
L^2	-	-	2.99 ± 0.6
SAHA	-	-	1.46 ± 0.2

The **Ru4L²** series of complexes all contain a mono-substituted arene (R = H in each case) with a methyleneamide linker to various R¹ groups. The methyl substituted **Ru4AL²** gave the highest IC₅₀ value of all the compounds tested (32.5 μM). Structurally **Ru4AL²** contains the least activating or sterically demanding functional groups on the arene which could contribute to low toxicity by general instability of the arene-metal bond in this case, or reduced lipophilic character compared to the other complexes in the **Ru4L²** series. This observation is supported by the **Ru5AL²** complex which contains an additional stabilising *para*-methyl substituent and displays 26-fold more potency than its **Ru4AL²** counterpart. The cytotoxicity is enhanced dramatically in the **Ru4L²** series by the presence of more lipophilic groups as seen with complexes **Ru4BL²** and **Ru4CL²** comprising

tert-butyl and phenyl R¹ groups, respectively. However, the toxicity is slightly reduced in the case of the 2-thiophene substituted **Ru4DL**². It could be speculated that the more lipophilic arenes of the **Ru4L**² series could improve overall drug uptake, which could justify the order of toxicity.

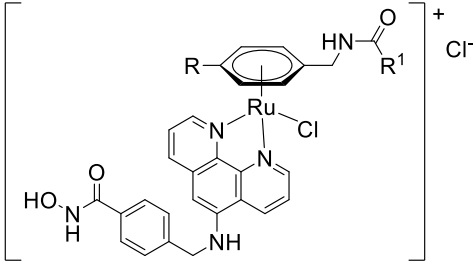
Comparing **Ru4DL**² and **Ru5DL**² offers another example where the *para*-methyl substituent appears to enhance activity. While the phenyl substituent can undergo π -stacking interactions to enhance activity, the thiophene moiety is the only R¹ substituent to provide a heteroatom capable of forming hydrogen bonds with target molecules. Although sulfur is considered a weaker hydrogen bond acceptor than oxygen, studies have indicated the H-bond angle can be crucial for the strength of the interaction.¹⁹⁹ The incorporation this H-bond acceptor to complexes **Ru4DL**² and **Ru5DL**² could be a contributing factor to the relatively low IC₅₀ values of both complexes, increasing potential interactions with the target molecule, enhancing activity. Significantly, the IC₅₀ value for **L**² is double that of SAHA, however the presence of the metal-arene in five of the complexes containing **L**² (**Ru1L**², **Ru4BL**², **Ru4CL**², **Ru5AL**² and **Ru5DL**²), the IC₅₀ values exist within experimental error of the SAHA control. In these cases, it is clear the inclusion of the metal-arene motif is beneficial to overall toxicity and is an initial result in support of enhancing the arene unit to improve overall activity.

4.3.2 Analysis of **L**³ Complexes

It is important to note that within this series, due to the poor yield of **Ru5DL**³ (R = Me; R¹ = 2-thiophene) and the quantity required for testing, cellular investigation of this complex was not performed. In comparison to those containing **L**², the **L**³ containing complexes display potency in the order **Ru1L**³ > **Ru5AL**³ > **Ru5BL**³ > **Ru5CL**³ indicating a general reduction in toxicity as the arene increases in size. The simplest *p*-cymene complex **Ru1L**³ gave an IC₅₀ value of 4.90 μ M, over 3-fold higher than **Ru1L**² possessing the same arene unit. This observation implies the ligand has an effect on the activity, whether generated from inability to access the target molecule as effectively, or via behaviour in the cellular environment. The influence of the amide linker in **L**² compared to the secondary amine linker in **L**³ could be a potential influence over the strength of the σ -donor bond character of the phenanthroline, inducing an assumed increase in lability of the metal-chloride bond. Despite the moderate effect the different phenanthroline ligands have on cytotoxicity, the **Ru5L**³ series clearly shows a combination of **L**³ and increasing arene size to be detrimental to overall toxicity.

The IC₅₀ values of the ligand is also notable, **L**³ in particular displays virtually a 6-fold increase in toxicity compared to its tubastatin A analogue (0.83 and 4.73 μ M, respectively) along with almost two-fold increase in toxicity compared to the SAHA control.

Table 4.6 IC₅₀ values for *L*³ containing complexes measured using the cell viability assay (96 h) against the human breast adenocarcinoma MCF7 cell lines. Entries are the mean value from three experiments. Control compounds include ligand *L*³ along with known HDAC inhibitors SAHA and tubastatin A.



Compound	R	R ¹	IC ₅₀ [μM]
Ru1L³	{Ru(<i>p</i> -cymene)}		4.90 ± 1.0
Ru5AL³	Me	Me	8.97 ± 2.5
Ru5BL³	Me	tBu	18.1 ± 5.4
Ru5CL³	Me	Ph	22.0 ± 3.4
<i>L</i> ³	-	-	0.83 ± 0.4
SAHA	-	-	1.46 ± 0.2
Tubastatin A	-	-	4.73 ± 0.5

Summary

- For *L*² complexes, 7 out of 10 complexes exhibited higher potency than the *L*² ligand alone.
- These 7 *L*² complexes IC₅₀ values were similar to the existing HDAC inhibitor control, SAHA.
- The IC₅₀ values for the *L*³ complexes is proportional to the size of the arene capping group – the larger the arene, the poorer the toxicity.
- Only complex **Ru1L³** possessed comparable toxicity to the known HDAC6 selective inhibitor, tubastatin A.
- Both the ligand and arene must be complementary to ensure a good level of toxicity.

4.4 Active Transport

Changing the temperature of cellular incubation can aid determination of the transport pathway of compounds into the cell. Active transport requires energy input to move ions and compounds across a cell membrane, often assisted by enzymes, therefore at low temperatures active transport does not occur. MCF7 cells were plated using the same method described for calculating cytotoxicity (Section 7.1.6.2) and exposed to complexes **Ru1L²** and **Ru1L³** at their known IC₅₀ concentrations (1.53 and 4.90 μM, respectively).⁴ Cells were allowed to incubate at room temperature for 1 h before being cooled to 4 °C for 24 h. After this time, cell number viability was 98% compared to the initial loading, showing no substantial change in cell number compared to the control plate (incubated at 37 °C for the same time). No increase of cell number is expected at 4 °C as at this temperature cellular processes cannot occur. However, no reduction in cell viability of those incubated with the complexes suggests there is no accumulation of complexes in cells at this

⁴ Active transport assays were undertaken by R. Pal, Department of Chemistry, Durham University.

temperature. This observation suggests that cellular uptake for complexes **Ru1L²** and **Ru1L³** is most likely driven by active transport. It could be postulated from this result, that the cellular uptake pathway for the series of complexes is independent of ligand (**L²** or **L³**), considering complexes **Ru1L²** and **Ru1L³** otherwise share the same arene-metal motif.

4.5 Cellular Ruthenium Accumulation

Depending on the localisation within the desired cellular target, quantitative uptake of a drug is often a necessity and can be a critical factor affecting the efficacy of drug candidates. In these cases, once inside the cell there are many processes and molecules that can influence therapeutic efficacy. However, given the intended target of these complexes, it is assumed that successful entrance and retention within the cell is required to produce cytotoxic effects. Having already established that active transport is the likely pathway across the cell membrane, it was deemed necessary to discern whether cellular accumulation of the complexes is a factor contributing to the varied toxicities observed in *Section 4.3*.

To measure cellular accumulation of ruthenium, inductively coupled plasma mass spectrometry (ICP-MS) was the chosen technique employed to quantify the concentration of ruthenium in a sample after incubation.⁵ Human breast adenocarcinoma MCF7 cancer cells were treated with each complex at the equipotent concentration of their respective IC₅₀ values and the cells then incubated at 37 °C for 96 h. The cells were then washed and the resulting material digested using concentrated nitric acid (0.6 mL) for a further 24 h at 37 °C. Samples were diluted 40-fold for ICP-MS analysis and the values calculated from the total ruthenium accumulation after incubation, relative to the initially calculated IC₅₀ values and are displayed as percentage accumulation in *Table 4.7*. The cellular accumulation is presented alongside the IC₅₀ values to identify any trends from the resulting data.

The complexes in series **Ru4L²** and **Ru5L²** present IC₅₀ values relative to Ru accumulation. The extent of cellular accumulation in the three complexes with the highest IC₅₀ values follows the order **Ru5BL²**>**Ru4DL²**>**Ru4AL²**, all displaying accumulation <10%. Complex **Ru4AL²** shows an IC₅₀ value of 32.5 μM; one order of magnitude higher than any other complex in series **Ru4L²** and **Ru5L²**. The poor toxicity is supported by the low level of Ru accumulation <1%. This result best represents the hypothesis that the lower the cellular accumulation of Ru, the less potent the complex, suggesting **Ru4AL²** is either unstable in the assay medium or is not effectively taken up by MCF7 cells. This observation is consistent with the analogous, methyl substituted complex

⁵ Cellular ruthenium accumulation was measured by C. J. Ottley, Department of Earth Sciences, Durham University.

Ru5AL² which displays a ~27-fold decrease in IC₅₀ by comparison to **Ru4AL²** and a near identical factor increase in cellular accumulation.

Table 4.7 Total cellular accumulation of ruthenium metal in human breast adenocarcinoma MCF7 cancer cell line determined using equipotent concentrations to IC₅₀. ^aThe IC₅₀ values are expressed as the concentration of each complex which causes 50% cancer cell growth inhibition. ^bTotal accumulation of Ru in MCF7 cells after 96 h of drug exposure at 37 °C relative to IC₅₀ values.

Compound	R	R ¹	IC ₅₀ ^a [μM]	Cellular accumulation ^b [%]
Ru1L²	{Ru(<i>p</i> -cymene)}		1.5 ± 0.4	7.9
Ru4AL²	H	Me	32.5 ± 2.2	0.5
Ru4BL²	H	tBu	1.4 ± 0.2	18.9
Ru4CL²	H	Ph	1.7 ± 0.3	13.8
Ru4DL²	H	2-thiophene	5.8 ± 1.5	3.5
Ru5AL²	Me	Me	1.2 ± 0.3	13.0
Ru5BL²	Me	tBu	5.2 ± 1.5	6.1
Ru5CL²	Me	Ph	2.1 ± 0.2	11.1
Ru5DL²	Me	2-thiophene	1.7 ± 0.3	12.2
Ru1L³	{Ru(<i>p</i> -cymene)}		4.9 ± 1.0	24.1
Ru5AL³	Me	Me	9.0 ± 2.5	18.7
Ru5BL³	Me	tBu	18 ± 5.4	43.9
Ru5CL³	Me	Ph	22 ± 3.4	48.6

Broadly, the apparent trend implies that toxicity of complexes in series **Ru4L²** and **Ru5L²** is uptake-dependent. Based on these observations the R substituent of the arene in these complexes appears to have little effect on toxicity, instead the overall tuned lipophilicity of each complex appears to be an overarching contributing factor to cellular uptake and cytotoxicity. The outlier to this trend is the parent complex **Ru1L²** which exhibits a low IC₅₀ value (1.5 μM) in contrast to its moderate Ru cellular accumulation (7.9%). Compared to the other complexes containing **L²**, its main structural difference is the absence of the amide linker within the arene. While adding bulky, hydrophobic substituents can increase the lipophilic surfaces within a molecule improving uptake, the amide linker provides a polar functionality with the ability to form hydrogen bonds. Such van der Waal interactions could be a hinderance for the other complexes, resulting in off-target binding. This proposition could be rationalised through the observations of complex **Ru1L²** which does not possess the amide linker and provides a marked level of toxicity relative to its accumulation, in comparison to the other complexes containing **L²**.

By contrast, the complexes containing **L³** appear to show an inverse relationship, with those complexes displaying the highest cellular Ru accumulation exhibiting the least potency. The cellular uptake trend for series **Ru5L³** is evidently influenced by lipophilicity, with the more

lipophilic R^1 substituents appearing to enhance cellular uptake. This effect is most pronounced for complexes **Ru5BL³** and **Ru5CL³** (containing t-butyl and phenyl R^1 groups, respectively), which show >25% Ru accumulation than any other complex tested. One distinct structural difference between the L^2 and L^3 containing complexes is the chain linkers. The tolyl moiety of the L^3 ligand provides a notable increase in lipophilic character compared to the L^2 six carbon aliphatic chain. This particular character of the L^3 ligand supplies an additional influence to cellular accumulation relative to the L^2 complexes, effectively demonstrated by **Ru5CL³** showing Ru uptake 4-fold higher than its **Ru5CL²** analogue. Considering both cytotoxicity and cellular accumulation in tandem, alongside the potency of the ligand L^3 alone, the size of the arene group in the **Ru5L³** series appears to have a negative impact on cytotoxicity once inside the cell. This could also be rationalised as off-target binding to hydrophobic intracellular proteins by the more lipophilic complexes.¹⁹³

While the varied uptake behaviour of the complexes discussed in this section appears to be largely governed by lipophilicity, it is imperative to consider the cellular uptake mechanisms potentially influencing the overall cytotoxicity or lack thereof. The extensive array of pathways associated with facilitated diffusion can be affected, not only by lipophilicity, but by the charged state of the complex or its binding affinity to transporter proteins such as the copper transporter CTR1.¹⁸¹ Increase in drug efflux is frequently observed as a cause of reduced cytotoxicity. For example, overexpression of the plasma membrane glycoprotein P-gp has been noted in cisplatin resistant cell lines as the cause for increase drug efflux, with P-gp displaying favourable substrate recognition of highly lipophilic and cationic species.⁵⁴

Considering the structural features of the complexes here, a discrete membrane component could be a contributing factor towards the low levels of Ru accumulation as seen for complexes **Ru4DL²** and **Ru5BL²**, potentially mediated by high levels of drug efflux. Additional experimentation would be applicable to identify the likely cause of poor accumulation, given some structurally analogous complexes in these series show disparate levels of Ru uptake. Coadministration of these complexes with verapamil – a known P-gp inhibitor – could determine the extent drug efflux, with respect to P-gp, effects overall cellular accumulation.

4.6 Isoform Selective HDAC Assays

Having established in *Chapter 3* that HDAC inhibition activity was the likely mechanism of action for complexes **Ru1L²** and **RhL²**, the design of the **Ru4L²**, **Ru5L²** and **Ru5L³** series were intended to develop isoform selectivity between the metal complexes. Based upon the moderate to good cytotoxicity displayed by all the complexes synthesised in this chapter, it was therefore necessary

to investigate any apparent relationship between the diverse piano-stool complexes and HDAC isoform selectivity.

Three distinct HDAC isoforms were chosen, one from each zinc-dependent class providing a range of possible binding topographies: HDAC1 (class I), HDAC4 (class IIa) and HDAC6 (class IIb). Purified human recombinant enzymes were used from commercially available kits (*Section 7.1.8*). Appropriate dilutions of assay components were made using assay buffer and stored on ice. The known pan-HDAC inhibitors SAHA and TSA were tested alongside complexes listed in *Table 4.5*, L^2 , L^3 and tubastatin A (a HDAC6 selective inhibitor). Each compound was dosed at 1 and 0.1 μM concentrations into wells containing master mixture comprising HDAC-specific acetylated substrate, BSA (1 mg/mL) and buffer. Upon addition of HDAC enzyme, the plate was incubated at 37 °C for 30 minutes. After this time, a developer was added and the plate incubated at room temperature for a further 15 minutes. The plate was excited at 360 nm and detection of emission was measured at 460 nm. Similar to the previous HDAC enzyme assay protocol described (*Chapter 3*), as a positive control, the assay was also run in the absence of any inhibitor. Results were calculated as a percentage of HDAC activity, relative to the positive control and are displayed in *Figure 4.4* for each individual HDAC isoform. All assays and controls were measured in triplicate and mean values are reported, along with standard errors.

Generally, all the compounds tested - with the exception of tubastatin A – reduced HDAC1 activity to <25% at 1 μM dose of inhibitor (*Figure 4.4A*) and of all the compounds tested, the parent complexes **Ru1L²** and **RhL²** exhibited the highest level of inhibition for HDAC1. The new series of complexes containing L^2 (from **Ru4AL²** to **Ru5DL²**) show similar or reduced HDAC1 activity at the more dilute 0.1 μM concentration when compared to the ligand L^2 alone. By contrast, as expected the L^3 containing complexes show the lowest levels of inhibition at the more dilute concentration, mirrored by the L^3 ligand and tubastatin A. Examples in the literature imply selectivity of class I HDACs is often observed in compounds containing the 2-aminoanilide zinc-binding motif with additional substituents to fit in a foot-pocket beside the zinc active-site.^{123,125,142} While this functionality was not exploited within these complexes, the intention of modifying the arene unit was instead intended to exploit interactions on the enzyme surface that may be difficult to access by a purely organic molecule.

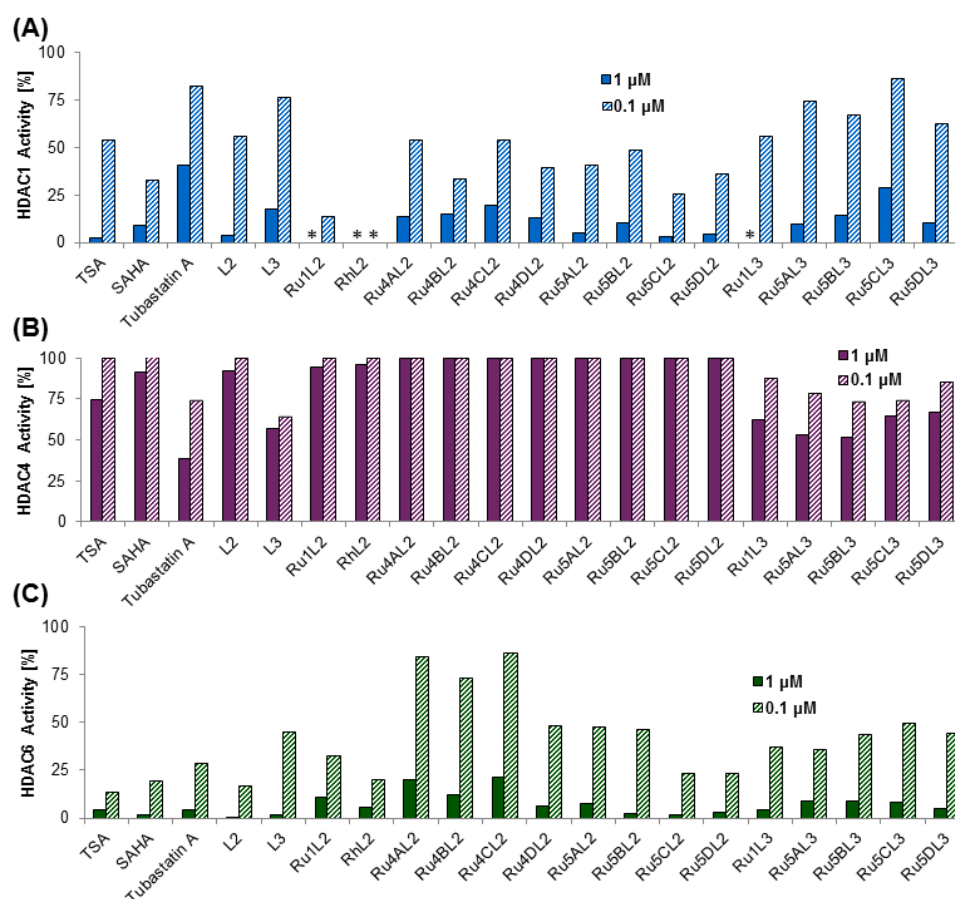
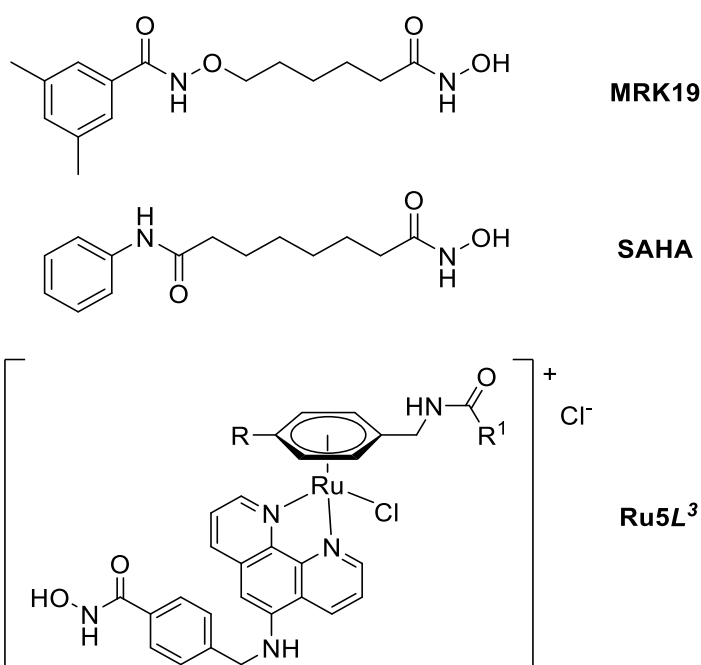


Figure 4.4 Compounds tested at 1 and 0.1 μM concentrations against (A) HDAC1, (B) HDAC4 and (C) HDAC6. Values are reported as an average of three experiments. (*) <math><1\%</math> HDAC enzyme activity.

In the case of complexes **Ru5CL²** and **Ru5DL²**, both incorporate the same **L²** ligand and display the highest overall inhibition of the new complex series for HDAC1. These complexes contain the R¹ substituents phenyl and thiophene, which are both aromatic and could result in π -stacking interactions with phenylalanine, tryptophan or tyrosine amino acid residues enhancing surface interactions and improving activity. Free rotation of the arene unit should also allow this motif to establish the most thermodynamically favourable conformation once the hydroxamic acid is bound to the zinc active-site. This could account for many of the other complexes displaying moderate inhibition activity towards HDAC1. However, it still remains that the parent ruthenium complex **Ru1L²** shows the best inhibition for HDAC1 compared to the other complexes, possessing only alkyl substituents. The isopropyl groups of the *p*-cymene could be accommodated into a small hydrophobic region on the enzyme surface, while additional substituents could hinder HDAC1 binding and may therefore not be accommodated as easily.

The class IIa HDAC enzyme results offer the most evident trend out of the three classes tested (Figure 4.4B). All metal complexes containing **L²** show negligible inhibition of HDAC4 at the higher 1 μM concentration. A comparable degree of HDAC4 activity is observed after dosing with the control compound SAHA along with **L²**, implying the six-carbon alkyl chain linker is not a

favourable structural trait of HDAC4 inhibitors. A distinct feature of the HDAC4 selective inhibitor **MRK19** (Section 1.3.4.3, $IC_{50} = 0.012 \mu\text{M}$) is the presence of an alkoxyamide moiety with a five-carbon chain linker connecting the hydroxamic acid binding group. The nitrogen of the **MRK19** alkoxyamide forms a hydrogen bond with the carboxylate group of Asp115 at the channel rim. While this interaction cannot be achieved by the L^2 complexes and other analogous compounds, L^3 , tubastatin A and the **Ru5L³** series possess a more accessible amine which could potentially give rise to a similar interaction as that observed for **MRK19**. The implication of a more favourable interaction by the L^3 ligand is reflected by the **Ru5L³** series, L^3 and analogous tubastatin A (only differing by capping group) all displaying moderate inhibitory activity towards HDAC4 at $1 \mu\text{M}$ concentration. Although this is a rational justification for the improved inhibition activity towards HDAC4 of the L^3 series relative to the L^2 series, other factors such as orientation, kinetics and zinc binding group could also contribute.



Finally, the screening of compounds against the class IIb enzyme HDAC6 showed comparable results to those for HDAC1, with all the compounds tested exhibiting inhibitory activity towards HDAC6 (Figure 4.4C). The organic control compounds all showed less than 50% HDAC enzyme activity at the lower concentration of $0.1 \mu\text{M}$ with L^2 displaying similar inhibition to SAHA. Broadly, the complexes containing L^3 show equivalent inhibitory profiles with complex **Ru1L³** reducing HDAC6 activity the most down to 4% at the $1 \mu\text{M}$ dose concentration. This trend was anticipated due to the presence of the bulkier tolyl linker in L^3 , a characteristic shared with tubastatin A which can accommodate the wider and shallower pocket of HDAC6 more effectively.¹⁴⁰ Complexes **Ru5CL²** and **Ru5DL²** of the new series exhibit the highest level of inhibition at both concentrations tested, near equivalent to each other. The presence of the bulkier

R¹ group on the arene could be a contributing factor to increased interactions and therefore enhanced inhibition. While the presence of the L³ ligand in the RuL³ series is clearly responsible for the increase in inhibition towards HDAC6 compared to HDAC1, many of the complexes and ligands display good inhibition towards both HDAC1 and HDAC6 enzymes. It could be argued that the calculated inhibition at two concentrations is not an adequate measurement to distinguish any selectivity clearly, primarily due to similar results in this concentration range between analogous complexes. This factor is crucial when taking into consideration many of the compounds tested inhibit enzyme activity to a degree more than 50% at 0.1 μM concentration and therefore require more scrutiny to determine whether any selectivity exists at lower concentrations. For this reason, a selection of complexes were chosen based upon their cytotoxicity and HDAC inhibitory profile and were subsequently tested against HDACs 1 and 6 to measure their IC₅₀ values and identify any specificity towards one particular enzyme.

4.6.1 HDAC1 & HDAC6 – IC₅₀ Results

Four complexes were chosen from the initial screening that possessed structural similarities to determine which feature or combination is likely to generate selectivity. The interchangeable features of the complexes comprise the incorporation of either L² or L³ combined with either a *p*-cymene or 5C arene, therefore including the parent compound Ru1L². Control compounds SAHA, the known pan-HDAC inhibitor expected to display no selectivity, tubastatin A shown to possess selectivity for HDAC6¹⁴⁰ and the ligands L² and L³ were test alongside the complexes. Each compound was tested in the concentration range 10 – 0.004 μM to calculate the IC₅₀ values for HDAC1 and HDAC6 using the same method described in Section 4.5 and are displayed in Table 4.8. An example dose response curve is shown in Figure 4.5.

Table 4.8 IC₅₀ values measured using commercially available kit (Section 7.1.8 BPS Bioscience) against HDAC1 and HDAC6 and are reported as the mean value of three experiments. Selectivity of HDAC6 over HDAC1 is displayed along with IC₅₀ values against MCF7 cells*.

Compound	R	R ¹	HDAC1 IC ₅₀ [μM]	HDAC6 IC ₅₀ [μM]	Selectivity factor	*IC ₅₀ [μM]
SAHA	-	-	0.03 ± 0.004	0.012 ± 0.001	2.5	1.46 ± 0.2
Tubastatin A	-	-	1.72 ± 0.1	0.04 ± 0.006	43	4.73 ± 0.5
L ²	-	-	0.06 ± 0.05	0.03 ± 0.02	2.0	2.99 ± 0.6
L ³	-	-	0.36 ± 0.03	0.15 ± 0.02	2.4	0.83 ± 0.4
Ru1L ²	<i>p</i> -cymene		0.24 ± 0.03	0.04 ± 0.002	6.0	1.53 ± 0.4
Ru5CL ²	Me	Ph	0.08 ± 0.01	0.03 ± 0.006	2.7	2.1 ± 0.2
Ru1L ³	<i>p</i> -cymene		0.24 ± 0.03	0.06 ± 0.001	4.0	4.90 ± 1.0
Ru5CL ³	Me	Ph	0.35 ± 0.05	0.08 ± 0.02	4.4	22.0 ± 3.4

Initially it is apparent that all the compounds tested were very active in inhibiting both enzymes, hence a selectivity factor was calculated to establish the degree of affinity for HDAC6 over HDAC1. SAHA, L^2 and L^3 all display a similar degree of selectivity together with comparable cytotoxicity values. Of these examples each inhibits HDAC1 and HDAC6 activity to the same order of magnitude. The poor enzyme specificity observed is reflected in the lower cytotoxicity IC_{50} values, likely to arise from such non-selective binding. By comparison, tubastatin A displays the highest level of selectivity, 43-fold selective for HDAC6 over HDAC1 considered to possess superior selective binding due to the combination of the tricyclic capping group enhancing interactions with the enzyme channel rim.¹⁴⁰ Additionally, the tolyl linker, a feature present in both tubastatin A and L^3 is linked to preferential binding to HDAC6 due to the unusual monodentate binding mode accessible by this motif disfavoured in the more sterically constricted active site of HDAC1.²⁰⁰ It is evidenced by the low level of selectivity of L^3 that the phenanthroline capping group in combination with the tolyl linker is not sufficient to create the level of selectivity boasted by tubastatin A.

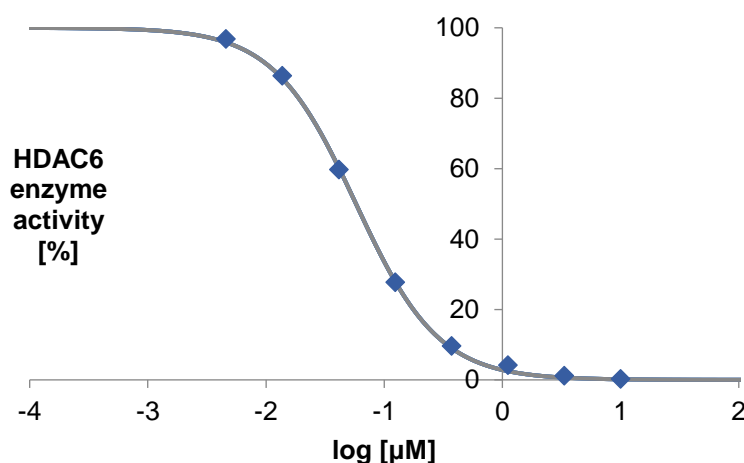


Figure 4.5 Dose response curve of complex **Ru1L³** against enzyme HDAC6 to calculate the IC_{50} value.

In contrast to the purely organic systems, with the exception of the control compound tubastatin A, the metal complexes exhibited more desirable results. The presence of the metal-arene appears to improve overall affinity and yield better selectivity towards HDAC6, with the exception of complex **Ru5CL²**. For the complexes containing L^2 , **Ru1L²** displays the highest selectivity factor of 6.0, triple that of the ligand alone, while **Ru5CL²** fails to demonstrate this level of selectivity. The arene moiety of **Ru5CL²** contains the bulkier phenyl group as well as an amide linker. Both of these functionalities could furnish interactions with the HDAC1 surface that the *p*-cymene of **Ru1L²** cannot, but unfortunately reduces the overall selectivity of complex **Ru5CL²**.

A significant result is the complexes containing L^3 (**Ru1L³** and **Ru5CL³**) show a similar degree of selectivity suggesting the presence of the tolyl linker is a contributing factor in improving their

affinity towards HDAC6. Nevertheless, it could be postulated that the more open surface of HDAC6 affords a more tolerant structure to accommodate the metal-arene capping group. This suggestion is supported by the generally low IC₅₀ values for HDAC6 by all the complexes tested. It is also possible that selectivity of complexes **Ru1L³** and **Ru5CL³** towards HDAC6 could develop from the orientation of the arene bound to the metal once the complex is accommodated into the enzyme channel. The tolyl linker has been shown to require a bent conformation, which would directly influence the location of the arene, further enhancing interactions with the enzyme surface. The equivalent selectivity of **Ru1L³** and **Ru5CL³** for HDAC6, is not reflected in their cytotoxicity. Consequently, poor toxicity of **Ru5CL³** compared to **Ru1L³** is presumably linked to reduced cellular uptake or off target binding. It could be assumed from these results that the **L³** ligand incorporation into complexes **Ru1L³** and **Ru5CL³** provides a degree of selectivity compared to **L²** and that in combination with the arene motif is likely to attribute to the overall selectivity. To support these suggestions, investigation of computational models would provide a valuable insight into potential binding modes and surface interactions.

4.6.2 HDAC6 Catalytic Domain Assay

The pronounced inhibition and consequent interest in HDAC6 selectivity in the previous experiment raised a subsidiary query. HDAC6 is distinct of all the zinc-dependent isozymes by virtue of it containing two catalytic domains, CD1 and CD2. One of these domains (CD2) is documented to catalyse the deacetylation of a variety of substrates including α -tubulin,¹³⁶ with CD2 inhibition resulting in microtubule hyperacetylation leading to cell cycle arrest and apoptosis. However, CD1 is also known to catalyse the deacetylation of acetyl-lysine substrates²⁰¹ and for this reason it was deemed necessary to determine the activity of the complexes synthesised here against CD1 and CD2.

The synthesis of individual HDAC6 catalytic domains was achieved by expression of zHDAC6 (*danio rerio* – zebrafish; a homologous enzyme of human HDAC6) through domain cloning.⁶ Each domain was sub-cloned into the modified pSAT1-LIC plasmid and transformed into *E. coli* ER2566 and BL21(DE3) competent cells using heat shock treatment. Single colonies were grown to O.D.₆₀₀ of 0.4-0.5 followed by induction of protein expression using isopropyl β -D-1-thiogalactopyranoside (IPTG). The cells were then harvested, lysed to break down into cellular components, washed and the desired proteins purified using a Nickel column.

Catalytic activity of the individual domains was established using an existing literature procedure to determine the appropriate concentrations of protein required to produce detectable and

⁶ Domain cloning and catalytic domain assays were undertaken by A. Kingdon and T. R. Blower in the Department of Biosciences, Durham University.

comparable activity.²⁰¹ An activity assay was undertaken (Section 7.1.9) to confirm the successful synthesis of the domains and the results showed zCD2 observed 18-fold deacetylase activity for the commercially available substrate compared to zCD1; consistent with the literature. The inhibitory assay therefore dosed the proteins in concentrations of 0.75 μM and 0.15 μM for zCD1 and zCD2, respectively. Complex **Ru1L³** was chosen due to its incorporation of the tolyl linker, demonstrated to improve overall selectivity towards HDAC6. The pan-HDAC inhibitor SAHA was used as a control compound. Similar to all the assays undertaken previously, a positive control in the absence of inhibitor was run alongside and the inhibition assay was undertaken using the method previously described in Section 4.4.1. The results were calculated as a percentage of catalytic activity for each domain, relative to the positive control and are displayed in Figure 4.6.

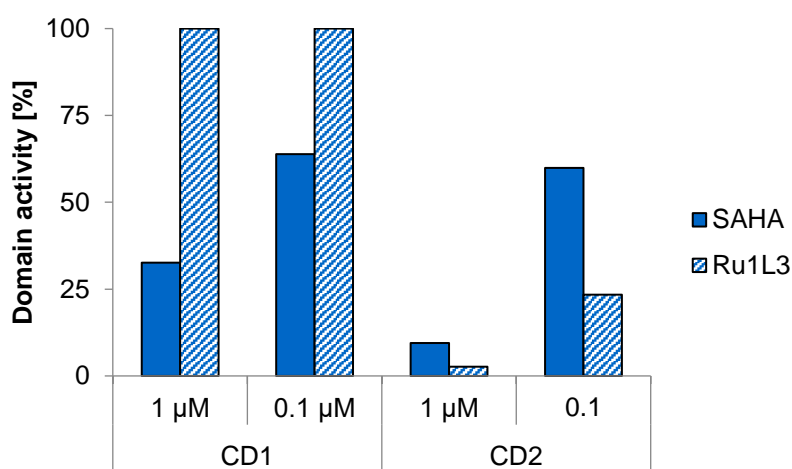


Figure 4.6 Measure of catalytic activity of HDAC6 cloned catalytic domains zCD1 and zCD2 after incubation with complex **Ru1L³** and SAHA control at 1 and 0.1 μM concentrations.

At 1 μM dose concentration, the control compound SAHA showed significant inhibition of domain catalytic activity for both zCD1 and zCD2, with inhibition 3-fold higher for zCD2. Having demonstrated the substrate used in this particular assay is deacetylated by both catalytic domains, an additive effect of multiple domain inhibitory activity of SAHA could account for its potent inhibitory activity observed towards the recombinant HDAC6 enzyme (Section 4.5.2, IC_{50} value = 0.012 μM). This result is consistent with the pan-HDAC inhibitor character of SAHA, which could additionally support the high cytotoxicity exhibited *in vitro* and presents more evidence for non-specific off-target binding.

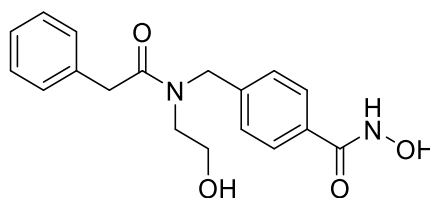
By contrast, **Ru1L³** displayed significant inhibition of zCD2 catalytic activity, with <25% activity observed at the lower 0.1 μM concentration. Unlike SAHA, **Ru1L³** showed no relative inhibitory activity towards zCD1, displaying >30-fold selectivity to zCD2 over zCD1 at 1 μM . This result is in agreement with the design of complex **Ru1L³**, improving selectivity not only between HDAC isoforms but for one specific HDAC6 catalytic domain. The inhibitory activity exhibited by **Ru1L³**

in this assay also promotes the target specificity desirable for drug candidates, inherently improving the efficacy of **Ru1L³** as a selective HDAC inhibitor. Previous studies have dictated the degree of inhibitory activity could be partially attributed to a combination of relative binding affinities to the individual catalytic domains, as well as the disparate concentrations of the proteins tested in such an assay.²⁰¹ In the case of **Ru1L³** it could be assumed that these factors are unlikely contributors due to its effectively tuned design providing the selectivity observed for zCD2.

4.7 Enzyme Modelling

Although crystal structure growth of complex **Ru1L³** in zHDAC6-CD2 was not successful, protein-ligand computational docking was attempted to mimic potential interactions of the complex with the protein active-site. Structural optimisation of complex **Ru1L³** was achieved using DFT calculations and assessed within Gaussian to confirm the lowest energy conformation of the complex.⁷ To construct an accurate depiction of a piano-stool complex, a ghost atom (GA) had to be employed to allow free rotation about the metal-arene bond. The GA was assigned in the centre of the arene as an atom with no nuclear charge or electrons, forming a bond to the metal centre and to each carbon in the bound arene. Bond distances and angles were surveyed to establish any inaccuracies within the arene when building **Ru1L³** using this method. Nevertheless, the angles and distances were all within 0.02 Å/° of the initial fixed arene providing six bonds to the ruthenium metal centre.

HDAC6-CD2 homology models were established using an existing crystal structure of zHDAC6-CD2 from *danio rerio* (zebrafish) (PDB: 5WVK) and the ligand HPB (*N*-hydroxy-4-[(*N*(2-hydroxyethyl)-2-phenylacetamido)methyl]benzamide) crystallised within the catalytic domain was removed and docking of complex **Ru1L³** was undertaken. Genetic Optimisation of Ligand Docking (GOLD) was implemented as the chosen docking programme, an approach shown to be favoured in the prediction of reliable docking positions (relative to the crystal structure) for organometallic complexes.²⁰²



HPB

⁷ DFT calculations were undertaken by A. Kingdon in the Department of Chemistry, Durham University.

The torsional angles of complex **Ru1L**³ were modified by GOLD to present the lowest energy binding conformation in the protein's active site. Possible conformations were fixed within the parameter of 10 Å to the zinc catalytic site (the length of the active-site channel) to ensure binding modes were predicted between the complex and the vacant zinc coordination sites. In this instance, ChemScore was employed as the fitness function which considers the free energy of binding (metal co-ordination, hydrophobic interactions, hydrogen-bond formation and rotatable-bond freezing), along with steric clashes and conformational restraints. The top ten docking conformations were ranked using ChemScore and assessed as potential binding modes. The principal factor used to elucidate the most cogent solutions was interaction between the hydroxamic acid and the zinc catalytic site; a prevalent binding mode of HDAC inhibitors due to its strong chelating ability to zinc. The five solutions with the highest ChemScore provided such rational binding outcomes.

The five binding modes were subsequently evaluated for their spacial accommodation of the enzyme active-site and surface, alongside interactions with additional amino acid residues to justify potential binding affinity. The solution poses were scrutinised relative to each other and the original protein-ligand crystal structure. A commonality shared by the five solutions was the placement of the planar phenanthroline moiety within the complex fitting flat to the wide pocket rim and the chloride ligand facing outwards. In *Figure 4.7A*, two solutions are superimposed (one yellow, one purple) to show the diverse conformations in relation to the hydrophobic surface and clearly illustrates the arene rotation movement as a variable to avoid conflicting interactions. While both poses offer minimal steric clash of the arene to the protein surface, upon closer inspection the hydroxamic acid in the yellow pose did not demonstrate the most desirable binding mode of the top solutions. By contrast, the solution displayed in purple provided the most rational prediction of **Ru1L**³, maximising amino acid residue interactions as well as incorporating a realistic zinc coordination. For this reason, the pose displayed in purple was chosen for further examination and will therefore be the focus of discussion here in.

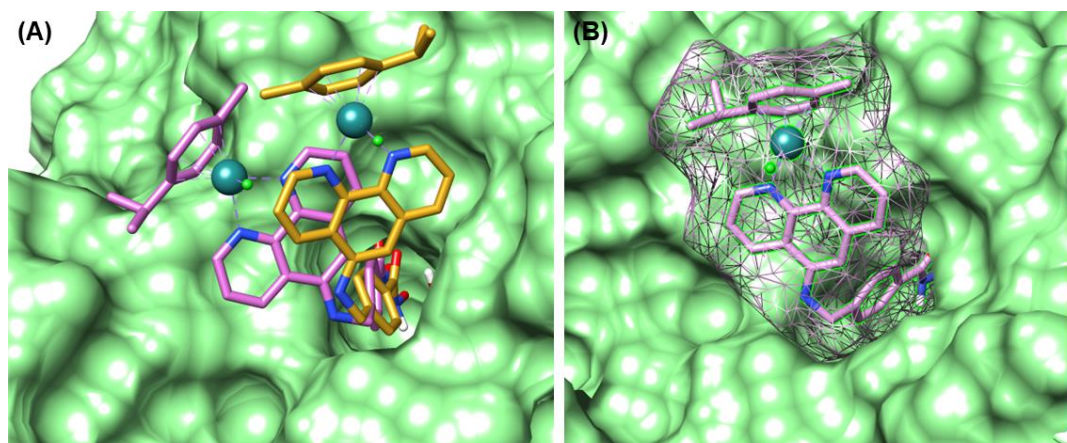


Figure 4.7 GOLD protein docking (PDB: 5WGK) of complex **Ru1L³** in zHDAC6-CD2. (A) Enzyme surface binding of docked **Ru1L³** in two rational binding modes; (B) Mesh view of preferred **Ru1L³** (purple) showing potential hydrophobic area of interactions.

The docking (*Figure 4.7B*) is shown to illustrate the area accommodated by the large piano-stool capping group into the wider HDAC6 channel rim. The surface likely provides hydrophobic interactions from residues Pro464 and Leu712 to the *p*-cymene arene in this docking solution. This surface-mesh visualisation sufficiently presents the additional space available beside complex **Ru1L³**, exploited by existing HDAC6-selective inhibitor tubastatin A fitting closer to the surface by π - π stacking of aromatic residues Phe680, His500, His611 and Phe620. It could be speculated that surrounding residues adjacent to the *p*-cymene arene of **Ru1L³**, such as Asp460 situated 5.5 Å from the arene isopropyl group could be accessible for interactions with the alternate amide linker or thiophene contained within the arene motif of complexes within the series.

Closer inspection of the favoured pose provided evidence of multiple interactions between the phenanthroline capping group and tolyl linker with the hydrophobic channel to the active-site. These residues include Phe583, Phe642, Phe643, Leu712, Gly582 and Tyr745. The specific arrangement of **Ru1L³** in the channel and its proximity to residues Phe583 and Phe643 suggests aromatic π - π stacking interactions are observed with the **L³** tolyl linker, sandwiched comfortably between the two residues. This interaction is a feature shared with the HBP ligand of the original protein-ligand crystallisation (*Figure 4.8C*). Another notable interaction is observed through the **L³** secondary amine which donates a hydrogen bond to Ser531 located at the channel edge (NH-O distance = 3.4 Å), constituting an energetically significant interaction.²⁰³

Binding in the catalytic site was first examined with the HPB ligand in mind, due to the shared phenylhydroxamate character of **Ru1L³**. HPB reveals a monodentate coordination with the zinc atom through its N-O⁻ group (Zn²⁺-O distance 1.9 Å) - a signature often observed by phenylhydroxamate HDAC6 inhibitors with bulky capping group substituents²⁰⁰ with a water molecule in the other vacant coordination site. This unusual binding motif was applied to **Ru1L³** (*Figure 4.8B*) which provided a bond through the N-O⁻ group to the zinc (Zn²⁺-O distance = 2.2

Å). The donation of a hydrogen bond from the water molecule to the hydroxamate C=O group was 2.7 Å. This coordination fulfils the trigonal bipyramidal geometry often observed at the zinc active-site.²⁰⁴ Nevertheless, analysis of the superimposed inhibitors in the enzyme active site (Figure 4.8C) showed that while the tolyl linker fits the channel in a comparable manner, the angle of binding to the zinc is distinct to each ligand with the hydroxamic acid inverted. The position of the hydroxamic acid based upon this docking solution for **Ru1L³** provides an alternative binding mode in the canonical bidentate form. Bonding of N-O⁻ and C=O coordinate the zinc at distances of 2.2 and 2.4 Å, respectively. Additional interactions are observed through the hydroxamate NH donating a hydrogen bond to the water (NH-O distance = 1.8 Å), along with an interaction between the hydroxamate NH with the Tyr745 residue in the active site (NH-O distance 2.4 Å). This binding mode offers the thermodynamically favoured chelation of the hydroxamic acid to the zinc ion in spite of the bulky metal-arene capping group.

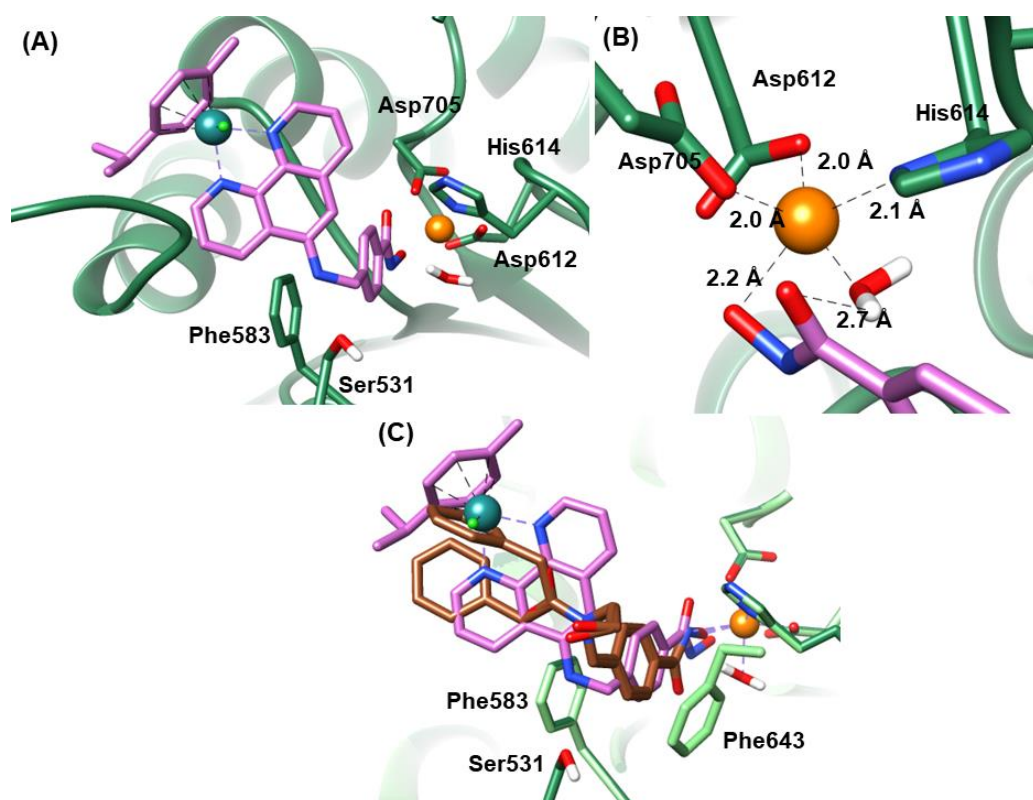


Figure 4.8 GOLD protein docking (PDB: 5WGK) of complex **Ru1L³** in zHDAC6-CD2. (A) Stick view of **Ru1L³** with amino acid residues labelled (zinc = orange); (B) Catalytic site showing bonding of amino acids to zinc (orange) and complex **Ru1L³** (purple), along with one water molecule; (C) **Ru1L³** superimposed onto HBP (tan) crystallised in zHDAC6-CD2. Hydrogens of inhibitors are omitted for clarity.

Even though the modelling described here offers an insight into the binding mode of **Ru1L³**, there were restrictions encountered through GOLD that should be taken into account. While the phenanthroline moiety is fixed as a planar aromatic structure and its accommodation into the active-site channel could be relatively accurate, GOLD did not allow the input parameter of assigning a coordination number to the zinc active site. This particular restriction forced the most

favourable spacial accommodation but perhaps not the most ideal coordination. By assigning a coordination number to the zinc, this could force accommodation of the capping group into a very different pose. In addition, the presence of the water molecule in the catalytic site is taken directly from the protein-ligand crystal structure with HPB. Due to the flipped conformation of the hydroxamic acid in **Ru1L³**, the water molecule may be forced into a different position within the catalytic site when the inhibitor is bound or may still act as a coordinating solvent.

Analysis of the modelled solutions of protein-ligand binding for complex **Ru1L³** gave an overall insight into the potential binding modes and interactions with the enzyme surface. The most rational solution presented a possible two binding modes that can be speculated between based on comparison with analogous inhibitors and the most chemically sound structure. Although models of such pseudo-octahedral complexes provide potentially contentious results due to restricted movement of the metal-arene capping group, one factor that remains cohesive is the tolyl linker enhancing specificity towards HDAC6. Through this model the specific π -stacking interactions were observed that promote the accommodation of a bulkier aromatic linker into the active-site channel. This is consistent with the HDAC assays undertaken in previous sections which showed promising selectivity of complexes containing **L³**. Further exploration into docking **L²** containing complexes would be valuable to compare and contrast the available interactions achieved by the flexibility of the aliphatic chain linker.

4.8 Conclusions

Fitting with the aims of the project, two complex series were designed and successfully synthesised based upon the parent complex **Ru1L²** and purified by preparative reverse-phase HPLC. Modifications were made to the arene capping group (**Ru4** and **Ru5**) and the chain linker of the bidentate ligand (**L³** from **L²**) to enhance selectivity between the zinc-dependent HDAC isoforms by improving drug-target interactions with the enzyme pocket and surface. Each series presented its own trends from the data collected.

Due to the limited availability of cell lines, the human breast cancer MCF7 cell line was tested in place of the lung carcinoma H460 seen in *Chapter 3*. The parent complex **Ru1L²** displayed a 13-fold increase in potency towards the MCF7 cells, implying a preferential toxicity profile towards this cell line over H460. For the complexes containing **L²**, 7 out of 10 were more toxic than the organic ligand alone ($IC_{50} = 2.99 \mu\text{M}$), with complex **Ru5AL²** demonstrating the highest potency at $1.24 \mu\text{M}$. The cytotoxicity for complexes **Ru4L²** (R = H) followed the order **Ru4BL²** \approx **Ru4CL²** $>$ **Ru4DL²** $>$ **Ru4AL²** (R¹ = tBu \approx Ph $>$ thiophene $>$ Me) implying within these complexes the increase in toxicity is intrinsically linked to lipophilicity of the arene. By contrast, this trend was much less pronounced for the **Ru5L²** series (R = Me), with complexes **Ru5AL²**,

Ru5CL² and **Ru5DL²** (R¹ = Me, Ph and thiophene) all exhibiting potency in a comparable range (IC₅₀ values 1.2 - 2.1 μM), however alike to the potency exhibited by the clinically approved drug SAHA (IC₅₀ = 1.42 μM). Complex **Ru5BL²** also displayed a low level of potency in the same order of magnitude (IC₅₀ = 5.2 μM) suggesting the presence of the *para*-Me substituent could have an influence on both stability and the overall lipophilic character. Moreover, the complexes containing **L³** consistently displayed lower cytotoxicity than **L³** alone (0.83 μM), with activity decreasing as the arene increases in size (**Ru1L³**>**Ru5AL³**>**Ru5BL³**>**Ru5CL³**).

Based upon the different toxicity profiles of the complex series containing either **L²** or **L³**, the cellular uptake pathways were investigated. Both complexes **Ru1L²** and **Ru1L³** showed no change in MCF7 cell viability, after incubation at 4 °C with the complexes at concentrations equipotent to their IC₅₀ values. This observation suggests the cellular uptake for these complexes and the pathway across the cell membrane is likely driven by active transport. Further analysis into Ru accumulation utilised ICP-MS to provide a quantitative measurement of complex entering the cells. For all complexes incorporating **L²**, cytotoxicity was higher for those complexes demonstrating higher levels of Ru accumulation. This evidence suggests that the cytotoxicity of the **L²** series is uptake-dependent. In spite of this apparent trend, the level of Ru accumulation relative to the IC₅₀ dose concentration were all fairly low (<20%). The degree of cytotoxicity in the **L³** series displayed the inverse relationship where by accumulation increased with increasing lipophilicity, while the most toxic complex remains **Ru1L³** with the smallest arene capping group (*p*-cymene). It is therefore assumed that the more lipophilic complexes in the **L³** series are likely participating in off-target binding and are unable to associate with their desired target.

Having established HDAC inhibition to be the most rational mechanism of action for complex **Ru1L²**, enzyme class selectivity was the successive area of attention in this chapter. All complexes were screened against HDAC1, HDAC4 and HDAC6 (Class I, IIa and IIb, respectively), to explore the potential interactions of the complexes with individual HDAC enzyme topology. Complexes containing **L³** exhibited moderate inhibition activity at 1 μM concentration towards HDAC4, while **L²** complexes displayed negligible inhibition against this isoform. Due to the similarly notable inhibitory profiles of the complexes against HDAC1 and HDAC6, specific complexes were chosen to provide more advanced inhibition data than two concentration points. Calculated IC₅₀ values showed complexes **Ru1L²**, **Ru5CL²**, **Ru1L³** and **Ru5CL³** all presented improved selectivity compared to their organic counterparts **L²** and **L³**. The parent complex **Ru1L²** displayed the highest degree of selectivity towards HDAC6 with a selectivity factor of 6.0, 3-fold more selective than the **L²** control. This particular observation implies the enhanced selectivity is likely due to the presence of the metal-arene capping group, which cannot be as well accommodated at the enzyme pocket rim of HDAC1. As anticipated, the complexes containing **L³** (**Ru1L³** and **Ru5CL³**) show a higher

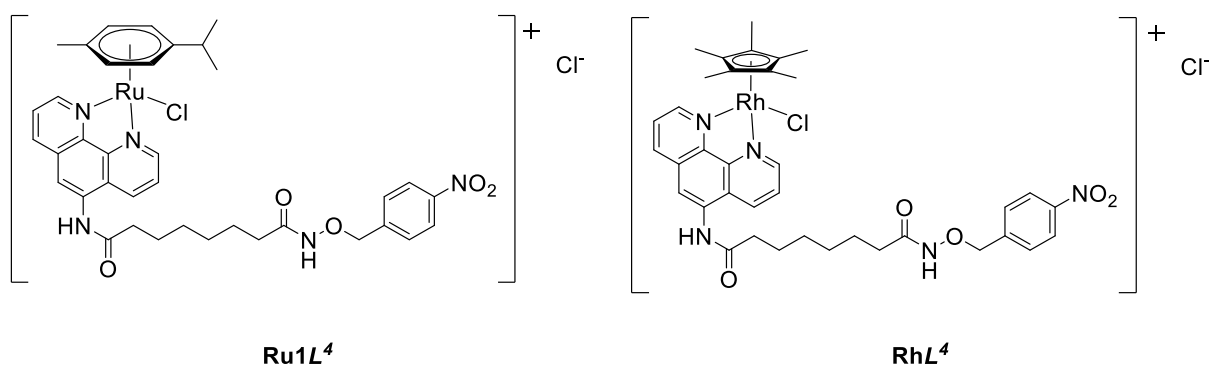
degree of selectivity than the ligand L^3 alone. Complex **Ru1** L^3 also displayed marked selectivity for the CD2 domain of HDAC6 compared to the SAHA control. In addition, enzyme modelling of complex **Ru1** L^3 in the homologous enzyme zHDAC6-CD2 provided a rational binding pose comprising chelation of the hydroxamic acid and π - π stacking interactions with Phe583 and Phe643 residues of the tolyl linker in the enzyme channel. The selectivity of the L^3 containing complexes can be partially justified by this specific interaction.

Taken together, the results in this chapter show that the introduction of metal complexes to known HDAC enzyme inhibitor motifs can produce a positive effect on both enzyme inhibition and cytotoxicity. Furthermore, changes to the metal coordination sphere can lead to modulation of the activity of the complex. While the observed differences in activity within the series presented herein were moderate, the principle of tuning activity through structural variation is clearly displayed. This bodes well for the future of metal complexes as enzyme inhibitors.

5. Hypoxia-Activated HDAC Inhibitors

5.1 Introduction

The importance of selectivity has already been established when designing a drug candidate, and has been exhibited by previously discussed examples such as those in *Chapter 4*. In addition to targeting a specific isoform within an enzyme family, the hypoxic conditions often associated with tumours can be exploited by prodrugs; activated in the reducing environment. Such drug design allows an inert species to produce toxicity within the targeted environment and can help alleviate unwanted toxicity towards healthy cells.



Two new complexes were synthesised (**Ru1L⁴** and **RhL⁴**) from the potent parent complexes **Ru1L²** and **RhL²**. The complexes were modified by incorporating the *p*-nitrobenzyl moiety as a protecting group for the hydroxamic acid using only two simple synthetic steps. The *p*-nitrobenzyl group had been previously described as a functionality, reducible under hypoxic conditions. NMR studies were employed in an attempt to observe the reduction products of the *p*-nitrobenzyl group alongside cytotoxicity under both normoxia and hypoxia conditions. The removal of the protecting group was predicted to undergo the transformation displayed in *Figure 5.1* to produce the active species.

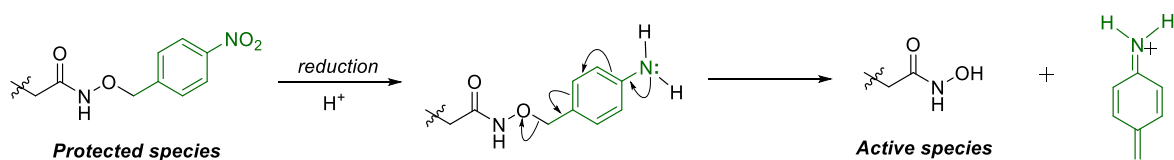
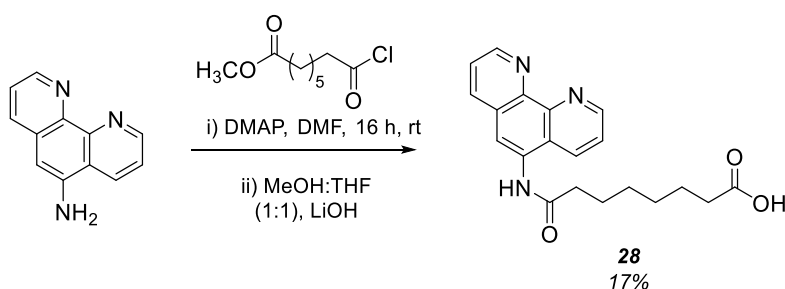


Figure 5.1 Proposed mechanism of *p*-nitrobenzyl group reduction.

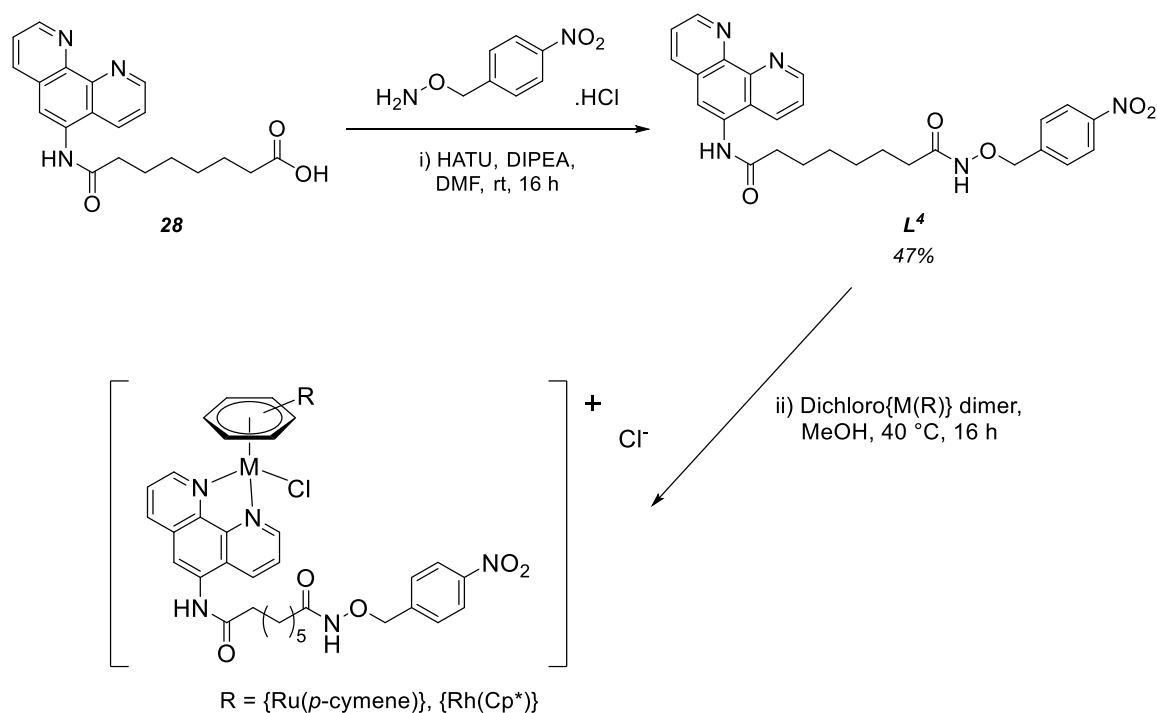
5.2 Synthetic Aspects

To synthesise the hypoxia-activated ligand, 1,10-phenanthrolin-5-amine and methyl 8-chloro-8-oxooctanoate were reacted in DMF using a catalytic quantity of DMAP (*Scheme 5.1i*). After 16 h the DMF was removed using vacuum distillation and the resulting red oil was suspended in MeOH:THF (1:1). Over the course of 3 days, 2.5 equivalents of aqueous LiOH were added (*Scheme 5.1ii*). After this time, complete ester hydrolysis was observed, confirmed by the presence of a broad singlet at 12.0 ppm in the $^1\text{H-NMR}$ spectrum, indicative of a carboxylic acid peak for compound **28**, along with the loss of the OMe peak at 3.90 ppm.



Scheme 5.1

The carboxylic acid derivative (**28**) was then coupled to commercially available *O*-(4-nitrobenzyl)hydroxylamine hydrochloride, using the coupling agent HATU^{184,185} (*Scheme 5.2i*). The reaction mixture was subsequently poured into saturated NaCl solution and the resulting precipitate filtered and washed with water to afford the protected ligand, **L⁴**. Complexation was undertaken by dissolving **L⁴** with 0.5 equivalents of selected commercially available dichloro{M(R)}dimers (*Scheme 5.2ii*) in MeOH, and heating at 40 °C for 16 h. The complexes were recrystallised from diethyl ether in relatively low yields (*Table 5.1*).



Scheme 5.2

Table 5.1 Yields and structural motifs of complexes containing L^4 .

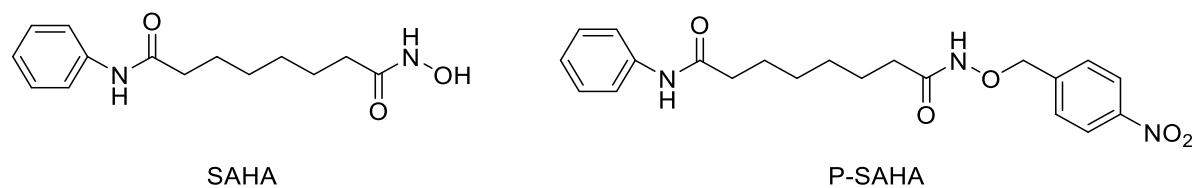
Complex	{M(R)}	Yield
Ru L^4	{Ru(<i>p</i> -cymene)}	34
Rh L^4	{Rh(Cp*)}	22

5.3 NMR Studies

To investigate the intrinsic properties of the redox-active *p*-nitrobenzyl protecting group within the compounds synthesised in this chapter, NMR studies were employed to monitor any structural changes, and help identify any reduction intermediates under conditions aimed to mimic regions of hypoxia. While the use of the redox-active *p*-nitrobenzyl protecting group was inspired from work conducted by Conway *et al.* detailed in Section 1.4,¹⁵⁸ it can be hypothesised that protection of the hydroxamic acid could provide different reduction products to the primary alcohol protection, previously described. It was therefore deemed important to investigate how effective this particular protecting group would be for the hydroxamic acid moiety.

In an attempt to discern the likely reduction products of the hydroxamic acid protected compounds, an NMR experiment was carried out. Owing to the low yields of the compounds synthesised in Section 5.2, the *p*-nitrobenzyl protected SAHA (P-SAHA)⁸ was used in this experiment. P-SAHA was assumed to reveal similar reduction products to the compounds synthesised in Section 5.2, due to structural similarities.

⁸ P-SAHA was synthesised by R. G. I. Thorpe.



To perform the reduction assay, P-SAHA (0.005 g, 0.013 mmol) was initially charged to a 5 mL vial and dissolved in deuterated DMSO (2 mL). To this solution, aqueous ammonium chloride (20 μ L, 10% wt/vol, D₂O) was added along with 0.5 μ L of dioxane as a ¹H-NMR reference. An aliquot was removed and subjected to ¹H-NMR to serve as T=0 (Figure 5.2). The reduction reaction was initiated by addition of zinc (0.002 g, 0.030 mmol) and monitored at intervals (Figure 5.2), with subsequent additions of zinc and heating. This method of reduction utilises single electron transfer from the zinc metal under slightly acidic conditions from the use of ammonium chloride solution, which has been shown to promote the formation of a hydroxylamine intermediate.^{205,206} NMR experiments were repeated and the principal results shown in Figure 5.2.

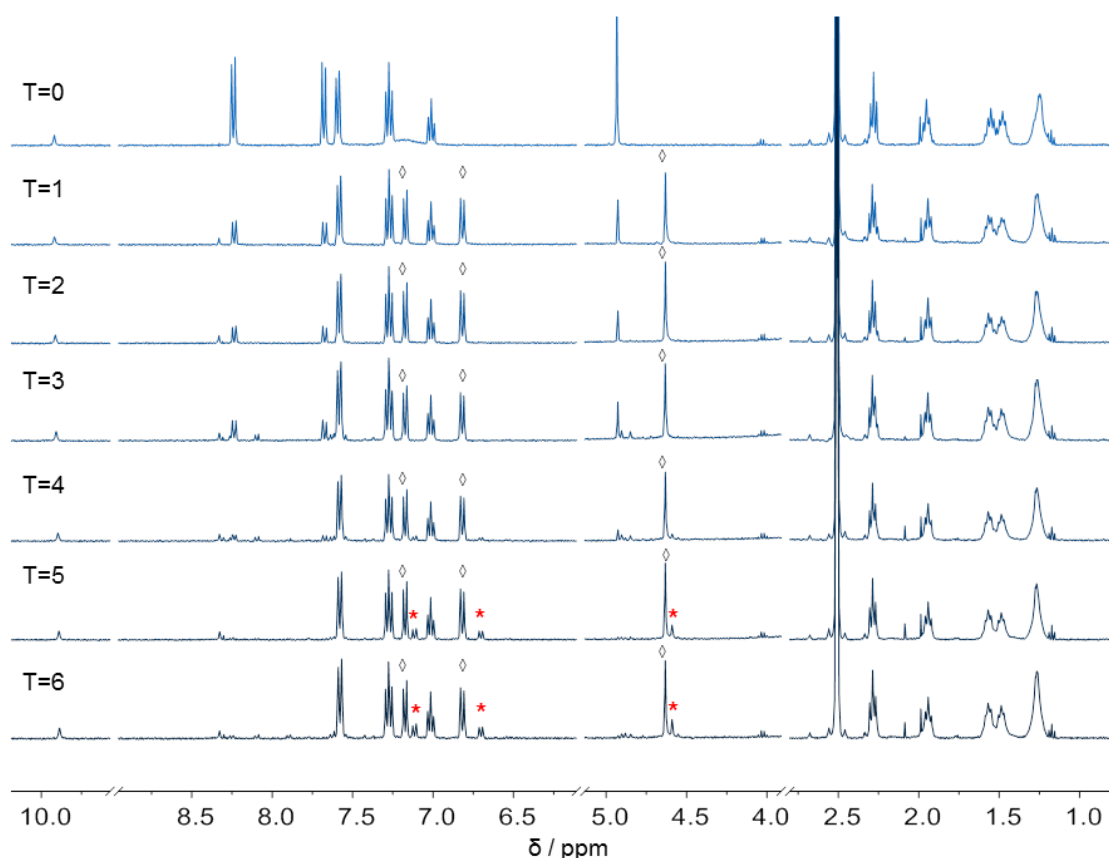


Figure 5.2 ¹H-NMR spectra (DMSO-d₆, 298 K, 400 MHz) of P-SAHA at increasing time intervals and varied conditions. T=0 (NH₄Cl, dioxane); T=1 (2 mg Zn, 10 min); T=2 (16 h); T=3 (40 °C, 2 h); T=4 (1 mg Zn, 10 min); T=5 (2 h); T=6 (16 h).

Upon addition of the zinc a new species was immediately observed (T=1, shown by \diamond). Reduction of the nitro group provided an upfield shift of the benzyl protecting group protons as denoted by \diamond and the CH₂ group (~4.6 ppm). This shift is anticipated given the loss of a highly electron withdrawing group such as a nitro-moiety. After 16 h, equilibrium was reached and the sample then subjected to heating at 40 °C for 2 h and the spectrum measured (T=3). No apparent change was observed. Addition of more zinc (T=4) showed the complete loss of the starting material *p*-nitrobenzyl protons and over time (T=5, T=6) the formation of another species with similar chemical shift ($*$) to the initial reduction product (\diamond) was observed.

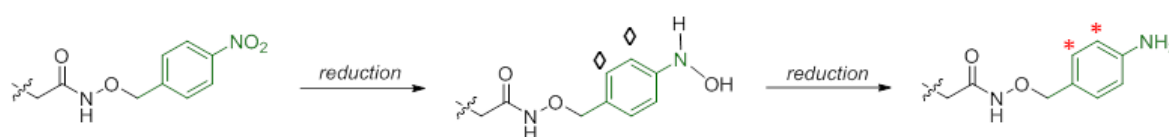


Figure 5.3 ¹H-NMR proposed reduction products.

This set of spectra clearly indicates the formation of two new species under these reaction conditions. Reduction of the nitro group increases the amount of water in the sample, reducing the ability to observe labile protons in the spectra such as the assumed products of this reaction. However, it could be rationalised that the 0.6 ppm upfield shift suggests the benzyl group has become more electron rich which could be accountable by the presence of either a hydroxylamine (\diamond) or an amine ($*$) functionality in place of the nitro group, illustrated in *Figure 5.3*. Conway used excess quantities of zinc to reduce the nitro group fully at ambient temperature over the course of 16 h. By comparison the NMR experiment undertaken here used just under 4 equivalents in two doses to form the reduction products, implying the reduction is dependent on the amount of zinc. Earlier ¹H-NMR experiments dosing zinc in similar excess to Conway, saw a significant increase in reaction temperature. This experiment observed the formation of a product with an *m/z* of 249.355 and a peak in the ¹H-NMR at 11.1 ppm. These collective observations suggested the formation of the carboxylic acid product rather than the desired hydroxamic acid. Excess zinc and the mildly acidic conditions could potentially promote acid catalysed hydrolysis to the carboxylic acid from the hydroxamic acid by protonation of the carbonyl oxygen and subsequent hydrolysis, likely aided by the internal increase in reaction temperature.

One notable observation of this experiment is the formation of precipitate in the reaction vessel and the subsequent decrease in total ¹H-NMR peak integrals of the new compound peaks (\diamond and $*$). At T=6 (*Figure 5.1*), a sample was removed for mass spectrometry analysis and run in MeOH where the precipitate dissolved. The mass spectrum revealed an *m/z* peak at 106.256 confirming the formation of the 4-methylidenecyclohexa-2,5-dien-1-iminium compound previously reported in *Figure 1.23* as the nitro-reduced fragment. This suggests that the precipitate is the fragmented

cation and would account for the loss of proton integration in the $^1\text{H-NMR}$ spectra as the reaction progresses. Regrettably, the full fragmentation experiment undertaken by Conway *et al.* utilising K_2HPO_4 (0.1 M) buffer and incubation at 37°C could not be replicated using $^1\text{H-NMR}$ spectroscopy. To ensure the compounds remained in solution a 1:1 mixture of K_2HPO_4 (D_2O) and the DMSO-d_6 solution containing the reduction products was made, unfortunately even on heating many of the reaction components precipitated out in this mixture and the fragmentation could not be monitored for P-SAHA using this method.

The NMR experiment described above successfully shows the reduction of the *p*-nitrobenzyl protecting group under mildly acidic conditions using zinc as a catalyst. While the fragmentation experiment could not be accomplished, the initial experiment provides evidence that fragmentation can occur for the hydroxamic acid without the need of a buffer. This could be due to the more favourable formation of the hydroxamic acid with the loss of 4-methylidencyclohexa-2,5-dien-1-iminium compared to that of the primary alcohol example. In the presence of excess zinc, some conversion into the carboxylic acid was observed. This is an undesirable reduction product due to the lack of potency documented for carboxylic acid derivatives as HDAC inhibitors;⁹² it is therefore necessary that the formation of the carboxylic acid is avoided to retain good potency *in vitro*.

5.4 Cytotoxicity

To suitably observe the potential hypoxia-activated behaviour of these complexes, cytotoxicity assays were to be undertaken under both normoxic and hypoxic conditions. It was assumed the protected compounds (SAHA, P-SAHA, $\text{Ru}1\text{L}^4$ and $\text{Rh}1\text{L}^4$) would display selective toxicity under only hypoxic conditions where the active species can form. This cytotoxicity data was unavailable at point of thesis submission.

Table 5.2 Impending results of hypoxia-active drugs and non-protected analogues under conditions of normoxia and hypoxia.

Compound	$\text{IC}_{50}[\mu\text{M}]$		Compound	$\text{IC}_{50}[\mu\text{M}]$	
	Normoxia	Hypoxia		Normoxia	Hypoxia
SAHA			$\text{Ru}1\text{L}^2$		
P-SAHA			$\text{Ru}1\text{L}^4$		
L^2			$\text{Rh}1\text{L}^2$		
L^4			$\text{Rh}1\text{L}^4$		

5.5 Conclusions

Complexes **Ru1L⁴** and **RhL⁴** were successfully synthesised based upon the potent parent complexes **Ru1L²** and **RhL²**. The new complexes possessed the known reducible functionality, *p*-nitrobenzyl; a novel method of protecting a hydroxamic acid. ¹H-NMR was chosen as a viable technique to assess the ability of the *p*-nitrobenzyl group to be reduced, fragment and ultimately provide the desired hydroxamic acid as the active species. By utilising commercially available materials, conditions were attained to mimic the enzyme reductase process observed *in vitro*. The organic analogue P-SAHA was tested using this method due to low yields of the final complexes. Analysis of the spectra from this experiment showed the reduction of the nitro group to the anticipated hydroxylamine and amine products, along with fragmentation discerned from the resulting precipitate. Due to the heat produced during the reaction, the hydroxylamine active-species was regrettably reduced to the carboxylic acid. While these conditions weren't entirely successful in providing the desired product, it displayed the clear reduction of the protecting *p*-nitro group and the required fragmentation.

The prospective cytotoxicity data could provide evidence of the successful reduction *in vitro* to the active hydroxamic species of complexes **Ru1L⁴** and **RhL⁴** under hypoxic conditions by comparing toxicity with the potent parent complexes under conditions of normoxia. Complexes **Ru1L⁴** and **RhL⁴** could provide the first examples of novel piano-stool hypoxic-active drug candidates.

6. Conclusions and Future Work

6.1 General Conclusions

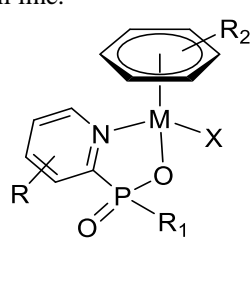
At the outset of the project, the overall aims were to produce piano-stool complexes bearing anticancer properties and to determine different mechanisms of action. Existing complexes within the literature containing the pseudo-octahedral geometry had demonstrated a range of mechanisms including, but not limited to: antimetastasis, DNA and protein-binding. However, there were ligand systems and target molecules yet to be explored for complexes containing the specific arene-metal motif. To assess the progress made over the past three years, it is necessary to recap the aims specified at the beginning of the project. The aims set out, were as follows:

- a) Design and synthesise DNA-binding piano-stool complexes:
 - i. Incorporating a ^{31}P spectroscopic handle
 - ii. Retaining aqueous stability
 - iii. Retention of the bidentate ligands under physiological conditions
- b) Target histone deacetylase inhibition with piano-stool complexes:
 - i. Synthesise potential HDAC inhibitors
 - ii. Test anticancer activity
 - iii. Determine mechanism of action
- c) Optimise selectivity towards specific HDAC isoforms:
 - i. Modify complexes to enhance topographical interactions
 - ii. Minimise off-target binding
- d) Incorporate a hypoxic-active motif into metal-based HDAC inhibitors:
 - i. Assess the efficiency of the protecting group
 - ii. Ensure reduction to active species

Consideration was initially given to the design and synthesis of DNA-binding complexes. The pyridylphosphinate ligand system was utilised due to its simple 2 or 3 step synthetic route from commercially available starting materials and its novelty compared to existing anticancer piano-stool complexes. Such a simple synthetic approach allowed the population of a small library of 25 complexes with a diverse range of substituents, along with incorporation of the desirable ^{31}P spectroscopic handle. Analysis of the complexes under various physiological conditions was monitored using NMR spectroscopy experiments. An essential criterion of these complexes to allow DNA-binding to occur is the exchange of the monodentate halide ligand at intracellular chloride concentration (4 mM), to form the more labile aqua-species. ^1H -NMR indicated the

preference of the aqua species in D₂O and the chloride species in extracellular chloride solution (100 mM concentration) as anticipated. Additionally, the aqua species must then be conserved to avoid formation of the less labile hydroxyl adduct, requiring the pK_a of the water bound ligand to be greater than physiological pH 7.4. The pyridylphosphinate complexes possessed pK_a values of in the range 7.7-10.9, implying the stability of the aqua-species, as desired.

Table 6.1 Selected pyridylphosphinate complexes: substituents. *IC₅₀ values against H460 non-small lung carcinoma cell line.



Complex	R	R ¹	{M(R ²)}	X	*IC ₅₀ [μM]
Ir2PP1	H	Ph	{Ir(Cp*)}	I	52 ± 2
Ir2PP2	H	Me	{Ir(CP*)}	I	53 ± 4

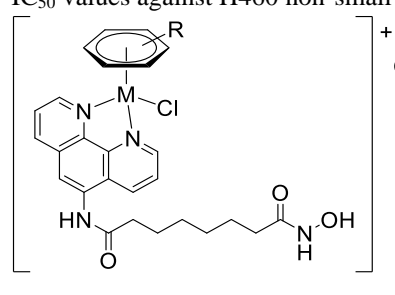
While these complexes displayed selective properties laid out in the project specification, the majority of the complexes possessed poor cytotoxicity against the H460 non-small lung carcinoma cell line tested, with IC₅₀ values >200 μM, unfortunately not meeting the end goal. The iridium iodide complexes **Ir2PP1** and **Ir2PP2** were exceptions displaying IC₅₀ values of 52 and 53 μM, respectively, although still ~65-fold less toxic than the control cisplatin (IC₅₀ = 0.80 μM). To rationalise the poor toxicity exhibited by the pyridylphosphinate complexes, their behaviour with other biomolecules was examined. Binding to 9-EtG was observed using mass spectrometry with the loss of the water ligand, suggesting the pyridylphosphinate complexes have the ability to bind to DNA as sought. However, similar experiments with amino acids such as L-histidine (2 equivalents) resulted in full substitution of the pyridylphosphinate ligand in favour of the amino acid. As a result, the pyridylphosphinate *N,O*-coordination was presumed to be a weak chelator relative to competing biomolecules and therefore unable to remain bound to the metal *in vitro*. This reduced structural integrity of the complexes was deemed the likely contribution to their poor cytotoxicity.

Despite the failure to achieve the DNA-binding therapeutic outcome, these complexes exhibited some unusual properties. For instance, each complex possessed a stereogenic centre at the metal and the phosphorus, giving rise to two diastereomers (specific to substituents) in both the solid and solution state. While this property was interesting, due to their poor toxicity, the pyridylphosphinate complexes were pursued no further. It is notable, that the partial lability of the Ru-pyridylphosphinate bond could have potential application in targeted delivery of drugs. A complex could be designed utilising the Ru-arene as a chaperone, delivering a masked active compound into a cell, before decomplexing in the presence of competitive chelators (e.g. histidine) to produce the free active drug. Such an avenue could be a potential future use of these complexes.

The project focus shifted instead to sourcing an alternative biomolecular target for anticancer therapy. Histone deacetylase enzymes (HDACs) were deemed a suitable target due to their key function within post-translational modification, which if dysregulated leads to formation of transformed cells and subsequent malignancies. Purely organic HDAC inhibitors were the prominent candidates in the literature, with only a few metal-based examples reported. No regard had previously been given to ruthenium piano-stool complexes, resulting in further reason to explore HDAC enzymes as a therapeutic target for these complexes.

The complexes **Ru1L²** and **RhL²** were successfully synthesised, incorporating the ligand **L²**, analogous to the clinically approved HDAC inhibitor, SAHA. A crucial design feature of these complexes was the inclusion of the hydroxamic acid – a strong chelator to the catalytic, zinc active site, inhibiting HDAC enzyme activity. In contrast to the pyridylphosphinate complexes, both complexes **Ru1L²** and **RhL²** showed negligible exchange of the monodentate chloride ligand under aqueous conditions, implying good aqueous stability. Additionally, these complexes exhibited moderate growth inhibition of the H460 non-small cell lung carcinoma cells (*Table 6.2*); a vast improvement over the initial pyridylphosphinate complexes.

Table 6.2 Piano-stool HDAC inhibitors containing **L²**: structure, HDAC activity against HeLa extract and *IC₅₀ values against H460 non-small cell lung carcinoma cell line.

	Complex	{M(R)}	IC ₅₀ [μM]	HDAC activity [%]	
				1 μM	0.1 μM
				Ru1L²	{Ru(<i>p</i> -cymene)}
RhL²	{Rh(Cp*)}	4.1 ± 0.4	1.1	15.4	

Subsequent experiments were undertaken to determine the likely mechanism of action of complexes **Ru1L²** and **RhL²**. It was established using plasmid DNA in gel electrophoresis experiments that these complexes neither underwent DNA-binding by covalent modification, nor through intercalation of DNA to a degree likely accountable for the activity exhibited. Bovine serum albumin (BSA) was utilised in a protein binding experiment to also eliminate protein interactions as a factor influencing cytotoxicity. While the binding isotherm suggested a 1:1 relationship between complex and the BSA substrate, the calculated binding constants implied only a low binding affinity for the protein. Finally, HDAC activity assays were performed using HeLa extract as a source of HDAC enzymes. Both complexes **Ru1L²** and **RhL²** displayed comparable, potent inhibition of HDAC activity at the lower concentration tested (0.1 μM, *Table 6.2*), irrespective of their somewhat different cytotoxicity. The biological assay results accumulatively suggest HDAC inhibition as the most likely mechanism of action. The complexes **Ru1L²** and **RhL²** were the first examples of Ru and Rh piano-stool HDAC inhibitors.

Having justified the mechanism of action matched the desired target, the focus shifted to optimisation of the efficacy and selectivity of the complexes. Within the HDAC family, there are 11 zinc-dependent enzymes each with specific localisation and substrates. Pan-inhibitors such as SAHA possess little selectivity between isoforms and can lead to unwanted side-effects. The parent complex **Ru1L²** was chosen for modification to enhance specificity and aim to reduce off-target binding.

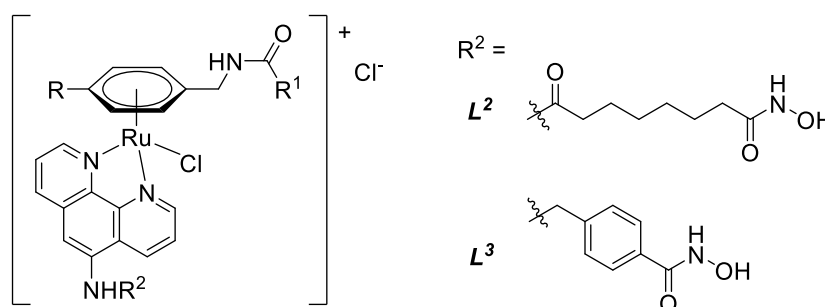


Figure 6.1 Ligand and general structure of complexes discussed in *Chapter 4*.

Two structural components of the parent complex **Ru1L²** were modified (*Figure 6.1*): the chain linker (**L²** and **L³**) to improve selectivity in the enzyme channel and the arene capping group (substituents R and R¹) to accommodate the channel rim to maximise potential interactions with the enzyme surface. Eight complexes containing **L²** and five containing **L³** were synthesised with various arene substituents (R = H, Me; R¹ = Me, tBu, Ph, thiophene) with all complexes subjected to a variety of biological testing. Cellular studies provided evidence of trends within the complex series depending on the ligand, **L**. Five of the eight new **L²** complexes showed improved toxicity over the organic ligand **L²** alone. Accumulation of Ru was proportional to IC₅₀ values within the **L²** series; the higher the uptake of Ru the more potent the complex. By contrast, the **L³** containing complexes exhibited the inverse relationship; the higher the Ru accumulation, the less potent the complex, with reduced potency relative to increase in size of the arene motif. Generally, it appears the **L³** ligand has a notable influence over complex uptake likely due to the more lipophilic tolyl moiety, yet the cytotoxicity was hindered by bulkier groups within the arene. However, across the **L²** complexes, such a trend in relation to the R¹ substituent is much less pronounced. Aside from the influence of complex modifications, the parent complex **Ru1L²** showed a 13-fold decrease in IC₅₀ value for MCF7 compared to the H460 cells, implying a favourable toxicity profile for this cell line. In support of these observations, the active transport assay testing **Ru1L²** and **Ru1L³** undertaken at 4 °C showed no change in cell viability, implying uptake is mediated by facilitated diffusion and is not determined by the bidentate ligand present in the complex.

Table 6.3 Selected results from Chapter 4. *IC₅₀ values and Ru accumulation were measured using the MCF7 human breast adenocarcinoma cell line.

Compound	R	R ¹	HDAC1 IC ₅₀ [μM]	HDAC6 IC ₅₀ [μM]	Selectivity factor	*IC ₅₀ [μM]	*Ru accumulation [%]
Tubastatin A	-	-	1.72 ± 0.1	0.04 ± 0.006	43	4.73 ± 0.5	-
L³	-	-	0.36 ± 0.03	0.15 ± 0.02	2.4	0.83 ± 0.4	-
Ru1L³	<i>p</i> -cymene		0.24 ± 0.03	0.06 ± 0.001	4.0	4.90 ± 1.0	24.1
Ru5CL³	Me	Ph	0.35 ± 0.05	0.08 ± 0.02	4.4	22.0 ± 3.4	48.6

Assessment of the selectivity between isoforms was tested using human recombinant enzymes of class I, IIa and IIb (HDAC1, 4 and 6, respectively). The initial assays measuring two concentrations (1 and 0.1 μM) showed comparable inhibition of HDAC1 and 6, with only complexes containing **L³** inhibiting activity of HDAC4. Due to the superior inhibition profiles exhibited towards HDAC1 and 6, these enzymes were chosen to demonstrate any significant selectivity between HDAC enzyme isoforms. Complexes **Ru1L³** and **Ru5CL³** (Table 6.3) all displayed inhibition activity in the nanomolar range towards both enzymes as well as selectivity towards HDAC6 as factors of 6.0, 4.0 and 4.4, respectively. While the selectivity factors (sf) are small by comparison to the HDAC6-selective control tubastatin A (sf = 43), these complexes displayed improved selectivity over both organic systems **L²** and **L³** (sf = 2.0 and 2.4, respectively). This particular result is encouraging, emphasising the ability of the metal-arene motif of these complexes to likely accommodate the wider channel rim of HDAC6 more efficiently.

Enzyme modelling of complex **Ru1L³** allowed closer inspection of potential interactions, specific to this complex while providing a three-dimensional platform to enable predictions of alternative complex binding possibilities. The accommodation of complex **Ru1L³** into the homologous zHDAC6-CD2 protein suggested favourable π-π stacking interactions between phenylalanine residues in the active-site channel, previously observed when the tolyl linker is present within other HDAC6-selective inhibitors. While this particular feature of the **Ru1L³** complex exposed a reasoning for selectivity towards HDAC6 of the **L³** containing complexes, it concurrently supports the rationale that the arene-metal motif of **Ru1L²** is the feature responsible for its improved selectivity towards HDAC6. This is deemed probable when considering the flexible alkyl chain linker of **Ru1L²** cannot produce such a comparable interaction in the catalytic channel as **Ru1L³**.

Collectively, these results suggest that the modified complexes display a selectivity not yet demonstrated by a piano-stool complex possessing HDAC enzyme inhibition as the mechanism of action. It is clear that the combination approach towards complex modification requires better understanding, in particular of specific off-target binding sites and the determination of the precise uptake pathway. With the current observations in hand, refinement of biological studies to further

distinguish the complex's localisation and behaviour within the cellular environment would be necessary to strengthen the use of these complexes as potential drug candidates.

6.2 Future Work

The most interesting findings of this work establish the ability of piano-stool complexes to be tuned towards selectivity between HDAC enzyme isoforms. While the selectivity factors are by no means exceptional, their novelty provides sufficient reason for continued development and warrants further exploration. Other examples of piano-stool complexes utilised as drug candidates are subjected to extensive scrutiny in the literature - far beyond that tested in this work - to elucidate a more informed account of the complex's behaviour. It would therefore be logical to undertake additional biological testing accordingly.

Due to the different toxicity profiles exhibited by complex **Ru1L²** towards the H460 and MCF7 cell lines, it would be applicable to test the cytotoxicity of the complexes against a broader range of cancer cell lines, including those resistant to cisplatin, in an attempt to observe any specificity. Additionally, healthy cells such as HBL-100 should be tested to determine whether these metal-based HDAC inhibitors show any cancer-cell selectivity. Uptake and localisation studies could be expanded upon to enlighten the different results between the **L²** and **L³** containing complexes. Transmission electron microscopy has been previously exploited by Dyson *et al.* to visualise the localisation of RAPTA complexes at a subcellular level.⁶¹ This technique, coupled with nanoscale secondary ion mass spectrometry (NanoSIMS), could discern if off-target localisation of **L³** complexes is a source of their poor cytotoxicity, relative to their good Ru uptake. As described by Sadler *et al.*, contrasting cellular uptake pathways could also be investigated. These assays include monitoring the extent of efflux and inhibition of efflux by co-administration of verapamil (an L-type calcium channel blocker enabling efflux evasion by the P-gp pathway – a pathway known to favour cationic and highly lipophilic drug molecules).⁶⁸ Pursuing such analysis would supply more information with regard to the complex's behaviour at a cellular level and highlight any influence of lipophilicity associated pathways.

As the molecular target, the HDAC enzyme activity could be further explored by following a variety of avenues. The extent of HDAC6 inhibition could be quantified using Western blotting to measure the acetylation levels of α -tubulin – the primary substrate for HDAC6 – in comparison to a control.¹⁴² The protein α -tubulin is linked to the regulation of the cytoskeleton, cell migration and plasticity; all features associated with aberrant HDAC activity and metastasis. Besides localisation, this could provide evidence of HDAC6 inhibition-generated cytotoxicity. Moreover, migration and invasion cellular assays could be undertaken to observe any antimetastasis effects brought about from HDAC6 inhibition. Specific HDAC enzyme interactions could be compared through

subsequent modelling of both HDAC1 and HDAC6 with complexes **Ru1L²** and **Ru1L³**, to enable a more succinct comparison of the potential binding modes. This could display particular interactions that give rise to the observed selectivity between the isoforms. As modelling is a binding prediction based on a set of parameters, enzyme-drug crystallisations could also be reattempted to afford a more accurate representation of interactions within the biological system.

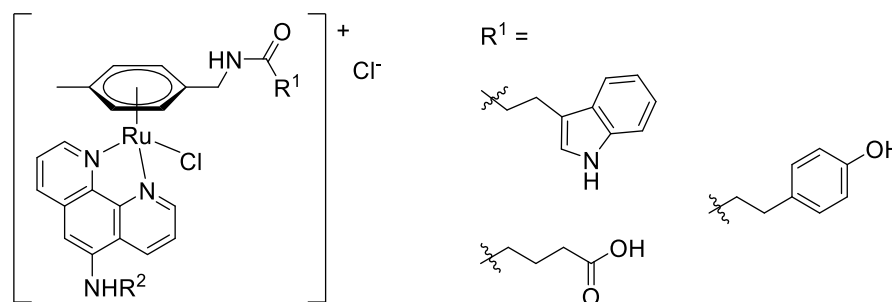


Figure 6.2 Alternative R¹ substituents.

Future development of the **L²** and **L³** containing complexes, beyond the investigation into their behaviour in biological systems, would be through structural modifications. Firstly, having now modelled a catalytic domain homologous to HDAC6, discrete surface amino acid residues can be visualised and arene design can be refined to improve interactions with the enzyme surface. The favoured pose of complex **Ru1L³**, docked in the HDAC6 homologue, displayed a selection of residues in close proximity to the arene motif for such interactions such as Asp460, not reached by the *p*-cymene of **Ru1L³**. To tune the arene, specific amino acid side chain groups such as those found in tyrosine, tryptophan or aspartate (*Figure 6.2*) could be incorporated using their commercially available carboxylic acid derivatives.

Without further biological testing and aside from assumptions based on lipophilicity, it remains unclear as to why the **L³** complexes are able to accumulate efficiently in the cell and yet display low levels of cytotoxicity. Both the differences in the size of the arene as well as the amide linker have been suggested as contributing to the complexes inability to reach the target or responsible for off-target binding. Given the amide linker shows no apparent residue interactions with the enzyme surface, this feature of the molecule could be changed. An alkene linker would reduce the number of hydrogen bond donors and acceptors within the arene motif and depending on its substituent, potentially enhance the lipophilicity in a desirable fashion. While the alkene would require more synthetic steps than the amide functionality, exchanging this moiety could prove advantageous. Finally, the HDAC assays discussed in *Chapter 4* displayed the ability of the **L³** containing complexes to partially inhibit HDAC4 activity. To improve selectivity towards the class IIa HDAC enzyme, the zinc-binding group could be modified to a trifluoromethylketone, a functional group already noted for possessing a penchant for the HDAC4 active site compared to the hydroxamic

acid.²⁰⁷ This small structural change could provide the first example of a class IIa selective metal-based HDAC inhibitor and would therefore be worth pursuing.

6.3 Final Remarks

The utilisation of metal complexes for therapeutics offers advantages over organic systems including (but not limited to): modular synthesis, variable geometry and oxidation state. Employing piano-stool complexes in particular as anticancer agents is far from an emerging research field. Existing complexes with this geometry are under development for a range of different biomolecular targets towards cancer treatment.

In this work, an improvement in enzyme isoform selectivity was observed by exploiting the pseudo-octahedral geometry of a complex to accommodate the enzyme surface more efficiently than their organic counterpart. While this result is promising, to compete with purely organic drugs, factors such as cellular accumulation, drug efflux, stability in physiological conditions and optimising target binding are of critical importance. For this reason, piano-stool complexes are yet to make any commercial impact as anticancer agents, unable to fulfil these criteria and retain such properties *in vivo*. However, the work described in the latter part of this report, has certainly laid the ground work for informed improvements towards establishing an effective piano-stool complex HDAC isoform-selective inhibitor; possessing the characteristics and efficacy of a potential future drug candidate.

7. Experimental

7.1 Experimental Procedures

7.1.1 General Procedures

Chemicals were purchased from Sigma Aldrich UK, Fluorochem, Merck and Fisher UK. Solvents were laboratory grade or dried by the Durham University SPS service. Dried solvents were stored over activated 3 Å molecular sieves. Reactions requiring anhydrous conditions were carried out under an atmosphere of dry argon or nitrogen using Schlenk-line techniques. Where appropriate, solvents were sparged with argon as a degas method.

Thin-layer chromatography was carried out on silica plates (Merck 5554) and visualised under UV (254/365 nm) irradiation or by staining with iodine, vanillin or potassium permanganate stains. Preparative column chromatography was carried out using silica (Merck Silica Gel 60, 230400 mesh), with additional Et₃N as stated.

pH measurements were carried out at 295 K using a Thermo Scientific Orion Star A111 pH meter with a Sigma-Aldrich micro-pH combination electrode. Calibration was performed using commercially available buffer solutions at pH = 4.0 ± 0.02, pH = 7.00 ± 0.02 and pH = 10.00 ± 0.02.

NMR spectra (¹H, ¹³C, ¹⁹F, ³¹P) were recorded on a Varian VXR-400 spectrometer (¹H at 399.97 Hz, ¹³C at 100.57 MHz, ¹⁹F at 76.50 MHz, ³¹P at 164.98 MHz) or a Varian VNMRS-700 spectrometer (¹H at 699.73 MHz, ¹³C at 175.95 MHz, ³¹P at 150.50 MHz). Spectra were recorded at 295 K in commercially available deuterated solvents and referenced internally to the residual solvent proton resonances. The multiplicity of each signal is indicated by s (singlet); d (doublet); t (triplet); q (quartet); quin (quintet) or sept (septet). The number of protons (n) for a given resonance signal is indicated by nH. Coupling constants (*J*) are quoted in Hz and are recorded to the nearest 0.1 Hz. Identical proton coupling constants (*J*) are averaged in each spectrum and reported to the nearest 0.1 Hz. The coupling constants are determined by analysis using MestReNova software. Spectra were assigned using COSY, HSQC, HMBC and NOESY experiments as necessary.

Both electrospray and high-resolution mass spectrometry were performed on a Thermo-Finnigan LTQ FT system using methanol as the carrier solvent. *m/z* values are reported in Daltons with specific isotopes identified.

7.1.2 X-Ray Studies

The X-ray single crystal data have been collected using $\lambda\text{MoK}\alpha$ radiation ($\lambda = 0.71073 \text{ \AA}$) on a Bruker D8Venture diffractometer (Photon100 CMOS detector, I μ S-microsource, focusing mirrors, 1° ω -scan) equipped with a Cryostream (Oxford Cryosystems) open-flow nitrogen cryostats at the temperature 120.0(2)K. The structures were solved by direct method and refined by full-matrix least squares on F2 for all data using SHELXTL [G.M. Sheldrick, Acta Cryst. (2008), A64, 112-122] and OLEX2 [O. V. Dolomanov, L. J. Bourhis, R. J. Gildea, J. A. K. Howard, H. Puschmann, J. Appl. Cryst. (2009), 42, 339- 341.] software. All non-hydrogen atoms were refined anisotropically, the hydrogen atoms were placed in the calculated positions and refined in riding mode. Crystallographic data for the structures have been deposited with the Cambridge Crystallographic Data Centre as supplementary publications CCDC 1457275 and 1457276.

Crystal data for **Ru1PP3**: $\text{C}_{22}\text{H}_{25}\text{ClNO}_2\text{PRu}$ ($M = 502.92$): monoclinic, space group $P2_1/c$, $a = 12.5685(6)$, $b = 8.1196(4)$, $c = 20.4312(10) \text{ \AA}$, $\beta = 91.535(2)^\circ$, $V = 2084.3(2) \text{ \AA}^3$, $Z = 4$, $T = 120.0(1) \text{ K}$, $\mu(\lambda\text{MoK}\alpha) = 0.975 \text{ mm}^{-1}$, $D_{\text{calc}} = 1.603 \text{ g mm}^{-3}$, 43150 reflections measured, 5811 unique reflections ($R_{\text{int}} = 0.0528$) were used in all calculations. The final R_1 was 0.0309 ($4673 > 2\sigma(I)$) and wR_2 was 0.0629 (all data), $\text{GOF} = 1.040$.

Crystal data for **Ir1PP6**: $\text{C}_{17}\text{H}_{24}\text{ClIrNO}_2\text{P} + \text{H}_2\text{O}$ ($M = 551.01$): monoclinic, space group Cc , $a = 14.7318(2)$, $b = 16.6565(2)$, $c = 8.3433(1) \text{ \AA}$, $\beta = 107.664(2)^\circ$, $V = 1950.75(4) \text{ \AA}^3$, $Z = 4$, $T = 120.0(1) \text{ K}$, $\mu(\lambda\text{MoK}\alpha) = 7.078 \text{ mm}^{-1}$, $D_{\text{calc}} = 1.876 \text{ g mm}^{-3}$, 20026 reflections measured, 5620 unique reflections ($R_{\text{int}} = 0.0416$) were used in all calculations. The final R_1 was 0.0202 ($5436 > 2\sigma(I)$) and wR_2 was 0.0497 (all data), $\text{GOF} = 1.076$, Flack parameter 0.033(5), Hoofit parameter 0.042(6).

7.1.3 HPLC Analysis

Reverse phase HPLC analysis was performed at 298 K on a Interchim PuriFlash 4250 system, Waters XBridge Prep-C18 $-19 \times 50 \text{ mm}$ ($5 \mu\text{m}$) column was used for complexes **Ru4AL**² to **Ru5DL**³ in Chapter 4, times varying from 2 –5 min. A solvent system of $\text{H}_2\text{O} / \text{MeOH}$ (gradient elution) was used. The UV/Vis and fluorescence detectors were set at appropriate wavelengths according to the species being analysed. Channel 1: UV600 SCAN – 225-600. Channel 2: UV600: SIG1 – 254 nm.

7.1.4 Optical Techniques

All samples for optical analyses were contained in quartz cuvettes with a path length of 1 cm and a polished base. Measurements were recorded at 295 K unless otherwise stated. UV/Vis absorbance spectra were measured on an ATI UNICAM UV4 UV/Vis spectrometer using Vision software. Samples were measured relative to a reference of pure solvent contained in a matched cell.

7.1.5 DNA Binding Experiments

Preparation of plasmid DNA substrates

Negatively supercoiled pSG483 (2927 bp), a pBlueScript SK+ (Agilent) derivative containing an Nb.BbvCI site, was prepared from *E. coli* XL-1 blue cells (Agilent) using a maxiprep kit (Qiagen). A portion of this sample was nicked with Nb.BbvCI (NEB) and an aliquot was removed to make a nicked pSG483 stock. The nicked form was then purified by phenol/chloroform extraction and ethanol precipitation prior to use.

DNA covalent modification assays

Supercoiled pSG483 plasmid DNA was mixed with 50 mM NaClO₄ to generate a master mix containing 500 ng of DNA per reaction and a final concentration of 10 mM NaClO₄. Two-fold dilutions of the test compounds were prepared using DMSO as solvent. 2 µl of a ten-fold concentrated test compound stock was added to 18 µl of reaction mix, then incubated for 24 hours at 37 °C. Following incubation, a 6x agarose gel loading dye (Fermentas) was added and samples were separated by electrophoresis in 1.4% (wt.vol⁻¹) TAE agarose gels (50 mM Tris-HCl, pH 7.9, 40 mM NaOAc, and 1 mM EDTA pH 8.0 running buffer), for 6–15 h at 2–2.5 V.cm⁻¹. To visualise the DNA, gels were poststained with 0.5 µg.ml⁻¹ ethidium bromide in TAE buffer for 30 min, destained in TAE buffer for a further 30 min, and exposed to UV illumination.

DNA intercalation assays

Reactions were constructed as for the above covalent modification assays, although the solvent for acridine orange was dH₂O. Following 30 min incubation at 37 °C, 2.5 µl of 10x ligase buffer and 1.5 µl of dH₂O was added together with 1 µl of T4 DNA ligase (Fermentas) or 1 µl of dH₂O for the no ligase control. These reactions were then quenched with 3 µl of stopping buffer [5% (wt.vol⁻¹) SDS and 125 mM EDTA], followed by adding 1 µl of 12 mg.ml⁻¹ proteinase K (Fermentas) and a further incubation at 37 °C for 30 min. Samples were stored on ice until immediately before gel loading, whereupon a 6x agarose gel loading dye was added and the

samples were warmed to 37 °C for 5 min. The reactions were separated by gel electrophoresis and visualised as above.

7.1.6 Cytotoxicity

7.1.6.1 MTT Assay – H460 Cell Line Procedure

Cytotoxicity of complexes in *Chapter 2* and *3*, cisplatin and SAHA against H460 non-small cell lung carcinoma cells was assessed using the MTT assay as follows: 500 cells were added to 96-flat bottomed well plates in RPMI media (containing 10% foetal bovine serum and 2mM L-Glutamine). After overnight incubation to allow for cell attachment, the medium was removed and replaced with fresh medium containing varying concentrations of the test compounds (0.01-200 µM), or solvent (dimethyl sulphoxide; DMSO) alone. The final concentration of DMSO in all cases did not exceed 0.1% and was not found to be cytotoxic. Chemosensitivity was assessed following a continuous 96 h exposure using a standard 3-[4, 5-dimethylthiazolyl]-2,5-diphenyltetrazolium bromide (MTT) assay. Using dose response curves, IC₅₀ values were determined (concentration required to inhibit cell growth by 50%, relative to control), representing data from at least three independent experiments.

7.1.6.2 Cell Viability Assay – MCF7 Cell Line Procedure

Cellular behaviour of complexes detailed in *Chapter 4*, SAHA, Tubastatin and ligands *L*² and *L*³ were conducted using Human chemotherapeutically resistant breast cancer cells (MCF7) cells using fluorescence and laser scanning confocal microscopy. Cells were maintained in exponential growth as monolayers in F-12/DMEM (Dulbecco's Modified Eagle Medium) 1:1 that was supplemented with 10% foetal bovine serum (FBS). Cells were grown in 75 cm² plastic culture flasks, with no prior surface treatment. Cultures were incubated at 37 °C, 20% average humidity and 5% (v/v) CO₂. Cells were harvested by treatment with 0.25% (v/v) trypsin solution for 5 min at 37 °C. Cell suspensions were pelleted by centrifugation at 1000 rpm for 3 min and were re-suspended by repeated aspiration with a sterile plastic pipette. Microscopy cells were seeded in 12-well plates on 13mm 0.17mm thick standard glass cover-slips or un-treated iBibi 100 uL live cell channels and allowed to grow to 40% – 60% confluence, at 37 °C in 5% CO₂. At this stage, the medium was replaced and cells were treated with compounds in varying concentrations (0.80 - 100 µM) and co-stains as appropriate.

Cell toxicity measurements were conducted using a ChemoMetec A/S NucleoCounter3000-Flexicyte instrument with Vial-cassette cell viability cartridge. The cellular stain Acridine Orange was used for cell detection and the nucleic acid stain DAPI was used to detect non-viable cells. The experiments were carried out in triplicate. Cell viability was corrected using a proliferation factor

(Equation 1) where: vib^I = corrected viability; n_x = number of cells after incubation; n_c = number of cells on loading; vib_x = measured viability.

$$vib^I = \left(\frac{n_x}{n_c}\right) vib_x \quad (1)$$

7.1.7 Cellular Uptake

In cellular uptake studies, cells were seeded in 6-well plates and allowed to grow to 80% – 100% confluence, at 37 °C in 5% CO₂. At this stage, the media was replaced with media containing complexes (**Ru1L²**, **RhL²**, **Ru4L²**, **Ru5L²**, **Ru1L³** and **Ru5L³**) and total cellular ruthenium was determined using inductively coupled plasma mass spectrometry (ICP-MS), by Dr. C. Ottley in the Department of Earth Sciences at Durham University.

Cells used for ICP-MS studies were prepared as follows. Cells were cultured in a 6- well plate to 90% confluence. Cells were then counted (10^7 cells based on a cell volume of $4000 \mu\text{m}^3$) and incubated with medium containing the complex and promoter/inhibitor before being washed three times with phosphate-buffered saline (PBS). The cells were then treated with trypsin and harvested and diluted to 1 mL with PBS. Concentrated nitric acid (Chem. Sci. 2018 Frawley, Linford, Starck, Pal, Parker) (0.6 mL) was added and the samples were digested for 24 h at 37 °C. These digested samples were submitted for ICP-MS measurements (Dr. Chris Ottley, Department of Earth Sciences, Durham University). The samples were run against a series of Ru standards, and the measured concentration was back calculated to find the total Ru concentration present in the original counted cells.

7.1.8 Enzyme Inhibition Assays

Enzo Life Sciences

HDAC enzyme inhibition assays were carried out for *Chapter 3* using a commercially available assay kit. HeLa nuclear extract, potential inhibitor (final concentration 1 μM or 100 nM) and assay buffer (50 mM Tris/Cl, pH 8.0, 137 mM NaCl, 2.7 mM KCl, 1 mM MgCl₂) were incubated in a 96 well plate at 37 °C for 15 min. Acetylated substrate (100 μM) was added and the mixture incubated at 37 °C for a further 20 min. Developer was added and the mixture incubated at 37 °C for a further 15 min. Fluorescence was measured using a Synergy H4 microplate reader ($\lambda_{\text{ex}} = 360 \text{ nm}$, $\lambda_{\text{em}} = 460 \text{ nm}$). Percentage HDAC activity is determined by quantification of fluorescence relative to control, with no added inhibitor.

BPS Bioscience

HDAC enzyme inhibition assays were carried out for *Chapter 4* using commercially available assay kits and undertaken in a 96 well plate. Human recombinant enzymes HDAC1 FLAG-tag His-tag, HDAC4 GST-tag His-tag and HDAC6 GST-tag were used. Potential inhibitors were dose in the concentration range from 10 to 0.004 μM from original DMSO stock (10 mM) and diluted using assay buffer (25 mM Tris/Cl, pH 8.0, 137 mM NaCl, 2.7 mM KCl, 1 mM MgCl_2). A master mixture was made using assay buffer, acetylated substrate specific to HDAC enzyme (200 μM) and BSA (1 mg/mL) in a ratio of buffer:substrate:BSA (6:1:1) and 40 μL added to each well plate. Buffer (10 μL) was added to all blank wells and buffer (5 μL) was added to all potential inhibitor wells. HDAC enzymes were diluted based on their stated activity and 5 μL was added to all wells except blanks and the plate incubated at 37 °C for 30 min. Developer was added and the mixture incubated at room temperature for a further 15 min. Fluorescence was measured using a Synergy H4 microplate reader ($\lambda_{\text{ex}} = 360 \text{ nm}$, $\lambda_{\text{em}} = 460 \text{ nm}$). Percentage HDAC activity is determined by quantification of fluorescence relative to control, with no added inhibitor.

7.1.9 HDAC Catalytic Domain vis Ligation Dependent Cloning

Protein Expression Trials:

For expression trials of the zHDAC6 catalytic domains, the expression constructs were produced through ligation independent cloning. The inserts encoding the individual catalytic domains (zCD1 – residues 60 – 489, zCD2 – residues 440-798) were produced by IDT. They were sub-cloned into modified pSAT1-LIC vector, producing a SENP-cleavable N-terminal His-SUMO tagged construct. This construct was transformed into *E. coli* ER2566 and BL21 (DE3) competent cells using heat shock treatment and selected using ampicillin.

Single colonies were grown in 2 x YT media (25 mL), in the presence of ampicillin (50 $\mu\text{g}/\text{mL}$). At O.D.₆₀₀ of 0.4-0.5, expression was induced with Isopropyl β -D-1-thiogalactopyranoside (IPTG, 1 mM), and ZnSO_4 (0.20 mM) was added to supplement the media. The cells were pelleted via centrifugation at 4,000 x g for 20 min and then resuspended in A500 (20 mM Tris HCl pH 7.9, 500 mM NaCl, 5 mM imidazole pH 8.0 and 10% glycerol). The cells were then lysed with sonication and the resulting lysate was clarified by centrifugation at 20,000 x g for 25 min. The supernatant was incubated with resin-NTA (150 μl , His60 Ni Superflow resin) for 2 hours at 4 °C. The resin was pelleted and then transferred to a spin column. This was washed with A500 before elution with B500 (20 mM Tris HCl pH 7.9, 500 mM NaCl, 250 mM imidazole pH 8.0 and 10% glycerol) was performed. SDS-PAGE gels were run to confirm the correct sized protein was expressed and protein concentrations were estimated using a Nanodrop.

Protein Expression and Purification:

The *E. coli* ER2566 transformed cells with pSAT1-LIC-CD1(or CD2) were used for large scale production of the catalytic domains. The bacteria were grown in 2 x YT media in the presence of ampicillin (50 µg/mL). Expression was induced using IPTG (1 mM) at O.D.₆₀₀ of 0.4; the media was supplemented with ZnSO₄ (0.20 mM) at the same time. The cell cultures were then grown overnight at 17.5 °C. Cells were recovered via centrifugation, followed by resuspension in A500. This cell suspension was then lysed by sonication and then centrifuged, to remove cell debris.

The supernatant was then loaded onto a Nickel column (HisTrap HP) in A500 and the target protein eluted directly onto an anion-exchange column (HiTrap Q column), using an A500 to B500 gradient on the FPLC. The protein was then eluted using an A500 to C1000 (20 mM Tris HCl pH 7.9, 1 M NaCl and 10 % glycerol) gradient. Fractions containing the catalytic domain were pooled and incubated overnight with sentrin protease at 4 °C. The untagged protein was then run through an ortho-Ni column (HisTrap HP). To further purify the protein, size-exclusion chromatography was performed (HiPrep 16/60 Sephacryl S-200 column), washed through with sizing buffer (50 mM Tris HCl pH 7.9, 500 mM KCl and 10% glycerol). If required, further size-exclusion chromatography was performed (HiPrep 16/60 Sephacryl S-300 column), using sizing buffer to finish purifying the protein.

The purest protein was concentrated to 8 mg/mL and dialysed overnight into crystallisation buffer (20 mM Tris HCl pH 7.9, 200 mM NaCl and 2.5 mM DTT). The rest was concentration to 1 mg/mL and stored at -80 °C in one-third storage buffer (50 mM Tris-HCl pH 7.9, 500 mM KCl and 70% glycerol) for biochemical assays.

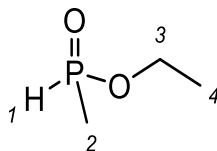
7.1.10 Molecular Modelling

DFT optimisation of complex **Ru1L³** was carried out using B3LYP hybrid functionals. For atoms H, C, N and O, the 6-31G* basis set was used, for Ru, the SDD basis set was required. Optimization calculations were carried out both in the gas phase and with a polarisable continuum model (PCM) of water. All optimised structures were validated to be their lowest energy structure through vibrational frequencies calculations. The NMR spectra were also calculated and compared to the experimental spectra. All calculations were carried out with Gaussian09.

Genetic Optimisation of Ligand Docking (GOLD) was used to perform molecular docking of complex **Ru1L³** to the zCD2 HDAC6 protein (PDB: 5WGK). The Hermes Visualiser was used to prepare the Ru Complex and protein before docking was undertaken, the ruthenium ion was treated as a dummy atom by GOLD. The region of interest was specified as within 10 Å of the zinc ion present in the binding site. The complex was subjected to 10 genetic algorithm runs, looking for

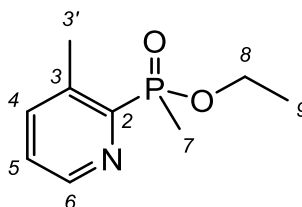
diverse solutions using the ChemScore fitness function. These were then analysed using the ChemScore components and the dockings evaluated using Chimera.

7.2 Synthetic Procedures



Ethyl methylphosphinate 1

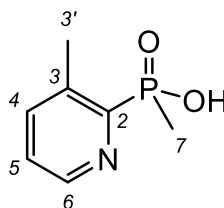
Diethyl methyl phosphonite (0.50 g, 3.67 mmol) was stirred at 0 °C and water added (0.064 mL, 3.67 mmol). The mixture was allowed to reach 22 °C (1 h) and then stirred for 16 h. The reaction mixture containing a 1:1 mixture of the *title compound* and ethanol was used without further purification (quantitative yield assumed). δ_{H} (CDCl₃) 7.20 (1H, d, $^1J_{\text{HP}}$ 537 Hz, H¹), 4.15 (1H, ddq, $^2J_{\text{HH}}$ -16.7 Hz $^3J_{\text{HP}}$ 9.5 Hz, $^3J_{\text{HH}}$ 7.1 Hz, H³), 4.06 (1H, ddq, $^2J_{\text{HH}}$ -16.7 Hz $^3J_{\text{HP}}$ 9.5 Hz, $^3J_{\text{HH}}$ 7.1 Hz, H^{3'}), 1.52 (3H, dd, $^2J_{\text{HP}}$ 14.0 Hz, $^3J_{\text{HH}}$ 4.0 Hz, H²), 1.35 (3H, t, $^3J_{\text{HH}}$ 7.1 Hz, H⁴); δ_{C} (CDCl₃) 62.3 (d, $^2J_{\text{CP}}$ 6.0 Hz, C³), 16.22 (d, $^3J_{\text{CP}}$ 6.0 Hz, C⁴), 15.09 (d, $^1J_{\text{CP}}$ 94.5 Hz, C²); δ_{P} (CDCl₃) 33.4; *m/z* (HRMS⁺) 109.0418 [M + H]⁺ (C₃H₁₀O₂P requires 109.0405).



Ethyl methyl(3-methylpyridin-2-yl)phosphinate 4

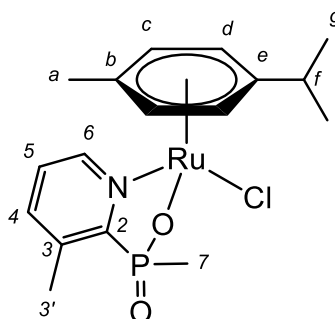
Ethyl methylphosphinate (0.48 g, 4.44 mmol), 2-bromo-3-methyl pyridine (0.050 mL, 4.44 mmol) and triethylamine (0.062 mL, 4.44 mmol) were dissolved in toluene (5 mL) and the mixture degassed. [1,1'-Bis(diphenylphosphino)ferrocene]dichloropalladium(II) (0.097 g, 0.13 mmol) was added and the mixture stirred at 120 °C for 16 h under an argon atmosphere. The solvent was removed under vacuum and the crude compound purified using column chromatography on silica (CH₂Cl₂ : 2% MeOH) providing the *title compound* as a dark red oil (0.280 g, 32%). δ_{H} (CDCl₃) 8.52 (1H, m, H⁶), 7.53 (1H, m, H⁵), 7.28 (1H, m, H⁴), 4.11 (1H, dq, $^2J_{\text{HH}}$ -16 Hz $^3J_{\text{HH}}$ 7.2 Hz, H⁸), 4.00 (1H, dq, $^2J_{\text{HH}}$ -16 Hz $^3J_{\text{HH}}$ 7.2 Hz, H⁸), 2.69 (3H, s, H³), 1.84 (3H, d, $^2J_{\text{HP}}$ 15 Hz, H⁷), 1.30 (3H, t, $^3J_{\text{HH}}$ 7.0 Hz, H⁹); δ_{C} (CDCl₃) 152.4 (d, $^1J_{\text{CP}}$ 161 Hz, C²), 146.7 (d, $^3J_{\text{CP}}$ 21 Hz, C⁶), 138.8 (d, $^4J_{\text{CP}}$ 9.5 Hz, C⁵), 138.5 (d, $^2J_{\text{CP}}$ 22 Hz, C³), 125.4 (d, $^3J_{\text{CP}}$ 2.6 Hz, C⁴), 60.7 (d, $^2J_{\text{CP}}$ 6.2 Hz, C⁸), 19.0

(s, C^{3'}), 16.4 (d, ³J_{CP} 6.3 Hz, C⁹), 14.0 (d, ¹J_{CP} 103 Hz, C⁷); δ_P (CDCl₃) 44.4; *m/z* (HRMS⁺) 200.0840 [M + H]⁺ (C₉H₁₅NO₂P requires 200.0842).



Methyl(3-methylpyridin-2-yl)phosphinic acid PP4

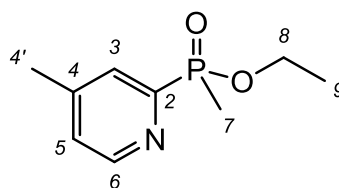
Ethyl methyl(3-methylpyridin-2-yl)phosphinate (0.28 g, 1.4 mmol) and 6M HCl (1.5 mL) were heated at 90 °C for 16 h. The solvent was removed under high vacuum and the brown oil was washed with dry methanol (2 x 2 mL) and dried under high vacuum. The mixture was used without further purification to give the *title compound* (assumed quantitative yield). δ_H (MeOD-d₄) 8.76 (1H, d, ³J_{HH} 5.6 Hz, H⁶), 8.57 (1H, dd, ³J_{HH} 7.1 Hz ⁴J_{HH} 3.1 Hz, H⁴), 8.12 (1H, t, ³J_{HH} 7.1 Hz, H⁵), 2.81 (3H, s, H^{3'}), 1.82 (3H, d, ²J_{HP} 16 Hz, H⁷); δ_C (MeOD-d₄) 148.9 (d, ³J_{CP} 7.1 Hz, C⁴), 147.3 (d, ¹J_{CP} 118 Hz, C²), 142.1 (d, ²J_{CP} 11.4 Hz, C³), 140.3 (d, ³J_{CP} 6.3 Hz, C⁶), 128.6 (d, ⁴J_{CP} 1.6 Hz, C⁵), 17.8 (d, ³J_{CP} 1.5 Hz, C^{3'}), 14.9 (d, ¹J_{CP} 106 Hz, C⁷); δ_P (MeOD-d₄) 26.1; *m/z* (HRMS⁺) 172.0527 [M + H]⁺ (C₇H₁₁NO₂P requires 172.0528).



Chloro(η⁶-p-cymene)(methyl(3-methylpyridin-2-yl)phosphate) ruthenium(II) Ru1PP4

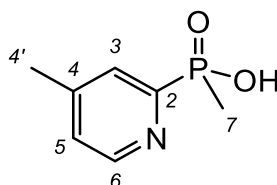
Methyl(3-methylpyridin-2-yl)phosphinic acid (0.10 g, 0.58 mmol) was dissolved in MeOH (2 mL) and the pH was raised to pH 8 with addition of sodium methoxide solution. A further 1 mL of methanol was added to the solution and dichloro(*p*-cymene) ruthenium(II) dimer (0.18 g, 0.29 mmol) suspended in the solution. The reaction mixture was stirred for 16 h under argon at room temperature. The solvent was then removed under vacuum and the dark red compound dissolved into dichloromethane (3 mL). The solution was filtered through a sintered funnel to remove excess salts. The solution was concentrated by removal of around CH₂Cl₂ (2 mL) under reduced pressure. The resultant solution was cooled in an acetone : dry ice bath and diethyl ether (4 mL) was added gradually. This gave the *title compound* as a yellow solid (0.14 g, 54%). δ_H

(MeOD-d₄) 9.14 (1H, d, ³J_{HH} 4.7 Hz, H⁶), 7.87 (1H, dd, ³J_{HH} 7.8 Hz ³J_{HH} 4.7 Hz, H⁵), 7.54 (1H, ddd, ³J_{HH} 7.8 Hz ⁴J_{HP} 5.4 Hz ⁴J_{HH} 1.6 Hz, H⁴), 5.74 (1H, d, ³J_{HH} 5.9 Hz, H^d), 5.68 (1H, d, ³J_{HH} 5.9 Hz, H^{d'}), 5.56 (1H, d, ³J_{HH} 5.9 Hz, H^c), 5.48 (1H, d, ³J_{HH} 5.9 Hz, H^{c'}), 2.86 (1H, septet, ³J_{HH} 6.9 Hz, H^f), 2.55 (3H, s, H³), 2.19 (3H, s, H^a), 1.43 (3H, d, ²J_{HP} 15.2 Hz, H⁷), 1.25 (3H, d, ³J_{HH} 6.9 Hz, H^g), 1.23 (3H, d, ³J_{HH} 6.9 Hz, H^{g'}); δ_{C} (MeOD-d₄) 156.1 (d, ¹J_{CP} 134 Hz, H²), 152.9 (d, ⁴J_{CP} 9.8 Hz, H⁶), 140.8 (d, ⁵J_{CP} 7.7 Hz, H⁵), 138.7 (d, ²J_{CP} 18.0 Hz, H³), 127.1 (d, ³J_{CP} 2.2 Hz, H⁴), 102.6 (C^e), 98.0 (C^b), 81.8 (C^d), 81.4 (C^{d'}), 80.8 (C^c), 80.3 (C^{c'}), 30.7 (C^f), 21.2 (C^g), 20.8 (C^{g'}), 18.2 (d, ¹J_{CP} 103 Hz, H⁷), 17.1 (C^a), 17.0 (C³); δ_{P} (MeOD-d₄) 48.3; *m/z* (HRMS⁺) 400.0543 [M - Cl]⁺ (C₁₇H₂₃NO₂P⁹⁶Ru requires 400.0542).



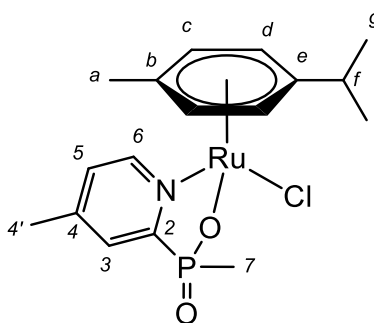
Ethyl methyl(4-methylpyridin-2-yl) phosphinate 6

Ethyl methylphosphinate (0.40 g, 3.7 mmol), 2-bromo-4-methyl pyridine (0.41 mL, 3.7 mmol) and triethylamine (0.51 mL, 3.7 mmol) were dissolved in toluene (5 mL); the resulting solution degassed (2 h). [1,1'-Bis(diphenylphosphino)ferrocene] dichloropalladium(II) (0.08 g, 0.11 mmol, 3% mol eq.) was added and the reaction then heated to 120 °C for 16 h. The solvent was removed under reduced pressure and the crude compound extracted into CH₂Cl₂ (20 mL) and washed with water (3 x 20 mL). The organic layer was dried with K₂CO₃, filtered and the solvent removed under vacuum. To purify the compound, column chromatography was utilised using silica (CH₂Cl₂ : 2% MeOH), providing a yellow oil of the *title compound* (0.38 g, 51%). δ_{H} (CDCl₃) 8.64 (1H, dd, ³J_{HH} 5.0 Hz, H⁶), 7.94 (1H, dd, ⁴J_{HH} 2.2 Hz, H³), 7.25 (1H, dd, ³J_{HH} 5.0 Hz ⁴J_{HH} 2.2 Hz, H⁵), 4.10 (1H, dq, ²J_{HH} -10 Hz ³J_{H-H} 8.0 Hz, H⁸), 3.86 (1H, dq, ²J_{HH} -10 Hz ³J_{HH} 8.0 Hz, H^{8'}), 2.44 (3H, s, H^{4'}), 1.78 (3H, d, ²J_{HP} 15 Hz, H⁷), 1.28 (3H, t, ³J_{HH} 8.0 Hz, H⁹); δ_{C} (CDCl₃) 154.0 (d, ¹J_{CP} 624 Hz, C²), 150.2 (d, ³J_{CP} 84 Hz, C⁶), 147.6 (d, ²J_{CP} 39 Hz, C³), 127.8 (d, ³J_{CP} 86 Hz, C⁴), 126.6 (d, ⁴J_{CP} 13 Hz, C⁵), 60.9 (d, ²J_{CP} 25 Hz, C⁸), 21.0 (d, ⁴J_{CP} 1.5 Hz, C^{4'}), 16.4 (d, ³J_{CP} 6.6 Hz, C⁹), 13.5 (d, ¹J_{CP} 106 Hz, C⁷); δ_{P} (CDCl₃) 40.2; *m/z* (HRMS⁺) 200.0835 [M + H]⁺ (C₉H₁₅NO₂P requires 200.0840).



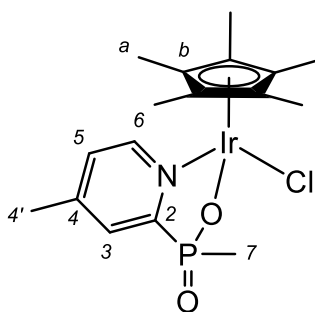
Methyl(4-methylpyridin-2-yl)phosphinic acid PP6

Ethyl methyl(4-methylpyridin-2-yl)phosphinate (0.38 g, 0.19 mmol) was suspended in 6M HCl (1.5 mL) and heated for 16 h at 90 °C. The solvent was removed under high vacuum and the brown oil washed with methanol (3 x 2 mL) and re dried under vacuum to provide the *title compound* as a pale brown solid (assumed quantitative yield). δ_{H} (MeOD- d_4) 8.81 (1H, dd, $^3J_{\text{HH}}$ 6.0 Hz, H^6), 8.33 (1H, d, $^4J_{\text{HH}}$ 3.0 Hz, H^3), 8.09 (1H, dd, $^3J_{\text{HH}}$ 6.0 Hz $^4J_{\text{HH}}$ 3.0 Hz, H^5), 2.77 (3H, s, H^f), 1.84 (3H, d $^2J_{\text{HP}}$ 16 Hz, H^7); δ_{C} (MeOD- d_4) 161.6 (d, $^3J_{\text{CP}}$ 32 Hz, C^6), 149.0 (d, $^1J_{\text{CP}}$ 494 Hz, C^2), 142.2 (d, $^3J_{\text{CP}}$ 29 Hz, C^4), 130.7 (d, $^2J_{\text{CP}}$ 46 Hz, C^3), 129.5 (d, $^4J_{\text{CP}}$ 4.0 Hz, C^5), 21.1 (s, C^f), 14.9 (d, $^1J_{\text{CP}}$ 423 Hz, C^7); δ_{P} (MeOD- d_4) 26.8; m/z (HRMS $^+$) 172.0514 [$\text{M} + \text{H}$] $^+$ ($\text{C}_7\text{H}_{11}\text{NO}_2\text{P}$ requires 172.0527).



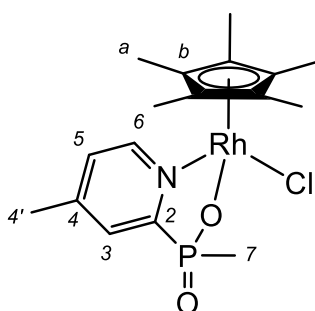
Chloro(η^6 -p-cymene)(methyl(4-methylpyridin-2-yl)phosphate) ruthenium(II) Ru1PP6

Methyl(4-methylpyridin-2-yl)phosphinic acid (0.13 g, 0.78 mmol) was dissolved in MeOH (2 mL) and the pH adjusted to pH 8 with addition of sodium methoxide solution. Dichloro(*p*-cymene) ruthenium(II) (0.24 g, 0.39 mmol) was added and the reaction mixture heated to 40 °C and stirred under argon for 16 h. The solvent was removed under vacuum to leave a dark orange residue which was dissolved into CH_2Cl_2 (3 mL). The precipitate was filtered under vacuum to remove excess salts. CH_2Cl_2 (2 mL) was then removed under vacuum and the concentrated solution cooled in an acetone : dry ice bath. Diethyl ether (4 mL) was added gradually to the cooled solution and a yellow precipitate formed. The precipitate was filtered using a sintered funnel to give the *title compound* as a yellow solid (0.16 g, 45%). δ_{H} (MeOD- d_4) 9.07 (1H, d, $^3J_{\text{HH}}$ 6.0 Hz, H^6), 7.59 (1H, d, $^4J_{\text{HH}}$ 4.0 Hz, H^3), 7.51(1H, d, $^3J_{\text{HH}}$ 6.0 Hz, $^4J_{\text{HH}}$ 4.0 Hz, H^5), 5.77 (1H, d, $^3J_{\text{HH}}$ 6.0 Hz, H^d), 5.70 (1H, d, $^3J_{\text{HH}}$ 6.0 Hz, H^d), 5.59 (1H, d, $^3J_{\text{HH}}$ 6.0 Hz, H^c), 5.50 (1H, d, $^3J_{\text{HH}}$ 6.0 Hz, H^c), 2.86 (septet, $^3J_{\text{HH}}$ 7.0 Hz, H^f), 2.49 (3H, s, H^f), 2.19 (3H, s, H^a), 1.40 (3H, d, $^2J_{\text{HP}}$ 15 Hz, H^7), 1.25 (3H, d, $^3J_{\text{HH}}$ 7.0 Hz, H^g), 1.24 (3H, d, $^3J_{\text{HH}}$ 7.0 Hz, H^g); δ_{C} (MeOD- d_4) 158.5 (d, $^1J_{\text{CP}}$ 136 Hz, C^2), 154.1 (d, $^3J_{\text{CP}}$ 10 Hz, C^6), 151.6 (d, $^3J_{\text{CP}}$ 8.5 Hz, C^4), 128.4 (d, $^4J_{\text{CP}}$ 2.0 Hz, C^5), 128.3 (d, $^2J_{\text{CP}}$ 19 Hz, C^3), 102.5 (C^e), 97.8 (C^b), 81.6 (C^d), 81.3 (C^d), 80.8 (C^c), 79.9 (C^c), 30.7 (C^f), 21.3 (C^g), 20.9 (C^g), 19.6 (C^d), 17.8 (d, $^1J_{\text{CP}}$ 102 Hz, C^7), 17.2 (C^a); δ_{P} (MeOD- d_4) 51.2; m/z (HRMS $^+$) 400.0541 [$\text{M} - \text{Cl}$] $^+$ ($\text{C}_{17}\text{H}_{23}\text{NO}_2\text{P}^{\text{96}}\text{Ru}$ requires 400.0542).



Chloro(η⁶-pentamethylcyclopentadienyl)(methyl(4-methylpyridin-2-yl)phosphate) iridium(III)
Ir1PP6

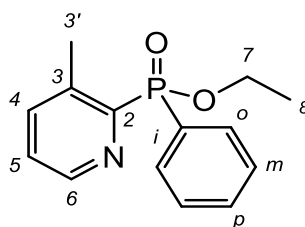
The crude **methyl(4-methylpyridin-2-yl)phosphinic acid** was neutralised using a solution of sodium methoxide (3 mL) to provide a solution of approximately pH 8. MeOH (2 mL) and dichloride(pentamethylcyclopentadienyl) iridium(III) dimer (0.069 g, 0.087 mmol) were added to the solution. The reaction mixture was stirred at 40 °C for 16 h under an argon atmosphere. The solvent was removed under vacuum to provide a dark orange oil which was then dissolved into CH₂Cl₂ (3 mL). The precipitate was filtered under vacuum to remove excess salts. The solvent was removed and the concentrated solution cooled in an acetone : dry ice bath. Diethyl ether (4 mL) was added gradually to the cooled solution to provide the *title compound* as a yellow oil (0.047 g, 38%). δ_{H} (MeOD-d₄) 8.61 (1H, d, ³J_{HH} 6.0 Hz, H⁶), 7.72 (1H, d, ⁴J_{HH} 3.5 Hz, H³), 7.50 (1H, d, ³J_{HH} 6.0 Hz, H⁵), 2.52 (3H, s, H^{4'}), 1.61 (15H, s, H^a), 1.58 (3H, d, ²J_{HP} 14 Hz, H⁷); δ_{C} (MeOD-d₄) 159.3 (d, ¹J_{CP} 135 Hz, C²), 151.8 (d, ³J_{CP} 8.5 Hz, C⁴), 151.6 (d, ²J_{CP} 9.5 Hz, C⁶), 129.0 (d, ⁴J_{CP} 2.0 Hz, C⁵), 127.9 (d, ³J_{CP} 19 Hz, C³), 85.5 (5C, s, C^b), 19.6 (d, ³J_{CP} 0.5 Hz, C^{4'}), 18.1 (d, ¹J_{CP} 104 Hz, C⁷), 7.5 (5C, s, C^a); δ_{P} (MeOD-d₄) 50.0; *m/z* (HRMS⁺) 496.1142 [M - Cl]⁺ (C₁₇H₂₄NO₂P¹⁹¹Ir requires 496.1151).



Chloro(η⁶-pentamethylcyclopentadienyl)(methyl(4-methylpyridin-2-yl)phosphate) rhodium(III)
RhPP6

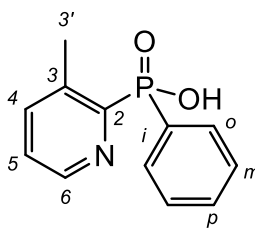
The crude **methyl(4-methylpyridin-2-yl)phosphinic acid** (0.039 g, 0.23 mmol) was neutralised using sodium methoxide solution (3 mL) to approximately pH 8, an additional aliquot of MeOH

(3 mL) was added along with dichloride(pentamethylcyclopentadienyl) rhodium(III) dimer (0.07 g, 0.11 mmol). The reaction mixture was stirred at 40 °C under an argon atmosphere for 16 h. The solvent was removed under vacuum to provide a dark orange oil. The crude compound was dissolved in CH₂Cl₂ (3 mL). The resulting precipitate was filtered under vacuum to remove excess salts. Most of the solvent was removed to leave a concentrated solution which was cooled in an acetone : dry ice bath. Diethyl ether (4 mL) was added gradually, this provided the *title compound* as an off-yellow solid (0.064 g, 63%). δ_{H} (MeOD-d₄) 8.67 (1H, d, ³J_{HH} 5.6 Hz, H⁶), 7.68 (1H, d, ⁴J_{HH} 3.5 Hz, H³), 7.58 (1H, d, ³J_{HH} 5.6 Hz H⁵), 2.52 (3H, s, H^{4'}), 1.69 (15H, s, H^a), 1.48 (3H, d, ²J_{HP} 15 Hz, H⁷); δ_{C} (MeOD-d₄) 160.2 (d, ¹J_{CP} 236 Hz, C²), 151.6 (d, ³J_{CP} 15 Hz, C⁴), 151.2 (d, ²J_{CP} 19 Hz, C⁶), 128.7 (d, ⁴J_{CP} 2.0 Hz, C⁵), 128.3 (d, ³J_{CP} 33 Hz, C³), 94.4 (5C, s, C^b), 19.6 (s, C^{4'}), 17.0 (d, ¹J_{CP} 179 Hz, C⁷), 7.6 (5C, s, C^a); δ_{P} (MeOD-d₄) 45.25; *m/z* (HRMS⁺) 408.0599 [M - Cl]⁺ (C₁₇H₂₄NO₂P¹⁰³Rh requires 408.0600).



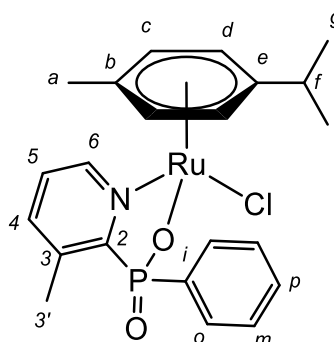
Ethyl phenyl(3-methylpyridin-2-yl) phosphinate 3

Ethyl phenylphosphonite (0.44 mL, 2.94 mmol), 2-bromo-3-methylpyridine (0.32 mL, 2.94 mmol) and triethylamine (0.41 mL, 2.94 mmol) were dissolved in toluene (5 mL) and the solution was degassed (2 h). [1,1'-Bis(diphenylphosphino)ferrocene]dichloropalladium(II) (0.064 g, 0.09 mmol, 3 mol % ratio) was added and the resulting solution was refluxed at 120 °C for 16 h. The solvent was removed and the crude product was purified using column chromatography (CH₂Cl₂ : 2% MeOH) to provide the *title compound* as a racemic yellow oil (0.62 g, 80%). δ_{H} (CDCl₃) 8.57 (1H, dd, ³J_{HH} 8.0 Hz ⁴J_{HH} 0.9 Hz, H⁶), 7.92 (2H, dq, ³J_{HH} 11 Hz ⁴J_{HH} 5.0 Hz, H^o), 7.57-7.52 (1H, m, H⁵), 7.57-7.52 (1H, m, H⁴), 7.47 (2H, tdd, ³J_{HH} 11 Hz ⁴J_{H-H} 5.0 Hz ⁵J_{HH} 1.3 Hz, H^m), 7.27 (1H, td, ³J_{HH} 11 Hz ⁴J_{HH} 5.0 Hz, H^p), 4.23 (2H, m, ²J_{HH} -12 Hz ³J_{HH} 9.0 Hz, H⁷), 2.67 (3H, s, H^{3'}), 1.41 (3H, t, ³J_{HH} 9.0 Hz H⁸); δ_{C} (CDCl₃) 152.4 (d, ¹J_{CP} 293 Hz, C²), 147.0 (d, ³J_{CP} 35.7 Hz, C⁶), 139.2 (d, ²J_{CP} 43.0 Hz, C³), 138.9 (d, ³J_{CP} 18.0 Hz, C⁴), 132.2 (C⁵), 132.1 (C^p), 131.2 (d, ¹J_{CP} 237.7 Hz, Cⁱ), 128.3 (2C, d, ²J_{CP} 22.8 Hz, C^o), 125.3 (2C, d, ³J_{CP} 6.0 Hz, C^m), 61.6 (d, ²J_{CP} 10.8 Hz, C⁷), 19.5 (C^{3'}), 16.5 (d, ³J_{CP} 10.7 Hz, C⁸); δ_{P} (CDCl₃) 28.9; *m/z* (HRMS⁺) 262.0998 [M + H]⁺ (C₁₄H₁₇NO₂P requires 262.0997).



Phenyl(3-methylpyridin-2-yl)phosphinic acid PP3

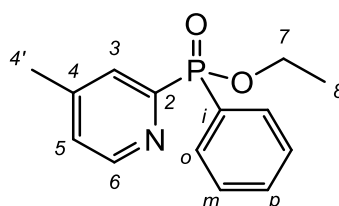
Ethyl phenyl(3-methylpyridin-2-yl) phosphinate (0.62 g, 2.36 mmol) was added to a solution of 6 M HCl (1.5 mL) and the solution heated to 90 °C for 16 h. The solvent was removed under high vacuum and washed with MeOH (2 x 2 mL) to yield the *title compound* as a brown oil (assumed quantitative yield). δ_{H} (MeOD- d_4) 8.83 (1H, d, $^3J_{\text{HH}}$ 5.2 Hz, H⁶), 8.47 (1H, dd, $^3J_{\text{HH}}$ 7.2 Hz $^4J_{\text{HH}}$ 2.6 Hz, H⁴), 8.11 (1H, dd, $^3J_{\text{HH}}$ 7.2 Hz $^3J_{\text{HH}}$ 5.2 Hz, H⁵), 7.86 (2H, ddd, $^3J_{\text{HH}}$ 7.4 Hz $^4J_{\text{HH}}$ 1.3 Hz $^5J_{\text{HH}}$ 0.7, H^o), 7.64 (1H, td, $^3J_{\text{HH}}$ 7.4 Hz $^4J_{\text{HH}}$ 1.3 Hz, H^p), 7.54 (2H, td, $^3J_{\text{HH}}$ 7.4 Hz $^4J_{\text{HH}}$ 1.3 Hz, H^m), 2.53 (3H, s, H^{3'}); δ_{C} (MeOD- d_4) 149.0 (d, $^3J_{\text{CP}}$ 7.4 Hz, C⁴), 147.5 (d, $^1J_{\text{CP}}$ 125 Hz, C²), 142.2 (d, $^2J_{\text{CP}}$ 12 Hz, C³), 140.3 (d, $^3J_{\text{CP}}$ 6.0 Hz, C⁶), 133.6 (d, $^2J_{\text{CP}}$ 11 Hz, C^p), 133.1 (d, $^3J_{\text{CP}}$ 2.9 Hz, C^o), 130.8 (d, $^1J_{\text{CP}}$ 147 Hz, Cⁱ), 128.8 (C⁵), 128.07 (C^m), 17.7 (d, $^3J_{\text{CP}}$ 1.6 Hz, C^{3'}); δ_{P} (MeOD- d_4) 12.6; m/z (HRMS⁺) 234.0688 [M + H]⁺ (C₁₂H₁₃NO₂P requires 234.0684).



Chloro(η^6 -*p*-cymene)(phenyl(3-methylpyridin-2-yl)phosphate) ruthenium(II) Ru1PP3

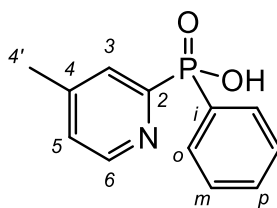
Phenyl(3-methylpyridin-2-yl)phosphinic acid (0.15 g, 0.64 mmol) was neutralised with sodium methoxide solution, transferred to a 50 mL round bottom flask and MeOH (5 mL) was added. Dichloro(*p*-cymene)ruthenium(II)dimer (0.20 g, 0.32 mmol, 0.5 eq.) was added and the reaction stirred at room temperature for 16 h under an inert atmosphere. The solvent was removed under vacuum to provide a dark orange residue which was then dissolved into CH₂Cl₂ (3 mL). The precipitate was filtered under vacuum to remove excess salts. The solution was reduced in volume and cooled in an acetone : dry ice bath. Diethyl ether (4 mL) was added gradually to the cooled solution. The resulting precipitate was filtered, washed with diethyl ether (5 mL) and dried to give the *title compound* as a yellow solid (0.17 g, 52%). δ_{H} (MeOD- d_4) 9.08 (1H, d, $^3J_{\text{HH}}$ 4.8 Hz, H⁶),

7.77 (2H, dd, $^3J_{\text{HH}}$ 7.4 Hz $^4J_{\text{HH}}$ 2.0 Hz, H^o), 7.70 (1H, dd, $^3J_{\text{HH}}$ 7.5 Hz $^3J_{\text{HH}}$ 4.8 Hz, H⁵), 7.53 (1H, ddd, $^3J_{\text{HH}}$ 7.5 Hz $^4J_{\text{PH}}$ 5.4 Hz $^4J_{\text{HH}}$ 1.5 Hz, H⁴), 7.46 (1H, tt, $^3J_{\text{HH}}$ 7.4 Hz $^4J_{\text{HH}}$ 2.0 Hz, H^p), 7.34 (2H, td, $^3J_{\text{HH}}$ 7.4 Hz $^4J_{\text{HH}}$ 2.0 Hz, H^m), 5.76 (1H, d, $^3J_{\text{HH}}$ 5.9 Hz, H^d), 5.72 (1H, d, $^3J_{\text{HH}}$ 5.9 Hz, H^{d'}), 5.60 (1H, d, $^3J_{\text{HH}}$ 5.9 Hz, H^c), 5.58 (1H, d, $^3J_{\text{HH}}$ 5.9 Hz, H^{c'}), 2.94 (1H, septet, $^3J_{\text{HH}}$ 6.9 Hz, H^f), 2.21 (3H, s, H^a), 2.04 (3H, s, H³), 1.30 (3H, d, $^3J_{\text{HH}}$ 6.9 Hz, H^g), 1.28 (3H, d, $^3J_{\text{HH}}$ 6.9 Hz, H^{g'}); δ_{C} (MeOD-d₄) 157.4 (d, $^1J_{\text{CP}}$ 143 Hz, C²), 152.9 (d, $^3J_{\text{CP}}$ 10 Hz, C⁶), 140.6 (d, $^3J_{\text{CP}}$ 7.7 Hz, C⁵), 138.5 (d, $^2J_{\text{CP}}$ 18.9 Hz, C³), 134.0 (d, $^1J_{\text{CP}}$ 143 Hz, Cⁱ), 132.8 (d, $^2J_{\text{CP}}$ 11 Hz, C^o), 131.6 (d, $^4J_{\text{CP}}$ 2.8 Hz, C^p), 127.6 (d, $^3J_{\text{CP}}$ 13 Hz, C^m), 127.2 (d, $^4J_{\text{CP}}$ 2.1 Hz, C⁴), 103.5 (C^e), 97.7 (C^b), 81.4 (C^d), 81.0 (C^c), 30.8 (C^f), 21.4 (C^g), 20.7 (C^{g'}), 17.2 (d, $^3J_{\text{CP}}$ 1.9 Hz, C^{3'}), 17.1 (C^a); δ_{P} (MeOD-d₄) 38.2; m/z (HRMS⁺) 462.0699 [M - Cl]⁺ (C₂₂H₂₅NO₂P⁹⁶Ru requires 462.0702).



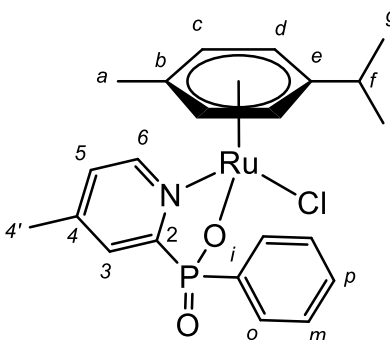
Ethyl phenyl(4-methylpyridin-2-yl) phosphinate 5

Ethyl phenylphosphinate (0.50 g, 2.94 mmol), 2-bromo-4-methylpyridine (0.32 mL, 2.94 mmol) and triethylamine (0.40 mL, 2.94 mmol) were dissolved in toluene (5 mL) and the solution degassed (2 h). [1,1'-Bis(diphenylphosphino)ferrocene]dichloropalladium(II) (0.10 g, 0.15 mmol, 3 mol %) was added and the resulting mixture refluxed for 16 h at 120 °C under argon. The solution was extracted into CH₂Cl₂ (30 mL), washed with 1 M HCl (2 x 50 mL), water (2 x 50 mL), dried over K₂CO₃, filtered and the solvent removed under pressure to give a dark brown oil. Purification was done using column chromatography on silica (CH₂Cl₂ : 0.5% MeOH) to give the *title compound* as a yellow oil (0.27 g, 34%). δ_{H} (CDCl₃) 8.60 (1H, d, $^3J_{\text{HH}}$ 7.0 Hz, H⁶), 7.98-7.95 (3H, m, H^o H³), 7.50 (1H, tq, $^3J_{\text{HH}}$ 7.5 Hz $^4J_{\text{HH}}$ 3.1 Hz, H^p), 7.43 (2H, tdd, $^3J_{\text{HH}}$ 7.5 Hz $^4J_{\text{HH}}$ 3.1 Hz $^5J_{\text{HH}}$ 1.4 Hz, H^m), 7.16 (1H, d, $^4J_{\text{HH}}$ 4.9 Hz, H⁵), 4.13 (1H, dqd, $^3J_{\text{HP}}$ 20 Hz $^2J_{\text{HH}}$ -12 Hz $^3J_{\text{HH}}$ 3.1 Hz, H⁷), 4.10 (1H, dqd, $^3J_{\text{HP}}$ 20 Hz $^2J_{\text{HH}}$ -12 Hz $^3J_{\text{HH}}$ 3.1, H^{7'}), 2.38 (3H, s, H^{4'}), 1.35 (3H, t, $^3J_{\text{HH}}$ 7.0 Hz, H⁸); δ_{C} (CDCl₃) 154.2 (d, $^1J_{\text{CP}}$ 166.1 Hz, C²), 150.3 (d, $^3J_{\text{CP}}$ 21.1 Hz, C⁶), 147.5 (d, $^3J_{\text{CP}}$ 10.4 Hz, C⁴), 132.3 (d, $^4J_{\text{CP}}$ 2.8 Hz, C^p), 132.2 (2C, d, $^2J_{\text{CP}}$ 9.7 Hz, C^o), 130.3 (d, $^1J_{\text{CP}}$ 137 Hz, Cⁱ), 129.2 (d, $^4J_{\text{CP}}$ 23 Hz, C³), 128.3 (2C, d, $^3J_{\text{CP}}$ 13 Hz, C^m), 126.4 (d, $^2J_{\text{CP}}$ 3.3 Hz C⁵), 61.6 (d, $^2J_{\text{CP}}$ 6.1 Hz, C⁷), 24.0 (d, $^4J_{\text{CP}}$ 6.1 Hz, C^{4'}), 16.5 (d, $^3J_{\text{CP}}$ 6.2 Hz, C⁸); δ_{P} (CDCl₃) 25.9; m/z (HRMS⁺) 262.1000 [M + H]⁺ (C₁₄H₁₇NO₂P requires 262.0997).



Phenyl(4-methylpyridin-2-yl)phosphinic acid PP5

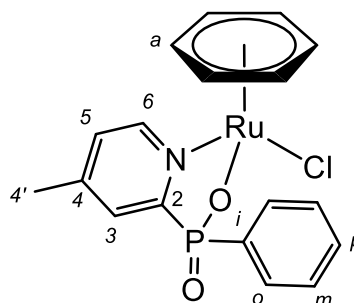
Ethyl phenyl(4-methylpyridin-2-yl) phosphinate (0.27 g, 1.1 mmol) was dissolved in a solution of 6M HCl (2.0 mL) and stirred at 90 °C under argon for 16 h. The acid was removed under high vacuum and washed with methanol (2 x 3 mL), also removed under vacuum. This yielded the *title compound* as a brown oil (assumed quantitative yield). δ_{H} (MeOD- d_4) 9.15 (1H, m, H⁶), 8.06 (1H, m, H⁵), 8.00 (2H, m, H^o), 7.68 (1H, m, H^p), 7.45 (1H, m, H³), 7.38 (2H, m, H^m), 2.58 (3H, s, H^{4'}); δ_{C} (MeOD- d_4) 159.3 (d, $^1J_{\text{CP}}$ 3.06 Hz, C²), 148.5 (C⁴), 142.8 (C⁶), 132.8 (C³), 132.3 (2C, C^o), 131.1 (C⁵), 129.7 (Cⁱ), 128.9 (2C, C^m), 128.8 (C^p), 22.5 (C^{4'}); δ_{P} (MeOD- d_4) 11.1; m/z (HRMS⁺) 234.0684 [M + H]⁺ (C₁₂H₁₃NO₂P requires 234.0682).



Chloro(η^6 -*p*-cymene)(phenyl(4-methylpyridin-2-yl)phosphate) ruthenium(II) Ru1PP5

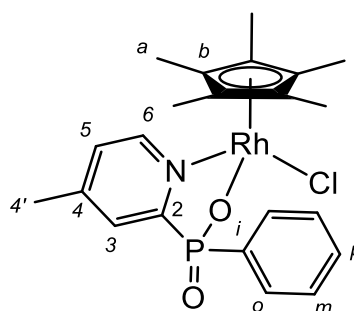
A solution of **phenyl(4-methylpyridin-2-yl)phosphinic acid** (0.080 g, 0.35 mmol) in MeOH (1 mL) was adjusted to pH 8 using sodium methoxide solution. Dichloro(*p*-cymene) ruthenium(II) dimer (0.11 g, 0.17 mmol) was added and the suspension was stirred for 16 h under argon at room temperature. MeOH was then removed under vacuum and the dark red residue was dissolved into CH₂Cl₂ (3 mL). The solution was filtered through a sintered funnel to remove salts. The volume of filtrate was then reduced and cooled in an acetone : dry ice bath. Diethyl ether (4 mL) was added gradually to the cooled solution and a yellow precipitate formed. The solution was filtered and the solid washed with diethyl ether (2 mL) and dried to give the *title compound* as a yellow solid (0.14 g, 86%). δ_{H} (MeOD- d_4) 8.98 (1H, d, $^3J_{\text{HH}}$ 5.8 Hz, H⁶), 7.84 (2H, ddd, $^3J_{\text{HP}}$ 14 Hz $^4J_{\text{HH}}$ 7.0 Hz $^5J_{\text{HH}}$ 1.3 Hz, H^o), 7.48 (1H, td, $^3J_{\text{HH}}$ 7.0 Hz $^4J_{\text{HH}}$ 1.3 Hz, H^p), 7.44 (1H, d, $^3J_{\text{HH}}$ 5.8 Hz, H⁵), 7.36 (2H, td, $^3J_{\text{HH}}$ 7.0 Hz $^4J_{\text{HP}}$ 3.4 Hz, H^m), 7.15 (1H, dd, $^4J_{\text{HP}}$ 7.0 Hz $^4J_{\text{HH}}$ 1.9 Hz, H³), 5.79 (1H, d, $^3J_{\text{HH}}$ 7.0 Hz, H^d), 5.73 (1H, d, $^3J_{\text{HH}}$ 7.0 Hz, H^{d'}), 5.64 (1H, d, $^3J_{\text{HH}}$ 7.0 Hz, H^c), 5.58 (1H, d, $^3J_{\text{HH}}$ 7.0 Hz, H^{c'}),

2.95 (1H, septet, $^3J_{\text{HH}}$ 6.8 Hz, H^f), 2.35 (3H, s, H^a), 2.24 (3H, s, H^{d'}), 1.29 (6H, d, $^3J_{\text{HH}}$ 6.8 Hz, H^g); δ_{C} (MeOD-d₄) 161.6 (d, $^1J_{\text{CP}}$ 125 Hz, C²), 154.1 (C⁶), 151.6 (C⁴), 132.8 (2C, d, $^2J_{\text{CP}}$ 10 Hz, C^o), 128.5 (C^p), 128.2 (d, $^1J_{\text{CP}}$ 140 Hz, Cⁱ), 128.1 (C³), 127.8 (C⁵), 127.7 (d, $^3J_{\text{CP}}$ 14 Hz, C^m), 103.4 (C^e), 97.7 (C^b), 81.26 (C^d), 80.9 (C^{d'}), 80.8 (C^c), 80.7 (C^{c'}), 30.8 (C^f), 19.38 (C^{4'}), 17.2 (C^a), 21.4 (C^g), 20.8 (C^{g'}); δ_{P} (MeOD-d₄) 39.0; m/z (HRMS⁺) 498.0479 [M - Cl]⁺ (C₂₂H₂₆NO₂P⁹⁶Ru requires 498.0466).



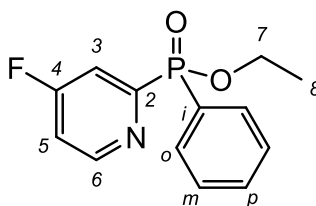
Chloro(η⁶-benzene)(phenyl(4-methylpyridin-2-yl)phosphate) ruthenium(II) Ru3PP5

A solution of **phenyl(4-methylpyridin-2-yl)phosphinic acid** (0.04 g, 0.17 mmol) in MeOH (4 mL) was adjusted to pH 8 using sodium methoxide solution. Dichloro(benzene) ruthenium(II) dimer (0.04 g, 0.09 mmol) was added and the resulting mixture heated to 40 °C and stirred for 16 h under argon. The same precipitation method was used as previously stated with complexes **Ru1PP4-Ru1PP5**) and the purified compound washed with diethyl ether (5 mL) to give the *title compound* as a dark yellow oil (0.05 g, 7%). δ_{H} (MeOD-d₄) 9.08 (1H, d, $^3J_{\text{HH}}$ 5.8 Hz, H⁶), 7.82 (2H, ddd, $^3J_{\text{HP}}$ 13 Hz $^3J_{\text{HH}}$ 7.4 Hz $^4J_{\text{HH}}$ 2.5 Hz, H^o), 7.49 (1H, dt, $^3J_{\text{HH}}$ 7.4 Hz $^4J_{\text{HP}}$ 2.5 Hz, H^p), 7.43 (1H, d, $^3J_{\text{HH}}$ 5.8 Hz, H⁵), 7.37 (2H, td, $^3J_{\text{HH}}$ 7.4 Hz $^4J_{\text{HH}}$ 2.5 Hz, H^m), 7.14 (1H, dd, $^3J_{\text{HP}}$ 6.6 Hz $^4J_{\text{HH}}$ 1.7 Hz, H⁵), 5.93 (6H, s, H^a), 2.34 (3H, s, H^{d'}); δ_{C} (MeOD-d₄) 159.1 (d, $^1J_{\text{CP}}$ 143.5 Hz, C²), 154.4 (d, $^3J_{\text{CP}}$ 10 Hz, C⁶), 151.4 (d, $^3J_{\text{CP}}$ 8.7 Hz, C⁴), 132.7 (2C, d, $^2J_{\text{CP}}$ 10 Hz, C^o), 132.6 (d, $^1J_{\text{CP}}$ 144 Hz, Cⁱ), 132.0 (d, $^4J_{\text{CP}}$ 2.7 Hz, C^p) 128.3 (d, $^2J_{\text{CP}}$ 20 Hz, C³), 128.2 (d, $^4J_{\text{CP}}$ 2.2 Hz, C⁵), 127.9 (2C, d, $^3J_{\text{CP}}$ 13 Hz, C^m), 83.3 (C^a), 19.4 (d, $^4J_{\text{CP}}$ 0.7 Hz, C^{4'}); δ_{P} (MeOD-d₄) 39.73; m/z (HRMS⁺) 441.9858 [M - Cl]⁺ (C₁₈H₁₈NO₂P⁹⁶Ru requires 441.9840).



**Chloro(η^6 -pentamethylcyclopentadienyl)(phenyl(4-methylpyridin-2-yl)phosphate) rhodium(III)
RhPP5**

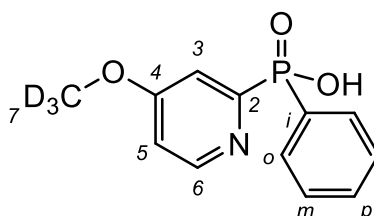
Phenyl(4-methylpyridin-2-yl)phosphinic acid (0.042 g, 0.18 mmol) was dissolved in MeOH (10 mL) and dichloro(pentamethylcyclopentadienyl) rhodium(III) dimer (0.055 g, 0.09 mmol) added and the resulting solution was heated to 40 °C under argon for 16 h. The solvent was removed under vacuum to leave a dark orange residue which was dissolved into CH₂Cl₂ (3 mL). Undissolved salts were removed by filtration. The concentrated solution was cooled in an acetone : dry ice bath. Diethyl ether (4 mL) was added gradually to the cooled solution and a yellow precipitate formed. The solid was filtered and washed with diethyl ether (5 mL) to provide the *title compound* as a brown oil (0.030 g, 33%). δ_{H} (MeOD-d₄) 8.64 (1H, d, $^3J_{\text{HH}}$ 6.0 Hz, H⁶), 7.85 (2H, ddd, $^3J_{\text{HP}}$ 12.0 Hz $^3J_{\text{HH}}$ 7.0 Hz $^4J_{\text{HH}}$ 1.6 Hz, H^o), 7.49-7.46 (2H, m, H^s H^p), 7.38 (2H, td, $^3J_{\text{HH}}$ 7.0 Hz $^4J_{\text{HP}}$ 1.6 Hz, H^m), 7.16 (1H, d, $^3J_{\text{HH}}$ 6.0 Hz, H³), 2.31 (3H, s, H^t), 1.71 (15H, s, H^a); δ_{C} (MeOD-d₄) 161.0 (d, $^1J_{\text{CP}}$ 143 Hz, C²), 151.2 (d, $^3J_{\text{CP}}$ 11 Hz, C⁶), 151.1 (d, $^3J_{\text{CP}}$ 9.0 Hz, C⁴), 134.3 (d, $^1J_{\text{CP}}$ 142 Hz, Cⁱ), 132.5 (2C, d, $^2J_{\text{CP}}$ 10 Hz, C^o), 131.6 (d, $^2J_{\text{CP}}$ 2.7 Hz, C³), 128.8 (d, $^4J_{\text{CP}}$ 19 Hz, C⁵), 128.4 (d, $^4J_{\text{CP}}$ 2.0 Hz, C^p), 127.8 (2C, d, $^3J_{\text{CP}}$ 13 Hz, C^m), 94.5 (d, $^3J_{\text{CP}}$ 9.0 Hz, C^b), 19.5 (d, $^4J_{\text{CP}}$ 0.7 Hz, C^{4'}), 7.68 (5C, C^a); δ_{P} (MeOD-d₄) 34.5 *m/z* (HRMS⁺) 470.0754 [M - Cl]⁺ (C₂₂H₂₆NO₂P¹⁰³Rh requires 470.0756).



Phenyl(4-fluoropyridin-2-yl) phosphinate 7

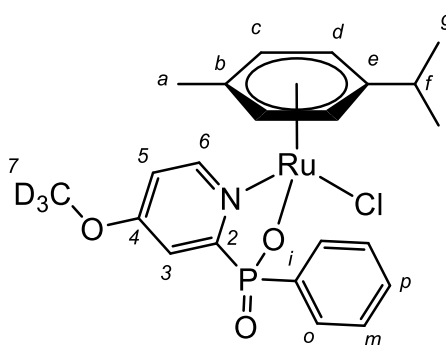
Ethyl phenylphosphonite (0.41 mL, 2.74 mmol), 2-bromo-4-fluoropyridine (0.48 g, 2.74 mmol) and triethylamine (0.38 mL, 2.74 mmol) were dissolved in toluene (10 mL) and the solution was degassed (2 h). [1,1'-Bis(diphenylphosphino)ferrocene]dichloropalladium(II) (0.06 g, 0.082 mmol, 3 mol %) was added and the solution heated to 120 °C for 16 h. The solvent was removed under vacuum and the residue dissolved into CH₂Cl₂ (30 mL). The solution was washed with 0.1 M HCl (30 mL) and water (2 x 30 mL), the organic layer then dried using K₂CO₃, filtered and solvent removed under pressure. The crude residue was purified using column chromatography on silica (CH₂Cl₂ : 1.8% MeOH) to provide the *title compound* as a pale yellow oil (0.13 g, 17%). δ_{H} (CDCl₃) 8.73 (1H, dd, $^4J_{\text{HF}}$ 7.6 Hz $^3J_{\text{HH}}$ 6.7 Hz, H⁶), 7.97 (2H, dt, $^3J_{\text{HP}}$ 12.0 Hz $^3J_{\text{HH}}$ 8.0 Hz, H^o), 7.87 (1H, dd, $^3J_{\text{HF}}$ 8.2 Hz $^4J_{\text{HH}}$ 2.3 Hz, H³), 7.54 (1H, tt, $^3J_{\text{HH}}$ 8.0 Hz $^4J_{\text{HH}}$ 2.0 Hz, H^p), 7.47 (2H, td, $^3J_{\text{HH}}$ 8.0 Hz $^4J_{\text{HP}}$ 2.0 Hz, H^m), 7.09 (1H, ddd, $^3J_{\text{HF}}$ 8.2 Hz $^3J_{\text{HH}}$ 6.7 Hz $^4J_{\text{HH}}$ 2.3 Hz, H⁵), 4.1 (2H, m, $^3J_{\text{HH}}$ 7.1 Hz, H⁷ H^{7'}), 1.38 (3H, t, $^3J_{\text{HH}}$ 7.1 Hz, H⁸); δ_{C} (CDCl₃) 168.5 (dd, $^1J_{\text{CF}}$ 265 Hz $^3J_{\text{CP}}$ 16 Hz,

C^4), 158.4 (dd, $^1J_{CP}$ 167 Hz $^3J_{CF}$ 4.5 Hz, C^2), 153.2 (dd, $^3J_{CF}$ 23 Hz $^3J_{CP}$ 6.1 Hz, C^6), 132.6 (d, $^4J_{CP}$ 2.7 Hz, C^p), 132.3 (2C, d, $^2J_{CP}$ 9.8 Hz, C^o), 129.5 (d, $^1J_{CP}$ 140 Hz, C^i), 128.5 (2C, d, $^3J_{CP}$ 13 Hz, C^m), 116.5 (dd, $^2J_{CF}$ 23 Hz $^4J_{CP}$ 17 Hz, C^3), 113.3 (dd, $^2J_{CF}$ 16 Hz $^2J_{CP}$ 2.5 Hz, C^5), 61.9 (d, $^2J_{CP}$ 6.2 Hz, C^7), 16.5 (d, $^2J_{CP}$ 6.2 Hz, C^8); δ_P (CDCl₃) 24.2 (d, $^4J_{FP}$ 11 Hz); δ_F (CDCl₃) -100.42 (dt, $^3J_{FP}$ 11 Hz); m/z (HRMS⁺) 266.0746 [M + H]⁺ (C₁₃H₁₃FNO₂P requires 266.0746).



Phenyl(4-d₃-methoxy)pyridin-2-ylphosphinic acid PP7

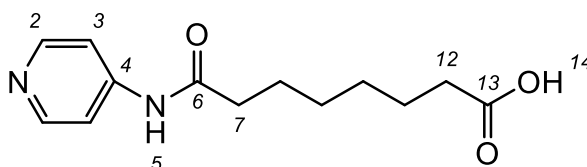
NaOH (0.042 g, 1.05 mmol) was dissolved in D₂O (1.5 mL) and added to a solution of phenyl(3-fluoropyridin-5-yl) phosphinate (0.14 g, 0.52 mmol) in MeOD (3 mL). The solution was stirred under argon at 30 °C, monitored directly by ¹H NMR. The solvent was lyophilised to yield a white solid (0.129 g, 96%). δ_H (MeOD-d₄) 8.49 (1H, dd, $^3J_{HH}$ 6.7 Hz $^5J_{HH}$ 1.6 Hz, H⁶), 7.91 (2H, dd, $^3J_{HH}$ 7.5 Hz $^4J_{HH}$ 5.0 Hz, H^o), 7.63 (1H, t, $^3J_{HH}$ 7.5 Hz, H^p), 7.56-7.52 (2H, m, H^m), 7.56-7.52 (1H, m, H³), 7.28 (1H, dd, $^3J_{HH}$ 6.7 Hz $^4J_{HH}$ 2.2 Hz, H⁵); δ_C (MeOD-d₄) 172.2 (d, $^3J_{CP}$ 11 Hz, C⁴), 152.5 (d, $^1J_{CP}$ 128 Hz, C²), 143.8 (d, $^3J_{CP}$ 7 Hz, C⁶), 132.9 (d, $^4J_{CP}$ 1.7 Hz, C^p), 131.6 (2C, d, $^2J_{CP}$ 10 Hz, C^o), 128.7 (2C, d, $^3J_{CP}$ 13 Hz, C^m), 128.5 (d, $^1J_{CP}$ 123 Hz, Cⁱ), 117.2 (d, $^2J_{CP}$ 12 Hz, C³), 114.5 (d, $^4J_{CP}$ 1.7 Hz, C⁵); δ_P (MeOD-d₄) 12.8; m/z (HRMS⁺) 236.0483 [M + H]⁺ (C₁₂H₁₀²H₃NO₃P requires 236.0477).



Chloro(η^6 -p-cymene)(phenyl(4-D₃-methoxy)pyridin-2-yl)phosphate ruthenium(II) Ru1PP7

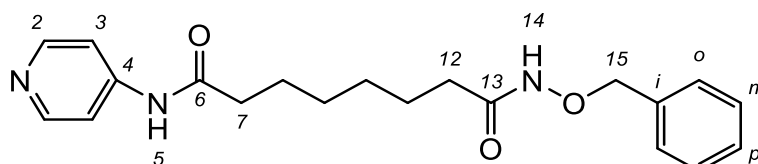
A solution of phenyl(4-d₃-methoxy)pyridin-2-ylphosphinic acid (0.13 g, 0.53 mmol) in MeOH (4 mL) was adjusted to pH 7 using dilute HCl solution (2 mL). Dichloro(η^6 -p-cymene)ruthenium(II)dimer (0.16 g, 0.26 mmol) was added and the solution stirred at 40 °C for 16 h under argon. The solvent was then removed under pressure leaving a dark red residue which was

dissolved into CH₂Cl₂ (3 mL). The solution was concentrated and cooled in an acetone: dry ice bath. Diethyl ether (3 mL) was added dropwise. The resulting precipitate was filtered and washed with diethyl ether (5 mL) to provide the *title compound* as a pale yellow solid (0.050 g, 17%). δ_{H} (MeOD-d₄) 8.93 (1H, d, ³J_{HH} 6.7 Hz, H⁶), 7.84 (2H, dd, ³J_{HP} 12.0 Hz ³J_{HH} 7.2 Hz, H^o), 7.47 (1H, t, ³J_{HH} 7.2 Hz, H^p), 7.36 (2H, td, ³J_{HH} 7.2 Hz, ⁴J_{HP} 3.0 Hz, H^m), 7.16 (1H, dd, ³J_{HP} 6.7 Hz ⁴J_{HH} 2.6 Hz, H^s), 6.76 (1H, dd, ³J_{HH} 6.7 Hz ⁴J_{HH} 2.6 Hz, H^s), 5.75 (1H, d, ³J_{HH} 6.0 Hz, H^d), 5.73 (1H, d, ³J_{HH} 6.0 Hz, H^d), 5.64 (1H, d, ³J_{HH} 6.0 Hz, H^c), 5.57 (1H, d, ³J_{HH} 6.0 Hz, H^c), 2.95 (1H, septet, ³J_{HH} 6.9 Hz, H^f), 2.27 (3H, s, H^a), 1.30 (6H, d, ³J_{HH} 6.9 Hz, H^g); δ_{C} (MeOD-d₄) 167.3 (d, ³J_{CP} 12 Hz, C⁴), 161.0 (d, ¹J_{CP} 143 Hz, C²), 155.7 (d, ³J_{CP} 12 Hz, C⁶), 134.5 (d, ¹J_{CP} 144 Hz, Cⁱ), 132.7 (2C, d, ²J_{CP} 11 Hz, C^o), 131.9 (d, ⁴J_{CP} 2.7 Hz, C^p), 127.8 (2C, d, ³J_{CP} 13 Hz, C^m), 114.1 (d, ⁴J_{CP} 21 Hz, C^s), 113.1 (d, ²J_{CP} 1.6 Hz, C^s), 103.1 (C^b), 97.5 (C^e), 81.0 (C^d), 80.8 (C^d), 80.7 (C^c), 80.5 (C^c), 30.8 (C^f), 21.4 (C^g), 20.8 (C^g), 17.3 (C^a); δ_{P} (MeOD-d₄) 39.2; m/z (HRMS⁺) 481.0842 [M - Cl]⁺ (C₂₂H₂₂H₃NO₃P⁹⁶Ru requires 481.0836).



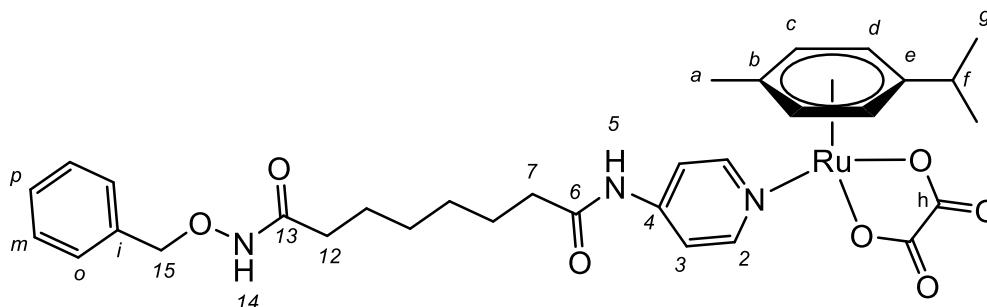
7-[(Pyridin-4-yl)carbamoyl]heptanoic acid 10

4-Aminopyridine (0.300 g, 3.19 mmol) and suberic anhydride (0.658 g, 4.20 mmol) were dissolved in THF (7 mL). Triethylamine (0.44 mL, 3.19 mmol) was added and the resulting solution refluxed for 16 h. The beige precipitate formed was filtered and used without further purification (0.727 g, 91%). δ_{H} (DMSO-d₆) 10.21 (1H, s, H⁵), 8.37 (2H, d, ³J_{HH} 4.8 Hz, H²), 7.52 (2H, dd, ³J_{HH} 4.8 Hz ⁴J_{HH} 1.3 Hz, H³), 2.31 (2H, t, ³J_{HH} 7.4 Hz, H¹²), 2.16 (2H, t, ³J_{HH} 7.4 Hz, H⁷), 1.55 (2H, quin, ³J_{HH} 7.2 Hz, H¹¹), 1.47 (2H, quin, ³J_{HH} 7.2 Hz, H⁸), 1.31-1.22 (2H, m, H⁹), 1.31-1.22 (2H, m, H¹⁰); δ_{C} (DMSO-d₆) 174.9 (C⁶), 172.9 (C¹³), 150.7 (2C, C²), 146.2 (C⁴), 113.5 (2C, C³), 36.8 (C¹²), 34.1 (C⁷), 28.8-27.7 (2C, C¹⁰ C⁹), 25.0 (C¹¹), 24.8 (C⁸); m/z (HRMS⁺) 251.1378 [M + H]⁺ (C₁₃H₁₉N₂O₃ requires 251.1396).



N¹⁴-(benzyloxy)-N⁵-(pyridin-4-yl)octanediamide 11

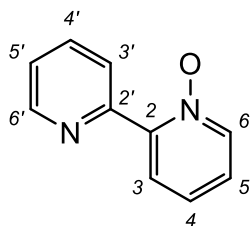
7-[(Pyridin-4-yl)carbamoyl]heptanoic acid (0.485 g, 1.94 mmol), 1-hydroxybenzotriazole (0.393 g, 2.91 mmol), 1-ethyl-3(3-dimethylaminopropyl)carbodiimide (0.575 g, 2.91 mmol), *O*-benzyl hydroxylamine hydrochloride (0.464 g, 2.91 mmol) were suspended in THF : H₂O (15 mL) with stirring. *N,N*-Diisopropylethylamine (0.606 g, 4.85 mmol) was added and the reagents dissolved. The solution was stirred for 16 h at room temperature. The reaction mixture was extracted with CH₂Cl₂ (3 x 20 mL) and the organic layer washed with saturated Na₂CO₃ solution. The organic layers were combined and dried with MgSO₄, filtered and dried under vacuum. The resulting yellow oil was recrystallized from EtOAc to give an off white solid as the *title compound* (0.201 g, 29%). δ_{H} (MeOH-d₄) 8.34 (2H, d, ³J_{HH} 6.0 Hz, H²), 7.62 (2H, d, ³J_{HH} 6.0 Hz, H³), 7.38 (2H, d, ³J_{HH} 7.5 Hz, H^o), 7.35-7.30 (1H, m, H^p), 7.35-7.30 (2H, m, H^m), 4.81 (2H, s, H¹⁵), 2.38 (2H, t, ³J_{HH} 7.5 Hz, H⁷), 2.03 (2H, t, ³J_{HH} 7.5 Hz, H¹²), 1.66 (2H, quin, ³J_{HH} 7.5 Hz, H⁸), 1.57 (2H, quin, ³J_{HH} 7.5 Hz, H¹¹), 1.35 (2H, m, H⁹), 1.30 (2H, m, H¹⁰); δ_{C} (MeOD-d₄) 173.8 (C⁶), 171.4 (C¹³), 149.2 (C²), 146.8 (C⁴), 135.5 (Cⁱ), 128.8 (2C, C^o), 128.2 (C^p), 128.0 (2C, C^m), 113.6 (2C, C³), 77.4 (C¹⁵), 36.5 (C⁷), 32.2 (C¹²), 28.4 (C⁹), 28.2 (C¹⁰), 24.9 (C¹¹), 24.7 (C⁸); *m/z* (HRMS⁺) 356.1951 [M + H]⁺ (C₂₀H₂₅N₃O₃ requires 356.1974).



Chloro(p-cymene)N¹⁴-(benzyloxy)-N⁵-(pyridin-4-yl)octanediamide ruthenium(II) oxalate 12

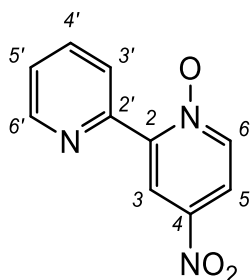
Sodium oxalate (0.022 g, 0.16 mmol) was dissolved in water (1.5 mL), dichloro(*p*-cymene) ruthenium(II) dimer (0.017 g, 0.028 mmol) and *N¹⁴-(benzyloxy)-N⁵-(pyridin-4-yl)octanediamide* (0.020 g, 0.056 mmol) were dissolved in MeOH (3 mL) and both solutions combined. The resulting solution was stirred for 16 h at room temperature. The solution was then filtered, the filtrate kept and solvent removed under vacuum to give the *title compound* as a yellow oil (0.030 g, 78%). δ_{H} (MeOH-d₄) 8.26 (2H, d, ³J_{HH} 7.0 Hz, H²), 7.72 (2H, d, ³J_{HH} 7.0 Hz, H³), 7.39 (2H, d, ³J_{HH} 7.0 Hz, H^o), 7.34 (2H, t, ³J_{HH} 7.0 Hz, H^m), 7.32-7.30 (1H, m, H^p), 5.77 (2H, d, ³J_{HH} 6.0 Hz, H^d), 5.54 (2H, d, ³J_{HH} 6.0 Hz, H^c), 4.82 (2H, s, H¹⁵), 2.85 (1H, septet, ³J_{HH} 6.9 Hz, H^f), 2.39 (2H, t, ³J_{HH} 7.2 Hz, H⁷), 2.09 (3H, s, H^a), 2.03 (2H, t, ³J_{HH} 7.2 Hz, H¹²), 1.64 (2H, quin, ³J_{HH} 7.2 Hz, H⁸), 1.56 (2H, quin, ³J_{HH} 7.2 Hz, H¹¹), 1.37-1.27 (4H, m, H⁹ H¹⁰), 1.31 (6H, d, ³J_{HH} 6.9 Hz, H⁸); δ_{C} (MeOD-d₄) 174.1 (C⁶), 171.4 (C¹³), 166.4 (2C, C^h), 152.9 (2C, C²), 148.3 (C⁴), 135.5 (Cⁱ), 128.8 (2C, C^o), 128.2 (C^p), 128.0 (2C, C^m), 114.7 (2C, C³), 101.9 (C^e), 97.3 (C^b), 82.3 (2C, C^d), 80.3 (2C, C^c), 77.5 (C¹⁵), 36.5

(C⁷), 32.2 (C¹²), 30.8 (C^f), 28.3 (C⁹), 28.2 (C¹⁰), 24.9 (C¹¹), 24.6 (C⁸), 21.2 (2C, C^g), 16.5 (C^a); *m/z* (HRMS⁺) 674.1951 [M + H]⁺ (C₃₂H₄₀N₃O₇⁹⁶Ru requires 674.1942).



2,2'-Bipyridine-1-oxide 14

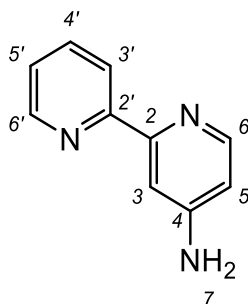
2,2'-Bipyridine (2.00 g, 12.8 mmol) was dissolved into trifluoroacetic acid (10 mL) and stirred at 10 °C. Aqueous hydrogen peroxide (35%) solution (1.7 mL, 13.2 mmol) was added dropwise and the resulting mixture allowed to warm to room temperature (3 h). The reaction mixture was extracted into CHCl₃ and washed with 3M NaOH (3 x 20 mL). The aqueous phase was re-extracted with CHCl₃ (2 x 20 mL) and the organic layers combined. The solution was dried with Na₂SO₄, filtered and solvent removed to dryness to give the *title compound* as a pale yellow oil (1.678 g, 76%). δ_{H} (CDCl₃) 8.86 (1H, dd, ³J_{HH} 8.0 Hz ⁴J_{HH} 1.5 Hz, H⁶), 8.70 (1H, ddd, ³J_{HH} 8.0 Hz, ⁴J_{HH} 4.8 Hz ⁵J_{HH} 1.5 Hz, H³), 8.29 (1H, dd, ³J_{HH} 7.0 Hz, ⁴J_{HH} 2.0 Hz, H^{6'}), 8.15 (1H, dd, ³J_{HH} 7.0 Hz, ⁴J_{HH} 2.0 Hz, H^{3'}), 7.80 (1H, td, ³J_{HH} 8.0 Hz ⁴J_{HH} 1.5 Hz, H⁵), 7.34 (1H, td, ³J_{HH} 7.0 Hz, ⁴J_{HH} 2.0 Hz, H^{4'}), 7.32 (1H, td, ³J_{HH} 8.0 Hz ⁵J_{HH} 1.5 Hz, H⁴), 7.24 (1H, td, ³J_{HH} 7.0 Hz, ⁴J_{HH} 2.0 Hz, H^{5'}); δ_{C} (CDCl₃) 149.6 (C²), 149.3 (C³), 147.3 (C^{2'}), 140.6 (C^{6'}), 136.2 (C⁵), 127.8 (C^{3'}), 125.7 (C^{4'}), 125.5 (C⁶), 125.2 (C⁵), 124.2 (C⁴); *m/z* (HRMS⁺) 173.0720 [M + H]⁺ (C₁₀H₉N₂O requires 173.0715).



4-Nitro-2,2'-bipyridine-1-oxide 15

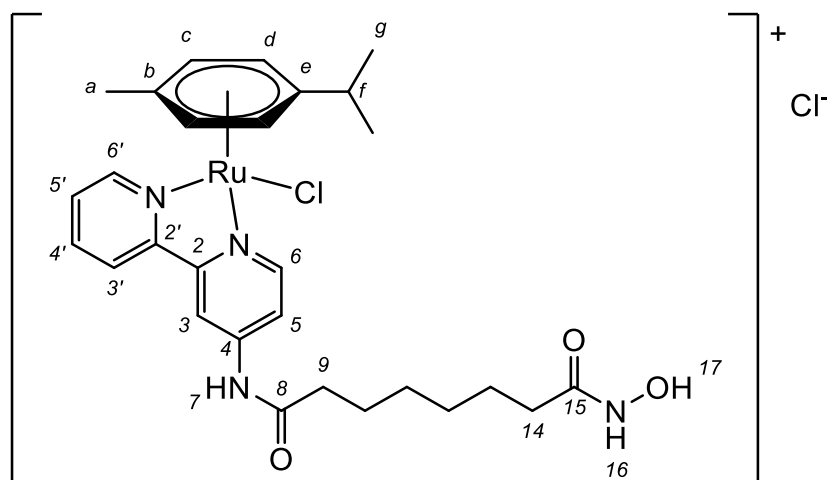
2,2'-Bipyridine-1-oxide (0.168 g, 9.74 mmol) was dissolved in conc. H₂SO₄ (15 mL) and stirred at 10 °C. Potassium nitrate (5.41 g, 53.5 mmol) was added and the resulting mixture heated to 80 °C for 30 h. The reaction was allowed to cool and then poured over ice (50 g) and neutralised with 3M NaOH. The precipitate that formed was filtered and washed with water and dried. The compound was suspended in CH₂Cl₂ (10 mL) and hexane (10 mL) added to allow the compound to precipitate. This yielded the *title compound* as a pale yellow solid (0.626 g, 29%). δ_{H} (CDCl₃) 9.15 (1H, d, ⁴J_{HH}

3.0 Hz, H³), 8.87 (1H, td, ³J_{HH} 7.0 Hz ⁴J_{HH} 3.0 Hz, H^{5'}), 8.78 (1H, ddd, ³J_{HH} 7.0 Hz ⁴J_{HH} 3.0 Hz ⁵J_{HH} 1.0 Hz, H^{6'}), 8.35 (1H, dd, ³J_{HH} 7.0 Hz ⁵J_{HH} 0.3 Hz, H⁶), 8.05 (1H, dd, ³J_{HH} 7.0 Hz ⁴J_{HH} 3.0 Hz, H⁵), 7.87 (1H, td, ³J_{HH} 7.0 Hz ⁴J_{HH} 3.0 Hz, H^{4'}), 7.42 (1H, ddd, ³J_{HH} 7.0 Hz ⁴J_{HH} 3.0 Hz ⁵J_{HH} 1.0 Hz, H³); δ_c (CDCl₃) 149.7 (C^{6'}), 148.1 (C²), 147.5 (C^{2'}), 142.4 (C⁴), 141.8 (C⁶), 136.7 (C^{4'}), 125.3 (C³), 125.1 (C⁵), 122.6 (C³), 118.8 (C⁵); *m/z* (HRMS⁺) 218.0570 [M + H]⁺ (C₁₀H₈N₃O₃ requires 218.0566).



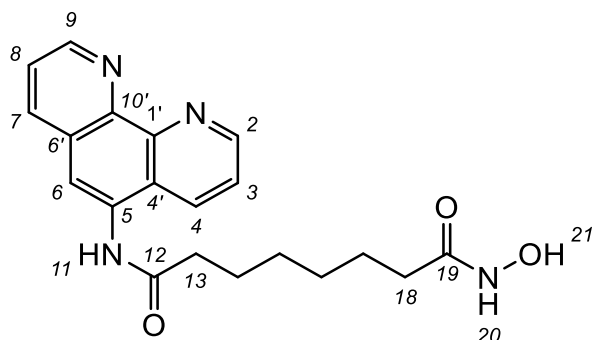
4-Amino-2,2'-bipyridine 16

4-Nitro-2,2'-bipyridine-1-oxide (0.374 g, 1.71 mmol) and tin(II) chloride dihydrate (1.54 g, 6.86 mmol), were suspended in conc. HCl (5 mL) and the reaction mixture heated to 90 °C for 24 h. Tin(II) chloride dihydrate (0.460 g, 2.05 mmol) was dissolved into HCl conc. (1 mL) and added to the solution which was heated at 90 °C for a further 24 h. The solution was then poured over ice (10 g) and 2M Na₂CO₃ solution added (pH 10). The aqueous solution was extracted with CH₂Cl₂ (3 x 50 mL), organic layers combined, dried over MgSO₄, filtered and solvent removed. The compound was sublimed at 140 °C for 24 h to give the *title compound* as a light brown solid (0.093 g, 25%). δ_H (CDCl₃) 8.63 (1H, dd, ³J_{HH} 8.0 Hz ⁴J_{HH} 2.0 Hz, H^{6'}), 8.34 (1H, d, ³J_{HH} 8.0 Hz, H^{3'}), 8.29 (1H, d, ³J_{HH} 6.0 Hz, H⁶), 7.77 (1H, td, ³J_{HH} 8.0 Hz ⁴J_{HH} 2.0 Hz, H^{4'}), 7.66 (1H, d, ⁴J_{HH} 3.0 Hz, H³), 7.27 (1H, td, ³J_{HH} 8.0 Hz ⁴J_{HH} 2.0 Hz, H^{5'}), 6.54 (1H, dd, ³J_{HH} 6.0 Hz ⁴J_{HH} 3.0 Hz, H⁵), 4.29 (2H, bs, H⁷); δ_c (CDCl₃) 156.7 (C²), 156.3 (C^{2'}), 153.6 (C⁴), 149.8 (C⁶), 148.8 (C^{6'}), 136.8 (C^{4'}), 123.6 (C⁵), 121.1 (C³), 109.6 (C⁵), 106.8 (C³); *m/z* (HRMS⁺) 172.0884 [M + H]⁺ (C₁₀H₁₀N₃ requires 172.0875).



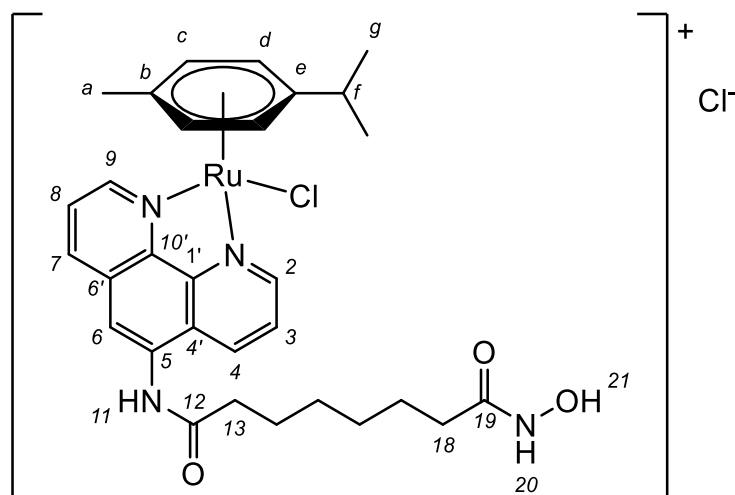
Chloro(η^6 -p-cymene)(N^7 -{[2,2'-bipyridine]-4-yl}- N^{16} -hydroxyoctanediamide) ruthenium(II) chloride Ru1L¹

N⁷-{[2,2'-Bipyridine]-4-yl}-N¹⁶-hydroxyoctanediamide (0.035 g, 0.102 mmol) and dichloro(*p*-cymene) ruthenium(II) dimer (0.031 g, 0.051 mmol) were suspended in anhydrous MeOH (5 mL) and stirred for 16 h at 40 °C under an inert atmosphere. The solvent volume was reduced to 1 mL and precipitated out into cold diethyl ether (3 mL). The resulting solution was filtered to give the *title compound* as an orange solid (0.029 g, 43%). δ_{H} (DMSO- d_6) 11.28 (1H, bs, H⁷), 9.50 (1H, d, ³ J_{HH} 7.0 Hz, H^{6'}), 9.28 (1H, d, ³ J_{HH} 6.5 Hz, H⁶), 8.68 (1H, s, H³), 8.24 (2H, m, H^{3'}, H^{4'}), 7.87-7.85 (1H, m, H⁵), 7.75 (1H, td, ³ J_{HH} 7.0 Hz ⁴ J_{HH} 2.0 Hz, H^{5'}), 6.16 (1H, d, ³ J_{HH} 6.0 Hz, H^d), 6.14 (1H, d, ³ J_{HH} 6.0 Hz, H^{d'}), 5.92 (1H, d, ³ J_{HH} 6.0 Hz, H^c), 5.88 (1H, d, ³ J_{HH} 6.0 Hz, H^{c'}), 2.54 (1H, septet, ³ J_{HH} 6.5 Hz, H^f), 2.44 (2H, t, ³ J_{HH} 7.0 Hz, H⁹) 2.26 (2H, t, ³ J_{HH} 7.0 Hz, H¹⁴), 2.14 (3H, s, H^a), 1.58 (2H, quin, ³ J_{HH} 7.0 Hz, H¹⁰), 1.49 (2H, quin, ³ J_{HH} 7.0 Hz, H¹³), 1.30-1.25 (4H, m, H¹¹, H¹²), 0.92 (3H, d, ³ J_{HH} 6.5 Hz H^g), 0.91 (3H, d, ³ J_{HH} 6.5 Hz, H^g); δ_{C} (DMSO- d_6) 173.8 (C⁸), 173.7 (C¹⁵), 156.4 (C⁶), 156.3 (C³), 155.0 (C²), 154.7 (C^{2'}), 149.0 (C⁴), 140.5 (C^{4'}), 127.9 (C⁵), 123.5 (C^{3'}), 116.4 (C⁵), 112.3 (C³), 103.7 (C^b), 103.6 (C^e), 86.9 (C^d), 86.7 (C^{d'}), 84.2 (C^c), 83.8 (C^{c'}), 36.9 (C⁹), 33.6 (C¹⁴), 30.7 (C^f), 28.6-28.5 (2C, C¹¹, C¹²), 24.8 (C¹⁰), 24.7 (C¹³), 22.1 (C^g), 22.0 (C^g), 18.7 (C^a); m/z (HRMS⁺) 608.2605 [M – Cl]⁺ (C₂₈H₃₆³⁵ClN₄O₃⁹⁶Ru requires 608.2881).



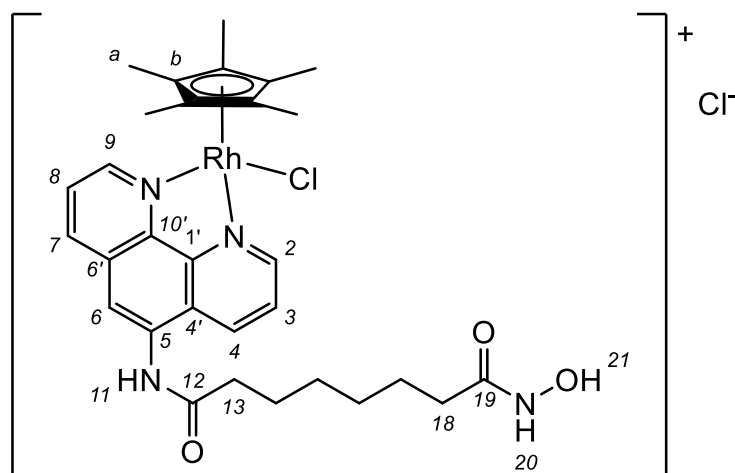
N²⁰-Hydroxy-N¹¹-(1,10-phenanthrolin-5-yl)octanediamide L²

1,10-Phenanthroline-5-amine (0.100 g, 0.51 mmol), methyl 8-chloro-8-oxooctanoate (0.158 g, 0.76 mmol) and 4-dimethylaminopyridine (0.01 g, 0.051 mmol) were dissolved in DMF (7 mL) and stirred for 16 h at room temperature under an inert atmosphere. The volume of solution was reduced by 70% and added dropwise to a stirring solution of diethyl ether (10 mL). The filtrate was decanted and the precipitate dried under vacuum. The solid was suspended in MeOH : hydroxylamine solution 50% (5 mL) and 1M NaOH solution was added (0.5 mL) with stirring for 30 min. The solution was neutralised to pH 7 and a precipitate formed on standing. The filtrate was decanted and the resulting solid dried under vacuum to give a beige solid (0.061 g, 32%). δ_{H} (DMSO- d_6) 10.3 (1H, s, H²¹), 10.1 (1H, s, H¹¹), 9.09 (1H, dd, ³J_{HH} 4.3 Hz ⁴J_{HH} 1.4 Hz, H²), 9.00 (1H, dd, ³J_{HH} 4.1 Hz ⁴J_{HH} 1.1 Hz, H⁹), 8.68 (1H, s, H²⁰), 8.56 (1H, dd, ³J_{HH} 8.0 Hz ⁴J_{HH} 1.4 Hz, H⁴), 8.41 (1H, dd, ³J_{HH} 7.7 Hz ⁴J_{HH} 1.1 Hz, H⁷), 8.13 (1H, s, H⁶), 7.80 (1H, dd, ³J_{HH} 8.0 Hz ³J_{HH} 4.3 Hz, H³), 7.70 (1H, dd, ³J_{HH} 7.7 Hz ³J_{HH} 4.5 Hz, H⁸), 2.47 (2H, t, ³J_{HH} 7.5 Hz, H¹³), 1.93 (2H, t, ³J_{HH} 7.5 Hz, H¹⁸), 1.65 (2H, quin, ³J_{HH} 7.5 Hz, H¹⁴), 1.50 (2H, quin, ³J_{HH} 7.5 Hz, H¹⁷), 1.35 (2H, m, H¹⁵), 1.29 (2H, m, H¹⁶); δ_{C} (DMSO- d_6) 172.8 (C¹²), 169.5 (C¹⁹), 150.2 (C²), 149.7 (C⁹), 146.3 (C¹), 144.2 (C^{10'}), 136.2 (C⁴), 132.2 (C⁵), 132.0 (C⁷), 128.5 (C⁶), 125.1 (C^{4'}), 123.9 (C⁸), 123.2 (C³), 120.5 (C⁶), 36.4 (C¹³), 32.7 (C¹⁸), 28.9 (C¹⁵), 28.8 (C¹⁶), 25.6 (C¹⁴), 25.5 (C¹⁷); m/z (HRMS⁺) 367.1764 [M + H]⁺ (C₂₀H₂₃N₄O₃ requires 367.1770).



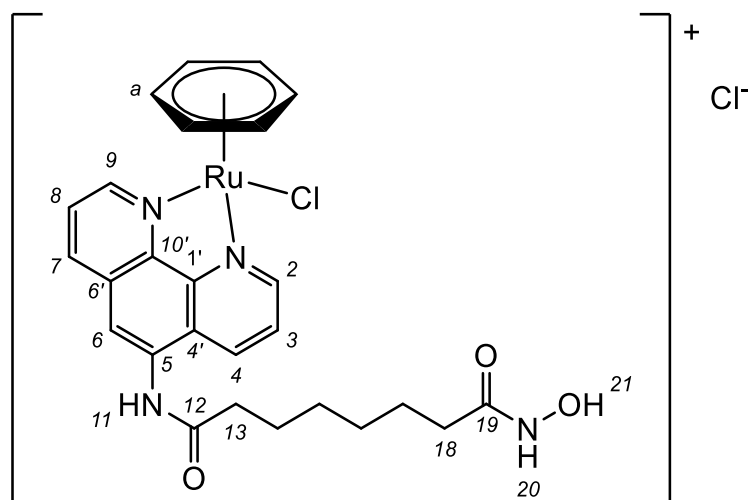
Chloro(η^6 -p-cymene)(N^{20} -hydroxy- N^{11} -(1,10-phenanthrolin-5-yl)octanediamide) ruthenium(II) chloride Ru1L²

N^{20} -Hydroxy- N^{11} -(1,10-phenanthrolin-5-yl)octanediamide (0.031 g, 0.084 mmol) and dichloro(*p*-cymene) ruthenium(II) dimer (0.025 g, 0.042 mmol) were suspended in anhydrous MeOH (5 mL) and stirred for 16 h at 40 °C under an inert atmosphere. The solvent volume was reduced to 1 mL and dropped into cold diethyl ether (3 mL). The resulting precipitate was filtered to give the title compounds as a yellow solid (0.032 g, 58%). δ_{H} (DMSO- d_6) 10.50 (1H, s, H¹¹), 10.30 (1H, s, H²¹), 9.94 (1H, d, ³ J_{HH} 5.0 Hz, H²), 9.81 (1H, d, ³ J_{HH} 5.0 Hz, H⁹), 9.05 (1H, d, ³ J_{HH} 8.6 Hz, H⁴), 8.86 (1H, d, ³ J_{HH} 6.5 Hz, H⁷), 8.63 (1H, s, H²⁰), 8.50 (1H, s, H⁶), 8.18 (1H, dd, ³ J_{HH} 8.6 ³ J_{HH} 5.0 Hz, H³), 8.08 (1H, dd, ³ J_{HH} 8.0 Hz ³ J_{HH} 5.0 Hz, H⁸), 6.34 (1H, d, ³ J_{HH} 5.5 Hz, H^d), 6.31 (1H, d, ³ J_{HH} 5.5 Hz, H^{d'}), 6.11 (1H, d, ³ J_{HH} 5.5 Hz, H^c), 6.08 (1H, d, ³ J_{HH} 5.5 Hz, H^{c'}), 2.59 (1H, septet, ³ J_{HH} 6.7 Hz, H^f), 2.56 (2H, t, ³ J_{HH} 7.5 Hz, H¹³), 2.15 (3H, s, H^a), 1.94 (2H, t, ³ J_{HH} 7.5 Hz, H¹⁸), 1.66 (2H, quin, ³ J_{HH} 7.5 Hz, H¹⁴), 1.50 (2H, quin, ³ J_{HH} 7.5 Hz, H¹⁷), 1.36-1.28 (4H, m, H¹⁵, H¹⁶), 0.89 (3H, d, ³ J_{HH} 5.5 Hz, H^e), 0.88 (3H, d, ³ J_{HH} 5.5 Hz, H^{e'}); δ_{C} (DMSO- d_6) 173.2 (C¹²), 169.5 (C¹⁹), 156.5 (C²), 155.2 (C⁹), 145.8 (C^{1'}), 143.2 (C^{10'}), 138.6 (C⁷), 135.3 (C⁴), 133.8 (C⁵), 130.1 (C^{6'}), 126.8 (C⁸), 126.5 (C^{4'}), 126.1 (C³), 119.1 (C⁶), 104.5 (C^e), 103.1 (C^b), 86.5 (C^{d'}), 86.3 (C^d), 84.4 (C^{c'}), 84.2 (C^c), 36.4 (C¹³), 32.7 (C¹⁸), 30.8 (C^f), 28.9 (C¹⁵), 28.8 (C¹⁶), 25.5 (C¹⁷), 25.4 (C¹⁴), 22.1 (C^g), 22.0 (C^{g'}), 18.6 (C^a); m/z (HRMS⁺) 612.1581 [M-2Cl+OH]⁺ (C₃₀H₃₆N₄O₄⁹⁶Ru requires 612.1603). Anal. Calcd for C₃₀H₃₆Cl₂N₄O₃Ru.(H₂O)_{2.5} : C, 50.20; H, 5.05; N, 7.80. Found: C, 50.07; H, 5.11; N, 7.69.



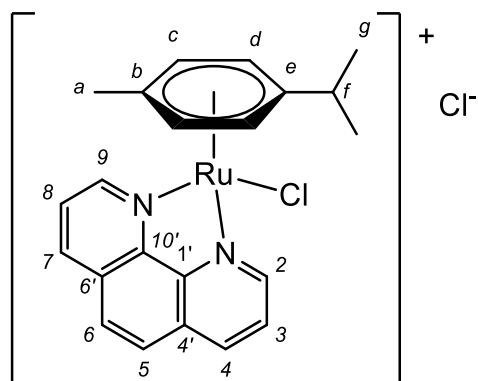
Chloro(η^5 -pentamethylcyclopentadienyl)(N^{20} -hydroxy- N^{11} -(1,10-phenanthrolin-5-yl)octanediamide) rhodium(III) chloride RhL^2

N^{20} -Hydroxy- N^{11} -(1,10-phenanthrolin-5-yl)octanediamide (0.028 g, 0.076 mmol) and (pentamethylcyclopentadienyl) rhodium(III) chloride dimer (0.023 g, 0.038 mmol) were dissolved in anhydrous MeOH (7 mL) and stirred for 16 h at 40 °C under an inert atmosphere. The resulting solution was reduced in volume to 1 mL and cold diethyl ether added dropwise (3 mL) and the precipitate collected to give the *title compound* as a yellow solid (0.029 g, 61%). δ_H (DMSO- d_6) 10.51 (1H, s, H^{11}), 10.38 (1H, s, H^{21}), 9.43 (1H, dd, $^3J_{HH}$ 5.3 Hz $^4J_{HH}$ 1.2 Hz, H^2), 9.32 (1H, dd, $^3J_{HH}$ 5.2 Hz $^4J_{HH}$ 1.2 Hz, H^9), 9.07 (1H, dd, $^3J_{HH}$ 8.7 Hz $^4J_{HH}$ 2.3 Hz, H^4), 8.91 (1H, dd, $^3J_{HH}$ 8.0 Hz $^4J_{HH}$ 1.2 Hz, H^7), 8.63 (1H, s, H^{20}), 8.54 (1H, s, H^6), 8.26 (1H, dd, $^3J_{HH}$ 8.7 Hz $^3J_{HH}$ 5.3 Hz, H^3), 8.16 (1H, dd, $^3J_{HH}$ 8.0 Hz $^3J_{HH}$ 5.2 Hz, H^8), 2.59 (2H, t, $^3J_{HH}$ 9.0 Hz, H^{13}), 1.96 (2H, t, $^3J_{HH}$ 9.0 Hz, H^{18}), 1.74 (15H, s, H^a), 1.71 (2H, quin, $^3J_{HH}$ 9.0 Hz, H^{14}), 1.52 (2H, quin, $^3J_{HH}$ 9.0 Hz, H^{17}), 1.41-1.29 (4H, m, H^{15} , H^{16}); δ_C (DMSO- d_6) 173.1 (C^{12}), 169.6 (C^{19}), 152.9 (C^2), 151.8 (C^9), 145.5 (C^1), 142.9 (C^{10}), 138.8 (C^7), 135.5 (C^4), 133.9 (C^6), 130.1 (C^5), 127.5 (C^8), 126.7 (C^3), 120.3 (C^6), 119.6 (C^4), 97.4 (5C, s, C^b), 36.3 (C^{13}), 32.6 (C^{18}), 29.0 (C^{15}), 28.8 (C^{16}), 25.4 (2C, m, C^{14} , C^{17}), 8.97 (5C, s, C^a); m/z (HRMS $^+$) 639.1615 [$M-Cl$] $^+$ ($C_{30}H_{37}N_4O_3^{35}Cl^{103}Rh$ requires 639.1609). Anal. Calcd for $C_{30}H_{37}Cl_2N_4O_3Rh \cdot (H_2O)_{3.5}$: C, 48.79; H, 5.05; N, 7.58. Found: C, 48.70; H, 5.17; N, 7.11.



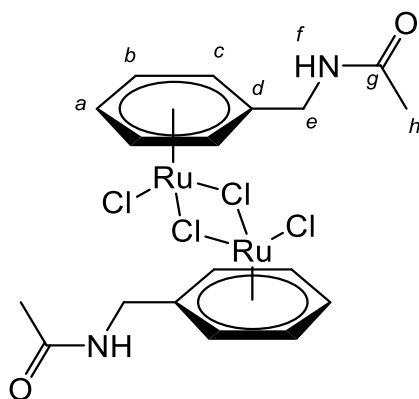
Chloro(η^6 -benzene)(N^{20} -Hydroxy- N^{11} -(1,10-phenanthrolin-5-yl)octanediamide) ruthenium(II) $Ru3L^2$

Dichloro(benzene)ruthenium(II) dimer (0.023 g, 0.047 mmol) and N^{20} -Hydroxy- N^{11} -(1,10-phenanthrolin-5-yl)octanediamide (0.032 g, 0.095 mmol) were dissolved in anhydrous MeOH (7 mL) and stirred for 16 h at 40 °C under an inert atmosphere. The resulting solution was added to diethyl ether (3 mL) and the filtrate decanted off. This gave the *title compound* as a yellow solid (0.032 g, 55%). δ_H (DMSO- d_6) 10.74 (1H, s, H^{11}), 10.39 (1H, s, H^{21}), 10.33 (1H, bs, H^{20}), 10.04 (1H, d, $^3J_{HH}$ 5.0 Hz, H^2), 9.91 (1H, d, $^3J_{HH}$ 3.8 Hz, H^9), 9.11 (1H, d, $^3J_{HH}$ 8.3 Hz, H^4), 8.86 (1H, d, $^3J_{HH}$ 8.1 Hz, H^7), 8.46 (1H, s, H^6), 8.15 (1H, m, H^4), 8.04 (1H, dd, $^3J_{HH}$ 8.1 Hz, $^3J_{HH}$ 3.8 Hz, H^8), 6.28 (6H, s, H^a), 2.58 (2H, t, $^3J_{HH}$ 7.0 Hz, H^{13}), 2.28 (2H, t, $^3J_{HH}$ 7.0 Hz, H^{18}), 1.54-1.47 (4H, m, H^{14} , H^{17}), 1.36-1.27 (4H, m, H^{15} , H^{16}); δ_C (DMSO- d_6) 173.8 (C^{19}), 173.2 (C^{12}), 156.7 (C^2), 155.5 (C^9), 146.0 (C^1), 143.3 ($C^{10'}$), 138.5 (C^7), 135.6 (C^3), 133.9 ($C^{4'}$), 130.1 (C^6), 128.7 (C^5), 126.7 (C^8), 125.9 (C^4), 119.0 (C^6), 87.0 (6C, s, C^a), 36.3 (C^{13}), 33.6 (C^{18}), 28.7-28.6 (2C, C^{15} , C^{16}), 25.5-24.8 (2C, C^{14} , C^{17}); m/z (HRMS $^+$) 575.0923 [$M-Cl$] $^+$ ($C_{26}H_{28}N_4O_3^{35}Cl^{96}Ru$ requires 575.0926).



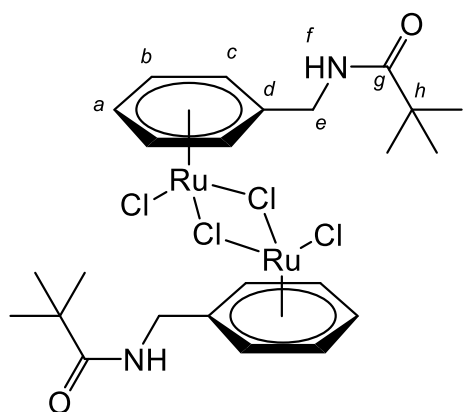
Chloro(η^6 -p-cymene)(1,10-phenanthroline) ruthenium(II) chloride

The title complex was synthesised according to literature procedure.¹⁸⁷ δ_{H} (DMSO- d_6) 9.95 (2H, dd, $^3J_{\text{HH}}$ 6.0 Hz, $^4J_{\text{HH}}$ 1.0 Hz, $\text{H}^2 \text{H}^9$), 8.91 (2H, dd, $^3J_{\text{HH}}$ 6.0 Hz, $^4J_{\text{HH}}$ 1.0 Hz, $\text{H}^4 \text{H}^7$), 8.27 (2H, s, $\text{H}^5 \text{H}^6$), 8.14 (2H, dd, $^3J_{\text{HH}}$ 6.0 Hz, $^3J_{\text{HH}}$ 6.0 Hz, $\text{H}^3 \text{H}^8$), 6.34 (2H, d, $^3J_{\text{HH}}$ 6.0 Hz, H^d), 6.11 (2H, d, $^3J_{\text{HH}}$ 6.0 Hz, H^e), 2.58 (1H, septet, $^3J_{\text{HH}}$ 7.0 Hz, H^f), 2.14 (3H, s, H^a), 0.87 (6H, d, $^3J_{\text{HH}}$ 7.0 Hz, H^g); δ_{C} (DMSO- d_6) 156.4 (2C, $\text{C}^2 \text{C}^9$), 145.5 (2C, $\text{C}^{1'} \text{C}^{10'}$), 139.2 (2C, $\text{C}^4 \text{C}^7$), 130.4 (2C, $\text{C}^{4'} \text{C}^{6'}$), 127.8 (2C, $\text{C}^5 \text{C}^6$), 126.8 (2C, $\text{C}^3 \text{C}^8$), 104.4 (C^e), 103.1 (C^b), 86.3 (2C, C^d), 84.2 (2C, C^c), 30.8 (C^f), 22.1 (2C, C^g), 18.6 (C^a); m/z (HRMS⁺) 445.0549 ($\text{C}_{22}\text{H}_{22}\text{ClN}_2^{96}\text{Ru}$ requires 445.0547).



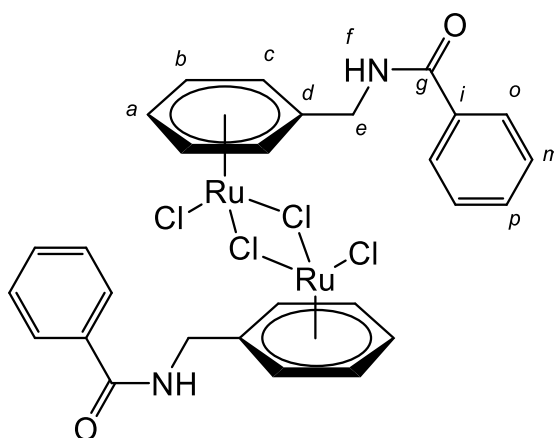
Dichloro(η^6 -*N*-acetylbenzamide) ruthenium(II) dimer Ru4A

N-[(Cyclohexa-1,4-dien-1-yl)methyl]acetamide (0.149 g, 0.986 mmol) and ruthenium(III) chloride hydrate (0.128 g, 0.493 mmol) were suspended in degassed EtOH (10 mL) and heated to 80 °C for 16 h under an argon atmosphere. The solution was then cooled in an ice bath for 2 h. The resulting precipitate was filtered and washed with cold EtOH (5 mL), diethylether (5 mL) and dried under vacuum to provide the *title compound* as a yellow-brown precipitate (0.070 g, 17%). δ_{H} (DMSO- d_6) 8.31 (2H, t, $^3J_{\text{HH}}$ 5.8 Hz, H^f), 6.02 (4H, t, $^3J_{\text{HH}}$ 5.8 Hz, H^b), 5.78 (4H, d, $^3J_{\text{HH}}$ 5.8 Hz, H^c), 5.75 (2H, t, $^3J_{\text{HH}}$ 5.8 Hz, H^a), 4.08 (4H, d, $^3J_{\text{HH}}$ 5.8 Hz, H^e), 1.84 (6H, s, H^h); δ_{C} (DMSO- d_6) 170.3 (2C, C^g), 103.4 (2C, C^d), 89.0 (4C, C^b), 85.4 (4C, C^c), 84.4 (2C, C^a), 40.5 (2C, C^e), 22.8 (2C, C^h); m/z (ASAP)⁺ 612.8804 [$\text{M}-\text{Cl}$]⁺ ($[\text{C}_{18}\text{H}_{22}\text{N}_2\text{O}_2^{35}\text{Cl}^{37}\text{Cl}_2^{104}\text{Ru}^{102}\text{Ru}]^+$ requires 612.8807).

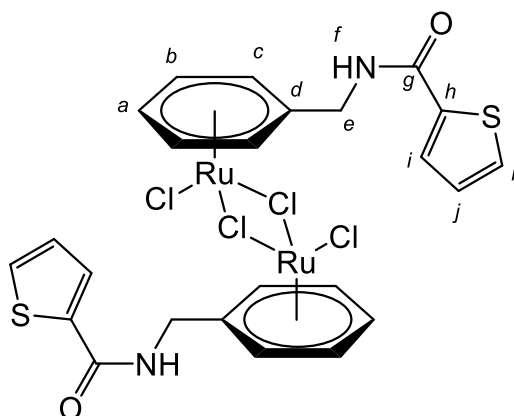


Dichloro(η^6 -*N*-trimethylacetylbenzylamide) ruthenium(II) dimer Ru4B

N-[(Cyclohexa-1,4-dien-1-yl)methyl]-2,2-dimethylpropanamide (0.110 g, 0.569 mmol) and ruthenium(III) chloride hydrate (0.074 g, 0.284 mmol) were suspended in degassed EtOH (10 mL) and heated to 80 °C for 16 h under an argon atmosphere. The solution was then cooled in an ice bath for 2 h. The resulting precipitate was filtered and washed with cold EtOH (5 mL), diethylether (5 mL) and dried under vacuum to provide the *title compound* as a brown precipitate (0.064 g, 25%). δ_{H} (DMSO- d_6) 7.93 (2H, t, $^3J_{\text{HH}}$ 5.4 Hz, H^f), 6.04 (4H, t, $^3J_{\text{HH}}$ 6.9 Hz, H^b), 5.79-5.77 (6H, m, H^a H^c), 4.12 (2H, d, $^3J_{\text{HH}}$ 5.4 Hz, H^e), 1.09 (18H, s, Hⁱ); δ_{C} (DMSO- d_6) 178.4 (2C, C^g), 103.8 (2C, C^d), 88.8 (4C, C^b), 85.5 (4C, C^c), 84.7 (2C, C^a), 40.8 (2C, C^e), 38.55 (2C, C^h), 27.7 (6C, Cⁱ); *m/z* (ASAP)⁺ 690.9734 [M-Cl]⁺ ([C₂₄H₃₄N₂O₂³⁵Cl₃¹⁰²Ru₂]⁺ requires 690.9767).

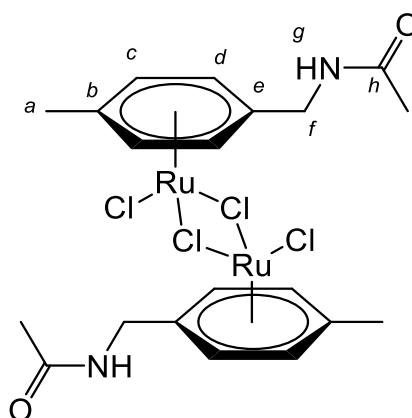
**Dichloro(*N*-benzoyl- η^6 -benzylamide) ruthenium(II) dimer Ru4C**

N-[(Cyclohexa-1,4-dien-1-yl)methyl]benzamide (0.181 g, 0.848 mmol) and ruthenium(III) chloride hydrate (0.110 g, 0.424 mmol) were suspended in degassed EtOH (10 mL) and heated to 80 °C for 16 h under an argon atmosphere. The solution was then cooled in an ice bath for 2 h. The resulting precipitate was filtered and washed with cold EtOH (5 mL), diethylether (5 mL) and dried under vacuum to provide the *title compound* as an orange-brown precipitate (0.128 g, 38%). δ_{H} (DMSO- d_6) 8.97 (2H, t, $^3J_{\text{HH}}$ 6.0 Hz, H^f), 7.85 (4H, dd, $^3J_{\text{HH}}$ 7.0 Hz $^4J_{\text{HH}}$ 1.3 Hz, H^o), 7.52 (2H, t, $^3J_{\text{HH}}$ 7.0 Hz, H^p), 7.45 (4H, t, $^3J_{\text{HH}}$ 7.0 Hz, H^m), 6.03 (4H, t, $^3J_{\text{HH}}$ 5.6 Hz, H^b), 5.91 (4H, d, $^3J_{\text{HH}}$ 5.6 Hz, H^c), 5.80 (2H, t, $^3J_{\text{HH}}$ 5.6 Hz, H^a), 4.31 (4H, d, $^3J_{\text{HH}}$ 6.0 Hz, H^e); δ_{C} (DMSO- d_6) 166.9 (2C, C^g), 134.0 (2C, Cⁱ), 132.0 (2C, C^p), 128.8 (4C, C^m), 127.7 (4C, C^o), 102.7 (2C, C^d), 88.6 (4C, C^b), 86.4 (4C, C^c), 85.0 (2C, C^a), 41.4 (2C, C^e); *m/z* (ASAP)⁺ 729.0135 [M-Cl]⁺ ([C₂₈H₂₆³⁵Cl₃N₂O₂¹⁰¹Ru₂]⁺ requires 729.9156).



Dichloro(η^6 -N-2-thiophenecarbonylbzylamide) ruthenium(II) dimer Ru4D

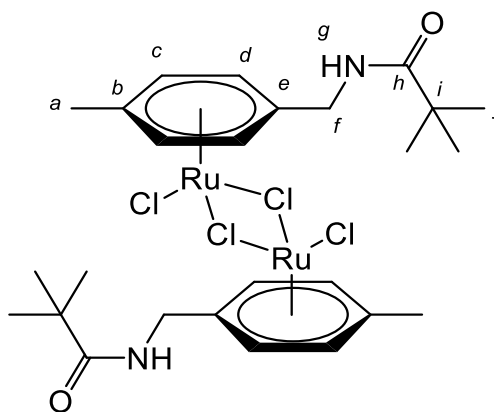
N-[(Cyclohexa-1,4-dien-1-yl)methyl]thiophene-2-carboxamide (0.193 g, 0.883 mmol) and ruthenium(III) chloride hydrate (0.114 g, 0.441 mmol) were suspended in degassed EtOH (10 mL) and heated to 80 °C for 16 h under an argon atmosphere. The solution was then cooled in an ice bath for 2 h. The resulting precipitate was filtered and washed with cold EtOH (5 mL), diethylether (5 mL) and dried under vacuum to provide the *title compound* as a brown solid (0.123 g, 36%); δ_{H} (DMSO- d_6) 9.01 (2H, t, $^3J_{\text{HH}}$ 5.7 Hz, H^f), 7.78-7.76 (4H, m, Hⁱ, H^k), 7.15 (2H, t, $^3J_{\text{HH}}$ 5.0 Hz, H^j), 6.05 (4H, t, $^3J_{\text{HH}}$ 6.0 Hz, H^b), 5.90 (4H, d, $^3J_{\text{HH}}$ 6.0 Hz, H^c), 5.81 (2H, t, $^3J_{\text{HH}}$ 6.0 Hz, H^a), 4.28 (4H, d, $^3J_{\text{HH}}$ 5.7 Hz, H^e); δ_{C} (DMSO- d_6) 161.9 (2C, C^g), 139.3 (2C, C^h), 131.8 (2C, C^k), 129.2 (2C, Cⁱ), 128.5 (2C, C^j), 102.5 (2C, C^d), 88.6 (4C, C^b), 86.4 (4C, C^c), 85.1 (2C, C^a), 41.2 (2C, C^e); m/z (HRMS)⁺ 744.8296 [M-Cl]⁺ ([C₂₄H₂₂N₂O₂³⁵Cl₂³⁷Cl¹⁰²Ru₂S₂]⁺ requires 744.8266).



Dichloro(η^6 -4-methyl-N-acetylbenzylamide) ruthenium(II) dimer Ru5A

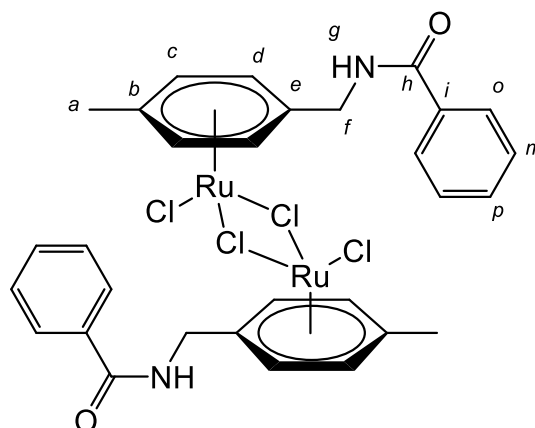
N-[(4-Methylcyclohexa-1,4-dien-1-yl)methyl]acetamide (0.085 g, 0.514 mmol) and ruthenium(III) chloride hydrate (0.066 g, 0.257 mmol) were suspended in degassed EtOH (10 mL) and heated to 80 °C for 16 h under an argon atmosphere. The homogenous solution was cooled in an ice bath for 2 h. The resulting precipitate was filtered, and washed with cold EtOH (5 mL), diethylether (5 mL)

and dried under vacuum to give the *title compound* (0.050 g, 29%) as a dark yellow solid; δ_{H} (DMSO- d_6) 8.19 (2H, t, $^3J_{\text{HH}}$ 5.6 Hz, H^{g}), 5.85 (4H, d, $^3J_{\text{HH}}$ 5.9 Hz, H^{d}), 5.78 (4H, d, $^3J_{\text{HH}}$ 5.9 Hz, H^{c}), 4.00 (4H, d, $^3J_{\text{HH}}$ 5.6 Hz, H^{f}), 2.06 (6H, s, H^{a}), 1.83 (6H, s, H^{i}); δ_{C} (DMSO- d_6) 170.2 (2C, C^{h}), 101.7 (2C, C^{b}), 96.8 (2C, C^{e}), 88.1 (4C, C^{d}), 86.5 (4C, C^{c}), 40.1 (2C, C^{f}), 22.8 (2C, C^{j}), 18.5 (2C, C^{a}); m/z (ASAP) $^+$ 634.9144 $[\text{M}-\text{Cl}]^+$ ($[\text{C}_{20}\text{H}_{26}^{37}\text{Cl}_3\text{N}_2\text{O}_2^{96}\text{Ru}^{101}\text{Ru}]^+$ requires 634.9145).



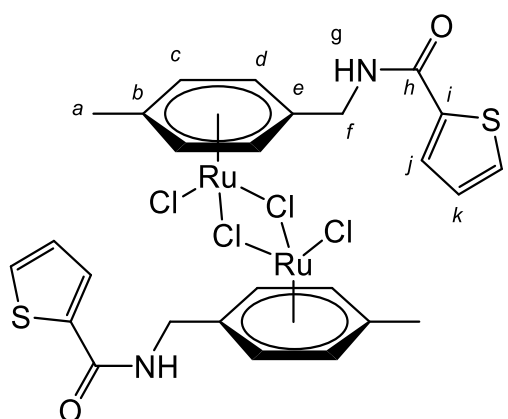
Dichloro(η^6 -4-methyl-N-trimethylacetylbenzylamide) ruthenium(II) dimer Ru4B

2,2-Dimethyl-N-[(cyclohexa-1,4-dien-1-yl)methyl]propanamide (0.186 g, 0.895 mmol) and ruthenium(III) chloride hydrate (0.116 g, 0.447 mmol) were suspended in degassed EtOH (10 mL) and the reaction mixture was heated to 80 °C for 16 h under an argon atmosphere. The reaction was then cooled in an ice bath for 2 h. The resulting precipitate was filtered and washed with cold EtOH (5 mL), diethyl ether (5 mL) and dried under vacuum to give the *title compound* (0.092 g, 27%) as a dark orange solid; δ_{H} (DMSO- d_6) 7.82 (2H, t, $^3J_{\text{HH}}$ 5.7 Hz, H^{g}), 5.84 (4H, d, $^3J_{\text{HH}}$ 6.0 Hz, H^{d}), 5.81 (4H, d, $^3J_{\text{HH}}$ 6.0 Hz, H^{c}), 4.05 (4H, d, $^3J_{\text{HH}}$ 5.7 Hz, H^{f}), 2.07 (6H, s, H^{a}), 1.08 (18H, s, H^{i}); δ_{C} (DMSO- d_6) 178.3 (2C, C^{h}), 102.0 (2C, C^{b}), 97.1 (2C, C^{e}), 88.1 (4C, C^{d}), 86.4 (4C, C^{c}), 40.3 (2C, C^{f}), 38.5 (2C, C^{i}), 27.7 (6C, C^{j}), 18.5 (2C, C^{a}); m/z (ASAP) $^+$ 719.0052 $[\text{M}-\text{Cl}]^+$ ($[\text{C}_{26}\text{H}_{38}^{35}\text{Cl}_3\text{N}_2\text{O}_2^{102}\text{Ru}_2]^+$ requires 719.0086).



Dichloro(η^6 -4-methyl-N-benzoylbzylamide) ruthenium(II) dimer Ru5C

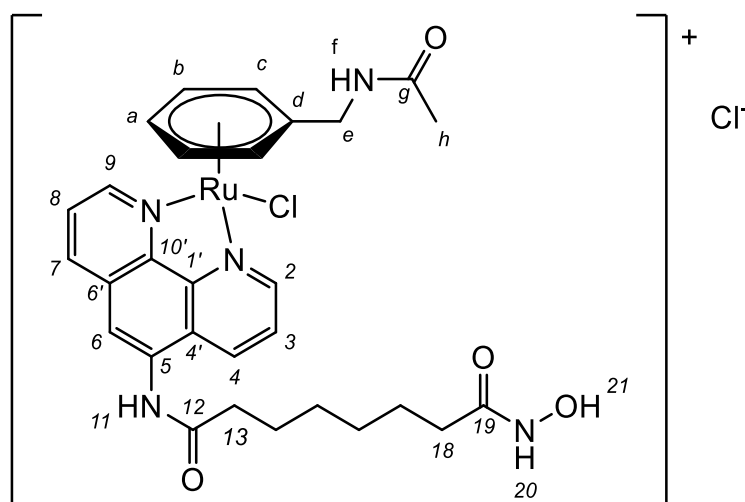
N-[(4-Methylcyclohexa-1,4-dien-1-yl)methyl]benzamide (0.087 g, 0.383 mmol) and ruthenium(III) chloride hydrate (0.049 g, 0.191 mmol) were suspended in degassed EtOH (7 mL) and the reaction mixture was heated to 80 °C for 16 h under an argon atmosphere. The reaction was then cooled in an ice bath for 2 h. The resulting precipitate was filtered and washed with cold EtOH (5 mL), diethylether (5 mL) and dried under vacuum to give the *title compound* (0.068 g, 45%) as an orange solid; δ_{H} (DMSO- d_6) 8.87 (2H, t, $^3J_{\text{HH}}$ 5.6 Hz, H^g), 7.84 (4H, dd, $^3J_{\text{HH}}$ 7.7 Hz $^4J_{\text{HH}}$ 1.4 Hz, H^o), 7.52 (2H, t, $^3J_{\text{HH}}$ 7.7 Hz, H^p), 7.44 (4H, t, $^3J_{\text{HH}}$ 7.7 Hz, H^m), 5.98 (4H, d, $^3J_{\text{HH}}$ 6.2 Hz, H^d), 5.80 (4H, d, $^3J_{\text{HH}}$ 6.2 Hz, H^c), 4.24 (4H, d, $^3J_{\text{HH}}$ 5.6 Hz, H^f), 2.06 (6H, s, H^a); δ_{C} (DMSO- d_6) 166.9 (2C, C^h), 134.0 (2C, Cⁱ), 132.0 (2C, C^p), 128.8 (4C, C^m), 127.7 (4C, C^o), 102.4 (2C, C^b), 95.9 (2C, C^e), 89.0 (4C, C^d), 86.1 (4C, C^c), 40.9 (2C, C^f), 18.5 (2C, C^a); m/z (HRMS)⁺ 761.0339 [M-Cl]⁺ ([C₃₀H₃₀³⁵Cl₂³⁷ClN₂O₂⁹⁹Ru¹⁰⁴Ru requires 760.9457).



Dichloro(η^6 -4-methyl-N-2-thiophenecarbonylbzylamide) ruthenium(II) dimer Ru5D

N-[(4-Methylcyclohexa-1,4-dien-1-yl)methyl]thiophene-2-carboxamide (0.103 g, 0.441 mmol) and ruthenium(III) chloride hydrate (0.057 g, 0.221 mmol) were suspended in degassed EtOH (10 mL) and the reaction mixture heated to 80 °C, for 16 h under an inert atmosphere. The precipitate

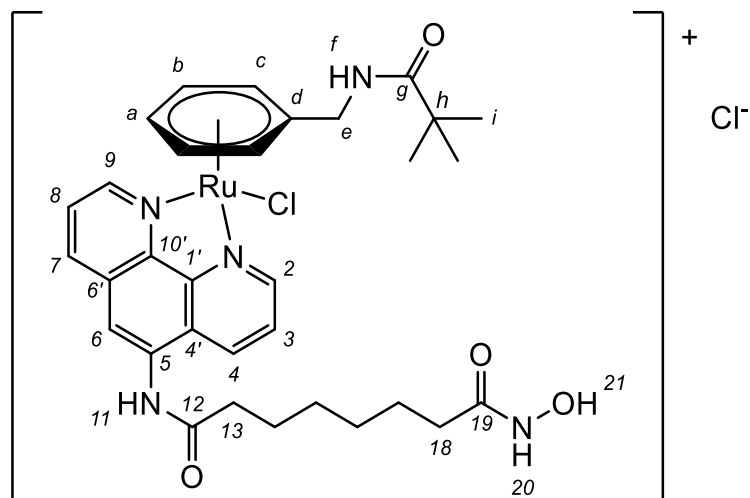
formed was filtered and washed with cold EtOH (5 mL), diethylether (5 mL) and dried under vacuum to give the *title compound* as a pale brown solid (0.028 g, 16%); δ_{H} (DMSO- d_6) 8.88 (2H, t, $^3J_{\text{HH}}$ 5.7 Hz, H^g), 7.76 (2H, dd, $^3J_{\text{HH}}$ 4.5 Hz $^3J_{\text{HH}}$ 1.1 Hz, H^l), 7.73 (2H, dd, $^3J_{\text{HH}}$ 4.5 Hz $^3J_{\text{HH}}$ 1.1 Hz, H^j), 7.13 (2H, t, $^3J_{\text{HH}}$ 4.5 Hz, H^k), 5.96 (4H, d, $^3J_{\text{HH}}$ 6.0 Hz, H^d), 5.80 (4H, d, $^3J_{\text{HH}}$ 6.0 Hz, H^c), 4.20 (4H, d, $^3J_{\text{HH}}$ 5.7 Hz, H^f), 2.06 (6H, s, H^a); δ_{C} (DMSO- d_6) 161.8 (2C, C^h), 139.4 (2C, Cⁱ), 131.7 (2C, C^l), 129.0 (2C, C^j), 128.4 (2C, C^k), 102.6 (2C, C^b), 95.6 (2C, C^e), 89.1 (4C, C^d), 86.1 (4C, C^c), 40.8 (2C, C^f), 18.5 (2C, C^a); m/z (ASAP)⁺ 769.9536 [M-Cl]⁺ ([C₂₆H₂₆³⁵Cl₃N₂O₂¹⁰¹Ru₂S₂]⁺ requires 769.8594).



Chloro(η^6 -N-acetylbenzylamide) N²⁰-hydroxy-N¹¹-(1,10-phenanthrolin-5-yl)octanediamide ruthenium(II) chloride Ru4AL²

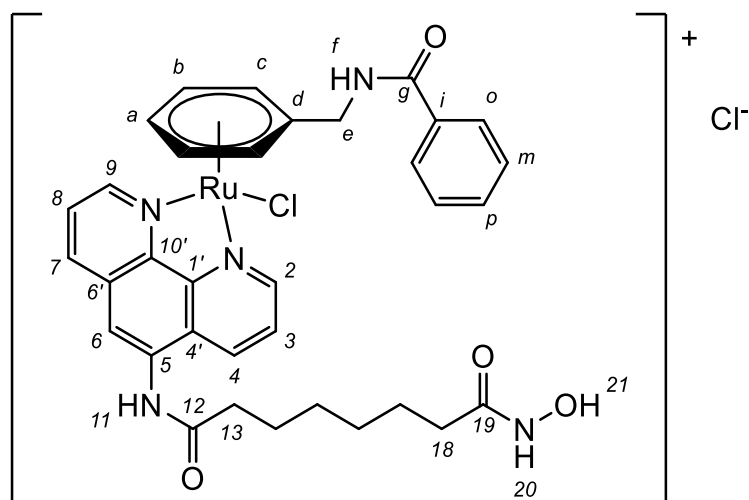
N²⁰-Hydroxy-N¹¹-(1,10-phenanthrolin-5-yl)octanediamide (0.025 g, 0.068 mmol) and **dichloro(η^6 -N-acetylbenzylamide) ruthenium(II) dimer** (0.022 g, 0.034 mmol) were suspended in anhydrous MeOH (10 mL) and the solution was heated to 40 °C under an argon atmosphere, for 16 h. The volume of the solution was reduced to 1.5 mL and purified by reverse phase HPLC (H₂O : MeOH) to yield the *title compound* (0.018 g, 76%) as a yellow solid; δ_{H} (DMSO- d_6) 10.6 (1H, s, H¹¹), 10.4 (1H, s, H²¹), 9.99 (1H, d, $^3J_{\text{HH}}$ 5.0 Hz, H²), 9.86 (1H, d, $^3J_{\text{HH}}$ 5.5 Hz, H⁹), 9.07 (1H, dd, $^3J_{\text{HH}}$ 8.4 Hz $^4J_{\text{HH}}$ 3.3 Hz, H⁴), 8.83 (1H, d, $^3J_{\text{HH}}$ 8.1 Hz, H⁷), 8.65 (1H, s, H²⁰), 8.52 (1H, t, $^3J_{\text{HH}}$ 5.8 Hz, H^f), 8.47 (1H, s, H⁶), 8.16 (1H, dd, $^3J_{\text{HH}}$ 8.4 Hz $^3J_{\text{HH}}$ 5.0 Hz H³), 8.06 (1H, dd, $^3J_{\text{HH}}$ 8.1 Hz $^3J_{\text{HH}}$ 5.5 Hz, H⁸), 6.39 (1H, d, $^3J_{\text{HH}}$ 5.8 Hz, H^c), 6.38 (1H, d, $^3J_{\text{HH}}$ 6.0 Hz, H^{c'}), 6.26 (2H, t, $^3J_{\text{HH}}$ 5.9 Hz, H^b H^{b'}), 5.96 (1H, t, $^3J_{\text{HH}}$ 5.9 Hz, H^a), 4.19 (2H, d, $^3J_{\text{HH}}$ 5.8 Hz, H^e), 2.57 (2H, t, $^3J_{\text{HH}}$ 6.5 Hz, H¹³), 1.94 (2H, t, $^3J_{\text{HH}}$ 6.5 Hz, H¹⁸), 1.75 (3H, s, H^h), 1.65 (2H, bm, H¹⁴), 1.49 (2H, bm, H¹⁷), 1.32-1.26 (4H, bm, H¹⁵ H¹⁶); δ_{C} (DMSO- d_6) 173.2 (C¹²), 170.2 (C^g), 169.5 (C¹⁹), 156.6 (C²), 155.4 (C⁹), 146.1 (C¹), 143.5 (C¹⁰), 138.5 (C⁷), 135.4 (C⁴), 133.8 (C^{4'}), 130.0 (C⁶), 126.7 (C⁸), 126.6 (C⁵), 125.9 (C³), 119.0 (C⁶), 102.7 (C^d), 87.6 (2C, C^b), 84.6 (2C, C^c), 84.4 (C^a), 40.4 (C^e), 36.4 (C¹³), 32.7

(C¹⁸), 28.9-28.8 (C¹⁵ C¹⁶), 25.5 (C¹⁷), 25.4 (C¹⁴), 22.7 (C^h); *m/z* (HRMS⁺) 646.1320 [M-Cl]⁺ (C₂₉H₃₃N₅O₄³⁵Cl⁹⁶Ru requires 646.1297).



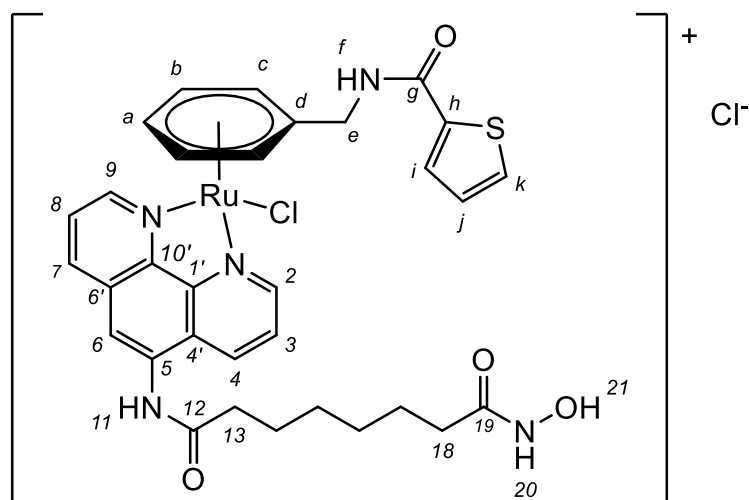
Chloro(η⁶-N-trimethylacetylbenzylamide) N²⁰-hydroxy-N¹¹-(1,10-phenanthrolin-5-yl)octanediamide ruthenium(II) chloride Ru4BL²

Dichloro(η⁶-N-trimethylacetylbenzylamide) ruthenium(II) dimer (0.035 g, 0.048 mmol) and **N²⁰-hydroxy-N¹¹-(1,10-phenanthrolin-5-yl)octanediamide** (0.035 g, 0.096 mmol) were suspended in anhydrous MeOH (10 mL) and the solution was heated to 40 °C under an argon atmosphere, for 16 h. The volume of the solution was reduced to 1.5 mL and purified by reverse phase HPLC (H₂O : MeOH) to yield the *title compound* (0.046 g, 66%) as a dark yellow solid; δ_{H} (DMSO-d₆) 10.6 (1H, s, H¹¹), 10.4 (1H, s, H²¹), 9.99 (1H, d, ³J_{HH} 4.9 Hz, H²), 9.85 (1H, d, ³J_{HH} 5.0 Hz, H⁹), 9.07 (1H, d, ³J_{HH} 8.5 Hz, H⁴), 8.82 (1H, d, ³J_{HH} 8.3 Hz, H⁷), 8.64 (1H, s, H²⁰), 8.47 (1H, s, H⁶), 8.17-8.14 (2H, bm, H³ H⁶), 8.05 (1H, dd, ³J_{HH} 8.3 Hz ³J_{HH} 5.0 Hz, H⁸), 6.39 (2H, t, ³J_{HH} 5.8 Hz, H^b), 6.22 (2H, d, ³J_{HH} 5.8 Hz, H^c), 5.95 (1H, t, ³J_{HH} 5.8 Hz, H^a), 4.18 (2H, d, ³J_{HH} 6.0 Hz, H^c), 2.57 (2H, t, ³J_{HH} 7.3 Hz, H¹³), 1.94 (2H, t, ³J_{HH} 7.3 Hz, H¹⁸), 1.65 (2H, quin, ³J_{HH} 7.3 Hz, H¹⁴), 1.49 (2H, quin, ³J_{HH} 7.3 Hz, H¹⁷), 1.36-1.33 (2H, bm, H¹⁵), 1.30-1.26 (2H, bm, H¹⁶), 0.98 (9H, s, Hⁱ); δ_{C} (DMSO-d₆) 178.2 (C⁸), 173.2 (C¹²), 169.5 (C¹⁹), 156.6 (C²), 155.3 (C⁹), 146.2 (C¹), 143.5 (C¹⁰), 138.5 (C⁷), 135.4 (C⁴), 133.8 (C⁵), 130.2 (C⁶), 126.6 (C⁸), 126.5 (C⁴), 125.9 (C³), 119.0 (C⁶), 103.1 (C^d), 87.7-87.6 (C^b C^{b'}), 84.5 (C^a), 84.4-84.3 (C^c C^{c'}), 40.6 (C^e), 38.4 (C^h), 36.4 (C¹³), 32.7 (C¹⁸), 28.9 (C¹⁵), 28.8 (C¹⁶), 27.6 (3C, Cⁱ), 25.5 (C¹⁷), 25.4 (C¹⁴); *m/z* (HRMS⁺) 688.1774 [M-Cl]⁺ (C₃₂H₃₉N₅O₄³⁵Cl⁹⁶Ru requires 688.1767).



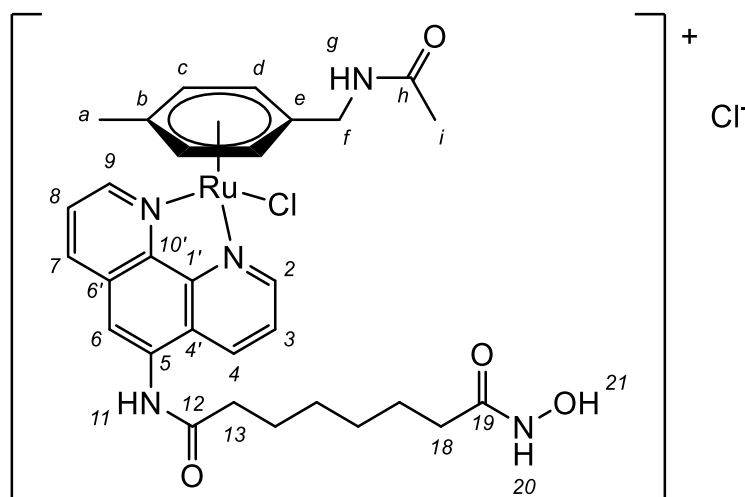
Chloro(N-benzoyl- η^6 -benzylamide) N^{20} -hydroxy- N^{11} -(1,10-phenanthroline-5-yl)octanediamide ruthenium(II) chloride Ru_4Cl^2

Dichloro(N-benzoyl- η^6 -benzylamide) ruthenium(II) dimer (0.040 g, 0.052 mmol) and **N^{20} -hydroxy- N^{11} -(1,10-phenanthroline-5-yl)octanediamide** (0.038 g, 0.104 mmol) were suspended in anhydrous MeOH (10 mL) and the solution was heated to 40 °C under an argon atmosphere, for 16 h. The volume of the solution was reduced to 1.5 mL and purified by reverse phase HPLC (H₂O : MeOH) to yield the *title compound* (0.012 g, 31%) as a dark yellow solid; δ_H (DMSO- d_6) 10.6 (1H, s, H¹¹), 10.4 (1H, s, H²¹), 10.0 (1H, d, ³J_{HH} 5.0 Hz, H²), 9.84 (1H, d, ³J_{HH} 5.1 Hz, H⁹), 9.15 (1H, t, ³J_{HH} 5.7 Hz, H⁶), 9.00 (1H, d, ³J_{HH} 8.5 Hz, H⁴), 8.75 (1H, d, ³J_{HH} 8.3 Hz, H⁷), 8.65 (1H, s, H²⁰), 8.43 (1H, s, H⁶), 8.10 (1H, dd, ³J_{HH} 8.5 Hz ³J_{HH} 5.0 Hz, H³), 8.00 (1H, dd, ³J_{HH} 8.3 Hz ³J_{HH} 5.1 Hz, H⁸), 7.64 (2H, d, ³J_{HH} 6.9 Hz, H^o), 7.40 (1H, t, ³J_{HH} 6.9 Hz, H^p), 7.37 (2H, t, ³J_{HH} 6.9 Hz, H^m), 6.43 (2H, d, ³J_{HH} 5.8 Hz, H^c), 6.37 (2H, t, ³J_{HH} 5.8 Hz, H^b), 6.05 (1H, t, ³J_{HH} 5.8 Hz, H^a), 4.35 (2H, d, ³J_{HH} 5.7 Hz, H^e), 2.57 (2H, t, ³J_{HH} 7.1 Hz, H¹³), 1.95 (2H, t, ³J_{HH} 7.1 Hz, H¹⁸), 1.68-1.64 (2H, bm, H¹⁴), 1.51-1.47 (2H, bm, H¹⁷), 1.38-1.34 (2H, bm, H¹⁵), 1.31-1.27 (2H, bm, H¹⁶); δ_C (DMSO- d_6) 173.2 (C¹²), 169.5 (C¹⁹), 166.5 (C⁸), 156.5 (C²), 155.2 (C⁹), 146.1 (C¹), 143.5 (C¹⁰), 138.4 (C⁷), 135.2 (C⁴), 133.8 (C⁶), 133.5 (Cⁱ), 131.9 (C^p), 130.1 (C^{4'}), 128.6 (2C, C^m), 127.6 (2C, C^o), 126.6 (C⁸), 126.5 (C⁵), 125.8 (C³), 118.9 (C⁶), 86.6 (C^a), 86.2 (2C, C^b), 86.1 (2C, C^c), 86.0 (C^d), 40.9 (C^e), 36.4 (C¹³), 32.7 (C¹⁸), 28.9 (C¹⁶), 28.8 (C¹⁵), 25.5 (C¹⁴), 25.4 (C¹⁷); m/z (HRMS⁺) 708.1465 [M-Cl]⁺ (C₃₄H₃₅N₅O₄³⁵Cl⁹⁶Ru requires 708.1454).



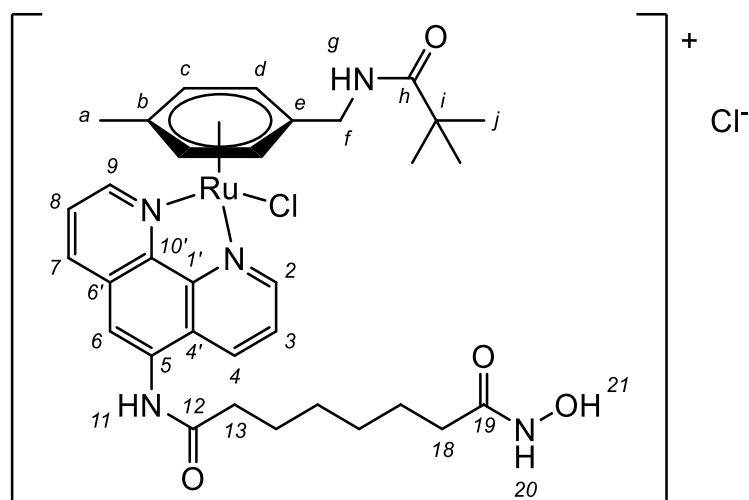
Chloro(η^6 -N-2-thiophenecarbonylbzylamide) N^{20} -hydroxy- N^{11} -(1,10-phenanthrolin-5-yl)octanediamide ruthenium(II) chloride Ru4DL²

Dichloro(η^6 -N-2-thiophenecarbonylbzylamide) ruthenium(II) dimer (0.052 g, 0.067 mmol) and **N^{20} -hydroxy- N^{11} -(1,10-phenanthrolin-5-yl)octanediamide** (0.048 g, 0.133 mmol) were dissolved in anhydrous MeOH (10 mL) and the reaction heated to 40 °C under an argon atmosphere for 16 h. The volume of the resulting solution was reduced to 1.5 mL and purified by reverse phase HPLC (H₂O : MeOH) to afford the *title compound* (0.024 g, 48%) as a pale brown solid; δ_{H} (DMSO-*d*₆) 10.5 (1H, s, H¹¹), 10.3 (1H, s, H²¹), 9.98 (1H, d, ³*J*_{HH} 5.3 Hz, H²), 9.85 (1H, d, ³*J*_{HH} 5.1 Hz, H⁹), 9.18 (1H, t, ³*J*_{HH} 5.7 Hz, H^f), 9.00 (1H, dd, ³*J*_{HH} 8.3 Hz ⁴*J*_{HH} 2.1 Hz, H⁴), 8.76 (1H, d, ³*J*_{HH} 8.3 Hz, H⁷), 8.63 (1H, s, H²⁰), 8.43 (1H, s, H⁶), 8.11 (1H, dd, ³*J*_{HH} 8.3 Hz ³*J*_{HH} 5.3 Hz, H³), 8.00 (1H, dd, ³*J*_{HH} 8.3 Hz ³*J*_{HH} 5.1 Hz, H⁸), 7.70 (1H, d, ³*J*_{HH} 4.1 Hz, H^k), 7.60 (1H, d, ³*J*_{HH} 4.1 Hz, Hⁱ), 7.07 (1H, t, ³*J*_{HH} 4.1 Hz, H^j), 6.42 (2H, d, ³*J*_{HH} 5.0 Hz, H^c), 6.37-6.35 (2H, bm, H^b), 6.05 (1H, t, ³*J*_{HH} 5.0 Hz, H^a), 4.32 (2H, d, ³*J*_{HH} 5.7 Hz, H^e), 2.56 (2H, t, ³*J*_{HH} 7.0 Hz, H¹³), 1.94 (2H, t, ³*J*_{HH} 7.0 Hz, H¹⁸), 1.68-1.64 (2H, bm, H¹⁴), 1.51-1.47 (2H, bm, H¹⁷), 1.37-1.33 (2H, bm, H¹⁵), 1.30-1.27 (2H, bm, H¹⁶); δ_{C} (DMSO-*d*₆) 173.1 (C¹²), 169.5 (C¹⁹), 161.6 (C^g), 156.5 (C²), 155.3 (C⁹), 146.1 (C¹), 143.5 (C^{10'}), 138.9 (C^h), 138.4 (C⁷), 135.2 (C⁴), 133.7 (C⁵), 131.7 (C^k), 130.2 (C^{6'}), 129.1 (Cⁱ), 128.3 (C^j), 126.6 (C⁸), 126.5 (C^{4'}), 125.7 (C³), 118.9 (C⁶), 101.4 (C^d), 86.6 (C^a), 86.2 (2C, C^b), 86.1 (2C, C^c), 40.7 (C^e), 36.4 (C¹³), 32.7 (C¹⁸), 28.9 (C¹⁶), 28.8 (C¹⁵), 25.5 (C¹⁷), 25.4 (C¹⁴); *m/z* (HRMS⁺) 714.1020 [M-Cl]⁺ (C₃₂H₃₃N₅O₄S³⁵Cl⁹⁶Ru requires 714.1018).



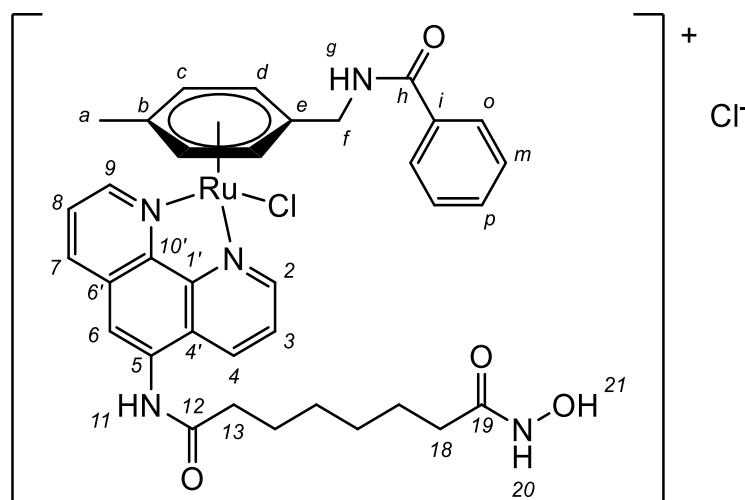
Chloro(η^6 -4-methyl-N-acetylbenzylamide) N^{20} -hydroxy- N^{11} -(1,10-phenanthrolin-5-yl)octanediamide ruthenium(II) chloride Ru5AL²

Dichloro(η^6 -4-methyl-N-acetylbenzylamide) ruthenium(II) dimer (0.038 g, 0.056 mmol) and **N^{20} -hydroxy- N^{11} -(1,10-phenanthrolin-5-yl)octanediamide** (0.041 g, 0.113 mmol) were dissolved in anhydrous MeOH (10 mL) and the reaction heated to 40 °C under an argon atmosphere for 16 h. The volume of the resulting solution was reduced to 1.5 mL and purified by reverse phase HPLC (H₂O : MeOH) to afford the *title compound* (0.053 g, 85%) as a yellow solid; δ_{H} (DMSO-*d*₆) 10.6 (1H, s, H¹¹), 10.4 (1H, s, H²¹), 9.92 (1H, d, ³*J*_{HH} 5.0 Hz, H²), 9.79 (1H, d, ³*J*_{HH} 5.0 Hz, H⁹), 9.06 (1H, d, ³*J*_{HH} 8.7 Hz, H⁴), 8.81 (1H, d, ³*J*_{HH} 8.2 Hz, H⁷), 8.64 (1H, s, H²⁰), 8.47 (1H, s, H⁶), 8.31 (1H, t, ³*J*_{HH} 5.7 Hz, H⁸), 8.15 (1H, dd, ³*J*_{HH} 8.7 Hz ³*J*_{HH} 5.0 Hz, H³), 8.04 (1H, dd, ³*J*_{HH} 8.2 Hz ³*J*_{HH} 5.0 Hz, H⁸), 6.36 (2H, m, H^d), 6.07 (1H, d, ³*J*_{HH} 5.7 Hz, H^c), 6.06 (1H, d, ³*J*_{HH} 5.7 Hz, H^{c'}), 3.43 (2H, d, ³*J*_{HH} 5.7 Hz, H^f), 2.56 (2H, t, ³*J*_{HH} 7.4 Hz, H¹³), 2.13 (3H, s, H^a), 1.93 (2H, t, ³*J*_{HH} 7.4 Hz, H¹⁸), 1.65 (2H, quin, ³*J*_{HH} 7.4 Hz, H¹⁴), 1.49 (2H, quin, ³*J*_{HH} 7.4 Hz, H¹⁷), 1.46 (3H, s, Hⁱ), 1.37-1.32 (2H, m, H¹⁵), 1.30-1.26 (2H, m, H¹⁷); δ_{C} (DMSO-*d*₆) 173.2 (C¹²), 169.6 (C^b), 169.5 (C¹⁹), 156.3 (C²), 155.1 (C⁹), 146.2 (C¹), 143.6 (C^{10'}), 138.4 (C⁷), 135.2 (C⁴), 133.8 (C⁵), 130.1 (C^{6'}), 127.6 (C^{4'}), 126.6 (C⁸), 125.8 (C³), 119.0 (C⁶), 104.8 (C^b), 95.4 (C^e), 88.5-88.4 (C^d, C^{d'}), 82.9-82.7 (C^c, C^{c'}), 39.3 (C^f), 36.4 (C¹³), 32.7 (C¹⁸), 28.9 (C¹⁶), 28.8 (C¹⁵), 25.5 (C¹⁷), 25.4 (C¹⁴), 22.4 (Cⁱ), 18.8 (C^a); *m/z* (HRMS⁺) 660.1476 [M-Cl]⁺ (C₃₀H₃₅N₅O₄³⁵Cl⁹⁶Ru requires 660.1454).



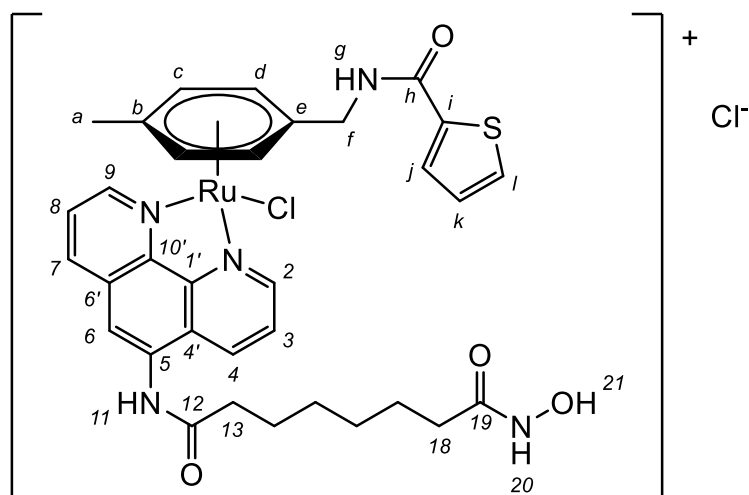
Chloro(η^6 -4-methyl-*N*-trimethylacetylbenzylamide) N^{20} -hydroxy- N^{11} -(1,10-phenanthrolin-5-yl)octanediamide ruthenium(II) chloride Ru5BL²

Dichloro(η^6 -4-methyl-*N*-trimethylacetylbenzylamide) ruthenium(II) dimer (0.037 g, 0.049 mmol) and ***N*²⁰-hydroxy-*N*¹¹-(1,10-phenanthrolin-5-yl)octanediamide** (0.035 g, 0.098 mmol) were dissolved in anhydrous MeOH (10 mL) and the reaction heated to 40 °C under an argon atmosphere for 16 h. The volume of the resulting solution was reduced to 1.5 mL and purified by reverse phase HPLC (H₂O : MeOH) to afford the *title compound* (0.027 g, 75%) as a yellow solid; δ_{H} (DMSO-*d*₆) 10.56 (1H, s, H¹¹), 10.36 (1H, s, H²¹), 9.94 (1H, d, ³*J*_{HH} 5.3 Hz, H²), 9.80 (1H, d, ³*J*_{HH} 5.5 Hz, H⁹), 9.05 (1H, d, ³*J*_{HH} 8.2 Hz, H⁴), 8.82 (1H, d, ³*J*_{HH} 8.1 Hz, H⁷), 8.64 (1H, s, H²⁰), 8.48 (1H, s, H⁶), 8.16 (1H, dd, ³*J*_{HH} 8.2 Hz ³*J*_{HH} 5.3 Hz, H³), 8.05 (1H, dd, ³*J*_{HH} 8.1 Hz ³*J*_{HH} 5.5 Hz, H⁸), 7.94 (1H, t, ³*J*_{HH} 5.8 Hz, H⁸), 6.29 (1H, d, ³*J*_{HH} 6.0 Hz, H^d), 6.28 (1H, d, ³*J*_{HH} 6.0 Hz, H^{d'}), 6.07 (2H, bm, H^c H^{c'}), 3.94 (2H, d, ³*J*_{HH} 5.8 Hz, H^f), 2.56 (2H, t, ³*J*_{HH} 7.2 Hz, H¹³), 2.15 (3H, s, H^a), 1.94 (2H, t, ³*J*_{HH} 7.2 Hz, H¹⁸), 1.66 (2H, 2H, quin, ³*J*_{HH} 7.2 Hz, H¹⁴), 1.49 (2H, quin, ³*J*_{HH} 7.2 Hz, H¹⁷), 1.38-1.33 (2H, m, H¹⁵), 1.31-1.27 (2H, m, H¹⁶), 0.80 (9H, s, Hⁱ); δ_{C} (DMSO-*d*₆) 177.8 (C^h), 173.1 (C¹²), 169.5 (C¹⁹), 156.2 (C²), 154.9 (C⁹), 146.4 (C^{1'}), 143.7 (C^{10'}), 138.4 (C⁷), 135.2 (C⁴), 133.7 (C^{4'}), 130.2 (C^{6'}), 126.6 (C⁸), 126.5 (C⁵), 125.8 (C³), 118.9 (C⁶), 104.4 (C^b), 95.8 (C⁶), 87.8-87.7 (C^d, C^{d'}), 83.3-83.1 (C^c, C^{c'}), 39.5 (C^f), 38.3 (Cⁱ), 36.4 (C¹³), 32.7 (C¹⁸), 28.8 (C¹⁵, C¹⁶), 27.5 (C^j), 25.4 (C¹⁴, C¹⁷), 18.9 (C^a); *m/z* (HRMS⁺) 702.1948 [M-Cl]⁺ (C₃₃H₄₁N₅O₄³⁵Cl⁹⁶Ru requires 702.1923).



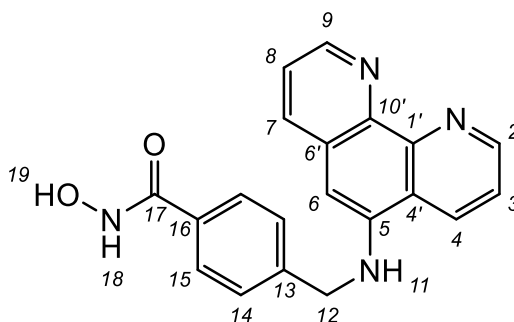
Chloro(4-methyl-N-benzoyl- η^6 -benzylamide) N^{20} -hydroxy- N^{11} -(1,10-phenanthroline-5-yl)octanediamide ruthenium(II) chloride Ru5Cl²

Dichloro(η^6 -4-methyl-N-benzoylbenzylamide) ruthenium(II) dimer (0.040 g, 0.050 mmol) and **N^{20} -hydroxy- N^{11} -(1,10-phenanthroline-5-yl)octanediamide** (0.036 g, 0.100 mmol) were dissolved in anhydrous MeOH (10 mL) and the reaction heated to 40 °C under an argon atmosphere for 16 h. The volume of the resulting solution was reduced to 1.5 mL and purified by reverse phase HPLC (H₂O : MeOH) to afford the *title compound* (0.050 g, 67%) as a yellow solid; δ_{H} (DMSO-*d*₆) 10.53 (1H, s, H¹¹), 10.38 (1H, s, H²¹), 9.92 (1H, d, ³*J*_{HH} 5.0 Hz, H²), 9.78 (1H, d, ³*J*_{HH} 4.8 Hz, H⁹), 8.96-8.94 (2H, m, H⁴, H⁸), 8.68 (1H, d, ³*J*_{HH} 8.0 Hz, H⁷), 8.65 (1H, s, H²⁰), 8.40 (1H, s, H⁶), 8.04 (1H, dd, ³*J*_{HH} 8.1 Hz ³*J*_{HH} 5.0 Hz, H³), 7.93 (1H, dd, ³*J*_{HH} 8.0 Hz ³*J*_{HH} 4.8 Hz, H⁸), 7.44 (1H, t, ³*J*_{HH} 7.0 Hz, H⁹), 7.36 (2H, d, ³*J*_{HH} 7.0 Hz, H⁹), 7.29 (2H, t, ³*J*_{HH} 7.0 Hz, H^m), 6.55 (2H, bm, H^d H^{d'}), 6.05 (1H, d, ³*J*_{HH} 7.0 Hz, H^c), 6.03 (1H, d, ³*J*_{HH} 7.0 Hz, H^{c'}), 4.12 (2H, d, ³*J*_{HH} 6.0 Hz, H^f), 2.59 (2H, t, ³*J*_{HH} 7.0 Hz, H¹³), 2.18 (3H, s, H^a), 1.96 (2H, t, ³*J*_{HH} 7.0 Hz, H¹⁸), 1.68 (2H, quin, ³*J*_{HH} 7.0 Hz, H¹⁴), 1.52 (2H, quin, ³*J*_{HH} 7.0 Hz, H¹⁷), 1.39-1.36 (2H, m, H¹⁵), 1.34-1.31 (2H, m, H¹⁶); δ_{C} (DMSO-*d*₆) 173.1 (C¹²), 169.5 (C¹⁹), 165.7 (C^b), 156.1 (C²), 154.9 (C⁹), 146.3 (C¹), 143.6 (C¹⁰), 138.2 (C⁷), 134.9 (C⁴), 133.6 (C^{4'}), 132.9 (Cⁱ), 131.8 (C^p), 130.2 (C⁶), 128.4 (2C, C^m), 127.7 (C⁵), 127.4 (2C, C^o), 126.4 (C⁸), 125.6 (C³), 118.7 (C⁶), 107.4 (C^b), 94.6 (C^e), 89.8-89.7 (C^d, C^{d'}), 81.5-81.2 (C^c, C^{c'}), 39.6 (C^f), 36.4 (C¹³), 32.7 (C¹⁸), 28.8 (C¹⁵, C¹⁶), 25.5 (C¹⁴, C¹⁷), 19.3 (C^a); *m/z* (HRMS⁺) 722.1605 [M-Cl]⁺ (C₃₅H₃₇N₅O₄³⁵Cl⁹⁶Ru requires 722.1610).



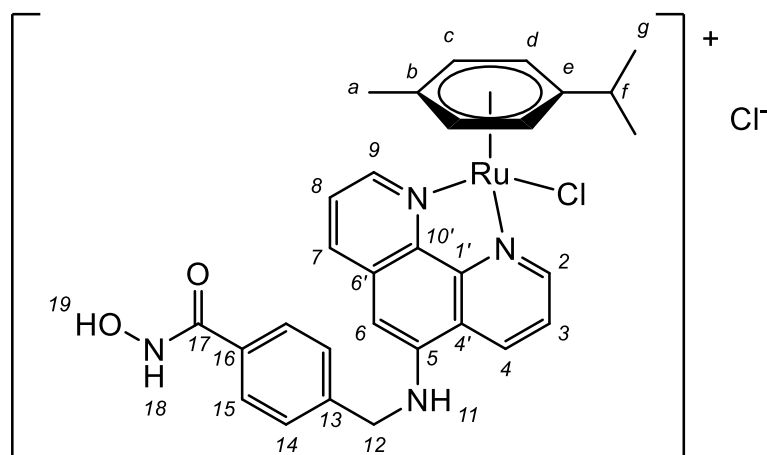
Chloro(4-methyl-N-2-thiophenecarbonyl- η^6 -benzylamide) N^{20} -hydroxy- N^{11} -(1,10-phenanthrolin-5-yl)octanediamide ruthenium(II) chloride Ru5DL²

Dichloro(η^6 -4-methyl-N-2-thiophenecarbonylbenzylamide) ruthenium(II) dimer (0.019 g, 0.024 mmol) and **N^{20} -hydroxy- N^{11} -(1,10-phenanthrolin-5-yl)octanediamide** (0.017 g, 0.048 mmol) were dissolved in anhydrous MeOH (10 mL) and the reaction heated to 40 °C under an argon atmosphere for 16 h. The volume of the resulting solution was reduced to 1.5 mL and purified by reverse phase HPLC (H₂O : MeOH) to afford the *title compound* (0.009 g, 50%) as a yellow solid; δ_{H} (DMSO-*d*₆) 10.45 (1H, s, H¹¹), 10.35 (1H, s, H²¹), 9.89 (1H, d, ³*J*_{HH} 4.8 Hz, H²), 9.75 (1H, d, ³*J*_{HH} 4.8 Hz, H⁹), 8.94-8.91 (2H, m, H^s H⁴), 8.67 (1H, d, ³*J*_{HH} 7.8 Hz, H⁷), 8.63 (1H, s, H²⁰), 8.40 (1H, s, H⁶), 8.04 (1H, dd, ³*J*_{HH} 8.4 Hz ³*J*_{HH} 4.8 Hz, H³), 7.92 (1H, dd, ³*J*_{HH} 7.8 Hz ³*J*_{HH} 4.8 Hz, H⁸), 7.62 (1H, dd, ³*J*_{HH} 4.0 Hz ⁴*J*_{HH} 1.0 Hz, H¹), 7.29 (1H, d, ³*J*_{HH} 4.0 Hz, H¹), 6.96 (1H, t, ³*J*_{HH} 4.0 Hz, H^k), 6.54 (2H, d, ³*J*_{HH} 6.5 Hz, H^d), 6.03 (1H, d, ³*J*_{HH} 6.5 Hz, H^c), 6.01 (1H, d, ³*J*_{HH} 6.5 Hz, H^c), 4.07 (2H, d, ³*J*_{HH} 6.5 Hz, H^f), 2.56 (2H, t, ³*J*_{HH} 6.7 Hz, H¹³), 2.17 (3H, s, H^a), 1.94 (2H, t, ³*J*_{HH} 6.7 Hz, H¹⁸), 1.66 (2H, quin, ³*J*_{HH} 6.7 Hz, H¹⁴), 1.49 (2H, quin, ³*J*_{HH} 6.7 Hz, H¹⁷), 1.38-1.33 (2H, m, H¹⁵), 1.31-1.27 (2H, m, H¹⁶); δ_{C} (DMSO-*d*₆) 173.1 (C¹²), 169.5 (C¹⁹), 160.9 (C^h), 156.1 (C²), 154.8 (C⁹), 146.2 (C¹), 143.6 (C¹⁰), 138.6 (Cⁱ), 138.2 (C⁷), 134.8 (C⁴), 133.6 (C⁴), 131.5 (C¹), 130.1 (C⁶), 128.8 (C^j), 128.0 (C^k), 127.6 (C⁵), 126.4 (C⁸), 125.6 (C³), 118.7 (C⁶), 107.5 (C^b), 94.5 (C^e), 89.9 (2C, C^d), 81.4-81.1 (2C, C^c C^c), 39.4 (C^f), 36.4 (C¹³), 32.7 (C¹⁸), 28.8 (2C, C¹⁵ C¹⁶), 25.5 (C¹⁴), 25.4 (C¹⁷), 19.3 (C^a); *m/z* (HRMS⁺) 728.1183 [M-Cl]⁺ (C₃₃H₃₅N₅O₄S³⁵Cl⁹⁶Ru requires 728.1174).



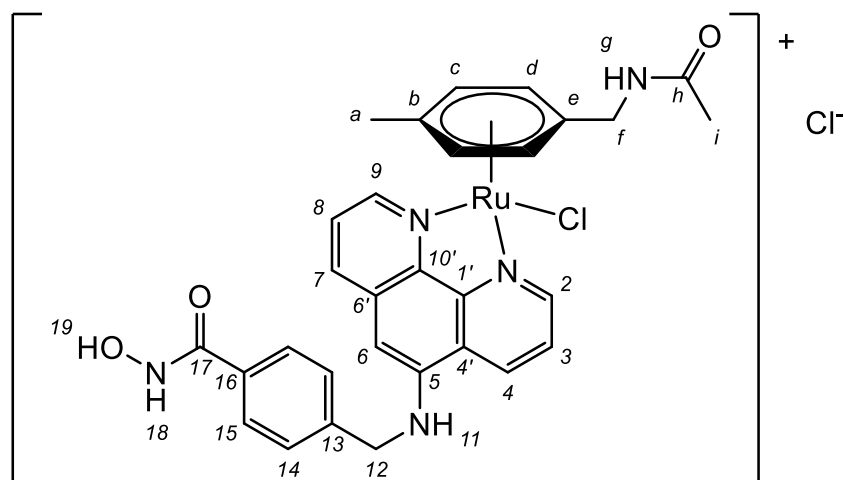
***N*¹⁸-Hydroxy-4-[(1,10-phenanthrolin-5-yl)amino]methyl}benzamide *L*³**

1,10-Phenanthroline-5-amine (0.050 g, 0.25 mmol), methyl 4-(bromomethyl)benzoate (0.059 g, 0.25 mmol) and trimethylamine (0.038 mL, 0.28 mmol) were suspended in anhydrous THF (10 mL) and the resulting mixture was heated at 60 °C, under an argon atmosphere for 16 h. The solution was extracted into ethyl acetate (20 mL) and washed with water (20 mL) and brine (20 mL). The organic layers were combined, dried over Na₂SO₄, filtered and solvent removed under vacuum. The crude orange solid was suspended in MeOH (3.75 mL), hydroxylamine (50%) solution (3.75 mL) and 1M NaOH (0.75 mL) were added and the mixture stirred for 30 min. The solution was neutralised and the resulting precipitate was filtered and washed with water to give the *title compound* (0.016 g, 9%). δ_{H} (DMSO-*d*₆) 11.1 (1H, s, H¹⁹), 9.08 (1H, dd, ³*J*_{HH} 4.3 Hz ⁴*J*_{HH} 1.5 Hz, H²), 8.95 (1H, s, H¹⁸), 8.87 (1H, dd, ³*J*_{HH} 8.6 Hz ⁴*J*_{HH} 1.5 Hz, H⁴), 8.65 (1H, dd, ³*J*_{HH} 4.4 Hz ⁴*J*_{HH} 1.6 Hz, H⁹), 8.05 (1H, d, ³*J*_{HH} 8.0 Hz, H⁷), 7.80 (1H, dd, ³*J*_{HH} 8.6 Hz ³*J*_{HH} 4.3 Hz, H³), 7.68 (2H, d, ³*J*_{HH} 8.1 Hz, H¹⁵), 7.52-7.50 (1H, m, H⁸), 7.50 (2H, d, ³*J*_{HH} 8.1 Hz, H¹⁴), 7.45 (1H, t, ³*J*_{HH} 5.5 Hz, H¹¹), 6.60 (1H, s, H⁶), 4.62 (2H, d, ³*J*_{HH} 5.5 Hz, H¹²); δ_{C} (DMSO-*d*₆) 164.5 (C¹⁷), 149.9 (C²), 144.6 (C⁹), 143.1 (C¹³), 142.1 (C^{1'}), 139.6 (C^{10'}), 134.7 (C⁷), 131.8 (C¹⁶), 131.7 (C^{6'}), 131.0 (C⁴), 127.5 (2C, C¹⁵), 127.4 (2C, C¹⁴), 123.9 (C⁸), 123.1 (C³), 122.5 (C^{4'}), 115.7 (C⁵), 99.0 (C⁶), 46.5 (C¹²); *m/z* (HRMS⁺) 345.1362 [M+H]⁺ (C₂₀H₁₇N₄O₂ requires 345.1352).



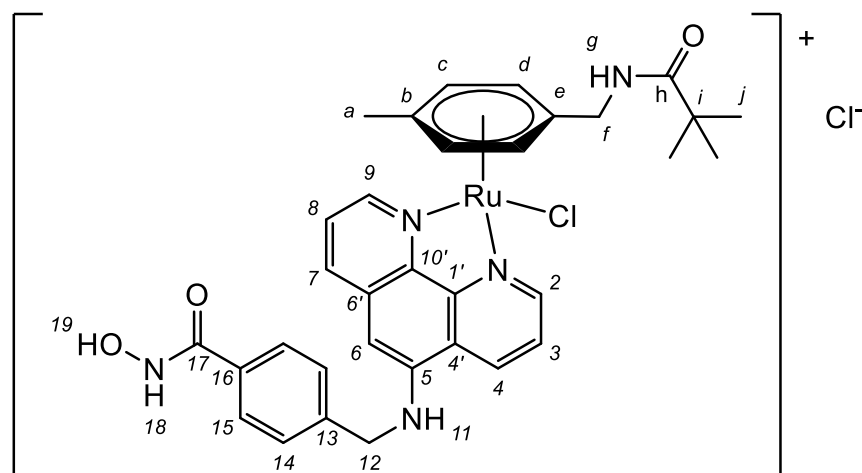
Chloro(p-cymene) N¹⁸-hydroxy-N¹¹-{[(1,10-phenanthrolin-5-yl)amino]methyl}benzamide ruthenium(II) chloride Ru1L³

N¹⁸-Hydroxy-4-{[(1,10-phenanthrolin-5-yl)amino]methyl}benzamide (0.022 g, 0.066 mmol) and **dichloro(p-cymene) ruthenium(II) dimer** (0.020 g, 0.033 mmol) were suspended in anhydrous MeOH (5 mL). The reaction was stirred under an inert atmosphere at 40 °C for 16 h. The volume of the solution was reduced and added to diethyl ether (10 mL). The resulting precipitate was purified by reverse phase HPLC (H₂O : MeOH) to provide the *title compound* as a light yellow solid (0.015 g, 36%). δ_{H} (DMSO-d₆) 11.1 (1H, s, H¹⁹), 9.89 (1H, d, ³J_{HH} 5.3 Hz, H²), 9.40 (1H, d, ³J_{HH} 4.8 Hz, H⁹), 9.30 (1H, d, ³J_{HH} 8.4 Hz, H⁴), 8.96 (1H, s, H¹⁸), 8.32 (1H, d, ³J_{HH} 8.0 Hz, H⁷), 8.20 (1H, m, H¹¹), 8.13 (1H, dd, ³J_{HH} 8.4 Hz ³J_{HH} 5.3 Hz, H³), 7.77 (1H, dd, ³J_{HH} 8.0 Hz ³J_{HH} 4.8 Hz, H⁸), 7.69 (2H, d, ³J_{HH} 8.0 Hz, H¹⁵), 7.51 (2H, d, ³J_{HH} 8.0 Hz, H¹⁴), 6.74 (1H, s, H⁶), 6.26 (1H, d, ³J_{HH} 5.2 Hz, H^d), 6.25 (1H, d, ³J_{HH} 5.2 Hz, H^{d'}), 6.04 (1H, d, ³J_{HH} 5.2 Hz, H^c), 6.01 (1H, d, ³J_{HH} 5.2 Hz, H^{c'}), 4.64 (2H, d, ³J_{HH} 5.5 Hz, H¹²), 2.57 (1H, septet, ³J_{HH} 7.2 Hz, H^f), 2.13 (3H, s, H^a), 0.89 (3H, d, ³J_{HH} 7.2 Hz, H^g), 0.87 (3H, d, ³J_{HH} 7.2 Hz, H^{g'}); δ_{C} (DMSO-d₆) 164.4 (C¹⁷), 156.1 (C²), 150.9 (C⁹), 146.4 (C¹), 143.5 (C⁵), 142.1 (C¹³), 139.7 (C¹⁰), 135.6 (C⁷), 134.0 (C⁴), 132.5 (C⁶), 132.0 (C¹⁶), 127.5 (2C, C¹⁵), 127.4 (2C, C¹⁴), 126.5 (C⁸), 125.4 (C³), 124.0 (C^{4'}), 104.1 (C^e), 103.0 (C^b), 98.3 (C⁶), 86.5 (C^d), 86.2 (C^{d'}), 84.3 (C^c), 84.1 (C^{c'}), 46.5 (C¹²), 30.8 (C^f), 22.1 (C^g), 22.0 (C^{g'}), 18.6 (C^a); *m/z* (HRMS⁺) 609.1140 [M-Cl]⁺ (C₃₀H₃₀N₄O₂³⁵Cl⁹⁶Ru requires 609.1133).



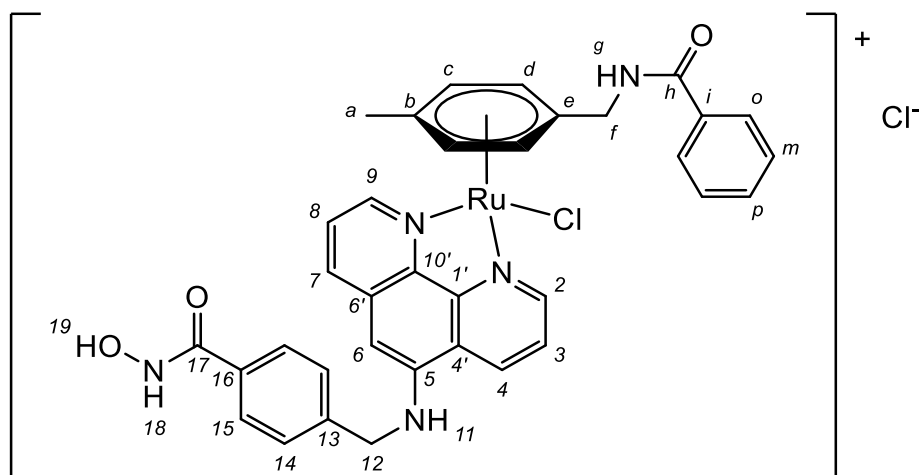
Chloro(η^6 -4-methyl-N-acetylbenzamide)N¹⁸-hydroxy-N¹¹-[(1,10-phenanthrolin-5-yl)amino]methylbenzamide ruthenium(II) chloride Ru5AL³

N¹⁸-Hydroxy-4-[(1,10-phenanthrolin-5-yl)amino]methylbenzamide (0.026 g, 0.075 mmol) and **dichloro(η^6 -4-methyl-N-acetylbenzamide) ruthenium(II) dimer** (0.025 g, 0.037 mmol) were suspended in MeOH (10 mL) and heated at 40 °C under an inert atmosphere for 16 h. The volume of solution was reduced by half and added, dropwise to diethyl ether (10 mL). The resulting precipitate was purified by reverse phase HPLC (H₂O : MeOH) to afford the *title compound* as a yellow solid (0.020 g, 39%). δ_{H} (DMSO-d₆) 11.1 (1H, s, H¹⁹), 9.87 (1H, d, ³J_{HH} 5.0 Hz, H²), 9.38 (1H, d, ³J_{HH} 5.0 Hz, H⁹), 9.26 (1H, d, ³J_{HH} 8.5 Hz, H⁴), 8.96 (1H, s, H¹⁸), 8.30-8.28 (2H, m, H⁸ H⁷), 8.16 (1H, t, ³J_{HH} 6.0 Hz, H¹¹), 8.10 (1H, dd, ³J_{HH} 8.5 Hz ³J_{HH} 5.4 Hz, H³), 7.74 (1H, dd, ³J_{HH} 8.3 Hz ³J_{HH} 5.0 Hz, H⁸), 7.67 (2H, d, ³J_{HH} 7.7 Hz, H¹⁵), 7.49 (2H, d, ³J_{HH} 7.7 Hz, H¹⁴), 6.72 (1H, s, H⁶), 6.28 (1H, d, ³J_{HH} 6.0 Hz, H^d), 6.27 (1H, d, ³J_{HH} 6.0 Hz, H^{d'}), 6.01 (1H, d, ³J_{HH} 6.0 Hz, H^c), 6.00 (1H, d, ³J_{HH} 6.0 Hz, H^{c'}), 4.64 (2H, d, ³J_{HH} 6.0 Hz, H¹²), 3.92 (2H, d, ³J_{HH} 6.5 Hz, H^f), 2.07 (3H, s, H^a), 1.50 (3H, s, Hⁱ); δ_{C} (DMSO-d₆) 169.7 (C^h), 164.4 (C¹⁷), 156.0 (C²), 150.8 (C⁹), 146.7 (C^{1'}), 143.4 (C⁵), 142.2 (C¹³), 140.1 (C^{10'}), 135.5 (C⁷), 133.9 (C⁴), 132.5 (C^{6'}), 131.8 (C¹⁶), 127.5 (2C, C¹⁵), 127.4 (2C, C¹⁴), 126.3 (C⁸), 125.2 (C³), 124.1 (C^{4'}), 103.7 (C^b), 98.3 (C⁶), 95.4 (C^e), 88.3 (C^d), 88.2 (C^{d'}), 83.4 (C^c), 83.1 (C^{c'}), 46.5 (C¹²), 39.5 (C^f), 22.5 (Cⁱ), 18.7 (C^a); *m/z* (HRMS⁺) 638.1055 [M-Cl]⁺ (C₃₀H₂₉N₅O₃³⁵Cl⁹⁶Ru requires 638.1035).



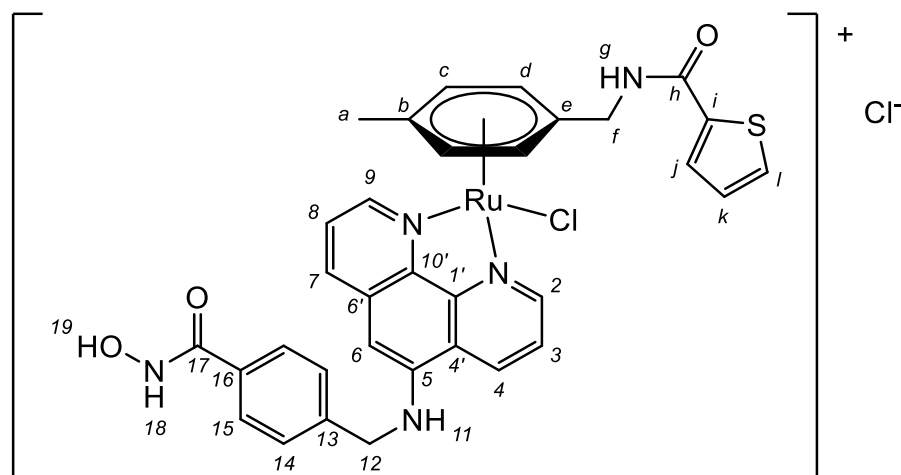
Chloro(η^6 -4-methyl-N-trimethylacetylbenzylamide) N^{18} -hydroxy- N^{11} -{[(1,10-phenanthrolin-5-yl)amino] methyl}benzamide ruthenium(II) chloride Ru5BL³

N^{18} -Hydroxy-4-{[(1,10-phenanthrolin-5-yl)amino]methyl}benzamide (0.022 g, 0.066 mmol) and **dichloro(η^6 -4-methyl-N-trimethylacetylbenzylamide) ruthenium(II) dimer** (0.025 g, 0.033 mmol) were suspended in anhydrous MeOH (5 mL). The reaction was stirred under an inert atmosphere at room temperature for 16 h. The volume of the solution was reduced and added to diethyl ether (10 mL), cooled in a dry ice: acetone bath. The resulting precipitate was purified by reverse phase HPLC (H₂O : MeOH) to provide the *title compound* as a light brown solid (0.029 g, 63%). δ_{H} (DMSO-*d*₆) 11.1 (1H, s, H¹⁹), 9.90 (1H, d, ³J_{HH} 4.9 Hz, H²), 9.40 (1H, d, ³J_{HH} 5.2 Hz, H⁹), 9.26 (1H, d, ³J_{HH} 8.3 Hz, H⁴), 8.98 (1H, s, H¹⁸), 8.31 (1H, d, ³J_{HH} 8.5 Hz, H⁷), 8.16-8.12 (2H, m, H³ H¹¹), 7.93 (1H, t, ³J_{HH} 5.8 Hz, H⁸), 7.77 (1H, dd, ³J_{HH} 8.5 Hz ³J_{HH} 5.2 Hz, H⁸), 7.71 (2H, d, ³J_{HH} 8.5 Hz, H¹⁵), 7.51 (2H, d, ³J_{HH} 8.5 Hz, H¹⁴), 6.73 (1H, s, H⁶), 6.25 (1H, d, ³J_{HH} 6.0 Hz, H^d), 6.20 (1H, d, ³J_{HH} 6.0 Hz, H^{d'}), 6.04 (1H, d, ³J_{HH} 5.8 Hz, H^c), 6.03 (1H, d, ³J_{HH} 5.8 Hz, H^{c'}), 4.67 (2H, d, ³J_{HH} 5.6 Hz, H¹²), 3.94 (2H, d, ³J_{HH} 5.8 Hz, H^f), 2.13 (3H, s, H^a), 0.82 (9H, s, Hⁱ); δ_{C} (DMSO-*d*₆) 177.8 (C^h), 164.4 (C¹⁷), 155.9 (C²), 150.7 (C⁹), 146.8 (C^{1'}), 143.4 (C⁵), 142.5 (C¹³), 140.2 (C^{10'}), 135.4 (C⁷), 133.8 (C⁴), 132.6 (C^{6'}), 131.9 (C¹⁶), 127.4 (2C, C¹⁵), 127.3 (2C, C¹⁴), 126.3 (C⁸), 125.2 (C³), 124.1 (C^{4'}), 103.6 (C^b), 98.2 (C⁶), 95.8 (C^e), 87.7 (C^d), 87.5 (C^{d'}), 83.6 (C^c), 83.4 (C^{c'}), 46.4 (C¹²), 39.5 (C^f), 38.3 (Cⁱ), 27.5 (C^j), 18.7 (C^a); *m/z* (HRMS⁺) 680.1503 [M-Cl]⁺ (C₃₃H₃₅N₅O₃³⁵Cl⁹⁶Ru requires 680.1504).



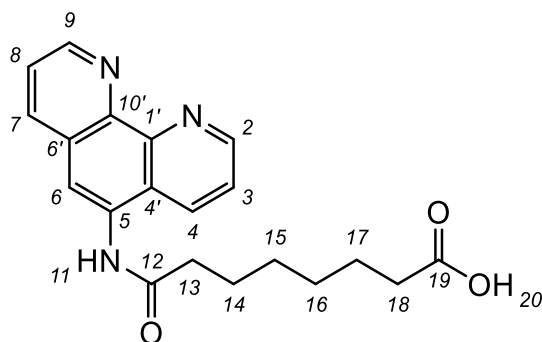
Chloro(4-methyl-N-benzoyl- η^6 -benzylamide)N¹⁸-hydroxy-N¹¹-[(1,10-phenanthrolin-5-yl)amino]methylbenzamide ruthenium(II) chloride Ru5Cl³

N¹⁸-Hydroxy-4-[(1,10-phenanthrolin-5-yl)amino]methylbenzamide (0.020 g, 0.058 mmol) and **dichloro(η^6 -4-methyl-N-benzoylbenzylamide) ruthenium(II) dimer** (0.023 g, 0.029 mmol) were suspended in anhydrous MeOH (5 mL). The reaction was stirred under an inert atmosphere at room temperature for 16 h. The volume of the solution was reduced and added to diethyl ether (10 mL), cooled in a dry ice: acetone bath. The resulting precipitate was purified by reverse phase HPLC (H₂O : MeOH) to provide the *title compound* as a yellow solid (0.010 g, 23%). δ_{H} (MeOD-d₄) 9.75 (1H, d, ³J_{HH} 5.3 Hz, H²), 9.26 (1H, d, ³J_{HH} 5.5 Hz, H⁹), 8.88 (1H, d, ³J_{HH} 8.0 Hz, H⁴), 7.95 (1H, d, ³J_{HH} 8.0 Hz, H⁷), 7.92 (1H, dd, ³J_{HH} 8.0 Hz ³J_{HH} 5.3 Hz, H³), 7.71 (2H, d, ³J_{HH} 8.3 Hz, H¹⁵), 7.55-7.53 (3H, m, H¹⁴, H⁸), 7.42 (1H, t, ³J_{HH} 8.1 Hz, H^p), 7.27 (2H, d, ³J_{HH} 8.1 Hz, H^o), 7.20 (2H, t, ³J_{HH} 8.1 Hz, H^m), 6.47 (1H, s, H⁶), 6.43 (1H, d, ³J_{HH} 6.3 Hz, H^d), 6.39 (1H, d, ³J_{HH} 6.3 Hz, H^{d'}), 5.87 (1H, d, ³J_{HH} 6.3 Hz, H^c), 5.85 (1H, d, ³J_{HH} 6.3 Hz, H^{c'}), 4.62 (1H, d, ²J_{HH} -16.4 Hz, H¹²), 4.56 (1H, d, ²J_{HH} -16.4 Hz, H^{12'}), 4.25 (1H, d, ²J_{HH} -15.0 Hz, H^f), 4.21 (1H, d, ²J_{HH} -15.0 Hz, H^{f'}), 2.25 (3H, s, H^a); δ_{C} (MeOD-d₄) 167.1 (C^h), 166.4 (C¹⁷), 154.8 (C²), 149.8 (C⁹), 146.8 (C^{1'}), 142.9 (C⁵), 142.3 (C¹³), 140.3 (C^{10'}), 135.1 (C⁷), 132.7 (C⁴), 132.6 (C^{6'}), 131.9 (Cⁱ), 131.2 (C^p), 131.0 (C¹⁶), 127.9 (2C, C^m), 127.1 (2C, C¹⁵), 126.9 (2C, C¹⁴), 126.6 (2C, C^o), 125.6 (C⁸), 124.5 (C³), 124.2 (C^{4'}), 107.6 (C^b), 98.7 (C⁶), 94.3 (C^e), 89.4 (C^d), 89.3 (C^{d'}), 81.3 (C^c), 80.9 (C^{c'}), 46.5 (C¹²), 39.3 (C^f), 18.0 (C^a); *m/z* (HRMS⁺) 700.1205 [M-Cl]⁺ (C₃₅H₃₁N₅O₃³⁵Cl⁹⁶Ru requires 700.1191).



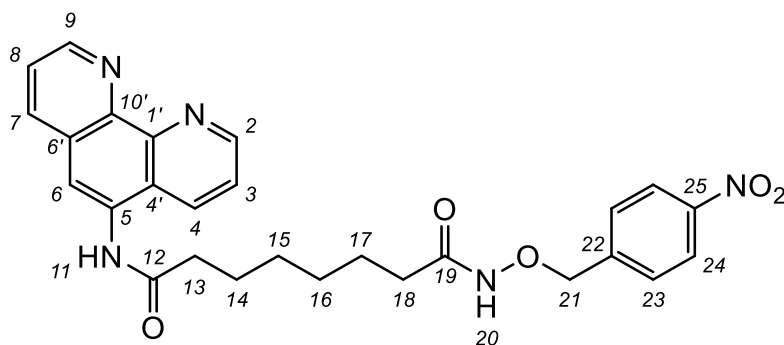
Chloro(4-methyl-N-2-thiophenecarbonyl- η^6 -benzylamide)N¹⁸-hydroxy-N¹¹-[(1,10-phenanthrolin-5-yl) amino]methyl]benzamide ruthenium(II) chloride Ru5DL³

N¹⁸-Hydroxy-4-[(1,10-phenanthrolin-5-yl)amino]methyl]benzamide (0.006 g, 0.018 mmol) and **dichloro(η^6 -4-methyl-N-2-thiophenecarbonylbenzylamide) ruthenium(II) dimer** (0.007 g, 0.009 mmol) were suspended in anhydrous MeOH (5 mL). The reaction was stirred under an inert atmosphere at room temperature for 16 h. The volume of the solution was reduced and added to diethyl ether (10 mL), cooled in a dry ice: acetone bath. The resulting precipitate was purified by reverse phase HPLC (H₂O : MeOH) to provide the *title compound* as a yellow solid (0.006 g, 46%). δ_{H} (MeOD-d₄) 9.73 (1H, d, ³J_{HH} 5.1 Hz, H²), 9.26 (1H, d, ³J_{HH} 5.2 Hz, H⁹), 8.90 (1H, d, ³J_{HH} 8.2 Hz, H⁴), 8.01 (1H, d, ³J_{HH} 8.0 Hz, H⁷), 7.91 (1H, dd, ³J_{HH} 8.2 Hz ³J_{HH} 5.1 Hz, H³), 7.73 (2H, d, ³J_{HH} 8.2 Hz, H¹⁵), 7.58-7.56 (3H, m, H⁸ H¹⁴), 7.45 (1H, dd, ³J_{HH} 5.0 ⁴J_{HH} 1.1 Hz, Hⁱ), 7.09 (1H, dd, ³J_{HH} 3.7 Hz ⁴J_{HH} 1.1 Hz, H^j), 6.89 (1H, dd, ³J_{HH} 5.0 Hz ³J_{HH} 3.7 Hz, H^k), 6.51 (1H, s, H⁶), 6.44 (1H, d, ³J_{HH} 6.2 Hz, H^d), 6.39 (1H, d, ³J_{HH} 6.2 Hz, H^{d'}), 5.86 (1H, d, ³J_{HH} 6.2 Hz, H^c), 5.85 (1H, d, ³J_{HH} 6.2 Hz, H^{c'}), 4.71 (1H, d, ²J_{HH} -16.8 Hz, H¹²), 4.62 (1H, d, ²J_{HH} -16.8 Hz, H^{12'}), 4.20 (1H, d, ²J_{HH} -15.2 Hz, H^f), 4.15 (1H, d, ²J_{HH} -15.2 Hz, H^{f'}), 2.28 (3H, s, H^a); δ_{C} (MeOD-d₄) 166.4 (C¹⁷), 161.7 (C^h), 154.7 (C²), 149.7 (C⁹), 146.8 (C¹), 143.0 (C⁵), 142.4 (C¹³), 140.4 (C^{10'}), 136.9 (Cⁱ), 135.0 (C⁴), 132.7 (C⁷), 132.6 (C¹⁶), 131.1 (C⁶), 130.8 (C^l), 128.3 (C^j), 127.2 (C^k), 127.1 (2C, C¹⁵), 127.0 (2C, C¹⁴), 125.5 (C⁸), 124.4 (C³), 124.3 (C^{4'}), 108.4 (C^b), 98.7 (C⁶), 93.9 (C^e), 89.8 (C^d), 89.6 (C^{d'}), 80.7 (C^c), 80.4 (C^{c'}), 46.5 (C¹²), 39.0 (C^f), 18.1 (C^a); *m/z* (HRMS⁺) 706.0768 [M-Cl]⁺ (C₃₃H₂₉N₅O₃S³⁵Cl⁹⁶Ru requires 706.0756).



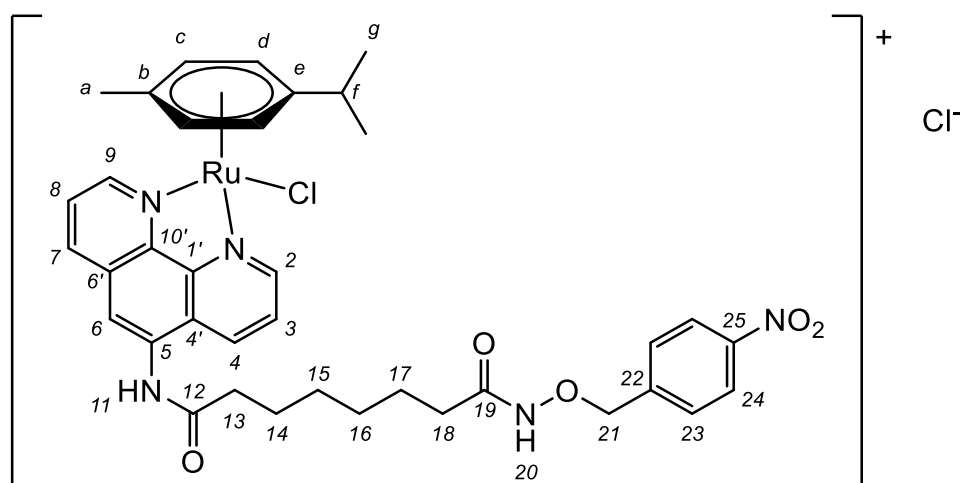
7-[(1,10-Phenanthrolin-5-yl)carbamoyl]heptanoic acid 28

1,10-Phenanthroline-5-amine (0.200 g, 1.02 mmol) and 4-(dimethylamino)pyridine (0.125 g, 1.02 mmol) were suspended in DMF (10 mL) and methyl 8-chloro-8-oxooctanoate (0.189 mL, 1.33 mmol) was added gradually. The reaction was stirred at room temperature for 16 h under an inert atmosphere. The volume of the solution was reduced and added dropwise to a stirring solution of diethyl ether and the filtrate decanted off. The resulting orange solid was then suspended in 10 mL of a MeOH/THF mixture (1:1) and LiOH was added (0.065 g, 1.56 mmol) and the reaction was stirred at ambient temperature for 48 h. The resulting solution was neutralised with 1M HCl, extracted into ethyl acetate (2 x 20 mL), dried over Na₂SO₄, filtered and recrystallized from ethyl acetate to give the *title compound* (0.130 g, 59%). δ_{H} (DMSO-*d*₆) 11.9 (1H, bs, H²⁰), 10.1 (1H, s, H¹¹), 9.09 (1H, dd, ³J_{HH} 4.4 Hz ⁴J_{HH} 1.4 Hz, H²), 9.00 (1H, dd, ³J_{HH} 7.9 Hz ⁴J_{HH} 4.3 Hz, H⁹), 8.57 (1H, dd, ³J_{HH} 8.5 Hz ⁴J_{HH} 1.4 Hz, H⁴), 8.41 (1H, dd, ³J_{HH} 7.9 Hz ⁴J_{HH} 1.6 Hz, H⁷), 8.14 (1H, s, H⁶), 7.80 (1H, dd, ³J_{HH} 8.5 Hz ³J_{HH} 4.4 Hz, H³), 7.70 (1H, dd, ³J_{HH} 7.9 Hz ³J_{HH} 4.3 Hz, H⁸), 2.52 (2H, t, ³J_{HH} 7.3 Hz, H¹³), 2.22 (2H, t, ³J_{HH} 7.3 Hz, H¹⁸), 1.68 (2H, quin, ³J_{HH} 7.3 Hz, H¹⁴), 1.53 (2H, quin, ³J_{HH} 7.3 Hz, H¹⁷), 1.42-1.38 (2H, m, H¹⁵), 1.37-1.34 (2H, m, H¹⁶); δ_{C} (DMSO-*d*₆) 174.9 (C¹⁹), 172.8 (C¹²), 150.2 (C²), 149.6 (C⁹), 146.3 (C¹), 144.2 (C¹⁰), 136.1 (C⁷), 132.1 (C⁵), 132.0 (C⁴), 128.5 (C⁶), 125.1 (C⁴), 123.9 (C⁸), 123.2 (C³), 120.4 (C⁶), 36.3 (C¹³), 34.1 (C¹⁸), 28.9 (C¹⁵), 28.7 (C¹⁶), 25.5 (C¹⁴), 24.8 (C¹⁷); *m/z* (HRMS⁺) 352.1670 [M+H]⁺ (C₂₀H₂₂N₃O₃ requires 352.1661).



N²⁰-[(4-Nitrophenyl)methoxy]-N¹¹-(1,10-phenanthrolin-5-yl)octanediamide L⁴

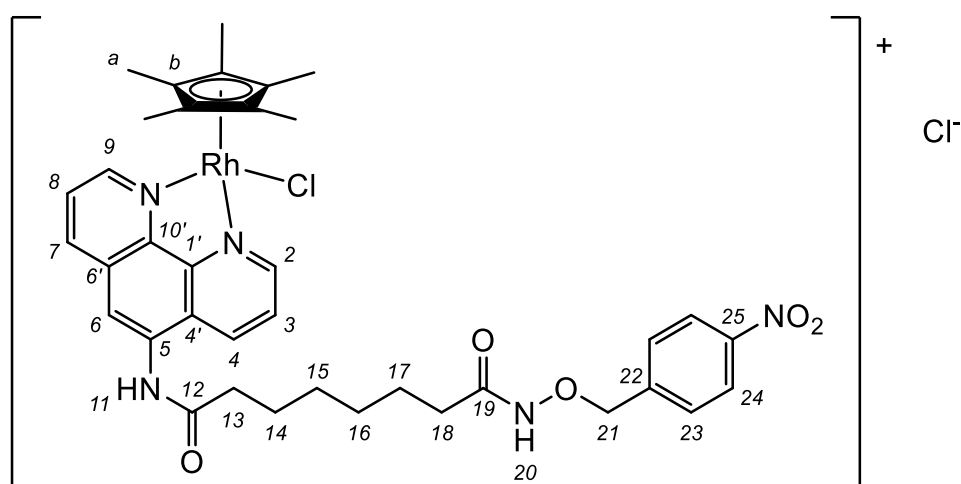
7-[(1,10-Phenanthrolin-5-yl)carbamoyl]heptanoic acid (0.130 g, 0.37 mmol) and *O*-(4-nitrobenzyl)hydroxylamine hydrochloride (0.114 g, 0.55 mmol) were suspended in anhydrous DMF (15 mL). HATU (0.126 g, 0.33 mmol) was added to the stirring solution, after 10 min diisopropylamine (0.156 mL, 0.92 mmol) was added and the solution was stirred at ambient temperature for 16 h. The solution was dropped into a saturated NaCl solution (40 mL). The resulting precipitate was filtered and washed with water to yield the *title compound* (0.087 g, 47%). δ_{H} (DMSO- d_6) 11.3 (1H, s, H²⁰), 10.4 (1H, s, H¹¹), 9.10 (1H, dd, ³J_{HH} 4.4 Hz ⁴J_{HH} 1.3 Hz, H²), 9.00 (1H, dd, ³J_{HH} 4.0 Hz ⁴J_{HH} 1.6 Hz, H⁹), 8.74 (1H, d, ³J_{HH} 8.6 Hz, H⁴), 8.50 (1H, d, ³J_{HH} 7.6 Hz, H⁷), 8.19 (2H, d, ³J_{HH} 7.4 Hz, H²⁴), 8.18 (1H, s, H⁶), 7.85 (1H, dd, ³J_{HH} 8.6 Hz ³J_{HH} 4.4 Hz, H³), 7.78 (1H, dd, ³J_{HH} 7.6 Hz ³J_{HH} 4.0 Hz, H⁸), 7.65 (2H, d, ³J_{HH} 7.4 Hz, H²³), 4.90 (2H, s, H²¹), 2.53 (2H, t, ³J_{HH} 7.5 Hz, H¹³), 1.96 (2H, t, ³J_{HH} 7.3 Hz, H¹⁸), 1.62 (2H, quin, ³J_{HH} 7.5 Hz, H¹⁴), 1.48 (2H, quin, ³J_{HH} 7.3 Hz, H¹⁷), 1.32 (2H, m, H¹⁵), 1.25 (2H, m, H¹⁶); δ_{C} (DMSO- d_6) 173.0 (C¹⁹), 170.0 (C¹²), 150.3 (C²), 149.5 (C⁹), 147.6 (C²⁵), 145.4 (C¹), 144.5 (C²²), 143.0 (C¹⁰), 137.0 (C⁷), 133.1 (C⁴), 132.6 (C⁵), 129.6 (2C, C²³), 128.6 (C⁶), 125.2 (C^{4'}), 124.3 (C⁸), 123.7 (2C, C²⁴), 123.5 (C³), 120.2 (C⁶), 75.8 (C²¹), 36.3 (C¹³), 32.6 (C¹⁸), 28.8 (C¹⁵), 28.7 (C¹⁶), 25.5 (C¹⁴), 25.2 (C¹⁷); *m/z* (HRMS⁺) 502.2093 [M+H]⁺ (C₂₇H₂₈N₅O₅ requires 502.2090).



Chloro(p-cymene)N²⁰-[(4-Nitrophenyl)methoxy]-N¹¹-(1,10-phenanthrolin-5-yl)octanediamide ruthenium(II) chloride Ru1L⁴

N²⁰-[(4-Nitrophenyl)methoxy]-N¹¹-(1,10-phenanthrolin-5-yl)octanediamide (0.030 g, 0.059 mmol) and (*p*-cymene)ruthenium(II) chloride dimer (0.018 g, 0.029 mmol) were dissolved in MeOH (10 mL) and the solution was heated to 40 °C for 16 h. The solvent was removed under vacuum to give the *title compound* as a yellow solid (0.017 g, 34%). δ_{H} (MeOD- d_4) 9.87 (1H, dd, ³J_{HH} 5.1 Hz ⁴J_{HH} 1.2 Hz, H²), 9.75 (1H, dd, ³J_{HH} 5.1 Hz ⁴J_{HH} 1.0 Hz, H⁹), 8.91 (1H, d, ³J_{HH} 8.6 Hz ⁴J_{HH} 1.2 Hz, H⁴), 8.71 (1H, d, ³J_{HH} 8.2 Hz ⁴J_{HH} 1.0, H⁷), 8.41 (1H, s, H⁶), 8.21 (2H, d, ³J_{HH} 8.3 Hz, H²⁴), 8.12 (1H, dd, ³J_{HH} 8.6 Hz ³J_{HH} 5.1 Hz, H³), 8.03 (1H, dd, ³J_{HH} 8.2 Hz ³J_{HH} 5.1 Hz, H⁸), 7.66

(2H, d, $^3J_{\text{HH}}$ 8.3 Hz, H²³), 6.23 (1H, d, $^3J_{\text{HH}}$ 6.7 Hz, H^d), 6.22 (1H, d, $^3J_{\text{HH}}$ 6.7 Hz, H^{d'}), 6.00 (1H, d, $^3J_{\text{HH}}$ 6.7 Hz, H^c), 5.99 (1H, d, $^3J_{\text{HH}}$ 6.7 Hz, H^{c'}), 4.96 (2H, s, H²¹), 2.66 (1H, sept, $^3J_{\text{HH}}$ 6.9 Hz, H^f), 2.61 (2H, t, $^3J_{\text{HH}}$ 7.3 Hz, H¹³), 2.25 (3H, s, H^a), 2.09 (2H, t, $^3J_{\text{HH}}$ 7.3 Hz, H¹⁸), 1.76 (2H, quin, $^3J_{\text{HH}}$ 7.3 Hz, H¹⁴), 1.62 (2H, quin, $^3J_{\text{HH}}$ 7.3 Hz, H¹⁷), 1.47-1.43 (2H, m, H¹⁵), 1.37-1.33 (2H, m, H¹⁶), 0.99 (3H, d, $^3J_{\text{HH}}$ 6.9 Hz, H^g), 0.98 (3H, d, $^3J_{\text{HH}}$ 6.9 Hz, H^{g'}); δ_{C} (MeOD-d₄) 174.3 (C¹²), 171.6 (C¹⁹), 155.6 (C²), 154.6 (C⁹), 147.9 (C²⁵), 146.0 (C^{1'}), 143.7 (C^{10'}), 143.2 (C²²), 138.1 (C⁷), 134.5 (C⁴), 133.4 (C⁵), 130.2 (C^{6'}), 129.4 (2C, C²⁴), 126.9 (C^{4'}), 126.3 (C⁸), 125.6 (C³), 123.0 (2C, C²⁴), 120.1 (C⁶), 105.0 (C^e), 103.4 (C^b), 86.1 (C^d), 85.9 (C^{d'}), 84.1 (C^c), 84.0 (C^{c'}), 76.0 (C²¹), 35.9 (C¹³), 32.2 (C¹⁸), 30.9 (C^f), 28.5 (C¹⁵), 28.2 (C¹⁶), 25.0 (C¹⁴), 24.9 (C¹⁷), 20.8 (C^g), 20.7 (C^{g'}), 17.4 (C^a); m/z (HRMS⁺) 766.1882 [M-Cl]⁺ (C₃₇H₄₁N₅O₅³⁵Cl⁹⁶Ru requires 766.1872).



Chloro(pentamethylcyclopentadienyl)N²⁰-[(4-Nitrophenyl)methoxy]-N¹¹-(1,10-phenanthrolin-5-yl)octanediamide rhodium(III) chloride RhL⁴

N²⁰-[(4-Nitrophenyl)methoxy]-N¹¹-(1,10-phenanthrolin-5-yl)octanediamide (0.025 g, 0.049 mmol) and dichloro(pentamethylcyclopentadienyl)rhodium(II) dimer (0.015 g, 0.025 mmol) were dissolved in MeOH (10 mL) and the resulting solution was heated to 40 °C, under an argon atmosphere for 16 h. The solvent was removed to give a dark yellow solid as the *title compound* (0.009 g, 22%). δ_{H} (MeOD-d₄) 9.39 (1H, d, $^3J_{\text{HH}}$ 5.5 Hz, H²), 9.28 (1H, d, $^3J_{\text{HH}}$ 5.3 Hz, H⁹), 8.91 (1H, d, $^3J_{\text{HH}}$ 8.8 Hz, H⁴), 8.73 (1H, d, $^3J_{\text{HH}}$ 8.2 Hz, H⁷), 8.39 (1H, s, H⁶), 8.19-8.17 (3H, m, H³ H²⁴), 8.09 (1H, dd, $^3J_{\text{HH}}$ 8.2 Hz $^3J_{\text{HH}}$ 5.3 Hz, H⁸), 7.64 (2H, d, $^3J_{\text{HH}}$ 8.1 Hz, H²³), 4.94 (2H, s, H²¹), 2.60 (2H, t, $^3J_{\text{HH}}$ 6.6 Hz, H¹³), 2.08 (2H, t, $^3J_{\text{HH}}$ 7.5 Hz, H¹⁸), 1.77 (15H, s, H^a), 1.75 (2H, quin, $^3J_{\text{HH}}$ 6.6 Hz, H¹⁴), 1.60 (2H, quin, $^3J_{\text{HH}}$ 7.5 Hz, H¹⁷), 1.46-1.42 (2H, m, H¹⁵), 1.36-1.32 (2H, m, H¹⁶); δ_{C} (MeOD-d₄) 174.4 (C¹²), 171.6 (C¹⁹), 152.1 (C²), 151.2 (C⁹), 147.8 (C²⁵), 145.6 (C^{1'}), 143.4 (C^{10'}), 143.2 (C²²), 138.5 (C⁷), 134.8 (C⁴), 133.4 (C⁵), 130.3 (C^{6'}), 129.3 (2C, C²³), 127.0 (C^{4'}), 126.7 (C⁸), 126.2 (C³), 123.0 (2C, C²⁴), 120.5 (C⁶), 97.5 (5C, C^b), 76.0 (C²¹), 35.9 (C¹³), 32.2 (C¹⁸), 28.5 (C¹⁵),

28.2 (C¹⁶), 25.0 (C¹⁴), 24.9 (C¹⁷), 7.59 (5C, C^a); *m/z* (HRMS⁺) 774.1962 [M-Cl]⁺
(C₃₇H₄₂N₅O₅³⁵Cl¹⁰³Rh requires 774.1930).

Appendix 1

Crystal Structure Data

Complex Ru1PP3

Table 2 Crystal data and structure refinement of **Ru1PP3**.

Empirical formula	C ₂₂ H ₂₅ ClNO ₂ PRu
Formula weight	502.92
Temperature/K	120.0
Crystal system	monoclinic
Space group	P2 ₁ /c
a/Å	12.5685(6)
b/Å	8.1196(4)
c/Å	20.4312(10)
α /°	90.00
β /°	91.5345(16)
γ /°	90.00
Volume/Å ³	2084.28(18)
Z	4
$\rho_{\text{calc}}/\text{cm}^3$	1.603
μ/mm^{-1}	0.975
F(000)	1024.0
Crystal size/mm ³	0.31 × 0.3 × 0.02
Radiation	MoK α ($\lambda = 0.71073$)
2 Θ range for data collection/°	5.08 to 59
Index ranges	-17 ≤ h ≤ 17, -11 ≤ k ≤ 11, -28 ≤ l ≤ 28
Reflections collected	43150
Independent reflections	5811 [$R_{\text{int}} = 0.0528$, $R_{\text{sigma}} = 0.0360$]
Data/restraints/parameters	5811/0/257
Goodness-of-fit on F ²	1.040
Final R indexes [$I \geq 2\sigma(I)$]	$R_1 = 0.0309$, $wR_2 = 0.0580$
Final R indexes [all data]	$R_1 = 0.0482$, $wR_2 = 0.0629$
Largest diff. peak/hole / e Å ⁻³	0.58/-0.57

Table 3 Selected bond lengths for **Ru1PP3**.

Atom		Length/Å	Atom		Length/Å
Ru1	Cl1	2.4155(6)	C3	C4	1.379(3)
Ru1	O1	2.0829(14)	C4	C5	1.380(3)
Ru1	N1	2.1109(17)	C7	C8	1.396(3)
Ru1	C13	2.195(2)	C7	C12	1.393(3)
Ru1	C14	2.194(2)	C8	C9	1.379(3)
Ru1	C15	2.181(2)	C9	C10	1.379(4)
Ru1	C16	2.192(2)	C10	C11	1.391(3)
Ru1	C17	2.161(2)	C11	C12	1.388(3)
Ru1	C18	2.172(2)	C13	C14	1.430(3)
P1	O1	1.5269(16)	C13	C18	1.410(3)
P1	O2	1.4769(16)	C13	C20	1.509(3)
P1	C1	1.835(2)	C14	C15	1.393(3)
P1	C7	1.798(2)	C15	C16	1.421(3)
N1	C1	1.357(3)	C16	C17	1.411(3)
N1	C5	1.343(3)	C16	C19	1.506(3)
C1	C2	1.393(3)	C17	C18	1.421(3)
C2	C3	1.389(3)	C20	C21	1.549(4)
C2	C6	1.503(3)	C20	C22	1.511(4)

Table 4 Selected bond angles for **Ru1PP3**.

Atom			Angle/°	Atom			Angle/°
O1	Ru1	Cl1	86.03(4)	C5	N1	C1	119.46(18)
O1	Ru1	N1	80.50(6)	N1	C1	P1	113.59(15)
O1	Ru1	C13	150.94(7)	N1	C1	C2	121.5(2)
O1	Ru1	C14	113.64(7)	C2	C1	P1	124.86(16)
O1	Ru1	C15	90.07(7)	C1	C2	C6	121.4(2)
O1	Ru1	C16	92.77(7)	C3	C2	C1	118.1(2)
O1	Ru1	C17	121.89(7)	C3	C2	C6	120.5(2)
O1	Ru1	C18	160.13(7)	C4	C3	C2	120.1(2)
N1	Ru1	Cl1	83.15(5)	C3	C4	C5	119.1(2)
N1	Ru1	C13	127.88(8)	N1	C5	C4	121.7(2)
N1	Ru1	C14	165.85(7)	C8	C7	P1	119.75(17)
N1	Ru1	C15	149.80(8)	C12	C7	P1	120.80(16)

N1	Ru1	C16	113.47(8)	C12	C7	C8	119.4(2)
N1	Ru1	C17	93.06(8)	C9	C8	C7	120.3(2)
N1	Ru1	C18	99.20(8)	C10	C9	C8	120.3(2)
C13	Ru1	C11	91.00(6)	C9	C10	C11	119.9(2)
C14	Ru1	C11	96.69(6)	C12	C11	C10	120.1(2)
C14	Ru1	C13	38.02(8)	C11	C12	C7	119.9(2)
C15	Ru1	C11	125.02(6)	C14	C13	Ru1	70.96(12)
C15	Ru1	C13	68.16(8)	C14	C13	C20	117.4(2)
C15	Ru1	C14	37.12(8)	C18	C13	Ru1	70.28(12)
C15	Ru1	C16	37.91(9)	C18	C13	C14	118.2(2)
C16	Ru1	C11	162.93(6)	C18	C13	C20	124.4(2)
C16	Ru1	C13	81.80(8)	C20	C13	Ru1	130.82(16)
C16	Ru1	C14	68.20(8)	C13	C14	Ru1	71.03(12)
C17	Ru1	C11	150.93(6)	C15	C14	Ru1	70.94(12)
C17	Ru1	C13	68.66(8)	C15	C14	C13	120.7(2)
C17	Ru1	C14	80.18(8)	C14	C15	Ru1	71.95(13)
C17	Ru1	C15	67.70(9)	C14	C15	C16	121.9(2)
C17	Ru1	C16	37.83(9)	C16	C15	Ru1	71.44(13)
C17	Ru1	C18	38.28(8)	C15	C16	Ru1	70.64(13)
C18	Ru1	C11	113.74(6)	C15	C16	C19	119.8(2)
C18	Ru1	C13	37.66(8)	C17	C16	Ru1	69.92(13)
C18	Ru1	C14	67.82(8)	C17	C16	C15	117.3(2)
C18	Ru1	C15	80.27(8)	C17	C16	C19	122.8(2)
C18	Ru1	C16	68.97(9)	C19	C16	Ru1	127.98(16)
O1	P1	C1	101.43(9)	C16	C17	Ru1	72.26(13)
O1	P1	C7	107.07(9)	C16	C17	C18	121.5(2)
O2	P1	O1	119.37(9)	C18	C17	Ru1	71.27(13)
O2	P1	C1	110.94(10)	C13	C18	Ru1	72.06(13)
O2	P1	C7	110.70(10)	C13	C18	C17	120.5(2)
C7	P1	C1	106.30(10)	C17	C18	Ru1	70.45(12)
P1	O1	Ru1	120.35(9)	C13	C20	C21	108.0(2)
C1	N1	Ru1	119.79(14)	C13	C20	C22	114.2(2)
C5	N1	Ru1	120.75(14)	C22	C20	C21	111.5(2)

Complex Ir1PP6

Table 5 Crystal data and structure refinement for complex Ir1PP6.

Empirical formula	C ₁₇ H ₂₄ ClIrNO ₂ P x H ₂ O
Formula weight	551.01
Temperature/K	120.0
Crystal system	monoclinic
Space group	Cc
a/Å	14.7318(2)
b/Å	16.6565(2)
c/Å	8.34330(10)
α/°	90.00
β/°	107.664(2)
γ/°	90.00
Volume/Å ³	1950.75(4)
Z	4
ρ _{calc} /cm ³	1.876
μ/mm ⁻¹	7.078
F(000)	1072.0
Crystal size/mm ³	0.25 × 0.23 × 0.03
Radiation	MoKα (λ = 0.71073)
2θ range for data collection/°	5.62 to 59.98
Index ranges	-20 ≤ h ≤ 20, -23 ≤ k ≤ 23, -11 ≤ l ≤ 11
Reflections collected	20026
Independent reflections	5620 [R _{int} = 0.0416, R _{sigma} = 0.0450]
Data/restraints/parameters	5620/2/227
Goodness-of-fit on F ²	1.076
Final R indexes [I ≥ 2σ (I)]	R ₁ = 0.0202, wR ₂ = 0.0489
Final R indexes [all data]	R ₁ = 0.0217, wR ₂ = 0.0497
Largest diff. peak/hole / e Å ⁻³	0.87/-0.99
Flack parameter	0.033(5)

Table 6 Selected bond lengths for complex **Ir1PP6**.

Atom		Length/Å	Atom		Length/Å
Ir1	Cl2	2.4328(11)	C2	C3	1.384(6)
Ir1	O1	2.125(3)	C3	C4	1.400(5)
Ir1	N1	2.112(3)	C3	C6	1.499(5)
Ir1	C8	2.171(5)	C4	C5	1.377(5)
Ir1	C9	2.164(4)	C8	C9	1.443(6)
Ir1	C10	2.144(4)	C8	C12	1.469(6)
Ir1	C11	2.140(4)	C8	C13	1.468(7)
Ir1	C12	2.144(3)	C9	C10	1.426(5)
P1	O1	1.530(3)	C9	C14	1.493(5)
P1	O2	1.497(3)	C10	C11	1.453(5)
P1	C1	1.823(3)	C10	C15	1.484(6)
P1	C7	1.791(4)	C11	C12	1.434(5)
N1	C1	1.374(4)	C11	C16	1.488(6)
N1	C5	1.332(4)	C12	C17	1.493(5)
C1	C2	1.379(5)			

Table 7 Selected bond angles for complex **Ir1PP6**.

Atom			Angle/°	Atom			Angle/°
O1	Ir1	Cl2	86.53(8)	N1	C1	C2	121.5(3)
O1	Ir1	C8	105.54(15)	C2	C1	P1	123.3(3)
O1	Ir1	C9	143.44(13)	C1	C2	C3	120.5(4)
O1	Ir1	C10	154.96(12)	C2	C3	C4	117.3(3)
O1	Ir1	C11	115.40(12)	C2	C3	C6	121.4(4)
O1	Ir1	C12	92.37(12)	C4	C3	C6	121.3(3)
N1	Ir1	Cl2	82.15(9)	C5	C4	C3	119.7(3)
N1	Ir1	O1	82.00(11)	N1	C5	C4	123.0(4)
N1	Ir1	C8	113.13(16)	C9	C8	Ir1	70.3(2)
N1	Ir1	C9	102.80(13)	C9	C8	C12	105.4(4)
N1	Ir1	C10	123.03(13)	C9	C8	C13	128.1(4)
N1	Ir1	C11	162.39(13)	C12	C8	Ir1	69.1(2)
N1	Ir1	C12	149.63(14)	C13	C8	Ir1	129.0(3)
C8	Ir1	Cl2	161.36(12)	C13	C8	C12	126.3(4)
C9	Ir1	Cl2	129.96(11)	C8	C9	Ir1	70.8(2)
C9	Ir1	C8	38.90(16)	C8	C9	C14	124.5(4)

C10	Ir1	C12	96.91(10)	C10	C9	Ir1	69.9(2)
C10	Ir1	C8	66.15(16)	C10	C9	C8	110.3(3)
C10	Ir1	C9	38.65(14)	C10	C9	C14	125.1(4)
C10	Ir1	C12	65.85(14)	C14	C9	Ir1	129.3(3)
C11	Ir1	C12	95.62(10)	C9	C10	Ir1	71.4(2)
C11	Ir1	C8	66.53(16)	C9	C10	C11	107.5(3)
C11	Ir1	C9	65.29(14)	C9	C10	C15	127.4(4)
C11	Ir1	C10	39.66(13)	C11	C10	Ir1	70.0(2)
C11	Ir1	C12	39.11(14)	C11	C10	C15	124.9(4)
C12	Ir1	C12	127.50(11)	C15	C10	Ir1	127.8(3)
C12	Ir1	C8	39.80(17)	C10	C11	Ir1	70.3(2)
C12	Ir1	C9	65.07(13)	C10	C11	C16	124.9(4)
O1	P1	C1	103.33(15)	C12	C11	Ir1	70.6(2)
O1	P1	C7	108.79(18)	C12	C11	C10	107.7(3)
O2	P1	O1	117.05(17)	C12	C11	C16	127.4(4)
O2	P1	C1	110.94(16)	C16	C11	Ir1	125.3(3)
O2	P1	C7	110.8(2)	C8	C12	Ir1	71.1(2)
C7	P1	C1	105.07(18)	C8	C12	C17	124.4(4)
P1	O1	Ir1	120.10(15)	C11	C12	Ir1	70.3(2)
C1	N1	Ir1	118.3(2)	C11	C12	C8	109.1(3)
C5	N1	Ir1	122.8(3)	C11	C12	C17	126.5(4)
C5	N1	C1	117.9(3)	C17	C12	Ir1	122.1(3)
N1	C1	P1	115.2(2)				

Appendix 2

Equations and Derivations

Acid Dissociation Constant (K_a) – Chapter 2

Data acquired from NMR ^1H and ^{31}P peak shifts in the formation of the hydroxyl species at varying pH of solutions was used to calculate the acid dissociation constant (K_a). This can be defined using the Henderson-Hasselbalch equation (*Equation 2*).

$$K_a = \frac{[A^-][H^+]}{[HA]} \quad (2)$$

As the independent variable in the NMR measurements, the equation must be rearranged to make pH the subject. *Equation 3* shows the log derivation of the Henderson-Hasselbalch and *Equation 4*, the rearrangement.

$$pK_a = pH - \log\left(\frac{\text{deprotonated}}{\text{protonated}}\right) \quad (3)$$

$$pH = pK_a + \log\left(\frac{\text{deprotonated}}{\text{protonated}}\right) \quad (4)$$

The initial calculation of the raw data was a correction of the chemical shift ($\delta_{\text{peak}} - \delta_{\text{reference}}$) and was plotted against pH for the peaks of interest for complexes in *Chapter 2*. A rough sigmoidal curve was plotted of this data and an estimate was made of the pK_a from the vertical mid-point of the graph. An ideal set of data were calculated using *Equation 4*, from the estimated pK_a and the maximum and minimum values of the existing graph ($\delta_{\text{protonated}}$ as the highest peak shift and $\delta_{\text{deprotonated}}$ as the lowest). *Equation 5* was also used to calculate a set of values from pH 2.0 – 13.00 in hundredth increments that were plotted as a sigmoidal curve over the existing data points.

$$\delta_{\text{calculated}} = \delta_{\text{deprotonated}} + \frac{(\delta_{\text{protonated}} - \delta_{\text{deprotonated}})}{10^{(pH - pK_a)} + 1} \quad (5)$$

To adjust the pK_a , error values were defined by subtracting the observed from the calculated values. The sum of these errors was used in a least squares non-linear regression to adjust the sigmoidal curve data, minimising the difference between the ideal and experimental data amending the pK_a value of each complex. *Equation 6* shows the rearrangement to calculate the overall pK_a error of the values using the observed chemical shift corresponding to the pH (assuming $pH = pK_a$.)

$$10^{(pH-pK_a)} = \left(\frac{\delta_{protonated} - \delta_{deprotonated}}{\delta_{observed} - \delta_{deprotonated}} \right) - 1 \quad (6)$$

Dose Response Curves – Chapters 2, 3 and 4

To calculate the IC_{50} measurements of cytotoxicity and enzyme inhibition, dose response sigmoidal curves were utilised (similarly to pK_a values). Concentration values must first be in log form before plotting the raw data. Estimations can be made of the inflection point and slope from this data with the saturation point known (MTT = Abs(0), Cell viability = 100%, HDAC enzyme activity = 100%). An ideal set of data for y was calculated using *Equation 7* in one hundredth increments, from the estimated values of IP = inflection point and a_1 = slope (SP = saturation point). This data was plotted over the raw data points.

$$y = \frac{\exp(a_1(x - IP))}{1 + \exp(a_1(x - IP))} SP \quad (7)$$

An ideal set of data, using the same number of experimental concentration points was also calculated using *Equation 6*, and an error calculated by subtracting the experimental data point (A_{obs}) from its corresponding calculated point (A_{calc}). Each error was then squared and summed to form the total error. Subsequently, the standard error in y (y_{err}) was then calculated using *Equation 8*, by taking the sum of the squared errors over the number of data points. This was square rooted to provide y_{err} .

$$y_{err} = \sqrt{\left(\frac{\sum_{i=x_{err}^0}^{x_{err}^1} i^2}{n} \right)} \quad (8)$$

The error in A_{obs} was then calculated using the saturation point and y_{err} using *Equation 9*.

$$A_{obs} = \left(\frac{SP}{2}\right) - y_{err} \quad (9)$$

Finally the error in inflection (IP_{err}) was calculated as a function of A_{obs} using *Equation 10*.

$$IP_{err} = LN(1/((\frac{SP}{A_{obs}}) - 1))/a_1 \quad (10)$$

UV-Vis Titrations

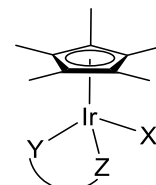
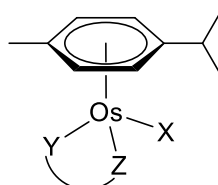
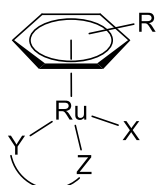
Molar extinction coefficients calculated using the Beer-Lambert Law – *Equation 11* (A = absorbance; ϵ = molar extinction coefficient; C = concentration; l = pathlength):

$$A = \epsilon Cl \quad (11)$$

Appendix 3

Key Ligands and Complexes

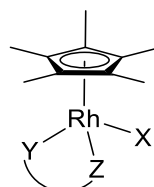
Chapter 2 Complexes & Ligands



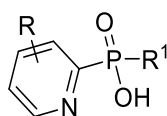
Complex	R	YZ	X
Ru1PP1^a	<i>p</i> Cy	<i>PP1</i>	Cl
Ru1PP2^a	<i>p</i> Cy	<i>PP2</i>	Cl
Ru1PP3	<i>p</i> Cy	<i>PP3</i>	Cl
Ru1PP4	<i>p</i> Cy	<i>PP4</i>	Cl
Ru1PP5	<i>p</i> Cy	<i>PP5</i>	Cl
Ru1PP6	<i>p</i> Cy	<i>PP6</i>	Cl
Ru1PP7	<i>p</i> Cy	<i>PP7</i>	Cl
Ru1PP8^a	<i>p</i> Cy	<i>PP8</i>	Cl
Ru1PP9^a	<i>p</i> Cy	<i>PP9</i>	Cl
Ru2PP1^a	<i>p</i> Cy	<i>PP1</i>	I
Ru2PP2^a	<i>p</i> Cy	<i>PP2</i>	I
Ru2PP6^a	<i>p</i> Cy	<i>PP6</i>	I
Ru2PP3^a	<i>p</i> Cy	<i>PP3</i>	I
Ru3PP1^a	<i>Bnz</i>	<i>PP1</i>	Cl
Ru3PP2^a	<i>Bnz</i>	<i>PP2</i>	Cl

Complex	YZ	X
OsPP1^a	<i>PP1</i>	Cl
OsPP2^a	<i>PP2</i>	Cl

Complex	YZ	X
Ir1PP1^a	<i>PP1</i>	Cl
Ir1PP2^a	<i>PP2</i>	Cl
Ir1PP6	<i>PP6</i>	Cl
Ir2PP1^a	<i>PP1</i>	I
Ir2PP2^a	<i>PP2</i>	I

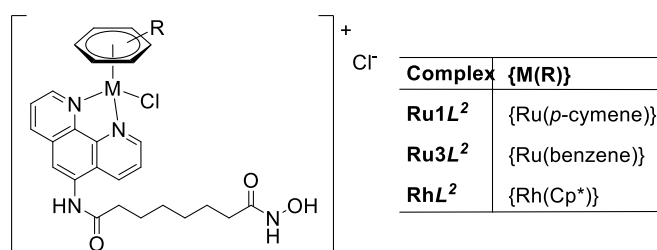
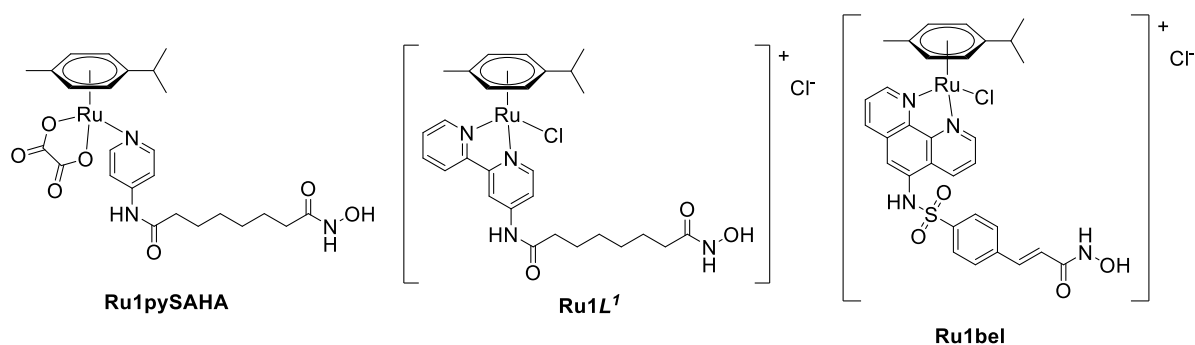


Complex	YZ	X
RhPP1^a	<i>PP1</i>	Cl
RhPP2^a	<i>PP2</i>	Cl
RhPP5	<i>PP5</i>	Cl
RhPP6	<i>PP6</i>	Cl

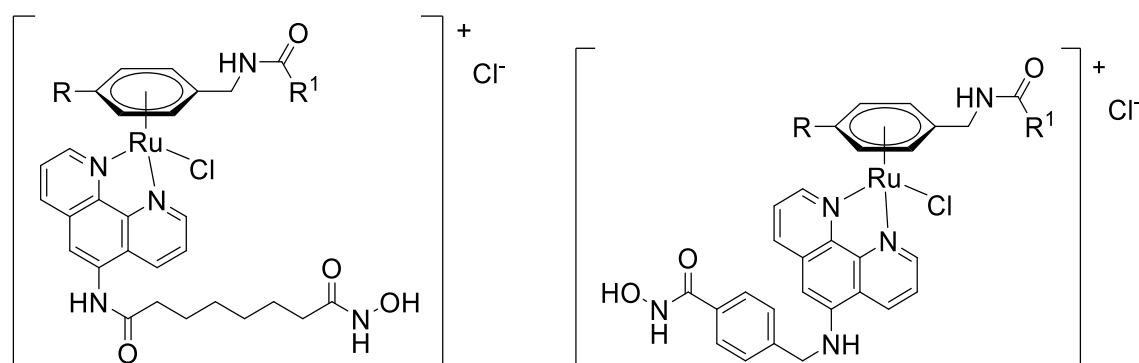


Ligand	R	R ¹
PP1^a	H	Ph
PP2^a	H	Me
PP3	3-Me	Ph
PP4	3-Me	Me
PP5	4-Me	Ph
PP6	4-Me	Me
PP7	4-OCD ₃	Ph
PP8^a	4-Cl	Ph
PP9^a	4-NH ₂	Ph

Chapter 3 Complexes



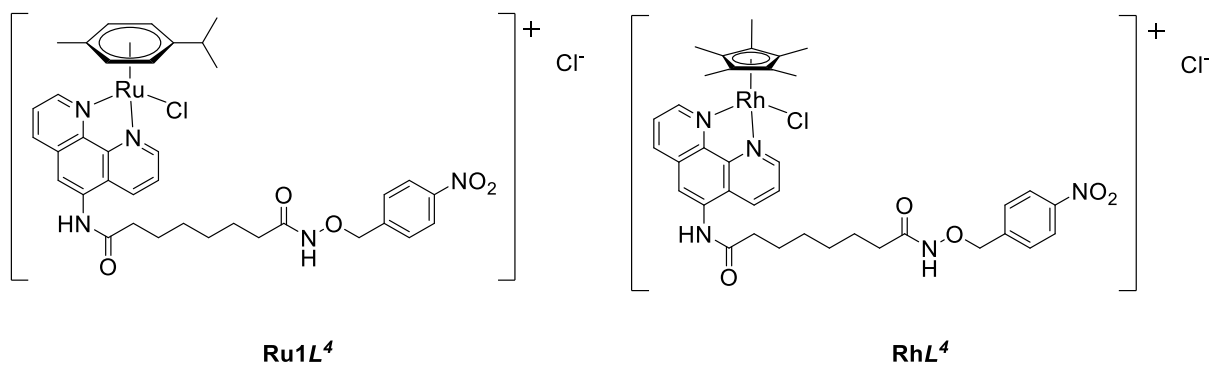
Chapter 4 Complexes



Complex	R	R ¹
Ru1L²	<i>p</i> -cymene	
Ru4AL²	H	Me
Ru4BL²	H	tBu
Ru4CL²	H	Ph
Ru4DL²	H	2-Thiophene
Ru5AL²	Me	Me
Ru5BL²	Me	tBu
Ru5CL²	Me	Ph
Ru5DL²	Me	2-Thiophene

Complex	R	R ¹
Ru1L³	<i>p</i> -cymene	
Ru5AL³	Me	Me
Ru5BL³	Me	tBu
Ru5CL³	Me	Ph
Ru5DL³	Me	2-Thiophene

Chapter 5 Complexes



Appendix 4

Publications

Chapter 2 [1] and *Chapter 3* [2] produced the following articles, respectively.

[1] J. M. Cross, N. Gallagher, J. H. Gill, M. Jain, A. W. McNeillis, K. L. Rockley, F. H. Tscherny, N. J. Wirszycyz, D. S. Yufit and J. W. Walton, *Dalton. Trans.*, 2016, **45**, 12807–12813.

[2] J. M. Cross, T. R. Blower, N. Gallagher, J. H. Gill, K. L. Rockley and J. W. Walton, *ChemPlusChem*, 2016, **81**, 1276–1280.

Oral & Poster Presentations

RSC Coordination and Organometallic Chemistry Discussion Group Meeting, Lancaster University, 2017, (*Poster presentation*)

RSC ISACS: Challenges in Inorganic Chemistry, University of Manchester, 2017 (*Poster presentation*)

Ferrocene Colloquium, Johannes Gutenberg Universitat, Germany, 2017 (*Oral presentation*)

Durham University Musgrave Seminar Series, 2016 (*Oral presentation - invited speaker*)

RSC Dalton Division Joint Interest Meeting, University of Warwick, 2016 (*Poster presentation*)

References

- 1 R. A. Willis, *The spread of tumours in the human body*, John Churchill, London, 1934, vol. 22.
- 2 G. Delaney, S. Jacob, C. Featherstone and M. Barton, *Cancer*, 2005, **104**, 1129–1137.
- 3 R. A. Lobo, *Nat. Rev. Endocrinol.*, 2017, **13**, 220–231.
- 4 B. A. Chabner and T. G. Roberts, *Nat. Rev. Cancer*, 2005, **5**, 65–72.
- 5 S. Farkona, E. P. Diamandis and I. M. Blasutig, *BMC Med.*, 2016, **14**, 73.
- 6 B. Alberts, D. Bray, J. Lewis, M. Raff, K. Roberts and J. D. Watson, Garland Science, New York, 1st edn., 1989.
- 7 T. Ozaki and A. Nakagawara, *Cancers (Basel)*, 2011, **3**, 994–1013.
- 8 H. Laatch, in *Anthracycline Chemistry and Biology*, ed. K. Krohn, Springer, 2008, pp. 3–74.
- 9 D. Agudelo, P. Bourassa, G. Bérubé and H.-A. Tajmir-Riahi, *Int. J. Biol. Macromol.*, 2014, **66**, 144–150.
- 10 K. Kiyomiya, J. Satoh, H. Horie, M. Kurebe, H. Nakagawa and S. Matsuo, *Int. J. Oncol.*, 2002, **21**, 1081–1085.
- 11 D. G. I. Kingston, *Trends Biotechnol.*, 1994, **12**, 222–227.
- 12 P. B. Schiff, J. Fant and S. B. Horwitz, *Nature*, 1979, **277**, 665–667.
- 13 I. Nakano, C. Z. Soe and R. Codd, *RSC Adv.*, 2015, **5**, 46437–46442.
- 14 D. D. von Hoff, M. W. Layard, P. Basa and H. L. Davis, *Ann. Intern. Med.*, 1979, **91**, 710.
- 15 S. J. Lippard, *Science.*, 1993, **261**, 699–700.
- 16 B. Rosenberg, L. Vancamp and T. Krigas, *Nature*, 1965, **205**, 698–699.
- 17 B. Rosenberg, L. Vancamp, J. E. Trosko and V. H. Mansour, *Nature*, 1969, **222**, 385–386.
- 18 B. Rosenberg, *Biochimie*, 1978, **60**, 859–867.
- 19 R. K. Murray, D. K. Granner, P. A. Mayes and V. W. Rodwell, *Harper's Illustrated Biochemistry*, McGraw-Hill Companies, 26th edn., 2003.
- 20 S. J. Lippard, *Science.*, 1982, **218**, 1075–1082.
- 21 S. Gowda, B. B. Mathew, C. N. Sudhamani and B. Naik, *Biomed. Biotechnol.*, 2014, **2**, 1–9.
- 22 H. C. Harder and B. Rosenberg, *Int. J. Cancer*, 1970, **6**, 207–216.

- 23 J. J. Roberts and M. F. Pera, in *Platinum, Gold and Other Metal Chemotherapeutic Agents*, ed. American Chemical Society, ACS Symposium Series, Washington, 1st edn., 1983, pp. 3–25.
- 24 S. E. Sherman, D. Gibson, A. H. Wang and S. J. Lippard, *Science.*, 1985, **230**, 412–417.
- 25 A. Pasini and F. Zunino, *Angew. Chem. Int. Ed.*, 1987, **26**, 615–624.
- 26 A. K. Godwin, A. Meister, P. J. O’Dwyer, C. S. Huang, T. C. Hamilton and M. E. Anderson, *Proc. Natl. Acad. Sci.*, 1992, **89**, 3070–3074.
- 27 K. Nakagawa, J. Yokota, M. Wada, Y. Sasaki, Y. Fujiwara, M. Sakai, M. Muramatsu, T. Terasaki, Y. Tsunokawa and M. Terada, *Jpn. J. Cancer Res.*, 1988, **79**, 301–304.
- 28 Z. H. Siddik, *Oncogene*, 2003, **22**, 7265–7279.
- 29 A. R. Timerbaev, C. G. Hartinger, S. S. Aleksenko and B. K. Keppler, *Chem. Rev.*, 2006, **106**, 2224–2248.
- 30 O. Rixe, W. Ortuzar, M. Alvarez, R. Parker, E. Reed, K. Paull and T. Fojo, *Biochem. Pharmacol.*, 1996, **52**, 1855–1865.
- 31 H. Choy, C. Park and M. Yao, *Clin. Cancer Res.*, 2008, **14**, 1633–1638.
- 32 D. Gibson, *Dalt. Trans.*, 2009, 10681–10689.
- 33 J. L. Carr, M. D. Tingle and M. J. McKeage, *Cancer Chemother. Pharmacol.*, 2006, **57**, 483–490.
- 34 D. Fink, S. Nebel, S. Aebi, H. Zheng, B. Cenni, A. Nehmé, R. D. Christen and S. B. Howell, *Cancer Res.*, 1996, **56**, 4881–4886.
- 35 S. Dasari and P. Bernard Tchounwou, *Eur. J. Pharmacol.*, 2014, **740**, 364–378.
- 36 L. Helm and A. E. Merbach, *Coord. Chem. Rev.*, 1999, **187**, 151–181.
- 37 C. S. Allardyce and P. J. Dyson, *Platin. Met. Rev.*, 2001, **45**, 62.
- 38 A. Bergamo, R. Gagliardi, V. Scarcia, A. Furlani, E. Alessio, G. Mestroni and G. Sava, *J. Pharmacol. Exp. Ther.*, 1999, **289**, 559–564.
- 39 G. Sava, S. Zorzet, C. Turrin, F. Vita, M. Soranzo, G. Zabucchi, M. Cocchietto, A. Bergamo, S. DiGiovine, G. Pezzoni, L. Sartor and S. Garbisa, *Clin. Cancer Res.*, 2003, **9**, 1898–1905.
- 40 D. Pluim, R. C. A. M. van Waardenburg, J. H. Beijnen and J. H. M. Schellens, *Cancer Chemother. Pharmacol.*, 2004, **54**, 71–78.
- 41 E. Alessio, *Eur. J. Inorg. Chem.*, 2017, 1549–1560.

- 42 S. Leijen, S. A. Burgers, P. Baas, D. Pluim, M. Tibben, E. Van Werkhoven, E. Alessio, G. Sava, J. H. Beijnen and J. H. M. Schellens, *Invest. New Drugs*, 2015, **33**, 201–214.
- 43 M. R. Berger, F. T. Garzon, B. K. Keppler and D. Schmahl, *Anticancer Res.*, 1989, **9**, 761–765.
- 44 C. G. Hartinger, S. Zorbas-Seifried, M. A. Jakupec, B. Kynast, H. Zorbas and B. K. Keppler, *J. Inorg. Biochem.*, 2006, **100**, 891–904.
- 45 M. Pongratz, P. Schluga, M. A. Jakupec, V. B. Arion, C. G. Hartinger, G. Allmaier and B. K. Keppler, *J. Anal. At. Spectrom.*, 2004, **19**, 46.
- 46 H. Sun, H. Li and P. J. Sadler, *Chem. Rev.*, 1999, **99**, 2817–2842.
- 47 C. G. Hartinger, M. A. Jakupec, S. Zorbas-Seifried, M. Groessler, A. Egger, W. Berger, H. Zorbas, P. J. Dyson and B. K. Keppler, *Chem. Biodivers.*, 2008, **5**, 2140–2155.
- 48 A. Pastore, G. Federici, E. Bertini and F. Piemonte, *Clin. Chim. Acta*, 2003, **333**, 19–39.
- 49 W. Han Ang and P. J. Dyson, *Eur. J. Inorg. Chem.*, 2006, 4003–4018.
- 50 G. Süß-Fink, *Dalton. Trans.*, 2010, **39**, 1673–1688.
- 51 A. L. Noffke, A. Habtemariam, A. M. Pizarro and P. J. Sadler, *Chem. Commun.*, 2012, **48**, 5219–5246.
- 52 Y. N. Vashisht Gopal, D. Jayaraju and A. K. Kondapi, *Biochemistry*, 1999, **38**, 4382–4388.
- 53 R. E. Morris, R. E. Aird, P. Del Socorro Murdoch, H. Chen, J. Cummings, N. D. Hughes, S. Parsons, A. Parkin, G. Boyd, D. I. Jodrell and P. J. Sadler, *J. Med. Chem.*, 2001, **44**, 3616–3621.
- 54 R. E. Aird, J. Cummings, A. A. Ritchie, M. Muir, D. I. Jodrell, R. E. Morris, H. Chen and P. J. Sadler, *Br. J. Cancer*, 2002, **86**, 1652–1657.
- 55 H. Chen, J. A. Parkinson, S. Parsons, R. A. Coxall, R. O. Gould and P. J. Sadler, *J. Am. Chem. Soc.*, 2002, **124**, 3064–3082.
- 56 H. Chen, J. A. Parkinson, R. E. Morris and P. J. Sadler, *J. Am. Chem. Soc.*, 2003, **125**, 173–186.
- 57 C. S. Allardyce, P. J. Dyson, D. J. Ellis and S. L. Heath, *Chem. Commun.*, 2001, 1396–1397.
- 58 C. Scolaro, A. Bergamo, L. Brescacin, R. Delfino, M. Cocchietto, G. Laurencyzy, T. J. Geldbach, G. Sava and P. J. Dyson, *J. Med. Chem.*, 2005, **48**, 4161–4171.
- 59 H. A. Wee, E. Daldini, C. Scolaro, R. Scopelliti, L. Juillerat-Jeannerat and P. J. Dyson,

- Inorg. Chem.*, 2006, **45**, 9006–9013.
- 60 A. Bergamo, A. Masi, P. J. Dyson and G. Sava, *Int. J. Oncol.*, 2008, **33**, 1281–1289.
- 61 R. Lee, S. Escrig, C. Maclachlan, G. Knott, A. Meibom, G. Sava and P. Dyson, *Int. J. Mol. Sci.*, 2017, **18**, 1869.
- 62 B. Wu, M. S. Ong, M. Groessler, Z. Adhireksan, C. G. Hartinger, P. J. Dyson and C. A. Davey, *Chem. Eur. J.*, 2011, **17**, 3562–3566.
- 63 K. D. Camm, A. El-Sokkary, A. L. Gott, P. G. Stockley, T. Belyaeva and P. C. McGowan, *Dalton. Trans.*, 2009, 10914–10925.
- 64 S. H. Van Rijt, A. J. Hebden, T. Amaresekera, R. J. Deeth, G. J. Clarkson, S. Parsons, P. C. McGowan and P. J. Sadler, *J. Med. Chem.*, 2009, **52**, 7753–7764.
- 65 A. F. A. Peacock, A. Habtemariam, R. Fernández, V. Walland, F. P. A. Fabbiani, S. Parsons, R. E. Aird, D. I. Jodrell and P. J. Sadler, *J. Am. Chem. Soc.*, 2006, **128**, 1739–1748.
- 66 A. F. A. Peacock, M. Melchart, R. J. Deeth, A. Habtemariam, S. Parsons and P. J. Sadler, *Chem. Eur. J.*, 2007, **13**, 2601–2613.
- 67 W. Kandioller, C. G. Hartinger, A. A. Nazarov, C. Bartel, M. Skocic, M. A. Jakupec, V. B. Arion and B. K. Keppler, *Chem. Eur. J.*, 2009, **15**, 12283–12291.
- 68 I. Romero-Canelón, A. M. Pizarro, A. Habtemariam and P. J. Sadler, *Metallomics*, 2012, **4**, 1271–1279.
- 69 M. V. Babak, S. M. Meier, K. V. M. Huber, J. Reynisson, A. A. Legin, M. A. Jakupec, A. Roller, A. Stukalov, M. Gridling, K. L. Bennett, J. Colinge, W. Berger, P. J. Dyson, G. Superti-Furga, B. K. Keppler and C. G. Hartinger, *Chem. Sci.*, 2015, **6**, 2449–2456.
- 70 C. Scolaro, T. J. Geldbach, S. Rochat, A. Dorcier, C. Gossens, A. Bergamo, M. Cocchietto, I. Tavernelli, G. Sava, U. Rothlisberger and P. J. Dyson, *Organometallics*, 2006, **25**, 756–765.
- 71 Z. Adhireksan, G. E. Davey, P. Campomanes, M. Groessler, C. M. Clavel, H. Yu, A. A. Nazarov, C. H. F. Yeo, W. H. Ang, P. Dröge, U. Rothlisberger, P. J. Dyson and C. A. Davey, *Nat. Commun.*, 2014, **5**, 3462.
- 72 K. J. Kilpin and P. J. Dyson, *Chem. Sci.*, 2013, **4**, 1410.
- 73 D. Griffith, J. P. Parker and C. J. Marmion, *Anticancer. Agents Med. Chem.*, 2010, **10**, 354–370.
- 74 E. Meggers, *Angew. Chem. Int. Ed.*, 2011, **50**, 2442–2448.
- 75 T. W. Failes and T. W. Hambley, *Dalton. Trans.*, 2006, 1895.

- 76 D. Griffith, M. P. Morgan and C. J. Marmion, *Chem. Commun.*, 2009, 6735.
- 77 G. Mokdsi and M. M. Harding, *J. Inorg. Biochem.*, 2001, **83**, 205–209.
- 78 H. Santos-Rosa and C. Caldas, *Eur. J. Cancer*, 2005, **41**, 2381–2402.
- 79 E. Pennisi, Massive project maps DNA tags that define each cell's identity, <http://www.sciencemag.org/news/2015/02/massive-project-maps-dna-tags-define-each-cells-identity>, (accessed 2 February 2016).
- 80 S. Ropero and M. Esteller, *Mol. Oncol.*, 2007, **1**, 19–25.
- 81 S. Minucci and P. G. Pelicci, *Nat. Rev. Cancer*, 2006, **6**, 38–51.
- 82 W.-G. Z. Zhiming Li, *Int. J. Biol. Sci.*, 2014, **10**, 757.
- 83 S. L. Gantt, S. G. Gattis and C. A. Fierke, *Biochemistry*, 2006, **45**, 6170–6178.
- 84 A. J. M. de Ruijter, A. H. van Gennip, H. N. Caron, S. Kemp and A. B. P. van Kuilenberg, *Biochem. J.*, 2003, **370**, 737–749.
- 85 X. Ma, H. H. Ezzeldin and R. B. Diasio, *Drugs*, 2009, **69**, 1911–1934.
- 86 P. A. Marks and R. Breslow, *Nat. Biotechnol.*, 2007, **25**, 84–90.
- 87 N. Tsuji, M. Kobayashi, K. Nagashima, Y. Wakisaka and K. Koizumi, *J. Antibiot. (Tokyo)*, 1976, **29**, 1–6.
- 88 M. Yoshida, M. Kijima, M. Akita and T. Beppu, *J. Biol. Chem.*, 1990, **265**, 17174–17179.
- 89 M. Yoshida, Y. Hoshikawa, K. Koseki, K. Mori and T. Beppu, *J. Antibiot. (Tokyo)*, 1990, **43**, 1101–1106.
- 90 G. Elaut, G. Laus, E. Alexandre, L. Richert, P. Bachellier, D. Tourwé, V. Rogiers and T. Vanhaecke, *J. Pharmacol. Exp. Ther.*, 2007, **321**, 400–408.
- 91 R. K. Singh, N. Lall, T. S. Leedahl, A. McGillivray, T. Mandal, M. Haldar, S. Mallik, G. Cook and D. K. Srivastava, *Biochemistry*, 2013, **52**, 8139–8149.
- 92 P. A. Marks, T. Miller and V. M. Richon, *Curr. Opin. Pharmacol.*, 2003, **3**, 344–351.
- 93 T. A. Miller, D. J. Witter and S. Belvedere, *J. Med. Chem.*, 2003, **46**, 5097–5116.
- 94 M. S. Finnin, J. R. Donigian, A. Cohen, V. M. Richon, R. A. Rifkind, P. A. Marks, R. Breslow and N. P. Pavletich, *Nature*, 1999, **401**, 188–193.
- 95 V. M. Richon, Y. Webb, R. Merger, T. Sheppard, B. Jursic, L. Ngo, F. Civoli, R. Breslow, R. a Rifkind and P. a Marks, *Proc. Natl. Acad. Sci.*, 1996, **93**, 5705–5708.
- 96 L. M. Butler, D. B. Agus, H. I. Scher, B. Higgins, A. Rose, C. Cordon-Cardo, H. T. Thaler,

- R. A. Rifkind, P. A. Marks and V. M. Richon, *Cancer Res.*, 2000, **60**, 5165–5170.
- 97 L. Qiu, M. J. Kelso, C. Hansen, M. L. West, D. P. Fairlie and P. G. Parsons, *Br. J. Cancer*, 1999, **80**, 1252–1258.
- 98 R. K. Lindemann, B. Gabrielli and R. W. Johnstone, *Cell Cycle*, 2004, **3**, 777–786.
- 99 C. Zhang, V. Richon, X. Ni, R. Talpur and M. Duvic, *J. Invest. Dermatol.*, 2005, **125**, 1045–1052.
- 100 B. S. Mann, J. R. Johnson, M. H. Cohen, R. Justice and R. Pazdur, *Oncologist*, 2007, **12**, 1247–1252.
- 101 Y. Chen, X. Wang, W. Xiang, L. He, M. Tang, F. Wang, T. Wang, Z. Yang, Y. Yi, H. Wang, T. Niu, L. Zheng, L. Lei, X. Li, H. Song and L. Chen, *J. Med. Chem.*, 2016, **59**, 5488–5504.
- 102 S. Shen and A. P. Kozikowski, *ChemMedChem*, 2016, **11**, 15–21.
- 103 H. J. Kim and S. C. Bae, *Am. J. Transl. Res.*, 2011, **3**, 166–179.
- 104 C. T. Lin, H. C. Lai, H. Y. Lee, W. H. Lin, C. C. Chang, T. Y. Chu, Y. W. Lin, K. Der Lee and M. H. Yu, *Cancer Sci.*, 2008, **99**, 1218–1226.
- 105 L. R. Kelland and M. Van Beusichem, *Cancer Res.*, 1992, **52**, 5065–5072.
- 106 D. M. Griffith, B. Duff, K. Y. Saponitsky, K. Kavanagh, M. P. Morgan, D. Egan and C. J. Marmion, *J. Inorg. Biochem.*, 2011, **105**, 793–799.
- 107 J. Yang, X. Sun, W. Mao, M. Sui, J. Tang and Y. Shen, *Mol. Pharm.*, 2012, **9**, 2793–2800.
- 108 S. D. Gore and M. A. Carducci, *Expert Opin. Investig. Drugs*, 2000, **9**, 2923–2934.
- 109 P. Štarha, Z. Trávníček, B. Drahoš, R. Herchel and Z. Dvořák, *Appl. Organomet. Chem.*, 2018, **32**, 1–11.
- 110 V. Brabec, D. M. Griffith, A. Kisova, H. Kostřhunova, L. Zerzankova, C. J. Marmion and J. Kasparikova, *Mol. Pharm.*, 2012, **9**, 1990–1999.
- 111 J. P. Parker, H. Nimir, D. M. Griffith, B. Duff, A. J. Chubb, M. P. Brennan, M. P. Morgan, D. A. Egan and C. J. Marmion, *J. Inorg. Biochem.*, 2013, **124**, 70–77.
- 112 J. Spencer, J. Amin, M. Wang, G. Packham, S. S. S. Alwi, G. J. Tizzard, S. J. Coles, R. M. Paranal, J. E. Bradner and T. D. Heightman, *ACS Med. Chem. Lett.*, 2011, **2**, 358–362.
- 113 M. Librizzi, A. Longo, R. Chiarelli, J. Amin, J. Spencer and C. Luparello, *Chem. Res. Toxicol.*, 2012, **25**, 2608–2616.
- 114 A. Rogalska, A. Koceva-Chyła and Z. Józwiak, *Chem. Biol. Interact.*, 2008, **176**, 58–70.

- 115 K. Jain, K. S. Paranandi, S. Sridharan and A. Basu, *Am. J. Cancer Res.*, 2013, **3**, 251–265.
- 116 M. Librizzi, F. Caradonna, I. Cruciata, J. Dębski, S. Sansook, M. Dadlez, J. Spencer and C. Luparello, *Chem. Res. Toxicol.*, 2017, **30**, 2187–2196.
- 117 R.-R. Ye, Z.-F. Ke, C.-P. Tan, L. He, L.-N. Ji and Z.-W. Mao, *Chem. Eur. J.*, 2013, **19**, 10160–10169.
- 118 R.-R. Ye, C.-P. Tan, L. He, M.-H. Chen, L.-N. Ji and Z.-W. Mao, *Chem. Commun.*, 2014, **50**, 10945–10948.
- 119 R.-R. Ye, C.-P. Tan, Y.-N. Lin, L.-N. Ji and Z.-W. Mao, *Chem. Commun.*, 2015, **51**, 8353–8356.
- 120 I. J. MacDonald and T. J. Dougherty, *J. Porphyr. Phthalocyanines*, 2001, **5**, 105–129.
- 121 K. A. Stephenson, S. R. Banerjee, T. Besanger, O. O. Sogbein, M. K. Levadala, N. McFarlane, J. A. Lemon, D. R. Boreham, K. P. Maresca, J. D. Brennan, J. W. Babich, J. Zubieta and J. F. Valliant, *J. Am. Chem. Soc.*, 2004, **126**, 8598–8599.
- 122 C. Choudhary, C. Kumar, F. Gnad, M. L. Nielsen, M. Rehman, T. C. Walther, J. V Olsen and M. Mann, *Science*, 2009, **325**, 834–840.
- 123 F. Thaler and C. Mercurio, *ChemMedChem*, 2014, **9**, 523–536.
- 124 B. E. Gryder, Q. H. Sodji and A. K. Oyelere, *Future Med. Chem.*, 2012, **4**, 505–524.
- 125 J. C. Bressi, A. J. Jennings, R. Skene, Y. Wu, R. Melkus, R. De Jong, S. O’Connell, C. E. Grimshaw, M. Navre and A. R. Gangloff, *Bioorg. Med. Chem. Lett.*, 2010, **20**, 3142–3145.
- 126 R. S. Broide, J. M. Redwine, N. Aftahi, W. Young, F. E. Bloom and C. J. Winrow, *J. Mol. Neurosci.*, 2007, **31**, 47–58.
- 127 M. Malvaez, S. C. McQuown, G. A. Rogge, M. Astarabadi, V. Jacques, S. Carreiro, J. R. Rusche and M. A. Wood, *Proc. Natl. Acad. Sci.*, 2013, **110**, 2647–2652.
- 128 A. Vannini, C. Volpari, G. Filocamo, E. C. Casavola, M. Brunetti, D. Renzoni, P. Chakravarty, C. Paolini, R. De Francesco, P. Gallinari, C. Steinkuhler and S. Di Marco, *Proc. Natl. Acad. Sci.*, 2004, **101**, 15064–15069.
- 129 W. J. Huang, Y. C. Wang, S. W. Chao, C. Y. Yang, L. C. Chen, M. H. Lin, W. C. Hou, M. Y. Chen, T. L. Lee, P. Yang and C. I. Chang, *ChemMedChem*, 2012, **7**, 1815–1824.
- 130 S. Balasubramanian, J. Ramos, W. Luo, M. Sirisawad, E. Verner and J. J. Buggy, *Leukemia*, 2008, **22**, 1026–1034.
- 131 E. Verdin, F. Dequiedt and H. G. Kasler, *Trends Genet.*, 2003, **19**, 286–293.

- 132 A. Lahm, C. Paolini, M. Pallaoro, M. C. Nardi, P. Jones, P. Neddermann, S. Sambucini, M. J. Bottomley, P. Lo Surdo, A. Carfi, U. Koch, R. De Francesco, C. Steinkuhler and P. Gallinari, *Proc. Natl. Acad. Sci.*, 2007, **104**, 17335–17340.
- 133 L. Marek, A. Hamacher, F. K. Hansen, K. Kuna, H. Gohlke, M. U. Kassack and T. Kurz, *J. Med. Chem.*, 2013, **56**, 427–436.
- 134 M. Lobera, K. P. Madauss, D. T. Pohlhaus, Q. G. Wright, M. Trocha, D. R. Schmidt, E. Baloglu, R. P. Trump, M. S. Head, G. A. Hofmann, M. Murray-Thompson, B. Schwartz, S. Chakravorty, Z. Wu, P. K. Mander, L. Kruidenier, R. A. Reid, W. Burkhardt, B. J. Turunen, J. X. Rong, C. Wagner, M. B. Moyer, C. Wells, X. Hong, J. T. Moore, J. D. Williams, D. Soler, S. Ghosh and M. A. Nolan, *Nat. Chem. Biol.*, 2013, **9**, 319–325.
- 135 G. I. Aldana-Masangkay and K. M. Sakamoto, *J. Biomed. Biotechnol.*, 2010, **2011**, 1–10.
- 136 C. Hubbert, A. Guardiola, R. Shao, Y. Kawaguchi, A. Ito, A. Nixon, M. Yoshida, X. F. Wang and T. P. Yao, *Nature*, 2002, **417**, 455–458.
- 137 M. Namdar, G. Perez, L. Ngo and P. A. Marks, *Proc. Natl. Acad. Sci.*, 2010, **107**, 20003–20008.
- 138 P. Yang, L. Zhang, Y. J. Zhang, J. Zhang and W. F. Xu, *Drug Discov. Ther.*, 2013, **7**, 233–42.
- 139 S. J. Haggarty, K. M. Koeller, J. C. Wong, C. M. Grozinger and S. L. Schreiber, *Proc. Natl. Acad. Sci. U. S. A.*, 2003, **100**, 4389–94.
- 140 K. V. Butler, J. Kalin, C. Brochier, G. Vistoli, B. Langley and A. P. Kozikowski, *J. Am. Chem. Soc.*, 2010, **132**, 10842–10846.
- 141 J. A. Bergman, K. Woan, P. Perez-Villarroel, A. Villagra, E. M. Sotomayor and A. P. Kozikowski, *J. Med. Chem.*, 2012, **55**, 9891–9899.
- 142 C. A. Ocasio, S. Sansook, R. Jones, J. M. Roberts, T. G. Scott, N. Tsoureas, P. Coxhead, M. Guille, G. J. Tizzard, S. J. Coles, H. Hochegger, J. E. Bradner and J. Spencer, *Organometallics*, 2017, **36**, 3276–3283.
- 143 Y. Jiang and J. Hsieh, *Proc. Natl. Acad. Sci.*, 2014, **111**, 13541–13546.
- 144 C. Y. Acevedo-Morantes, E. Meléndez, S. P. Singh and J. E. Ramírez-Vick, *J. Cancer Sci. Ther.*, 2012, **4**, 271–275.
- 145 P. Göbel, F. Ritterbusch, M. Helms, M. Bischof, K. Harms, M. Jung and E. Meggers, *Eur. J. Inorg. Chem.*, 2015, **2015**, 1654–1659.
- 146 A. M. Shannon, D. J. Bouchier-Hayes, C. M. Condrón and D. Toomey, *Cancer Treat. Rev.*,

- 2003, **29**, 297–307.
- 147 R. H. Thomlinson, *J. Clin. Pathol.*, 1977, **11**, 105–113.
- 148 J. M. Brown and W. R. Wilson, *Nat. Rev. Cancer*, 2004, **4**, 437–447.
- 149 E. K. Rofstad, *Int. J. Radiat. Biol.*, 2000, **76**, 589–605.
- 150 W. A. Denny, *Futur. Oncol.*, 2010, **6**, 419–428.
- 151 R. M. Sutherland, *Science*, 1988, **240**, 177–184.
- 152 E. M. Zeman, J. M. Brown, M. J. Lemmon, V. K. Hirst and W. W. Lee, *Int. J. Radiat. Oncol.*, 1986, **12**, 1239–1242.
- 153 Y. M. Delahoussaye, M. P. Hay, F. B. Pruijn, W. A. Denny and J. M. Brown, *Biochem. Pharmacol.*, 2003, **65**, 1807–1815.
- 154 J. Brown, *Br. J. Cancer*, 1993, **67**, 1163–1170.
- 155 W. R. Wilson and M. P. Hay, *Nat. Rev. Cancer*, 2011, **11**, 393–410.
- 156 K. B. Peters and J. M. Brown, *Cancer Res.*, 2002, **62**, 5248–5253.
- 157 S. B. Reddy and S. K. Williamson, *Expert Opin. Investig. Drugs*, 2009, **18**, 77–87.
- 158 L. J. O'Connor, C. Cazares-Körner, J. Saha, C. N. G. Evans, M. R. L. Stratford, E. M. Hammond and S. J. Conway, *Nat. Protoc.*, 2016, **11**, 781–794.
- 159 C. Cazares-Körner, I. M. Pires, I. D. Swallow, S. C. Grayer, L. J. O'Connor, M. M. Olcina, M. Christlieb, S. J. Conway and E. M. Hammond, *ACS Chem. Biol.*, 2013, **8**, 1451–1459.
- 160 N. Graf and S. J. Lippard, *Adv. Drug Deliv. Rev.*, 2012, **64**, 993–1004.
- 161 S. R. Bramhall, A. Rosemurgy, P. D. Brown, C. Bowry and J. A. C. Buckles, *J. Clin. Oncol.*, 2001, **19**, 3447–3455.
- 162 T. W. Failes, C. Cullinane, C. I. Diakos, N. Yamamoto, J. G. Lyons and T. W. Hambley, *Chem. Eur. J.*, 2007, **13**, 2974–2982.
- 163 N. Yamamoto, A. K. Renfrew, B. J. Kim, N. S. Bryce and T. W. Hambley, *J. Med. Chem.*, 2012, **55**, 11013–11021.
- 164 E. Wexselblatt and D. Gibson, *J. Inorg. Biochem.*, 2012, **117**, 220–229.
- 165 S. J. Butler, M. Delbianco, L. Lamarque, B. K. McMahon, E. R. Neil, R. Pal, D. Parker, J. W. Walton and J. M. Zwieter, *Dalton. Trans.*, 2015, **44**, 4791–4803.
- 166 A. J. Palmer, S. H. Ford, S. J. Butler, T. J. Hawkins, P. J. Hussey, R. Pal, J. W. Walton and D. Parker, *RSC Adv.*, 2014, **4**, 9356–9366.

- 167 M. Soulié, F. Latzko, E. Bourrier, V. Placide, S. J. Butler, R. Pal, J. W. Walton, P. L. Baldeck, B. Le guennic, C. Andraud, J. M. Zwier, L. Lamarque, D. Parker and O. Maury, *Chem. Eur. J.*, 2014, **20**, 8636–8646.
- 168 J. M. Cross, N. Gallagher, J. H. Gill, M. Jain, A. W. McNeillis, K. L. Rockley, F. H. Tscherny, N. J. Wirszycz, D. S. Yufit and J. W. Walton, *Dalton. Trans.*, 2016, **45**, 12807–12813.
- 169 J. W. Walton, R. Carr, N. H. Evans, A. M. Funk, A. M. Kenwright, D. Parker, D. S. Yufit, M. Botta, S. De Pinto and K. L. Wong, *Inorg. Chem.*, 2012, **51**, 8042–8056.
- 170 J. W. Walton, A. Bourdolle, S. J. Butler, M. Soulie, M. Delbianco, B. K. McMahon, R. Pal, H. Puschmann, J. M. Zwier, L. Lamarque, O. Maury, C. Andraud and D. Parker, *Chem. Commun.*, 2013, **49**, 1600–1602.
- 171 C. Gossens, I. Tavernelli and U. Rothlisberger, *J. Phys. Chem. A*, 2009, **113**, 11888–11897.
- 172 A. A. F. Peacock, S. Parsons and P. J. Sadler, *J. Am. Chem. Soc.*, 2007, **129**, 3348–3357.
- 173 J. C. Dabrowiak, *Metals in Medicine*, John Wiley & Sons, Ltd., 2nd edn., 2017.
- 174 J. Bezençon, M. B. Wittwer, B. Cutting, M. Smieško, B. Wagner, M. Kansy and B. Ernst, *J. Pharm. Biomed. Anal.*, 2014, **93**, 147–155.
- 175 A. Krężel and W. Bal, *J. Inorg. Biochem.*, 2004, **98**, 161–166.
- 176 P. Moore, *Inorganic Reactions Mechanisms*, CRC Press, Boca Raton, 4th edn., 1988.
- 177 S. H. van Rijt, A. F. A. Peacock, R. D. L. Johnstone, S. Parsons and P. J. Sadler, *Inorg. Chem.*, 2009, **48**, 1753–1762.
- 178 M. Melchart, A. Habtemariam, S. Parsons, S. A. Moggach and P. J. Sadler, *Inorganica. Chim. Acta*, 2006, **359**, 3020–3028.
- 179 W. Kandioller, C. G. Hartinger, A. A. Nazarov, M. L. Kuznetsov, R. O. John, C. Bartel, M. A. Jakupec, V. B. Arion and B. K. Keppler, *Organometallics*, 2009, **28**, 4249–4251.
- 180 S. H. van Rijt, I. Romero-Canelón, Y. Fu, S. D. Shnyder and P. J. Sadler, *Metallomics*, 2014, **6**, 1014–1022.
- 181 I. Romero-Canelón, L. Salassa and P. J. Sadler, *J. Med. Chem.*, 2013, **56**, 1291–1300.
- 182 K. Karidi, A. Garoufis, A. Tsipis, N. Hadjiliadis, H. den Dulk and J. Reedijk, *Dalton. Trans.*, 2005, 1176–1187.
- 183 T. G. Scrase, M. J. O'Neill, A. J. Peel, P. W. Senior, P. D. Matthews, H. Shi, S. R. Boss and P. D. Barker, *Inorg. Chem.*, 2015, **54**, 3118–3124.

- 184 C. A. G. N. Montalbetti and V. Falque, *Tetrahedron*, 2005, **61**, 10827–10852.
- 185 E. Valeur and M. Bradley, *Chem. Soc. Rev.*, 2009, **38**, 606–631.
- 186 Z. Zhou, G. H. Sarova, S. Zhang, Z. Ou, F. T. Tat, K. M. Kadish, L. Echegoyen, D. M. Guldi, D. I. Schuster and S. R. Wilson, *Chem. Eur. J.*, 2006, **12**, 4241–4248.
- 187 R. Lavoie, G. Bouchain, S. Frechette, S. H. Woo, E. A. Khalil, S. Leit, M. Fournel, P. T. Yan, M.-C. Trachy-Bourget, C. Beaulieu, Z. Li, J. Besterman and D. Delorme, *Bioorg. Med. Chem. Lett.*, 2001, **11**, 2847–2850.
- 188 J. M. Cross, T. R. Blower, N. Gallagher, J. H. Gill, K. L. Rockley and J. W. Walton, *Chempluschem*, 2016, **81**, 1276–1280.
- 189 Y. Geldmacher, M. Oleszak and W. S. Sheldrick, *Inorganica. Chim. Acta*, 2012, **393**, 84–102.
- 190 S. Betanzos-Lara, O. Novakova, R. J. Deeth, A. M. Pizarro, G. J. Clarkson, B. Liskova, V. Brabec, P. J. Sadler and A. Habtemariam, *J. Biol. Inorg. Chem.*, 2012, **17**, 1033–1051.
- 191 M. H. Baik, R. A. Friesner and S. J. Lippard, *J. Am. Chem. Soc.*, 2003, **125**, 14082–14092.
- 192 T. Higashi, K. Inami and M. Mochizuki, *J. Heterocycl. Chem.*, 2008, **45**, 1889–1892.
- 193 A. Kotsiou and C. Tesseromatis, in *Oral Bioavailability*, John Wiley & Sons, Inc., Hoboken, NJ, USA, 2011, pp. 145–166.
- 194 M. J. Costanzo, M. N. Patel, K. A. Petersen and P. F. Vogt, *Tetrahedron Lett.*, 2009, **50**, 5463–5466.
- 195 J. Yang, J. Tummatorn, R. Slegeris, S. F. Tlais and G. B. Dudley, *Org. Lett.*, 2011, **13**, 2065–2067.
- 196 A. Fürstner and C. C. Stimson, *Angew. Chemie*, 2007, **119**, 9001–9005.
- 197 M. Gozzi, B. Schwarze, M.-B. Sárosi, P. Lönnecke, D. Drača, D. Maksimović-Ivanić, S. Mijatović and E. Hey-Hawkins, *Dalt. Trans.*, 2017, **46**, 12067–12080.
- 198 M. A. Bennett and A. K. Smith, *Dalton. Trans.*, 1974, 233–241.
- 199 S. Scheiner, in *Noncovalent Forces*, ed. S. Scheiner, Springer International Publishing, 2015, pp. 15–24.
- 200 N. J. Porter, A. Mahendran, R. Breslow and D. W. Christianson, *Proc. Natl. Acad. Sci.*, 2017, **114**, 18–23.
- 201 Y. Miyake, J. J. Keusch, L. Wang, M. Saito, D. Hess, X. Wang, B. J. Melancon, P. Helquist, H. Gut and P. Matthias, *Nat. Chem. Biol.*, 2016, **12**, 748–754.

- 202 A. A. Adeniyi and P. A. Ajibade, *Molecules*, 2013, **18**, 3760–3778.
- 203 G. A. Jeffrey, *An Introduction to Hydrogen Bonding*, Oxford University Press, 1997.
- 204 R. Wu, Z. Lu, Z. Cao and Y. Zhang, *J. Am. Chem. Soc.*, 2011, **133**, 6110–6113.
- 205 S. M. Kelly and B. H. Lipshutz, *Org. Lett.*, 2014, **16**, 98–101.
- 206 K. Abiraj and D. C. Gowda, *J. Chem. Res.*, 2003, 332–333.
- 207 A. S. Madsen, H. M. E. Kristensen, G. Lanz and C. A. Olsen, *ChemMedChem*, 2014, **9**, 614–626.